Università degli Studi di Torino
Scuola di Dottorato in Scienza ed Alta Tecnologia

Unveiling the Nature of Faraway Worlds:
Intensive characterisation of *K2* transiting exoplanets

Oscar Ignacio Barragán Villanueva

Università degli Studi di Torino
Scuola di Dottorato in Scienza ed Alta Tecnologia

Indirizzo di Fisica ed Astrofisica

Unveiling the Nature of Faraway Worlds:
Intensive characterisation of *K2* transiting exoplanets

Oscar Ignacio Barragán Villanueva

Supervisor: Prof. Davide Gandolfi

iv

To all the people who contributed
to make these last three years,
unforgettable and happy.

—

A toda la gente que contribuyó
a hacer de estos últimos tres años,
inolvidables y felices.

—

A tutte le persone che hanno contribuito
per fare questi ultimi tre anni,
indimenticabili e felici.

Me di cuenta el porque decidí ser astrónomo,
ya que mientras hay gente que hace astronomía por sentirse más grande,
yo lo hago para sentirme niño.

Agradecimientos
Acknowledgements

Quizá tú piensas que estos últimos tres años han tratado sobre como un terricola fue capaz de desentrañar misterios de mundos lejanos sentado frente a una computadora con frecuentes sobredosis de café. Pero realmente estos últimos tres años han tratado de nosotros, de aquellos momentos que tú y yo pasamos juntos. Las constantes serendipias de la vida trajeron a mi vida personas que soy dichoso de conocer. Y yo al ser tan afortunado de tener que agradecer a tantos nombres, he decidido hacer esta sección de agradecimientos un poco más personal. Así que escribiré las experiencias que tuvimos juntos, y si tú sonríes cuando lo leas, ten por seguro que me refiero a ti. Obviamente, puede que haya más de un *gracias* para ti.

You might think that these last three years have been about how a human was able to study faraway worlds remaining sited in front of a computer with a constant overdose of coffee. But in reality, these years have been about us, about all the moments that we spent together. The constant serendipity of life brought me a lot of people who make me feel blissful. I feel really fortunate that I need to say "thank you" to a lot of people. I have thus decided to make this acknowledgement section more personal. I write our experiences, and if you smile while reading them, be sure that the acknowledgement was written for you. Obviously, there may be more than one "thanks" for you.

- A ti que me apoyaste a seguir este sueño, aunque esto implicara estar lejos.
  To you who gave me your support to follow this dream, even if this has kept us apart.

- A ti que no importa donde fuera, me hiciste sentir en casa.
  To you who, no matter where, make me feel at home.

- A ti que disfrutas mis locuras tanto como yo.
  To you who enjoy my craziness just like me.

- A ti con quien compartí un viaje en el que aprendimos juntos.
  To you with whom I shared a trip in which we both learned together.

- A ti con quien compartí cafés y buenas charlas.
  To you with whom I shared coffees and good talks.

- A ti con quien compartí una cerveza (o muchas más).
  To you with whom I shared one beer (or even more).

- A ti que siempre me apoyaste incondicionalmente.
  To you who always supported me, no matter what.

- A ti con quien compartí un sinnúmero de risas.
  To you with whom I shared a countless number of laughs.

- A ti que me enseñaste cosas nuevas, ya sea académicas o personales.
  To you who taught me new things, both academic and personal.

- Y sobre todo a ti, que no importa cuantos mundos haya afuera, haces que este sea siempre mi favorito.
  And of course to you, because it does not matter how many worlds exist out there, you make this my favourite one.

¡Muchas Gracias! Grazie mille! Thanks a lot!

Abstract

A new branch of astrophysics was born with the discovery of the first planet orbiting a star other than the Sun. Since then, astronomers have developed techniques to detect and characterise exoplanets. The two more successful techniques are the transit and radial velocity methods. They allow us to measure the planetary radius and minimum mass, respectively. By combining transit photometry with RV measurements, it is possible to measure the true mass and determine the planetary mean density. This allows us to study planets' internal structure and composition and gives us important hints as to their formation and evolution.

In its extended *K2* mission, *Kepler* is surveying different stellar fields located along the ecliptic, performing 80-day-long continuous observations of 10 000–20 000 stars per campaign. The *K2* mission is an unique opportunity to gain knowledge of transiting exoplanets. *K2* is targeting a number of bright stars ($V \lesssim 13\,\mathrm{mag}$) higher than the original *Kepler* mission. This is a definitive advantage for any RV follow-up observations. The opportunity for exoplanetary science is terrific!

We present an intensive high-precision radial velocity follow-up of bright *K2* stars ($V \lesssim 13\,\mathrm{mag}$) hosting transiting planets. We developed numerical tools, which allowed us to simultaneously model radial velocity measurements and transit light curves in order to derive planetary masses and radii.

We derived the masses, radii, and bulk densities of the exoplanets transiting the stars K2-19, K2-98, K2-139, K2-141, K2-111, HD 3167, GJ 9827 observed by *K2*, and π Mensae observed by *TESS*.

We were able to infer the internal structure, composition, dynamical evolution, tidal interaction, architecture, and the existence/absence of atmospheres of the characterised exoplanets. Some of the planets here presented join the small group of short-period planets known to have rocky terrestrial compositions. The densities of the remaining objects are indicative of planets with a composition comprising a solid core surrounded by a thick atmospheric envelope. Because of the brightness of the host stars, most of the systems here presented are highly suitable for a wide range of further studies to characterise the planetary atmosphere and dynamical properties.

This thesis contributes to the exoplanet science by itself. It adds new well-characterised planets to the relatively small sample of super-Earths and Neptunes whose masses and radii are both well-determined. These results will contribute to solve many unanswered questions about the nature of faraway worlds.

List of publications that present work from this thesis

1. **Barragán O.** et al., 2018, *K2-141 b: A 5-$M_\oplus$ super-Earth transiting a K7 V star every 6.7 hours*, A&A, 612, A95.

2. **Barragán O.** et al., 2018, *K2-139 b: a low-mass warm Jupiter on a 29-day orbit transiting an active K0 V star*, MNRAS, 475, 1765.

3. **Barragán O.**, et al., 2016, *K2-98 b: A 32-$M_\oplus$ Neptune-sized planet in a 10-day orbit transiting an F8 star*, AJ, 152, 6.

4. **Barragán O.**, Gandolfi D., & Antoniciello G., 2019, `pyaneti`: *a fast and powerful software suite for multi-planet radial velocity and transit fitting*, MNRAS, 482, 1017.

5. Fridlund M., Gaidos E., **Barragán O.**, et al., 2017, *K2-111 b - A short period super-Earth transiting a metal poor, evolved old star*, A&A, 604, A16.

6. Gandolfi D., **Barragán O.**, et al, 2017, *The transiting multi-planet system HD3167: a 5.7 $M_\oplus$ Super-Earth and a 8.3 $M_\oplus$ mini-Neptune*, AJ, 154, 123.

7. Gandolfi D., **Barragán O.**, et al, 2018, *TESS's first planet: a super-Earth transiting the naked-eye star π Mensae*, A&A, 619, L10.

8. Guenther E. W., **Barragán O.**, et al., 2017, *K2-106, a system containing a metal rich planet and a planet of lower density*, A&A, 608, A93.

9. Livingston J., Endl M., Dai F., Cochran W. D., **Barragán O.**, et al., 2018, *44 Validated Planets from K2 Campaign 10*, AJ, 156, 78.

10. Nespral D., Gandolfi D., Deeg, H. J., Borsato, L., Fridlund M. C. V., **Barragán O.**, et al. 2016, *Mass determination of K2-19b and K2-19c from radial velocities and transit timing variations*, A&A, 601, A128.

11. Niraula P., Redfield S., Dai F., **Barragán O.**, 2017, *Three Super-Earths Transiting the nearby star GJ 9827*, AJ, 154, 266.

12. Palle E., Nowak G., Luque R., Hidalgo D., **Barragán O.** et al., 2018, *Detection and Doppler monitoring of EPIC 246471491, a system of four transiting planets smaller than Neptune*, A&A, submitted, (arXiv:1808.00575).

13. Persson C. M., Fridlund M., **Barragán O.**, et al., 2018, *An 8 $M_\oplus$ super-Earth in a 2.2 day orbit around the K5V star K2-216*, A&A, 18, A33.

14. Prieto-Arranz J., Palle E., Gandolfi D., **Barragán O.**, et al., 2018, *Mass determination of the 1:3:5 near-resonant planets transiting GJ 9827 (K2-135)*, A&A, 618, A116.

Contents

Acronyms

CCD .... Charged coupled device

EPIC .... Ecliptic Plane Input Catalog

FITS .... Flexible image transport system

LC .... Light curve

LDC .... Limb darkening coefficients

MAST .... Mikulski Archive for Space Telescopes

MCMC .... Markov chain Monte Carlo

ppm .... Parts per million

RV .... Radial velocity

TPF .... Target pixel file

USP .... Ultra-short period

Units

In this work we use the unit conventions described by Prša et al. (2016, Resolution B3 of the IAU general assembly of 2015).

- Solar radius, $R_\odot = 6.957 \times 10^{10}$ cm.
- Solar mass, $M_\odot = 1.988 \times 10^{33}$ g.
- Solar effective temperature, $T_\odot = 5772$ K.
- Jupiter radius, $1 R_{\rm J} = 7.1492 \times 10^9$ cm.
- Jupiter mass, $1 M_{\rm J} = 1.898 \times 10^{30}$ g.
- Earth radius, $1 R_\oplus = 6.3781 \times 10^8$ cm.
- Earth mass, $1 M_\oplus = 5.971 \times 10^{27}$ g.
- Astronomical Unit, $\mathrm{AU} = 1.4960 \times 10^{13}$ cm.
- Gravitational constant, $\mathrm{G} = 6.67408 \times 10^8 \, \mathrm{cm}^3 \, \mathrm{g}^{-1} \, \mathrm{s}^{-2}$.

CHAPTER 1

INTRODUCTION

1.1 Dancing stars

Since the dawn of time, humankind has been amazed by the mystery of the night. A countless number of stars illuminated the clear nights of all the civilisations that populated our World.

This immutable beauty was complemented by five dancing stars in the sky. Ancient Greeks called those moving stars *planets*, which means wanderers. Planets were entities of unknown nature, but of great interest for all cultures. Their dance around our World should tell us something about the Universe we live in.

Later in time, observations driven by curiosity showed that the planets' motion in the sky is complex. Yet, they follow irregular patterns, an encrypted choreography. The decoding of this motion taught us that planets move around the Sun. And something more important, our World also revolves around the Sun, our World is a planet. This realisation unveiled the true nature of those dancing stars: planets are worlds.

When we learned about the existence of other worlds, we changed our perception of our place in the Universe. By unveiling their nature we will know if we are a common manifestation of nature, or, if we are just a serendipitous instant in the Cosmos.

1.2 Towards the first faraway world

"Each Sun is the centre of as many worlds which are distributed in as many distinct series in an infinite number of concentric systems", those are the words of an Italian philosopher from the XVI century called Giordano Bruno (Bruno & Williams, 1887). He probably thought about this after he learned that our World is part of a system of worlds which revolve around the Sun. The existence of faraway worlds persisted when we learned that the motion of the planets around the Sun was a consequence of a physical phenomenon called *gravity*. As Isaac Newton said: "if the fixed stars are the centres of other like systems, these [...] must be all subject to the dominion of One; especially since the light of the fixed stars is of the same nature with the light of the Sun ..." (see the translation to English of *Principia* by Cohen et al., 1999). Therefore, if stars are faraway Suns, why

should not exist faraway worlds?

A great step to understand the existence of other worlds came to us when the first models of the Solar System formation appeared in the XVIII century. Swedenborg (1734) devised that the Solar System – including the Sun, planets and minor bodies – originated from the same structure. This idea was taken by Kant (1755) and Laplace (1976) to suggest that the Solar System formed from a large cloud of gas. Nowadays, the formation of the Solar System via the collapse of nebula is accepted. The currently accepted idea is called the *solar nebular disc model* (SNDM, Safronov, 1972). This model suggests that stars are formed from the collapse of dense clouds in star nurseries inside the galaxy. When such clouds become unstable, matter collapse to dense clumps. If the cloud has angular momentum, this collapse generates a rotating disc. The central region of such a structure, also called circumstellar disc, becomes a star, while planets may form in the disc. If stars formed in a similar way than the Sun, they may have planets.

All the evidence about the existence of planets around faraway stars was there: galaxies have regions with gas and molecules; gas collapses in these zones to create circumstellar discs; from these structures stars and planets form. But the final piece in the puzzle was still missing: the detection of a faraway planet.

At the beginning of the XX century, it was accepted that faraway planets should exist. But, the first claimed discoveries were refuted with improved methods and observations (e.g., Jensen & Ulrych, 1973; Reuyl & Holmberg, 1943; Strand, 1943). Struve (1952) tried to answer the question: "How should we proceed to detect them?". He argued that close-in planet mass companions could be discovered indirectly by the detection of periodic variations on the radial velocity of the hosting star. He also discussed the possible indirect detection of planets by detecting the loss of light when the planet eclipses its host star. Could astronomers be able to "translate" light variations into faraway worlds?

The nineties marked the first confirmed detection of extrasolar planetary mass objects around the millisecond pulsar PSR 1257+12 by Wolszczan & Frail (1992). They confirmed the existence of three Earth-mass bodies by measuring the nanosecond changes of the pulsar period. This was the first irrefutable evidence of planet-mass objects orbiting an extrasolar object. However, the community was still searching for planetary objects around *other Suns*.

The wait for faraway worlds that lasted more than 400 years ended when Mayor & Queloz (1995) detected a planet-mass object orbiting a main-sequence star. They discovered the presence of a Jupiter-mass companion around the star 51 Pegasi. They detected the oscillations of the radial velocity of the star induced by the planet, as predicted by Struve (1952, for more details see Sect., 1.4.1). At this point in history we learned that 51 Pegasi is the centre of a system orbited by the faraway planet 51 Peg b, the first extrasolar planet, or also called, *exoplanet*. This was the beginning of a new age in astronomy: the era of faraway worlds.

1.3   What is an exoplanet?

The fist official definition of "planet" was established in 2006 at the International Astronomical Union (IAU) assembly. According to the IAU resolutions B5 and B6[1], a solar system body is a planet if fulfils the three requirements:

1. it orbits around the Sun.

2. it has sufficient mass for its self-gravity to overcome rigid body forces so that it assumes a hydrostatic equilibrium (nearly round) shape.

---

[1]They can be consulted at https://www.iau.org/static/resolutions/Resolution_GA26-5-6.pdf.

3. it has cleared the neighbourhood around its orbit.

By following this definition, there are eight planets in the Solar System. The five bright naked-eye planets (Mercury, Venus, Mars, Jupiter ans Saturn), the two planets discovered by a telescope (Uranus and Neptune), and our planet Earth.

A formal definition of exoplanets has to expand the Solar System planet definition to a more general context. This was done during the IAU general assembly in 2018, when a general definition of planet – which includes exoplanets – was discussed. The new resolution defines planets as objects with true masses below the limiting mass for thermonuclear fusion of deuterium (currently estimated to be 13 Jupiter masses for objects of solar metallicity) that orbits stars, brown dwarfs, or stellar remnants and that have a mass ratio with the central object below the L4/L5 instability ($M/M_{\text{central}} < 2/(25 + \sqrt{521}) \approx 1/25$), no matter how they formed. The minimum mass required for an extrasolar object to be considered a planet is the same as that used for the planets of our Solar System (Mamajek, 2018).

1.3.1 Exoplanet nomenclature

The scientific nomenclature for the designations of exoplanets usually consists of two elements: 1) a proper noun or abbreviation, sometimes with associated numbers, 2) followed by a lower-case letter[2].

The first element can derive from a number of sources. A common source is an exoplanet's host star's widely recognised, common or astronomical catalogue name. Alternatively, exoplanets are often named after the scientific instrument or project that discovered the exoplanet (such as WASP-, CoRoT-, Kepler- or K2-). However, it is preferred to use stellar names already in existing catalogues (such as HD or GJ).

Unlike the proper noun, the letter has to be used universally in almost all nomenclature styles. The letter indicates the order of the planet's discovery around its host star. The first exoplanet discovered in another system is designated with the letter b; the second, c; the third, d; and so on. The letter does not indicate the planet's orbital placement around its host star, so Exoplanet-c can be closer to, or farther away from, the star that it co-orbits with Exoplanet-b. For multiple systems, it is recommended to identify the central system with parentheses when the planets orbit more than one star (e.g., Kelper-16(AB) b), using upper cases for the central objects and lower case for the planetary objects.

This thesis focuses on exoplanets discovered with the NASA's *K2* mission. For the newly discovered planets, we adopt NASA exoplanet naming policy[3].

1.4 Detection methods

In this work, we will focus only on the description and achievements of two methods which detect exoplanets by the observable effects on their host stars: the radial velocity and transit methods. We warn the reader about the existence of other techniques to discover exoplanets, e.g., direct imaging (Boccaletti, 2011), pulsar timing (Wolszczan & Frail, 1992), astrometry (Benedict et al., 2002), and microlensing (Bond et al., 2004). We note that out of the 3823 exoplanets known to date[4], 3601 have been discovered with the RV and transit methods. Figure 1.1 shows the planet mass *vs* orbital period plot. The different colours/symbols refer to the different detection methods.

---

[2]According to the IAU exoplanet name designation https://www.iau.org/public/themes/naming_exoplanets/.

[3]Available at https://exoplanetarchive.ipac.caltech.edu/docs/K2Numbers.html.

[4]As of Sept. 10, 2018, www.exoplanet.eu.
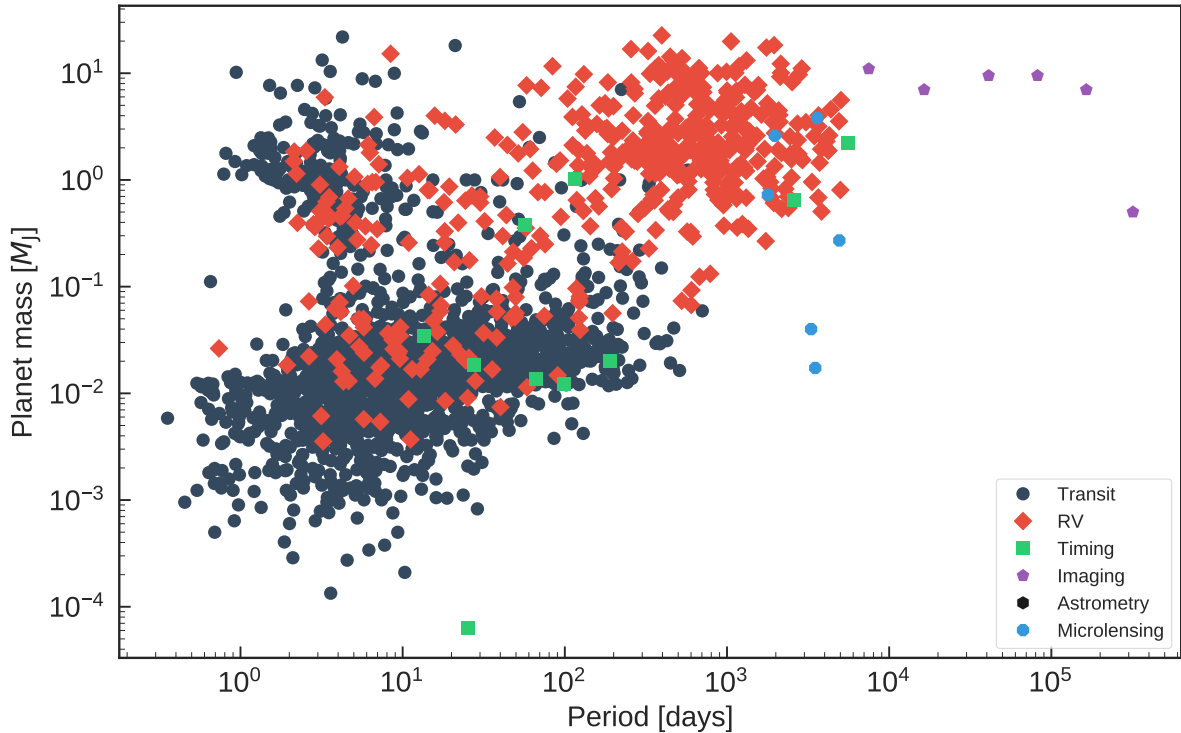
Figure 1.1: Planet mass *vs* orbital period plot. Different colours/symbols refer to a discovery technique. The figure was created with data downloaded from exoplanets.org, as of Sept. 07, 2018.

1.4.1 Radial Velocity method

The radial velocity (RV) of a star is defined as the velocity component along the line-of-sight of an observer. It can be measured through Doppler spectroscopy by comparing the measured wavelengths of known spectral lines to wavelengths from laboratory measurements. A positive RV indicates that the distance between the star and the observer is increasing, whereas a negative RV indicates that the distance between the source and the observer is decreasing.

If a star hosts a planet, then both objects orbit around their centre of mass – the so called *barycentre*. Provided the plane of the orbit is not face-on (i.e., at right angle to the line of sight), the stellar RV changes periodically as the the star moves around the centre of mass of the system (Sect. 2.2). The RV variations induced by the unseen planet can be measured by observing the periodic red and blue shift of the stellar spectral lines (Doppler effect). By detecting the periodic RV variation, we can indirectly infer the presence of a planet around a star (Hatzes, 2016).

The detection of the Doppler reflex motion induced by the presence of a planetary companion requires spectrographs with precision ranging from $\sim$0.01 to 100 m s^{-1}, depending on the planetary mass and orbital radius (see also Chapter 4). The most massive planet in the solar system, Jupiter, has an orbital period of P=11.9 years, corresponding to a semi-major axis of a=5.2 AU. Jupiter induces a Doppler velocity variation in the Sun of 11.2 m s^{-1}. If Jupiter were orbiting the Sun every 3 days, the RV semi-amplitude would be $\sim$150 m s^{-1}. For an Earth-mass planet, the reflex motion of the Sun is 0.01 m s^{-1} and 0.6 m s^{-1} for P=1 day and P=1 year, respectively.

The Doppler reflex motion induced by a planet is proportional to $\propto M_{\mathrm{p}}/M_{\star}^{2/3}$, where M_{p} is the mass of the planet and $M_{\star}$ is the mass of the star. If the stellar mass is known by an independent method (e.g., spectroscopy, astereoseismology), we can estimate the

planet mass. However, the radial velocity technique provides only the velocity component of the star along the line of sight. Therefore, this method allows us to measure only the *planet minimum mass* defined as $M_\mathrm{p} \sin i$, where i is the orbital inclination with respect the plane tangential to the celestial sphere at the location of the system's centre of mass. In order to determine the *planet true mass* it is necessary to measure the orbit inclination using other methods, such as the transit method (see Sect. 1.4.2). The RV method allows also to measure the orbital parameters such as period, eccentricity, and angle of periastron (see Sect. 2.2).

We can rightfully argue that the RV technique has played – and it is still playing! – a major role in exoplanet science. It is the method that started the quest for "exoworlds"and it is the second most successful detection technique, with about 800 planet discoveries announced so far[5]. The first "Doppler-evidence" of the presence of a planet orbiting a star other than the Sun came between the end of the eighties and the beginning of the nineties, when spectrographs reached the $10\,\mathrm{m\,s^{-1}}$ precision (Hatzes, 2016). The radial velocity survey conducted by Campbell et al. (1988) suggested the presence of a planet orbiting the sub-giant star $\gamma\,\mathrm{Cep\,A}$. However, the claim was retracted in 1992 because the quality of the data was not good enough to firmly establish the discovery. The planet was later confirmed by Hatzes et al. (2003) by combining observations spanning 21 years. Latham et al. (1989) reported on the discovery of a sub-stellar companion with a minimum mass of $M_\mathrm{p} \sin i = 11\,M_\mathrm{J}$ orbiting the solar-like star HD 114762 every 84 days. Although the minimum mass of HD 114762 b is below the deuterium burning limit($13\,M_\mathrm{J}$), the object was not classified as a planet because the orbit inclination, and thus the planet true mass, were unknown.

The first confirmed extrasolar planet was announced by Mayor & Queloz (1995), who discovered that the star 51 Peg hosts a Jupiter-mass companion on a 4.2-day. The discovery was made using high-precision RV measurements collected with the ELODIE spectrograph installed at the 1.93 m telescope of the Observatoire de Haute-Provence in France. Given the planet minimum mass of $0.47\,M_\mathrm{J}$, the probability that 51 Peg b is a brown dwarf is less than 1%, suggesting that the unseen companion is actually a planet.

The discovery of 51 Peg b was followed by numerous other RV detections, making exoplanet research one of the most vibrant and exciting field in modern astrophysics. Although in the past 10 years the transit method (Sect. 1.4.2) has surpassed the RV technique in terms of number of planet discoveries, the RV method still plays a fundamental role in transit discoveries as it provides the planetary mass and the orbit eccentricity (e.g., Hatzes, 2016, see also Sect 2.2).

Figure 1.1 shows the planet mass *vs* period diagram. It is clear how the RV method is biased towards massive and short period planets. This is a consequence of the dependence of the induced RV variation on the planetary mass and orbital period ($\propto M_\mathrm{p}\,P^{-1/3}$; see Chapter 4 for more details). Nevertheless, mass measurements have been possible even for objects in the Earth-mass domain thanks to state-of-the-art spectrographs that have allowed to measure stellar RV variation with a precision of $\sim 1\,\mathrm{m\,s^{-1}}$(e.g., HARPS, HARPS-N, Mayor et al., 2003; Cosentino et al., 2012, see Sect. 4.3). Fortunately, upcoming instruments will provide measurements with even higher precision (`ESPRESSO`, `SPIRou`, Pepe et al., 2010; Donati et al., 2017); the future of Doppler spectroscopy is promising!

---

[5]Source `http://exoplanet.eu`, as of Sept. 2018.

1.4.2   Transit method

An eclipse occurs when an astronomical body is obscured by a second one. A *transit* is a special case of eclipse, in which a smaller object passes in front of a larger body. If the orbit inclination is close to $90°$, the presence of a planet orbiting its host star can be inferred by detecting the periodic drops of stellar flux caused by the planet partly occulting the stellar disc.

The transit depth yields the planet-to-star radius ratio $R_{\mathrm{p}}/R_{\star}$. If the stellar radius is known via, e.g., spectroscopy combined with parallax and broad-band photometry, transiting planets provide us with one of the fundamental parameter needed to investigate the nature of these fascinating new worlds: *the radius*. The fraction of light occulted by a planet during a transit is indeed proportional to its size, being about 1% for a Jupiter-size object and 100 times smaller for an Earth-size planet transiting a Solar-like star.

If we assume random inclination of planetary orbits, the probability of a transit to happen goes as $\approx 0.0046\,(R_{\star}/R_{\odot})\,(1\mathrm{AU}/a)$, where $R_{\star}$ is the host star radius and a is the semi-major axis of the orbit of the planet (Cameron, 2016). The probability of observing the transit of a planet with $a = 1\,\mathrm{AU}$ in front of a Sun-like star is only 0.46%. The probability drops to 0.09% if the planet is a Jupiter analogue ($a = 5.2\,\mathrm{AU}$). For short-period exoplanets ($P < 10\,\mathrm{d}$), the transit probability ranges between 2 and 10% (Cameron, 2016).

The first exoplanets discovered by RV surveys were short-period, Jupiter-mass planets orbiting main-sequence stars. Their radii were expected to be comparable to that of Jupiter, implying a transit depth of $\sim$1% – a signal detectable using the photometric detectors available at the end of the twentieth century. The small star-planet separation translated into a transit probability of about 10%, implying that 1 out of 10 planets should have transited its host star. Once the orbital solution of these planets were announced, photometric follow-up observations were conducted around the time of inferior conjunction in order to search for transits (Cameron, 2016). Shortly after the discovery of the first $\sim$10 close-in giant planets, Henry et al. (1999) and Charbonneau et al. (2000) were able to detect a transit of the giant planet HD 209458 b across the surface of its host star, making it the first known transiting extrasolar planet. Because the modelling of the transit light curve provides the orbit inclination i (see Sect. 2.4.2), HD 209458 b was also the first exoplanet with a measured true mass.

To overcome the low geometric probability of observing a transit, search programs on field stars require the simultaneous observations of a large number of targets. The wide-field photometric search for transiting planets around field stars became a reality at the beginning of the XXI century with the improvement of photometric detectors (Cameron, 2016). The most successful transit surveys, such as the transatlantic exoplanet survey (TrES, Alonso et al., 2004), the wide-angle search for planets (WASP, Pollacco et al., 2006), the Hungarian automated telescope network (HATNet and HATSouth Bakos et al., 2004, 2013) and the kilodegree extremely little telescope (KELT, Pepper et al., 2007) entered in service and started publishing new discoveries of transiting planets. Together they have surveyed about 80% of the sky, and published hundreds of confirmed discoveries of short period (P < 10 days) gas-giant and ice-giant planets transiting stars brighter than $V < 13$ mag.

The ground-based detection of planets smaller than Neptune ($R_{\mathrm{p}} < 4R_{\oplus}$) is rendered unfeasible by the Earth's atmosphere (see also Sect. 3.1). Because the transit depth is proportional to the square of the planet-to-star radius ratio, small transiting planets can still be detected using ground-based facilities if one focus on small stars, such as M dwarfs. The transit of an Earth-size planet around an M dwarf is hundred of times stronger than
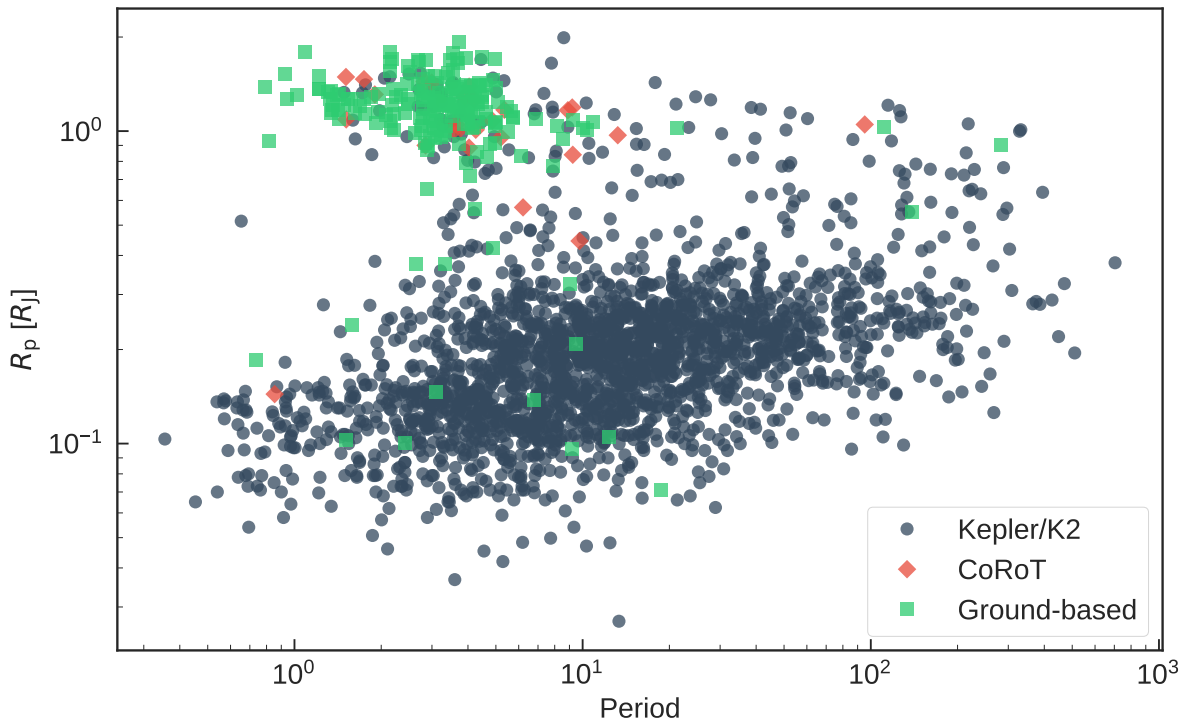
Figure 1.2: Planet radius *vs* orbital period plot for transiting exoplanets. Different colours/symbols represent different detection surveys. This plot was created with data downloaded from exoplanets.org as of Sept. 07, 2018.

around a G-type star (see Sect. 3.1). Ground-based searches for terrestrial-size planets transiting M-type dwarfs are MEarth (Irwin et al., 2015; Nutzman & Charbonneau, 2008), and the Transiting planets and planetesimals small telescope (TRAPPIST, Gillon et al., 2011; Jehin et al., 2011). They have proved that small planets can be detected with ground-based facilities (e.g., Charbonneau et al., 2009; Gillon et al., 2017).

Figure 1.2 displays the planetary radius *vs* orbital period plot for transiting exoplanets. The figure shows that transiting planets discovered by ground-based surveys are mainly short-period gas-giant planets. The few Earth-size planets found by ground-based surveys are all transiting M dwarfs.

The detection of small planets ($R_{\mathrm{p}} < 4R_{\oplus}$) transiting Sun-like stars requires space-borne photometry (see also Chapter 3). The search for transiting exoplanets from space started with the pioneering mission *CoRoT* (*COnvection, ROtation et Transits planétaires*, Auvergne et al., 2009). The mission was operational from 2006 to 2012. *CoRoT* was responsible for the discovery of 36 new transiting exoplanets. One of its major achievements was the discovery of CoRoT-7 b, the first transiting super-Earth with a measured radius (Léger et al., 2009). More details about the legacy of the *CoRoT* mission can be found in the A&A special issue about *CoRoT* (Vol. 506, 1, October IV 2009) and in the *CoRoT* legacy book (CoRot Team, 2016).

The *Kepler* mission continued the search for transiting exoplanets from space (Borucki et al., 2008) in 2009-2013. This mission monitored continuously more than 150,000 stars during four years. *Kepler* has detected more than 4,600 exoplanet candidates, from which more than 2,300 have been confirmed/validated. Further details about the *Kepler* mission are presented in Chapter 3.

The *Kepler* spacecraft suffered a serious breakdown in its navigational system in May 2013, which compromised the precise pointing of the telescope. This ended the nominal

mission. A new mission concept, called *K2*, continued the *Kepler*'s search for other worlds, albeit in a modified fashion (Howell et al., 2014, see also Chapter 3). *K2* has provided more than 300 new transiting exoplanets[6]. A significant fraction of *K2* exoplanets discoveries represent the core of this thesis and are described in Chapter 6.

Exoplanets discoveries from the *CoRoT* and *Kepler*/*K2* space missions are shown in the planet radius *vs* orbital period diagram in Figure 1.2. It is worth noting that space-based missions have led to the discovery of thousands of planets with different radii, ranging from Earth-size to inflated Jupiter-size planets.

Future exoplanet transit-search survey conducted with both ground-based (e.g., *SPECU-LOOS*, Gillon et al., 2013), and space-based (e.g., *TESS*, *PLATO*, *CHEOPS*; Ricker et al., 2015; Rauer et al., 2014; Broeg et al., 2013) facilities will provide us with a wealth of photometric time-series data sets with thousands new exoplanets.

1.5   Exoplanets' properties

The detection of planets orbiting stars other than the Sun is a fascinating result by itself. But discovery is just the first step to understand the nature of faraway worlds. Therefore, after an exoplanet is discovered, the next step is to characterise its physical properties. The radial velocity and transit methods provide planetary masses, radii, and thus densities. The analysis of these parameters helps us to unveil the nature and properties of exoplanetary systems (see, e.g., Winn & Fabrycky, 2015).

1.5.1   The mass-radius diagram

Exoplanet masses and radii are fundamental quantities in order to understand their nature. However, out of the almost 4000 exoplanets discovered so far, only 521 have both, mass and radius measurements with a precision better than 50 per cent. Figure 1.3 shows the mass-radius diagram for such planets (source: TEPCat, www.astro.keele.ac.uk/jkt/tepcat/, as of Sept. 07, 2018; Southworth, 2011).

The first thing we note in the mass-radius diagram is that planets are clustered in different region of the diagram, each region separated by a transition point. Planetary masses and radii seem to follow different relations (with different dispersion). Hatzes & Rauer (2015) found a transition in the mass-radius diagram at $\approx 0.3\,M_{\rm J}$, which separates the exoplanet population in two classes: giant and low-mass planets. This division is marked in Figure 1.3. Chen & Kipping (2017) studied this same break point with a more robust statistical approach. They found that the break point happens at $0.41 \pm 0.07\,M_{\rm J}$ (Figure 1.3). As Hatzes & Rauer (2015) and Chen & Kipping (2017) pointed out, this limit has a physical origin caused by self-compression of the planet triggered by accumulation of gas. According to planet formation theories, when a massive core forms, the planet grows in radius as more gas is accreted. At some point, the planet mass is enough to start self-compression. This stops the growth of the planet radius and accounts for the almost-flat relation between mass and radius for Jovian planets (Figure 1.3).

In the low-mass regime of the mass-radius diagram ($\lesssim 0.3\,M_{\rm J}$), a distinction between terrain and volatile envelope planets was revealed once the sample of small planets with mass and radius measurements increased. Weiss & Marcy (2014) found that, on average, planets with radii below $1.5\,R_{\oplus}$ increase in density with increasing radius. For planets with radii above $1.5\,R_{\oplus}$, the average planet density rapidly decreases with increasing radius, indicating that these planets have a large fraction of volatiles by volume overlying a rocky core. Chen & Kipping (2017) also studied this transition region with the same statistical

---

[6]As of Sept. 10, 2018, https://archive.stsci.edu/k2/published_planets.
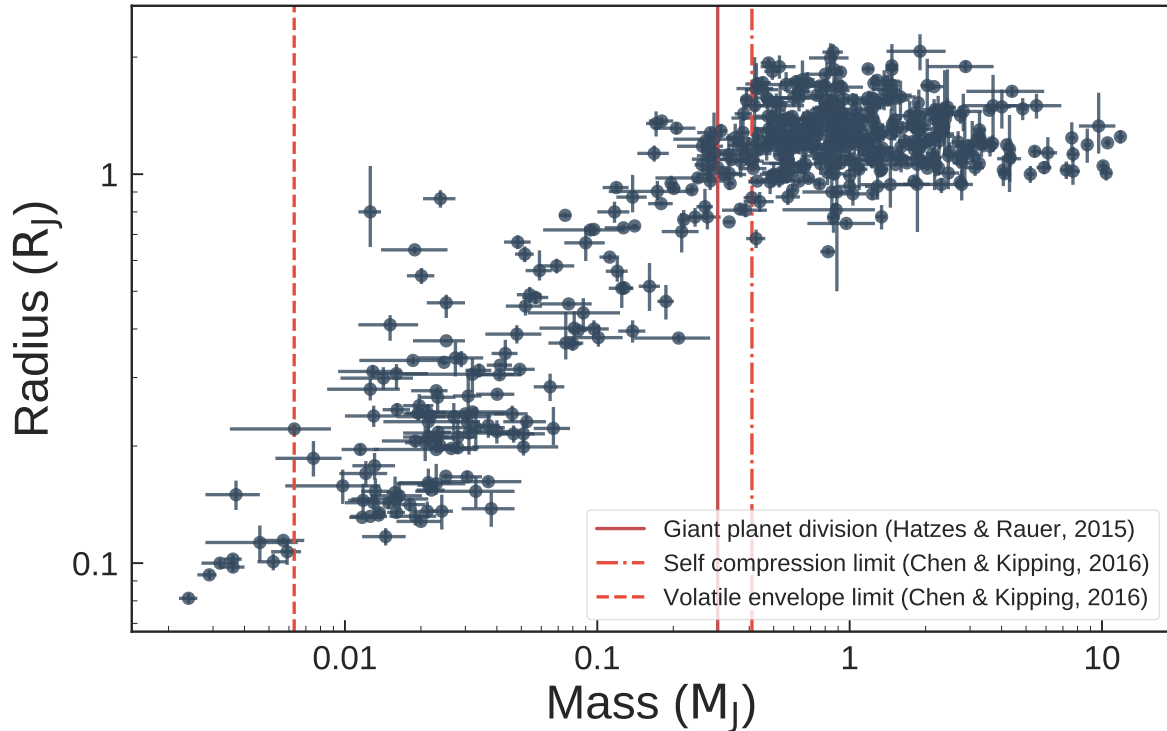
Figure 1.3: Mass-radius diagram for the 521 exoplanets whose masses and radii are known with a precision better than 50%. The high-mass–low-mass planet division found by Hatzes & Rauer (2015) is shown with a thick line. The self-compression and volatile envelope limits described by Chen & Kipping (2017) are marked with a dot-dashed and dashed line, respectively. This figure was created with data retrieved from www.astro.keele.ac.uk/jkt/tepcat/ as of Sept. 07, 2018.

approach that for the self-compression limit. They found that the transition to volatile rich planets occurs at a mass transition point of $2.0 \pm 0.7 M_{\oplus}$. Figure 1.3 shows this limit for planets with volatile envelope.

The general picture that we have learned from the mass-radius diagram is that there seems to be three kind of planets: Terrain or solid surface worlds, Neptunian planets with volatile envelope, and H/He rich Jovian planets (Chen & Kipping, 2017).

1.5.2 Exoplanets' internal composition

Masses and radii of exoplanets teach us about the general properties of faraway worlds. Both quantities allows us to determine the planet bulk density – an important "ingridient" needed to infer internal structure and composition of exoplanets. It is possible to infer internal structure of exoplanets by comparing their masses and radii with theoretical predictions that rely on composition models of multi-layer interior planets (Zeng et al., 2016).

Zeng et al. (2016) created mass-radius relations of evolved multi-layer interior planets which combine different fractions of iron (Fe), silicates ($MgSiO_3$) and water (H_2O). Figure 1.4 shows Zeng et al. (2016)'s composition models over-plotted on the mass-radius diagram for small planets. The plot also displays small exoplanets ($M_p < 10 M_{\oplus}$, $R_p < 3 R_{\oplus}$) whose masses and radii have been measured with a precision of at least 20%. The internal compositions of planets can be inferred by comparison the with different theoretical compositional models from Zeng et al. (2016). Figure 1.4 shows that planets with masses $M_p \lesssim 2 M_{\oplus}$ are rocky objects that seem to follow a tight mass-radius relation, albeit with
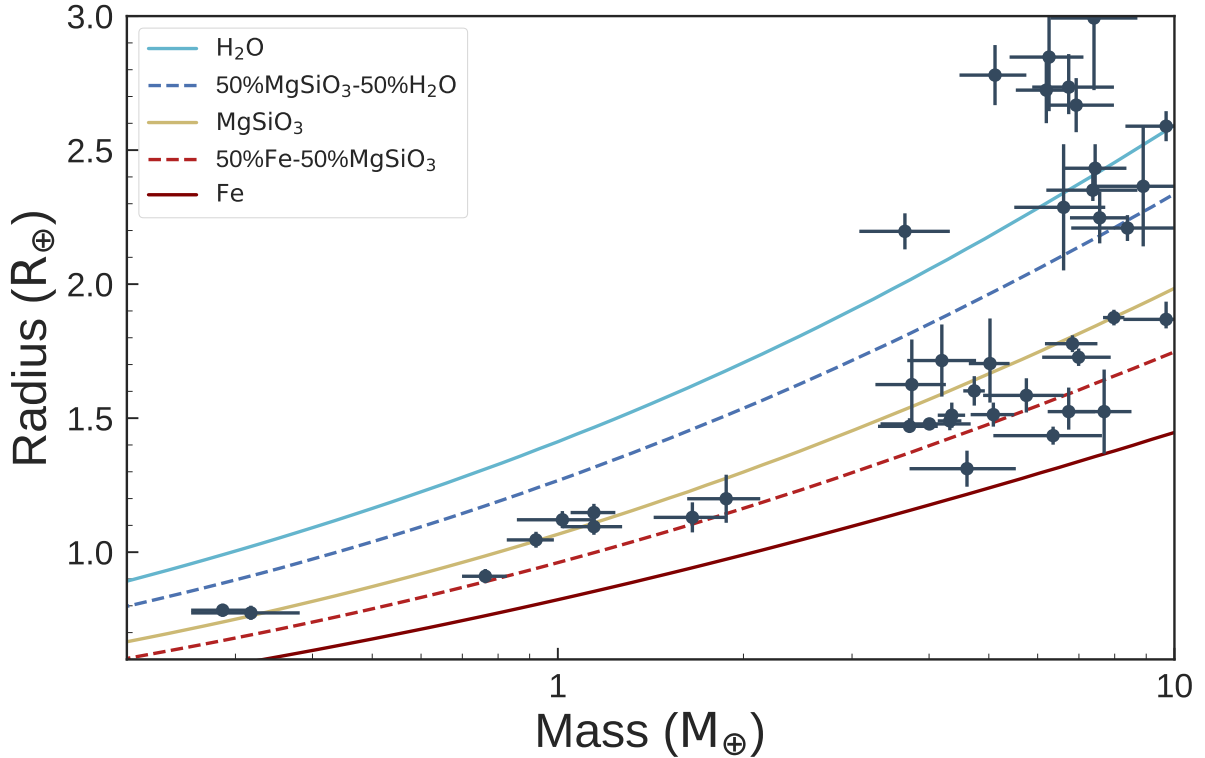
Figure 1.4: Mass *vs* radius plot. The composition models from Zeng et al. (2016) are displayed with different lines and colours. Circles with error bars mark mass and radius of exoplanets measured with a precision better than 20% (data downloaded from `www.astro.keele.ac.uk/jkt/tepcat/` as of Sept. 07, 2018.)

slightly different mixture of silicates and iron. This tight mass-radius relation of low-mass exoplanets was analysed previously by Dressing et al. (2015). They found that the best fit to those planets follows a composition which consists of 17% iron and 83% silicates. Zeng et al. (2016) used exoplanets with masses and radii measurements with precision better than 30% to find that the iron/silicates ratio is 0.26 ± 0.07. Both results indicate that exoplanets with masses $M_{\rm p} \lesssim 2\,M_\oplus$ may be solid bodies with a thin atmosphere or no volatile envelope at all. On the other hand, planets with masses $M_{\rm p} \gtrsim 2\,M_\oplus$ tend to have different radii (Figure 1.4). Some of them fall on theoretical models rich in iron and silicates, while others are better explained with models containing lighter materials. This suggests that the latter might have volatile-rich envelopes.

Fortney et al. (2007) computed different planetary radii models for a wide range of planet masses. Their models also considered the planet-star distance and the system age. Figure 1.5 shows the mass-radius diagram for gas-giant planets ($M_{\rm p} > 0.3 M_{\rm J}$) with semi-major axes ~ 0.1 AU, and mass and radius measurements with a precision better than 20%. The plot also displays Fortney et al. (2007) models for different core masses for planets with semi-major axes of ~ 0.1 AU in 4.5 Gyr old systems. The mass of the cores of gaseous exoplanets can be inferred by comparing their positions with theoretical models (see, e.g., Sect., 6.2).

The knowledge of the core's mass can shed insights into the planet's formation mechanism. Boley et al. (2016) suggested that massive cores ($M_{\rm core} \gtrsim 20 M_\oplus$) can be built up from the merging of tightly packed inner planets formed at the early stages of the circum-stellar disc. Huang et al. (2016) suggested that these cores can initiate runaway
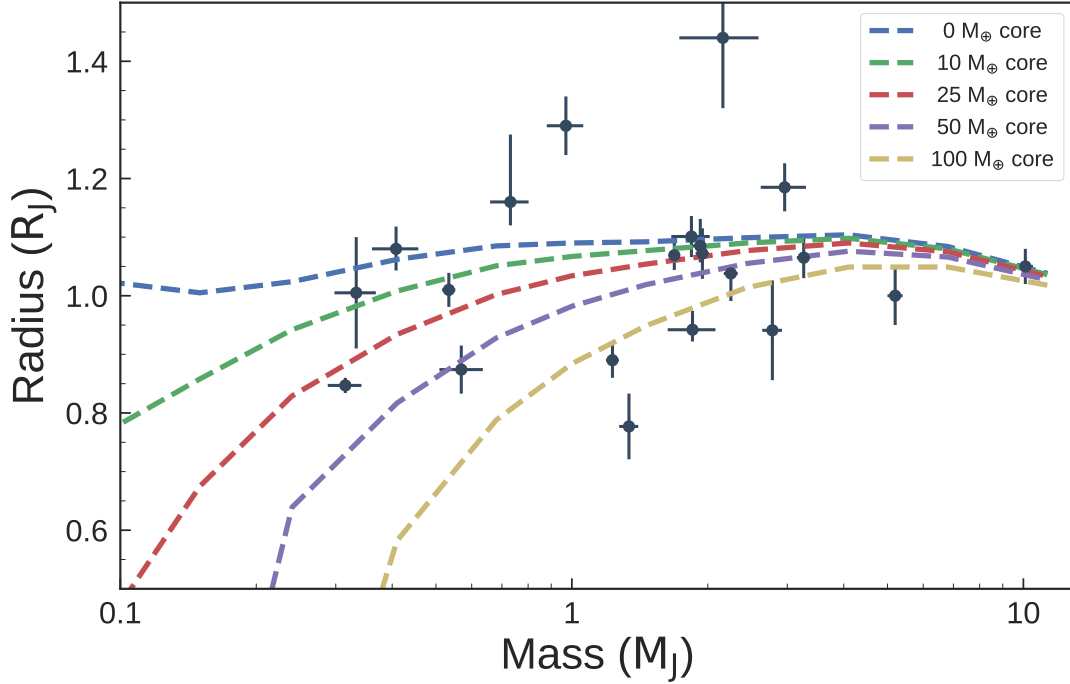
Figure 1.5: Mass-radius diagram for gas-giant planets ($M_{\rm p} > 0.3 M_{\rm J}$) with semi-major axes $\sim$0.1 AU and mass and radius measurements with a precision better than 20%. Dashed lines correspond to different solid core masses (assuming semi-major axis of the orbit equal to 0.1 AU and a system age of 4.5 Gyr, Fortney et al., 2007). This image was created with data downloaded from `www.astro.keele.ac.uk/jkt/tepcat/` as of Sept. 07, 2018.

accretion if they are formed in a region with enough gas around them, while those without enough volatiles remain super-Earths and represent the population of massive rocky planets unveiled by *Kepler* around solar-like stars (e.g., Demory, 2014).

In this section we have described some models that can be used to infer the properties of planet interiors. We warn the reader that alternative models exist in the literature.

1.5.3 The radius gap and photo-evaporation

Using precise radii for 2024 *Kepler* planets with $P_{\rm orb} < 100\,{\rm d}$, Fulton et al. (2017) found a deficit of objects with $1.5 \lesssim R_{\rm p} \lesssim 2\,R_{\oplus}$. This gap divides close-in small planets into two distinct classes: one population comprises planets with $R_{\rm p} \lesssim 1.5\,R_{\oplus}$, the other sub-Neptunes with $2 \lesssim R_{\rm p} \lesssim 3.0\,R_{\oplus}$. Theoretical models suggest that the observed gap might be due to photo-evaporation (e.g., Lopez & Fortney, 2014; Owen & Wu, 2013). According to these models, close-in (a $\lesssim 0.1$ AU) planets in the sub-Neptunes regime would lose their atmosphere within a few hundred Myr due to the intense level of photo-ionising radiation from their host stars, forming bare rocky cores.

Van Eylen et al. (2018a) revised the presence, location, and shape of such a valley using a small sample of exoplanets transiting stars with highly accurate stellar parameters determined from asteroseismology. They also detected a clear bimodal distribution, with super-Earths ($R_{\rm p} = 1.5\,R_{\oplus}$) and sub-Neptunes ($R_{\rm p} = 1.5\,R_{\oplus}$) separated by a deficiency around $2\,R_{\oplus}$. They found that the valley is characterised as a power law $R \propto P^{\gamma}$ with $\gamma \approx -0.09$. The negative slope further suggests that photo-evaporation is the main mechanism behind the radius gap.

1.6   Objective of this thesis

Space-based transit surveys have given us ground-breaking new insights into the demographics of exoplanets in our Galaxy. *Kepler* has unveiled a *cornucopia* of small planets that have no counterpart in the Solar System. About 25 % of Sun-like stars in our galaxy host super-Earths (R_p=1-2 $R_\oplus$, M_p=1-10 $M_\oplus$) and sub-Neptunes (R_p=2-4 $R_\oplus$, M_p=10-40 $M_\oplus$) with orbital periods shorter than 100 days (Batalha et al., 2013; Marcy et al., 2014; Mulders et al., 2016; Silburt et al., 2015). Although the superb photometry of *Kepler* has given us access to the small-radius domain, our knowledge on the composition of super-Earths and sub-Neptunes is still quite limited. Mass determinations with a precision (better than 20–25 %) that allows us to distinguish between different internal compositions have been possible only for a few dozen super-Earths and Neptunes. This is because of the small RV variation induced by such planets and the faintness of most of Kepler host stars (V > 13 mag). Precise masses and mean densities are especially important for small planets, since a wide diversity of compositions are possible a priori.

The *Kepler-K2* mission is a unique opportunity to gain knowledge on small close-in planets. **$K2$ observes stars that are on average 3 magnitudes brighter than those targeted by the original *Kepler* mission**. The opportunity for exoplanetary science is terrific! *K2* allows us to detect close-in (a≤0.1 AU) super-Earth- and Neptune-size transiting planets around bright stars, a definitive advantage for any RV follow-up.

By focusing on bright *K2* stars ($V < 13$ mag), and by combining the exquisite transit space-borne photometry form *K2* with high-precision RV measurements (1 m s^{-1}), we now want to tackle ambitious planet detections. The main objective of this thesis is **to characterise in terms of mass, radius, and bulk density transiting exoplanets discovered by the *K2* space mission around bright stars. The main object is to infer their internal structure and composition, gaining precious insights into their formation and evolution.**

We focus on the RV follow-up of bright ($V < 13$ mag) stars observed by *K2*. We do this using state-of-the-art high-precision spectrographs around the world. This allows us to estimate planetary masses with a precision better than ($< 20 - 25\%$). We want to address the following key questions at the frontier of exoplanet science:

- What are the composition and structure of exoplanets?

- Do exoplanets migrate or form *in situ*?

- Do exoplanets in multi-planet system share the same composition?

- What is behind the so-called "small planet radius gap"?

The specific goals we want to achieve are:

- To carry-out Doppler follow-up observations of *K2* planet candidates.

- To develop a robust data analysis tool that is able to deal with any exoplanetary system configuration and architecture, handling large amounts of transit and RV time-series data.

- To perform a joint data analysis once the *K2* and RV data have been acquired.

- To report the discoveries in high-impact factor, peer-reviewed journals.

1.7 Contents

This thesis is divided as follows:

1. Chapter 2 is devoted to the theoretical derivation of the RV and transit equations. Those equations are needed to model the RV and transit data, and infer the planetary system parameters. We begin with the solution of the two-body problem to introduce orbital motion. We proceed with the description of the planetary motion in three dimensions, as observed by a faraway observer. We show how the projections of a three-dimensional orbit lead to the RV and transit equations. We also describe the generalisation for multi-planet systems.

2. Details about space-borne, time-series photometry are given in Chapter 3. We first briefly describe the challenges on transit detection and describe the different parameter spaces probed by ground- and space-based surveys. We continue describing the general aspects of the *Kepler* mission, and later introduce the *K2* mission.

3. Chapter 4 provides the technical details about the RV method. The chapter starts with a description of the technique and provides an overview of the difficulties of the method. We then describe the general aspects about high-precision spectrographs. The chapter continues with the description of observations carried out using different spectrographs as part of the work presented in this thesis.

4. The data analysis methods used in this thesis are described in Chapter 5. Basic concepts about Bayesian statistics are handled at the beginning of the chapter. We then follow with a description of the Markov chain Monte Carlo technique used to estimate posterior distributions with emphasis on the ensemble sampler algorithm. After this, we describe the code `pyaneti`, a fast, powerful, and robust software suite, which combines transit and RV equations to infer exoplanet parameters. This code was developed during the course of the work here presented and is freely available to the community.

5. Chapter 6 presents the results obtained in this thesis. They consist on the characterisation of significant number of exoplanets revealed by *K2* in different campaigns.

6. Chapter 7 summarises the main results and conclusions of this work.

CHAPTER 2

RADIAL VELOCITY AND TRANSIT EQUATIONS

I deduced that the forces which keep the planets in their orbs must [be] reciprocally as the squares of their distances from the centres about which they revolve: and thereby compared the force requisite to keep the Moon in her Orb with the force of gravity at the surface of the Earth; and found them answer pretty nearly. Issac Newton (see the English translation of Isaac Newton's *Principia* by Cohen et al., 1999).

2.1 Orbital motion

The motion of a planet around a star is a natural consequence of gravity[1]. According to Newton's universal law of gravitation, the attraction between two bodies is directly proportional to the product of their masses m_1 and m_2 and inversely proportional to the square of the distance r between their centres. The magnitude of this force is given by

$$F = -\frac{Gm_1m_2}{r^2}, \tag{2.1}$$

where $G = 6.67428 \times 10^{-11} \mathrm{m}^3 \, \mathrm{kg}^{-1} \, \mathrm{s}^{-2}$ (Prša et al., 2016) is the universal gravitational constant.

Let us consider the motion of two masses m_1 (the star) and m_2 (the planet) with position vectors $\mathbf{r}_1$ and $\mathbf{r}_2$ referred to an inertial frame whose origin is the point $\mathbf{O}$. This configuration is displayed in Figure 2.1. The relative motion of the planet with respect to the star is given by the vector $\mathbf{r} = \mathbf{r}_2 - \mathbf{r}_1$. By following Newton's second law of motion, the gravitational forces acting on both bodies are

$$\mathbf{F}_1 = m_1\ddot{\mathbf{r}}_1 = +\frac{Gm_1m_2}{r^3}\,\mathbf{r}, \tag{2.2}$$

and

---

[1]In this thesis we follow the derivation of the orbital motion described by Murray & Correia (2010).
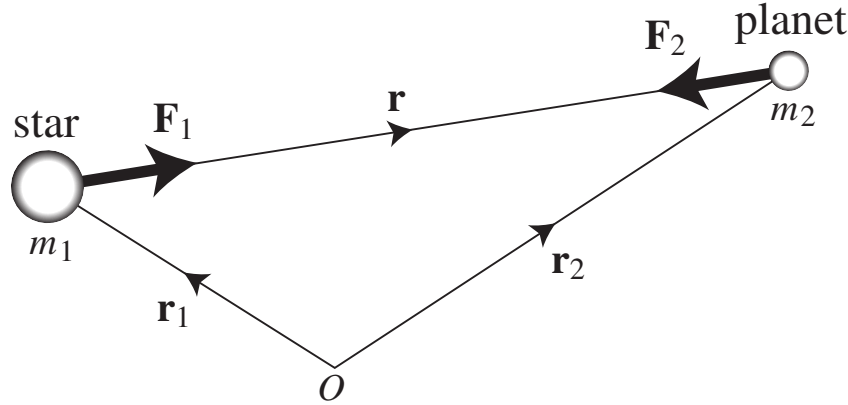
Figure 2.1: Diagram of forces acting on a star (m_1) and on a planet (m_2) with position vectors r_1 and r_2, respectively. (from Murray & Correia, 2010).

$$\mathbf{F}_2 = m_2\ddot{\mathbf{r}}_2 = -\frac{\mathrm{G}m_1m_2}{r^3}\,\mathbf{r}. \tag{2.3}$$

Now let us consider the motion of the planet (m_2) with respect to the star (m_1). We can combine equations (2.2) and (2.3) to write an equation for the relative motion acceleration $\ddot{\mathbf{r}} = \ddot{\mathbf{r}}_2 - \ddot{\mathbf{r}}_1$ as

$$\ddot{\mathbf{r}} + \mathrm{G}\left(m_1 + m_2\right)\frac{\mathbf{r}}{r^3} = 0. \tag{2.4}$$

This is the *equation of relative motion*. In order to solve it and find the path of m_2 relative to m_1 we must first derive the constants of the motion. If we compute the vector product of $\mathbf{r}$ with equation (2.4), we obtain

$$\mathbf{r} \times \left(\ddot{\mathbf{r}} + \mathrm{G}\left(m_1 + m_2\right)\frac{\mathbf{r}}{r^3}\right) = \mathbf{r} \times \ddot{\mathbf{r}} = \mathbf{0}, \tag{2.5}$$

since $\mathbf{r} \times \mathbf{r} = \mathbf{0}$. We can now integrate equation (2.5) with respect to time to have

$$\mathbf{r} \times \dot{\mathbf{r}} = \mathbf{h}, \tag{2.6}$$

where $\mathbf{h}$ is a constant vector which is simultaneously perpendicular to both $\mathbf{r}$ and $\dot{\mathbf{r}}$. Therefore the motion of the planet with respect to the star lies in a plane (hereafter called "the orbit plane") perpendicular to the direction defined by $\mathbf{h}$. This also implies that the position and velocity vectors always lie in the same plane. Equation (2.6) is commonly referred to as the *angular momentum integral* and $\mathbf{h}$ is a constant quantity of the two body problem.

Since $\mathbf{r}$ and $\dot{\mathbf{r}}$ always lie in the same plane (the orbit plane) it is natural that we now restrict ourselves to considering motion in that plane. In order to describe the relative motion of the planet with respect to an origin centred on the star, we will use the polar coordinate system (r, θ) with an arbitrary reference line corresponding to $\theta = 0$. The polar coordinates r and θ are related to the Cartesian coordinates x and y from equations:

$$x = r\cos\theta \quad \text{and} \quad y = r\sin\theta. \tag{2.7}$$

Given that vectors are invariant under coordinate transformations, we can calculate $\mathbf{r}$, $\dot{\mathbf{r}}$, $\ddot{\mathbf{r}}$ using the transformation

$$x^i = \frac{\mathrm{d}x^i}{\mathrm{d}x^j}x^j. \tag{2.8}$$

By combining Eq. (2.7) with Eq. (2.8), the position $\mathbf{r}$, velocity $\dot{\mathbf{r}}$, and acceleration $\ddot{\mathbf{r}}$ vectors can be written in polar coordinates as

$$\mathbf{r} = r\hat{\mathbf{r}}, \tag{2.9}$$

$$\dot{\mathbf{r}} = \dot{r}\hat{\mathbf{r}} + r\dot{\theta}\hat{\theta}, \tag{2.10}$$

$$\ddot{\mathbf{r}} = (\ddot{r} - r\dot{\theta}^2)\hat{\mathbf{r}} + \left[\frac{1}{r}\frac{\mathrm{d}}{\mathrm{d}t}\left(r^2\dot{\theta}\right)\right]\hat{\theta}, \tag{2.11}$$

where $\hat{\mathbf{r}}$ and $\hat{\theta}$ denote unit vectors along and perpendicular to the radius vector, respectively. By combining Eqs (2.9) and (2.11) with Eq. (2.4) we have

$$(\ddot{r} - r\dot{\theta}^2)\hat{\mathbf{r}} + \left[\frac{1}{r}\frac{\mathrm{d}}{\mathrm{d}t}\left(r^2\dot{\theta}\right)\right]\hat{\theta} + \mathrm{G}\left(m_1 + m_2\right)\frac{r}{r^3}\hat{\mathbf{r}} = \mathbf{0}. \tag{2.12}$$

In order to solve Eq. (2.12) we need to separate its $\hat{\mathbf{r}}$ and $\hat{\theta}$ components. If we substitute Eqs. (2.9) and (2.10) in Eq. (2.6) we obtain

$$\mathbf{h} = \mathbf{r} \times \dot{\mathbf{r}} = r^2\dot{\theta}\hat{z}, \tag{2.13}$$

where $\hat{\mathbf{z}}$ is a unit vector perpendicular to the orbital plane forming a right-handed triad with $\hat{\mathbf{r}}$ and $\hat{\theta}$. Following Eqs. (2.6) and (2.13), the magnitude of the vector $\mathbf{h}$ is a constant of the motion given by $h = r^2\dot{\theta}$. The derivative of h appears in the $\hat{\theta}$ component in Eq. (2.12). This implies that the $\hat{\theta}$ component in Eq. (2.12) has to be zero. Therefore the orbital motion is described by the following equation

$$(\ddot{r} - r\dot{\theta}^2) = -\mathrm{G}\left(m_1 + m_2\right)\frac{1}{r^2}. \tag{2.14}$$

Equation (2.14) can be solved following the procedure described by Murray & Correia (2010). If we define $u = 1/r$, we can rewrite $\ddot{r}$ as

$$\ddot{r} = -(r^2\dot{\theta})^2 u^2 \frac{\mathrm{d}^2 u}{\mathrm{d}\theta^2} = -h^2 u^2 \frac{\mathrm{d}^2 u}{\mathrm{d}\theta^2}, \tag{2.15}$$

where $h = r^2\dot{\theta}$. This allows us to rewrite Eq. (2.14) as

$$\frac{\mathrm{d}^2 u}{\mathrm{d}\theta^2} + u = \frac{\mathrm{G}(m_1 + m_2)}{h^2}. \tag{2.16}$$

Equation (2.16) is called Binet's equation. Its general solution is

$$u = \frac{\mathrm{G}(m_1 + m_2)}{h^2}\left[1 + e\cos\left(\theta - \varpi\right)\right], \tag{2.17}$$

where e and ϖ are two constants of integration. If we rewrite Eq. (2.17) in terms of r, we have

$$r = \frac{h^2}{\mathrm{G}(m_1 + m_2)}\frac{1}{1 + e\cos\left(\theta - \varpi\right)}. \tag{2.18}$$

Equation (2.18) defines the relative orbital motion of the planet in the two body problem in function of the polar coordinates r and θ. In order to understand the implication of Eq. (2.18) on the shape of the orbit, we define the quantity p as

$$p \equiv \frac{h^2}{\mathrm{G}(m_1 + m_2)}, \tag{2.19}$$

to rewrite Eq. (2.18) as

$$r = \frac{p}{1 + e\cos(\theta - \varpi)}. \tag{2.20}$$

Equation (2.20) is equivalent to Eq. (2.18) but it is written following the general equation of a conic section curve in polar coordinates. For this set of curves, the variable e is called *eccentricity* and p is the *semi-latus rectum*. If $e = 0$ the curve is a circle, if $0 < e < 1$ an ellipse, if $e = 1$ a parabola, and if $e > 1$ a hyperbola. For planetary systems, we are interested in cases where the planet and star are gravitationally bound, i.e., the orbit is closed ($e < 1$). Consequently, throughout this thesis we concentrate on elliptical motion. In this case the semi-latus rectum relates with the ellipse properties as

$$p = a(1 - e^2), \tag{2.21}$$

where the constant a is the semi-major axis of the ellipse (see Fig. 2.2). We can now use Eq. (2.21) to rewrite r in terms of the orbital geometry as

$$r = \frac{a\left(1 - e^2\right)}{1 + e\cos(\theta - \varpi)}. \tag{2.22}$$

In celestial mechanics it is customary to use the term longitude when referring to any angle that is measured with respect to an arbitrary reference line fixed in inertial space. The angle θ – called the *true longitude* – is the angle on the orbital plane between the reference line and the planet's position. The angle ϖ is called the *longitude of periastron*. It is defined as the angle on the orbital plane between the reference line and the periastron, i.e., the point of closest approach between the two orbiting bodies[2]. It is usually more convenient to refer the angular coordinate to the periastron rather than to the arbitrary reference line. This leads to the introduction of the angle $\nu \equiv \theta - \varpi$ (see Fig. 2.2), which is called the *true anomaly*[3]. Equation (2.20) can now be rewritten as

$$r = a\frac{(1 - e^2)}{1 + e\cos\nu}. \tag{2.23}$$

2.1.1   Kepler's laws

For a gravitationally bound system, Eq. (2.23) describes the relative orbit of a planet about a star, with the latter occupying one of the two foci of the ellipse. Kepler's first law of planetary motion, i.e., *the planets move in ellipses with the Sun at one focus*, is a consequence of the inverse square law of the gravitational force. Figure 2.2 show a diagram of the elliptical orbit of the planet.

Let us consider the motion of the mass m_2 during the time interval $\mathrm{d}t$. The areal velocity $\dot{A}$, i.e., the area $\mathrm{d}A$ swept out by the radius vector r in time $\mathrm{d}t$, is given by

$$\dot{A} \equiv \frac{\mathrm{d}A}{\mathrm{d}t} = \frac{1}{\mathrm{d}t}\int_0^r r\mathrm{d}r\mathrm{d}\theta \tag{2.24}$$

---

[2]Analogously, the apoastron is defined as the orbital point of greatest separation between the star and the planet. The orbital radius at periastron and apoastron are $r_p = a(1 - e)$ and $r_a = a(1 + e)$, respectively.

[3]The periastron is at $\nu = 0$, wheres the apoastron is at $\nu = \pi$.
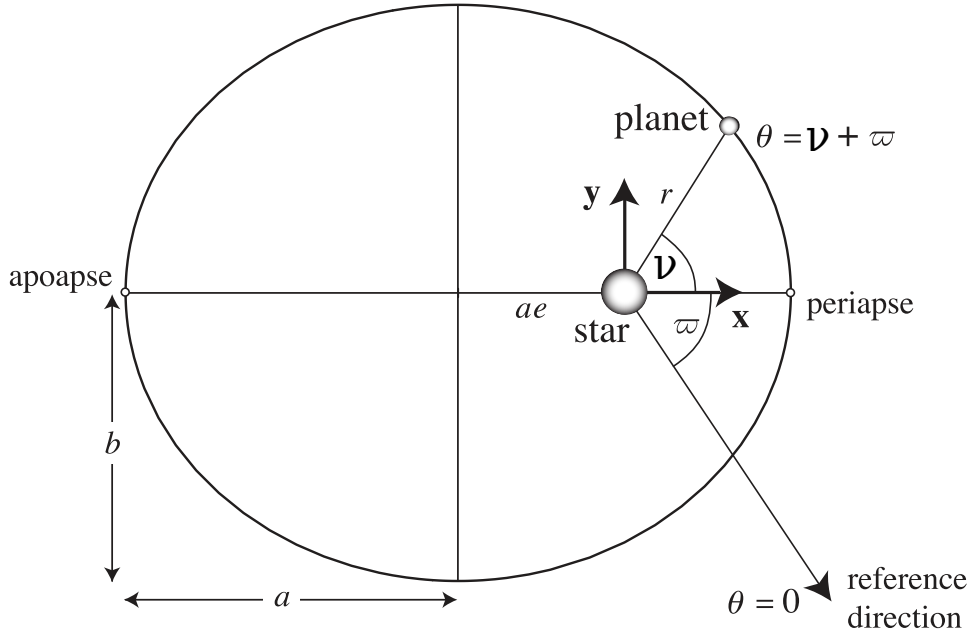
Figure 2.2:   The geometry of the ellipse of semi-major axis a, semi-minor axis b, eccentricity e and longitude of periapse ϖ (from Murray & Correia, 2010) .

If we integrate Eq. (2.24) with respect to r and use $h = r^2\dot{\theta}$, we have

$$\dot{A} = \frac{1}{2}r^2\dot{\theta} = \frac{1}{2}h. \tag{2.25}$$

Since h is a constant this implies that equal areas are swept out in equal times and hence Eq. (2.25) is the mathematical form of Kepler's second law of planetary motion: *a radius vector from the Sun to a planet sweeps out equal areas in equal times*. Note that this does not require an inverse square law of force, but only that the force is directed along the line joining the two masses.

We have demonstrated that, for a bound system, the planet orbits the star in a closed orbit. We thus expect a periodicity in the planetary motion. Based on Eq. (2.23), the planet occupies the same position after the radius vector r has turned through an angle of 2π. The time P needed by the planet to complete a full orbit is called the *orbital period*. By integrating Eq. (2.25) over the orbital period P we obtain

$$A = \frac{1}{2}hP. \tag{2.26}$$

where A is the area enclosed by the ellipse. We know that the area of an ellipse is also given by $A = \pi ab$, where the semi-minor axis b is related to the semi-major axis a and the eccentricity e through $b^2 = a^2(1 - e^2)$. If we combine this with Eq. (2.21) we obtain

$$A^2 = \frac{1}{4}h^2 P^2 = \pi^2 a^4 \left(1 - e^2\right). \tag{2.27}$$

If we combine Eq. (2.19) with Eq. (2.27) we derive

$$P^2 = \frac{4\pi^2}{\mathrm{G}(m_1 + m_2)}a^3. \tag{2.28}$$

Equation (2.28) gives a relation between the orbital period P and the semi-major axis a of the orbit. Note that P is independent of e and is a function of the sum of the two masses $m_1 + m_2$ and the semi-major axis a only.

In the case of planets orbiting their host star, we have $m_2 \ll m_1$ and $m_1 + m_2 \approx m_1$. The term $(4\pi^2)/(\mathrm{G}\,m_1)$ is therefore constant, implying that for any orbiting planet, *the square of the orbital period P^2 is directly proportional to the cube of the semi-major axis a^3*, which corresponds to Kepler's third law of planetary motion.

2.1.2   Orbital position as a function of time

In the previous sections we solved the equation of motion of the two-body problem to describe the path of the planet with respect to the star. We showed that, given the value of the true anomaly ν, we can calculate the orbital radius r of the planet provided that we know the eccentricity e and the semi-major axis a of its orbit. However, in practice we usually want to calculate the location of the planet as function of time and our solution to the two-body problem (Eq. 2.23) does not contain the time explicitly.

In order to describe the planetary orbit as function of time we need two complementary angles[4] called the *eccentric anomaly* ϵ and the *mean anomaly* μ. The true and eccentric anomalies are related as

$$\nu = 2\arctan\left[\sqrt{\frac{1+e}{1-e}}\tan\left(\frac{\epsilon}{2}\right)\right],\tag{2.29}$$

whereas the eccentric anomaly relates to the mean anomaly μ as

$$\mu = \epsilon - e\sin(\epsilon).\tag{2.30}$$

The explicit dependence on time t is given by the mean anomaly definition

$$\mu = \frac{2\pi}{P}\left(t - T_{\mathrm{p}}\right).\tag{2.31}$$

Equation (2.31) depends explicitly on time t and on a given "zero time" T_{p}. Following the definition of ν, this "zero time" has to be the time of periastron passage. The true anomaly can then be obtained in terms of t by solving Eqs. (2.31), (2.30), and (2.29). In this way we can obtain the orbit position as function of time. We note that Eq. (2.30) cannot be solved analytically for cases where $e \neq 0$. We have to use either series expansions, or iterative methods (e.g., Newton-Raphson).

In the case of a circular orbit, i.e., $e = 0$, the problem simplifies. The true anomaly can be obtained directly as

$$\nu = \frac{2\pi}{P}\left(t - T_{\mathrm{p}}\right).\tag{2.32}$$

However, for this case T_{p} remains undefined because any point along the orbit can be used to define a "zero time". The time of the planet minimum conjunction T_0 is commonly adopted for circular orbits[5].

---

[4]The derivation of the relations between these angles is out of the scope of the present work. We refer the reader to Murray & Dermott (2000) for details.

[5]The time of planet minimum (or inferior) conjunction T_0 occurs when the planet passes between the observer and the reference star
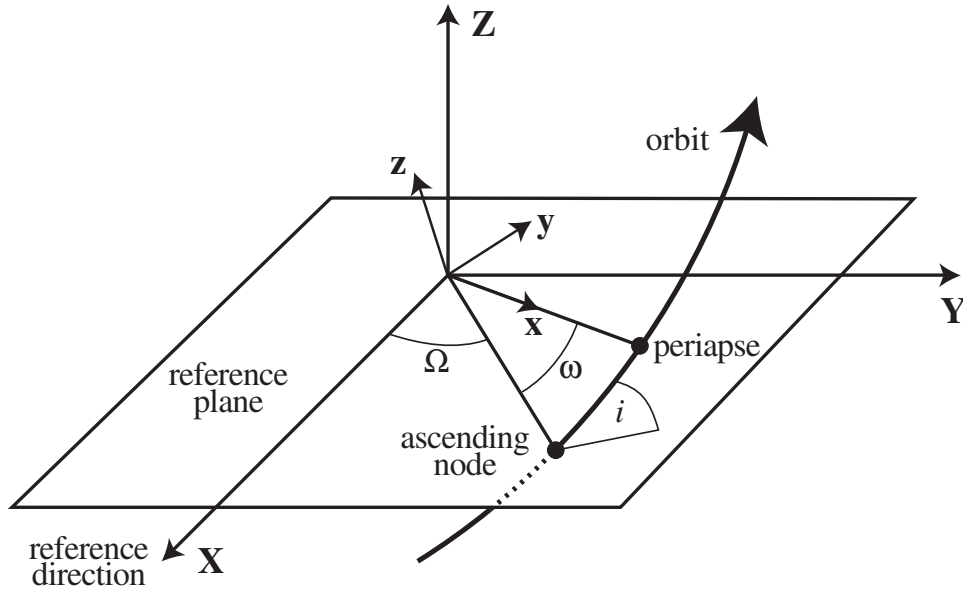
Figure 2.3: The relationship between the (x,y,z) and (X,Y,Z) coordinate systems and the angles ω, i and Ω (from Murray & Correia, 2010).

2.1.3 Orbit in three-dimensions

Let us define a three-dimensional coordinate system (x, y, z) centered on the star. The x-axis lies along the major (long) axis of the ellipse in the direction of periapse, the y-axis is perpendicular to the x-axis and lies in the orbital plane, while the z-axis is mutually perpendicular to both the x- and y-axes forming a right-handed triad (Fig. 2.3). By definition the orbital motion is confined to the x-y plane. The planet's position vector is given by

$$\mathbf{r} = (x, y, 0) = x\,\hat{\mathbf{x}} + y\,\hat{\mathbf{y}} + 0\,\hat{\mathbf{z}} \tag{2.33}$$

where $\hat{\mathbf{x}}$, $\hat{\mathbf{y}}$, and $\hat{\mathbf{z}}$ are three orthogonal unit vectors.

Let us consider now a second standard coordinate system centered on the star where the direction of the reference line in the reference plane forms the X-axis. The Y-axis is in the reference plane at right-angles to the X-axis, while the Z-axis is perpendicular to both the X- and Y-axes forming a right-handed triad. (Fig. 2.3).

The orbital plane does not have a preferred projection and intersects the reference plane X-Y in a line called *line of nodes*. The orbit crosses the line of nodes in two points, the ascending and descending nodes. They are the points where the planet goes from below to above and from above to below the reference plane X-Y, respectively. The *longitude of ascending node* Ω is the angle in the reference plane X-Y between the reference line of the XYZ system and the radius vector from the star to the ascending node. The *argument of periapse* ω is the angle on the orbital plane between this same radius vector and the periapse of the orbit. The *orbit inclination i* the angle between the reference plane X-Y and orbital plane. The inclination is always in the range $0 \leq i \leq 180°$. An orbit is said to be prograde if $i < 90°$, while if $i \geq 90°$ the motion is said to be retrograde. Figure 2.3 shows the ascending node, the three angles (Ω, ω and i), the reference plane X-Y, and the reference direction X.

It is clear that coordinates in the (x, y, z) system can be expressed in terms of the (X, Y, Z) system by means of a series of three rotations: (i) a rotation about the z-axis through an angle ω so that the x-axis coincides with the line of nodes, (ii) a rotation

about the x-axis through an angle i so that the two planes are coincident and finally (iii) a rotation about the z-axis through an angle Ω. This is written in a matrix form as

$$\begin{pmatrix} X \\ Y \\ Z \end{pmatrix} = \begin{pmatrix} \cos\Omega & -\sin\Omega & 0 \\ \sin\Omega & \cos\Omega & 0 \\ 0 & 0 & 1 \end{pmatrix} \begin{pmatrix} 1 & 0 & 0 \\ 0 & \cos i & -\sin i \\ 0 & \sin i & \cos i \end{pmatrix} \begin{pmatrix} \cos\omega & -\sin\omega & 0 \\ \sin\omega & \cos\omega & 0 \\ 0 & 0 & 1 \end{pmatrix} \begin{pmatrix} x \\ y \\ z \end{pmatrix}. \quad (2.34)$$

Simplifying equation (2.34) and using the Cartesian form of the orbit solution ($x = r\cos\nu$, $y = r\sin\nu$), the coordinates on the reference frame are

$$X = r\left[\cos\Omega\cos(\nu + \omega) - \sin\Omega\sin(\nu + \omega)\cos i\right], \quad (2.35)$$

$$Y = r\left[\sin\Omega\cos(\nu + \omega) + \cos\Omega\sin(\nu + \omega)\cos i\right], \quad (2.36)$$

$$Z = r\sin(\nu + \omega)\sin i. \quad (2.37)$$

The reference plane X-Y is usually taken to be the plane of the sky perpendicular to the line of sight, with the Z-axis oriented towards the observer. The reference X axis is usually oriented towards the celestial North pole. For this case we do not have a preferred direction and for concreteness we can assume $\Omega = \pi$. Equations (2.35), (2.36) and (2.37) can thus be rewritten as

$$X = -r\cos(\nu + \omega), \quad (2.38)$$
$$Y = -r\sin(\nu + \omega)\cos i, \quad (2.39)$$
$$Z = r\sin(\nu + \omega)\sin i. \quad (2.40)$$

Equations (2.38), (2.39) and (2.40) form the basis to describe the orbital motion in the two-body system as seen from Earth.

2.1.4   Barycentric motion

In order to determine the observable effects of an orbiting planet on a star it helps if we consider the motion in the centre of mass or barycentric system (see Fig. 2.4). For a given inertial frame centred in $\mathbf{O}$, the position vector of the centre of mass of the system is

$$\mathbf{R} = \frac{m_1\mathbf{r}_1 + m_2\mathbf{r}_2}{m_1 + m_2}. \quad (2.41)$$

By combining equations (2.2) and (2.3) we have

$$\ddot{\mathbf{R}} = \ddot{\mathbf{r}}(m_1 + m_2) = 0. \quad (2.42)$$

If we integrate equation (2.42) with respect to time, we see that the velocity of the centre of mass is constant, i.e., $\dot{\mathbf{R}} = \mathbf{V} = \text{constant}$. This implies that either the centre of mass is stationary (the case when $\mathbf{V} = 0$), or it is moving with a constant velocity (the case when $\mathbf{V} \neq 0$) in a straight line with respect to the origin $\mathbf{O}$. Then, if we define $\mathbf{R}_1 = \mathbf{r}_1 - \mathbf{R}$ and $\mathbf{R}_2 = \mathbf{r}_2 - \mathbf{R}$, we have

$$m_1\mathbf{R}_1 + m_2\mathbf{R}_2 = \mathbf{0}. \quad (2.43)$$

This implies that $\mathbf{R}_1$ is always in the opposite direction to $\mathbf{R}_2$, and hence that the barycentre is always on the line joining the two bodies m_1 and m_2. By definition the sum of the magnitudes of the vectors $\mathbf{R}_1$ and $\mathbf{R_2}$, namely R_1 and R_2, has to satisfy
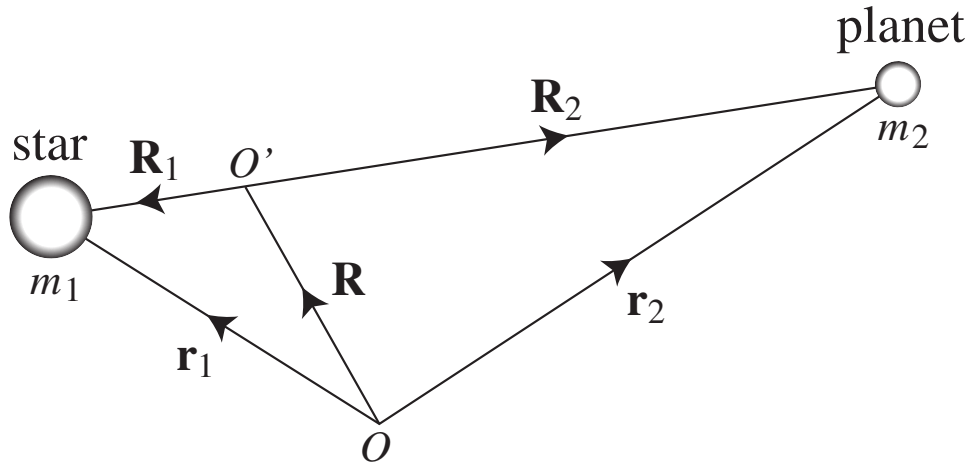
Figure 2.4: The position vectors of star and planet with respect to the origin, **O**, and with respect to the centre of mass of the star- planet system, **O**′ (from Murray & Correia, 2010).

$$R_1 + R_2 = r, \tag{2.44}$$

where r is the separation between the masses m_1 and m_2. From Eq. (2.43) we know that the distances of the star and planet from their common centre of mass are related by $m_1 R_1 = -m_2 R_2$. Hence

$$R_1 = \frac{m_2}{m_1 + m_2} r, \tag{2.45}$$

and

$$R_2 = -\frac{m_1}{m_1 + m_2} r, \tag{2.46}$$

which are the positions of the two bodies with respect to the barycentre. We note that equations (2.45) and (2.46) depend linearly on r. Therefore each object will orbit the barycentre of the system in an ellipse with the same eccentricity but the semi-major axes is reduced in scale by a factor

$$a_1 = \frac{m_2}{m_1 + m_2} a, \tag{2.47}$$

and

$$a_2 = \frac{m_1}{m_1 + m_2} a, \tag{2.48}$$

The orbital periods of the two masses must each be equal to the period P, although the semi-major axes are not. Each mass then moves on its own elliptical orbit with respect to the common centre of mass, and the periapses of their orbits differ by π (i.e., the argument of periapse of the star is $\omega_\star = \omega_\mathrm{p} + \pi$, where ω_p is the argument of periapse of the planet).

2.2   Radial velocity equations

Since $\mathbf{R}_1 = \mathbf{r}_1 - \mathbf{R}$ (Sect. 2.1.4), the position vector of the star $\mathbf{r_1}$ from the observer in **O** is
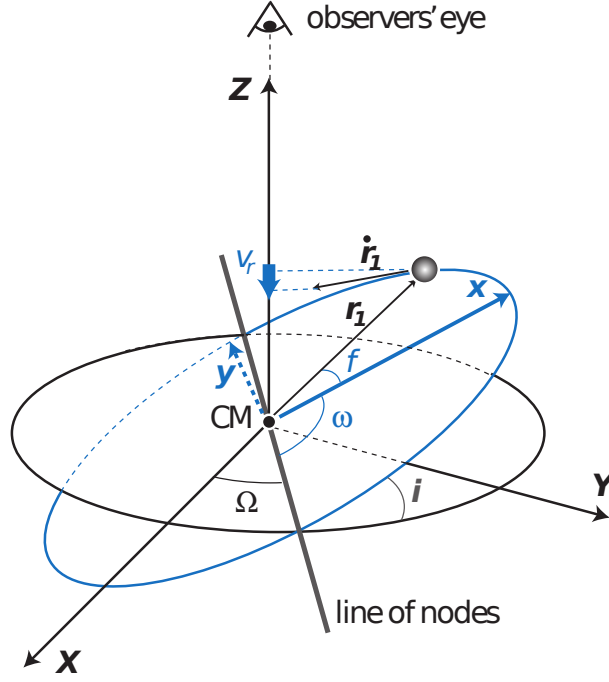
Figure 2.5: The relation between the star's velocity around the centre of mass, $\dot{\mathbf{r}}$, and its radial component along the line of sight, v_r (from Murray & Correia, 2010).

$$\mathbf{r}_1 = \mathbf{R} + \mathbf{R}_1. \tag{2.49}$$

The velocity of the star as seen by the observer is then obtained by deriving Eq. (2.49) with respect to time, i.e., $\dot{\mathbf{r}}_1$. The stellar velocity vector has three components along the three axis X, Y, and Z. We remember that our reference plane X-Y is the plane of the sky perpendicular to the line of sight (i.e., the plane tangential to the celestial sphere at the centre of mass position), with the Z-axis oriented towards the observer. The projection of the star velocity in the X-Y plane generates changes of position in the sky-plane, which can be measured with astrometry techniques (e.g., Benedict et al., 2002). The Z-component of the velocity vector, i.e., the component along the line of sight to the star, causes a Doppler shift of the stellar light, which can be measured with spectroscopic techniques (see Chapter 4). We will now derive the analytical expression of the Z-component of the star's velocity v_r, also known as *radial velocity* (RV). Figure 2.5 shows a scheme of the relation between the star's velocity around the barycentre and v_r. Since $\mathbf{r}_1 = \mathbf{R} + \mathbf{R}_1$ this gives

$$v_r = \dot{\mathbf{r}}_1 \cdot \hat{Z} = v_z + \frac{m_1}{m_1 + m_2}\dot{Z}, \tag{2.50}$$

where $v_z = \dot{\mathbf{R}} \cdot \hat{\mathbf{Z}}$ is the proper motion of the barycentre along the line of sight and the term $\dot{Z}$ is calculated from Eq. (2.40) as

$$\dot{Z} = \sin i \left[\dot{r}\sin(\nu + \omega_\star) + r\dot{\nu}\cos(\nu + \omega_\star)\right], \tag{2.51}$$

where $\omega_\star = \omega_\mathrm{p} + \pi$ is the argument of periastron of the stellar orbit. In order to eliminate the dependence on $\dot{r}$ and $\dot{\nu}$, we first calculate the time derivative of Eq. (2.23)

$$\dot{r} = a_1 e \frac{1 - e^2}{(1 + e\cos\nu)^2}\sin\nu\dot{\nu} = r\frac{e\sin\nu}{1 + e\cos\nu}\dot{\nu}. \tag{2.52}$$

If we combine Eqs. (2.26) and (2.27) and given that $h = r^2\dot{\theta}$ and $\dot{\theta} = \dot{\nu}$, we have

$$\left(\frac{1}{2}r^2\dot{\nu}P\right)^2 = \pi^2 a_1^4 \left(1 - e^2\right). \tag{2.53}$$

Simplifying Eq. (2.53) we get

$$r\dot{\nu} = 2\pi \frac{a_1^2\sqrt{1-e^2}}{rP}, \tag{2.54}$$

and using Eq. (2.54) in Eq. (2.52) we obtain

$$\dot{r} = \frac{2\pi a_1 e \sin\nu}{P\sqrt{1-e^2}}. \tag{2.55}$$

We now use Eq. (2.23) in Eq. (2.54)

$$r\dot{\nu} = \frac{2\pi a_1(1 + e\cos\nu)}{P\sqrt{1-e^2}}. \tag{2.56}$$

If we combine Eqs. (2.55) and (2.56) with Eq. (2.51), we have

$$\dot{Z} = \sin i \frac{2\pi a_1}{P\sqrt{1-e^2}}\left[e\sin\nu\sin(\nu + \omega_\star) + (1 + e\cos\nu)\cos(\nu + \omega_\star)\right]. \tag{2.57}$$

Simplifying Eq. (2.57), we can rewrite Eq. (2.50) as

$$v_{\rm r} = v_{\rm z} + K\left[\cos(\nu + \omega_\star) + e\cos\omega_\star\right] \tag{2.58}$$

where

$$K \equiv \frac{m_2}{m_1 + m_2} \frac{2\pi a_1}{P\sqrt{1-e^2}} \sin i, \tag{2.59}$$

is called the RV semi-amplitude. Equations (2.58) and (2.59) give the RV of the star in terms of the parameters that we presented in the previous sections, namely, the two masses m_1 and m_2, the orbital period P, the eccentricity e, the orbit inclination i, and the semi-major axis of the stellar orbit a_1.

The curve that shows how the stellar velocity along the line of sight changes over time as the star orbits around the centre of mass is called *radial velocity curve*. Figure 2.6 shows different RV curves for different values of $\omega_\star$ and e. The RV is plotted as a function of the orbital phase, which is defined as $(t - T_0)/P$, where $0 \leq t \leq P$ and T_0 is the time of minimum conjunction of the planet.

2.2.1 Multi-planet case

We demonstrated that the change of the stellar velocity component along the line of sight to the host star, induced by the presence of the orbiting planet, is described by Eq. (2.58). However, a planetary system may contain more than one planet orbiting the star. It is well known that for cases where more than two bodies interact gravitationally, there is no analytical solution. In such cases, numerical integration are needed.

In special cases where there is a gravitational dominating body (the star) being orbited by a given number $N_{\rm p}$ of minor bodies (the planets), the gravitational interaction between the low mass bodies can be neglected. Therefore, the Doppler reflex motion induced by each small mass can be solved independently using the equations derived for the two body
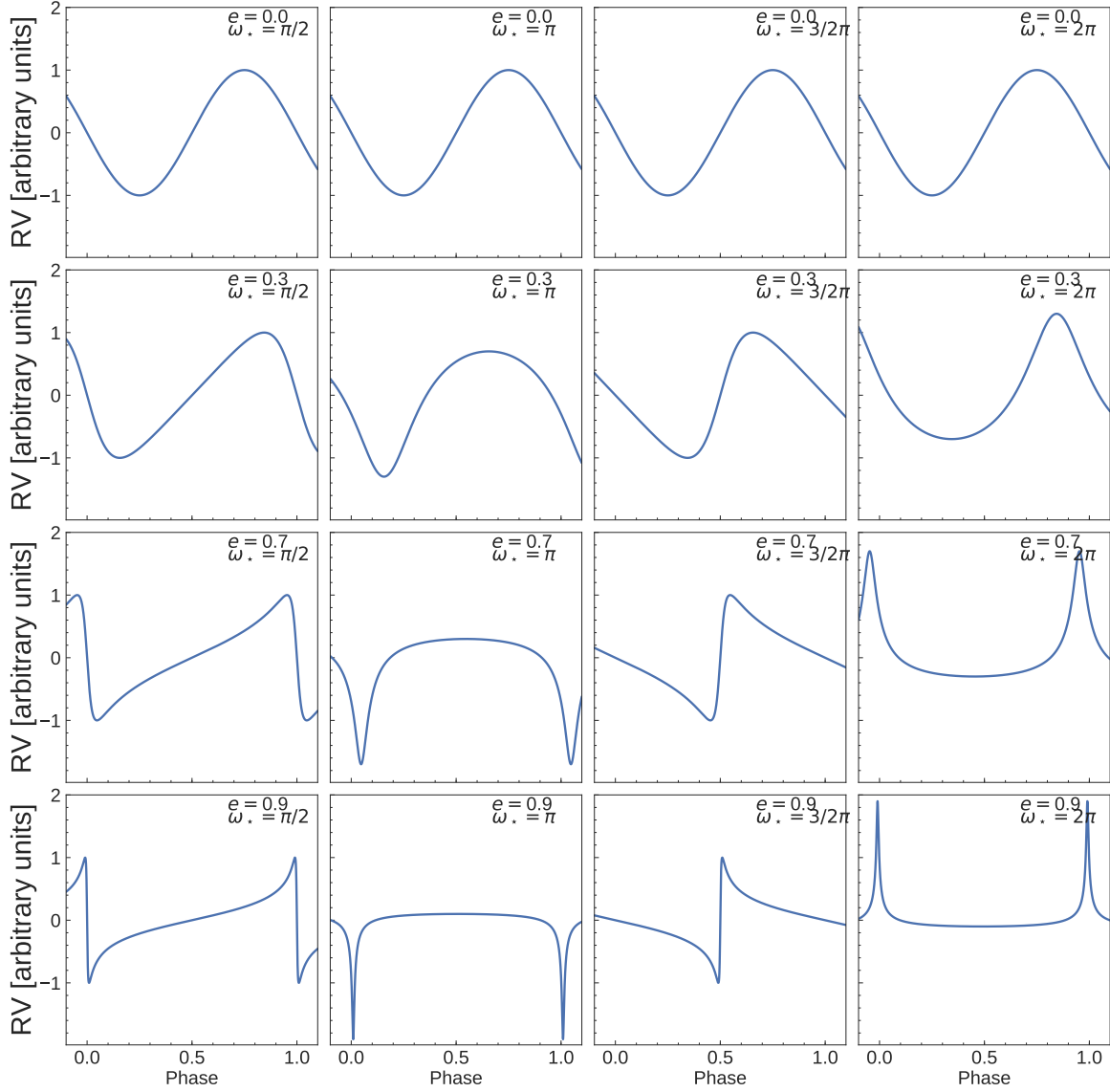
Figure 2.6: Radial velocity curves for different values of e and $\omega_\star$. The barycentric velocity v_z is fixed to zero. The plase is defined as $(t - T_0)/P$, where $0 \leq t \leq P$ and T_0 is the time of minimum conjunction of the planet.

problem, by using a Keplerian orbit for each planet. By following this approximation, if a star is orbited by N_p planets the general expression for Eq. (2.58) is then

$$v_\mathrm{r} = v_z + \sum_{j=1}^{N_\mathrm{p}} K_j \left[\cos(\nu_j + \omega_{\star,j}) + e_j \cos \omega_{\star,j} \right], \qquad (2.60)$$

where each planet j has its own set of parameters $T_{0,j}, P_j, e_j, \omega_{\star,j}, K_j$. The term γ_i depends on the spectrograph i and accounts for possible instrumental offsets. We show in Fig. 2.7 an example of the RV curve computed with Eq. (2.60) for a star orbited by three planets.

2.2.2 Planet mass

The RV semi-amplitude K can be determined from RV measurements. Equation (2.59) relates K with the orbital elements and the masses of both bodies. If we combine Eq. (2.28)
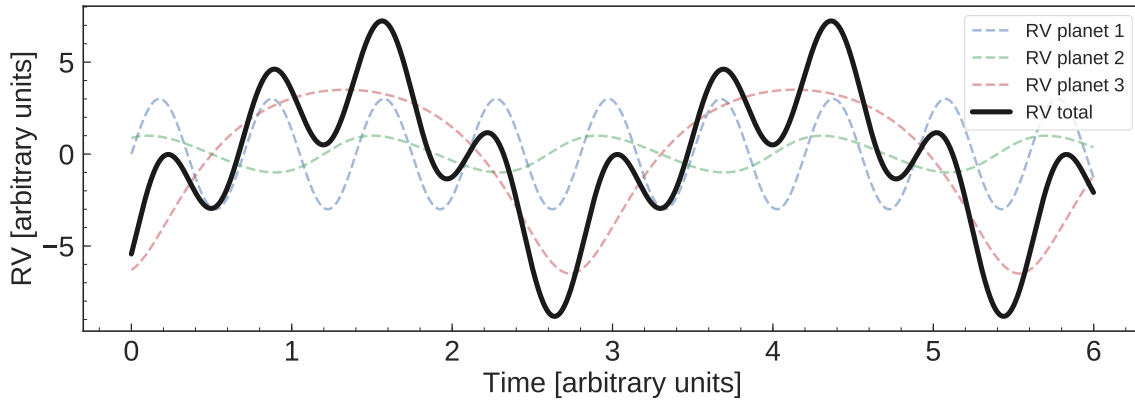
Figure 2.7: Synthetic RV curve of a star orbited by three planets (thick black line), and RV curves of the individual components (dashed lines). The three orbits have different parameters. The total RV curve is the sum of the three RV curves.

with Eq. (2.59) we can eliminate a from Eq. (2.59) to get

$$K = \left(\frac{2\pi G}{P}\right)^{1/3} \frac{m_2}{(m_2 + m_1)^{2/3}} \frac{1}{(1 - e^2)^{1/2}} \sin i. \tag{2.61}$$

Equation (2.61) depends on the orbit inclination i, which cannot be determined from RV observations. If we can measure the stellar mass with an independent method – such as spectroscopy or astereoseismology – Eq. (2.61) provides the planet mass multiplied by $\sin i$, also known as the *planet minimum mass*. In order to determine the planet *true mass*, we need to measure the orbit inclination using complemetary methods, such as the transit method (see Sect. 2.3).

Given that Eq. (2.61) is transcendental in terms of m_2, there are two approaches to calculate the planet minimum mass. Since $m_1 \gg m_2$, we can assume that $m_1 + m_2 \approx m_1$. This gives

$$m_2 \sin i \approx K \left(\frac{2\pi G}{P}\right)^{-1/3} m_1^{2/3} \left(1 - e^2\right)^{1/2}. \tag{2.62}$$

Equation (2.62) can be used to estimate $m_2 \sin i$ directly but it fails when m_2 gets comparable with m_1. We can also define the function

$$f(m_2) = \left(\frac{2\pi G}{P}\right)^{1/3} \frac{m_2}{(m_2 + m_1)^{2/3}} \frac{1}{(1 - e^2)^{1/2}} \sin i - K, \tag{2.63}$$

We can then solve Eq. (2.63) numerically using iterative methods to find the solution for m_2. This approach does not fail when m_2 increases.

2.3   Transit equations

In Section 1.4.2 we described how the presence of a planet orbiting its host star can be inferred by detecting the periodic drops of stellar flux observed when the planet is transiting its host star. An useful quantity to describe planetary transits is the projected distance in the sky (plane X-Y) between the planet and star centres. If we combine equations (2.23), (2.39), and (2.38), this distance is written as

$$d = \sqrt{X^2 + Y^2} = \sqrt{r^2 \cos^2(\nu + \omega_\star) + r^2 \sin^2(\nu + \omega_\star) \cos^2 i}. \tag{2.64}$$

We note that d depends on the true anomaly $\nu(t)$, which in turn is a function of time according to Eqs. (2.29), (2.30), and (2.31). Following Eastman et al. (2013), we define the projected distance δ using the argument of periastron of the star $\omega_\star$ instead of the argument of periastron of the planet ω_p. Following the definition of r given in Eq. (2.23), we can now define the scaled projected distance as the ratio of the distance d and the stellar radius $R_\star$, as[6]

$$\delta = \frac{a}{R_\star} \frac{1 - e^2}{1 + e \cos \nu} \sqrt{1 - \sin^2(\nu + \omega_\star) \sin^2 i}. \tag{2.65}$$

If we define

$$r_{\mathrm{p}} \equiv \frac{R_{\mathrm{p}}}{R_\star}, \tag{2.66}$$

as the planet-to-star radius ratio, from equation (2.65), the transit of an exoplanet occurs only when $\delta < 1 + r_{\mathrm{p}}$ and $\sin(\nu + \omega_\star) > 0$ (star behind the planet). On the other hand, the planet's occultation – also known as secondary eclipse – occurs if $\delta < 1 + r_{\mathrm{p}}$ and $\sin(\nu + \omega_\star) < 0$ (planet behind the star).

In order to analytically describe how the total flux $F(t)$ changes as a function of time due to the presence of a transiting planet, we need to account for the disc-integrated stellar flux $F_\star(t)$, the planet flux $F_{\mathrm{p}}(t)$ (both, reflected light and thermal emission), and the loss of light when transits/occulations occur $\lambda(\delta, r_{\mathrm{p}})$. The total flux $F(t)$ is given by

$$F(t) = F_\star(t) + F_{\mathrm{p}}(t) - \lambda(\delta, r_{\mathrm{p}}). \tag{2.67}$$

We will assume that the stellar flux $F_\star(t)$ is constant and equal to 1, and that any variation can be expressed as a fraction of the stellar light. We also assume that the planet contribution to the light curve is negligible ($F_{\mathrm{p}} = 0$), i.e., we assume that occulations and phase curve have no effect on the observed light curve. Under these assumptions, Eq. (2.67) can be re-written as

$$F(t) = 1 - \lambda(\delta, r_{\mathrm{p}}). \tag{2.68}$$

By definition $\lambda = 0$ when $\delta > 1 + r_{\mathrm{p}}$. For cases where $\delta < 1 + r_{\mathrm{p}}$, the change of light depends on the analytical form of λ, which accounts for the loss of light as the planet crosses the stellar disc. There are different approaches to define the analytical form of $\lambda(\delta, r_{\mathrm{p}})$.

2.3.1 Star as an uniform source of light

To a first approximation, we can think of the star as an uniform source of light (Seager & Mallén-Ornelas, 2003). The stellar flux is described by a constant function $I = I_0$. For this case, an analytic instructive model solution for λ is (Mandel & Agol, 2002)

$$\lambda(\delta, r_{\mathrm{p}}) = \begin{cases} 0 & : \delta > 1 + r_{\mathrm{p}} \\ \frac{1}{\pi}\left[r_{\mathrm{p}}^2 \kappa_0 + \kappa_1 - \sqrt{\frac{4\delta^2 - \left(1 + \delta^2 - r_{\mathrm{p}}^2\right)^2}{4}} \right] & : 1 - r_{\mathrm{p}} < \delta < 1 + r_{\mathrm{p}} \\ r_{\mathrm{p}}^2 & : \delta < 1 - r_{\mathrm{p}} \end{cases} \tag{2.69}$$

---

[6]The semi-major axis of the relative orbit is defined as $a = a_1 + a_2$, where a_2 and a_2 are respectively the semi-major axes of the planet's and star's orbit with respect to the centre of mass.
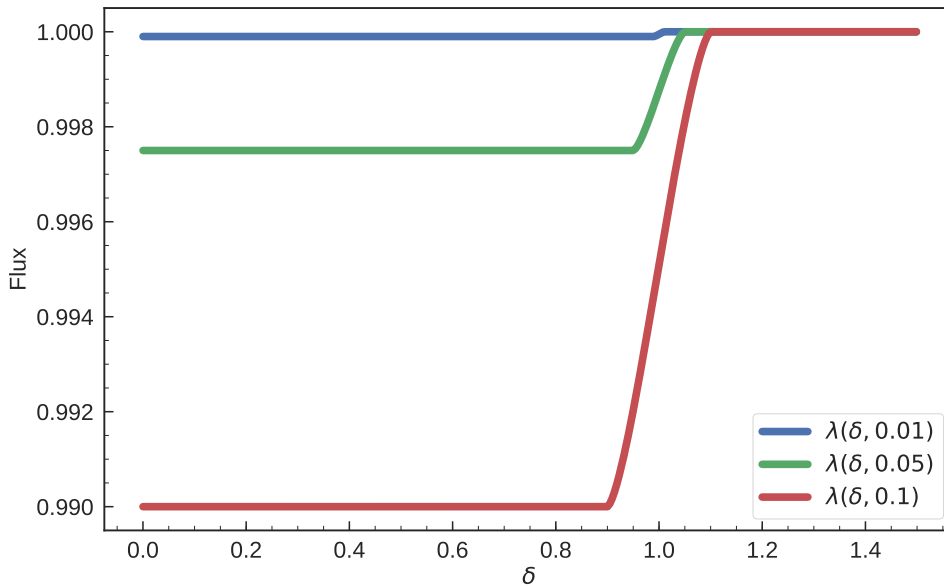
Figure 2.8: Synthetic transit light curves for a star assumed an uniform source of light. Transits were calculated for planets with radii of 10% (red, $\lambda(\delta, 0.1)$), 5% (green, $\lambda(\delta, 0.05)$) and 1% (blue, $\lambda(\delta, 0.01)$) the stellar radius.

where $\kappa_0 = \cos^{-1}\left[(r_p^2 + \delta^2 - 1)/(2r_p\delta)\right]$ and $\kappa_1 = \cos^{-1}\left[(1 - r_p^2 + \delta^2)/(2\delta)\right]$. Let us examine Eq. (2.69) to infer the main properties of a transit. First, when the planet does not occult the stellar disc ($\delta > 1 + r_p$) there is no light decrease. Second, during the transit ingress and egress ($1 - r_p < \delta < 1 + r_p$), the light decreases and increases continuously. Third, once the planet's disc is entirely in front of the stellar disc ($\delta < 1 - r_p$), the loss of flux is constant and equal to the planet-to-star area ratio, $r_p^2 = (R_p/R_\star)^2$. Figure 2.8 shows the stellar flux for different values of r_p as function of δ.

2.3.2 Star as a non-uniform source of light

Real stellar discs are not uniform sources of light. Variations in temperature and opacity make them look brighter in the centre and fainter at the edge (the limb), a phenomenon known as *limb darkening* (see, e.g., Claret & Bloemen, 2011). This crucially affects the shape of the transit signature a planet imprints in the observed stellar flux when passing in front of its host star. For instance, the intensity of the occulted light does not remain constant when $\delta < 1 - r_p$ (i.e., when the planet is entirely in front of the stellar disc). A larger flux decrease is observed when the planet transits close to the star centre than near the edge.

To account for the effects of limb darkening, the intensity of the stellar disc I can be parametrized by laws $I = I(\mu)$ which depend on $\mu = \cos\theta$, where θ is the angle between the line of sight and the normal to a given point of the stellar surface. Some of the most widely used limb darkening laws in exoplanet transit light-curve fitting are given by linear, logarithmic or exponential equations (see, e.g., Claret & Hauschildt, 2003; Espinoza & Jordán, 2015). In this work we adopt the quadratic limb darkening model as described by Mandel & Agol (2002).

2.3.3 Quadratic limb darkening model

The flux in the stellar disc can be parametrized as a quadratic function in terms of μ as (see, e.g., Mandel & Agol, 2002)
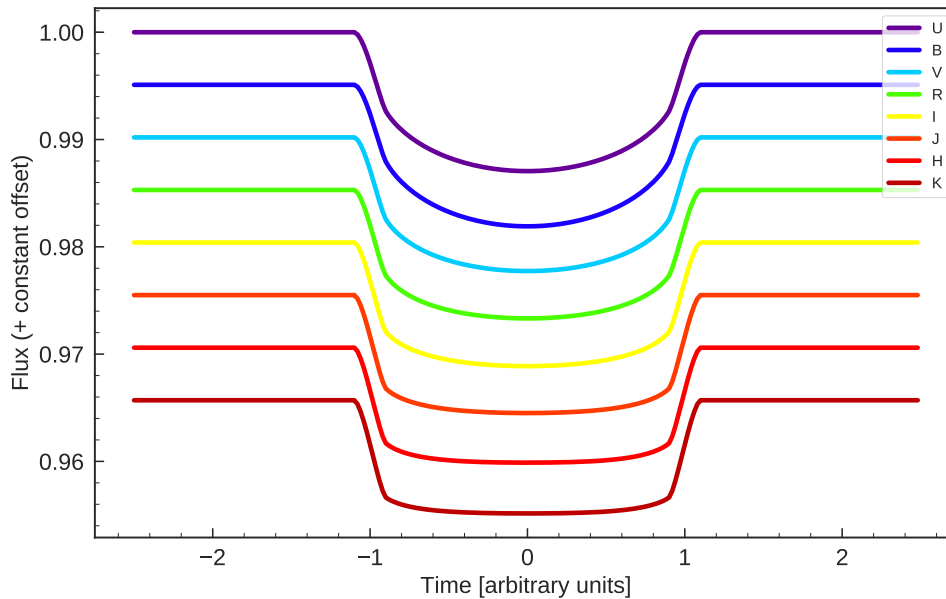
Figure 2.9: Theoretical light curves of a Sun-like star transited by a planet 10% its size. Different colours show a different Johnson-Cousins' filter.

$$I = 1 - u_1(1 - \mu) - u_2(1 - \mu)^2, \tag{2.70}$$

where u_1 and u_2 are limb darkening coefficients constrained to $u_1 + u_2 < 1$. These coefficients depend on the stellar type and wavelength. Following this approach, the light curve function has the form

$$F = F(\delta, r_{\mathrm{p}}, u_1, u_2), \tag{2.71}$$

for a given wavelength bandpass. The parameters r_{p}, u_1 and u_2 are different for different bandpasses. The analytic solution for F is described in terms of complete elliptic integrals of the third kind. This mathematical treatment is out of the scope of this thesis and we refer the reader to Mandel & Agol (2002) for more details.

Figure 2.9 shows synthetic transit light curves at different wavelengths for a Jupiter-size planet passing in front of a Sun-like star. The adopted bandpass correspond to those of the U, B, V, R, U, J, H, and K Johnson-Cousins filters. The limb darkening coefficients for each bandpass are extracted from Claret & Bloemen (2011). The adopted stellar parameters are $T_{\mathrm{eff}} = 5800\,\mathrm{K}$, $\log(g) = 4.5$ (cgs), and [Fe/H]=0.0 (dex). Note how a "real" transit light curve does not have a flat bottom, as in the case of an uniform source (cfr. Fig. 2.8). Note also how the effects of limb darkening are remarkably stronger at shorter wavelengths (Claret & Bloemen, 2011).

2.3.4   Multiple transiting planets

Multi-planet systems exist and more than one planet may transit its host star (e.g., Gandolfi et al., 2017; Guenther et al., 2017; Gillon et al., 2017). For a system where there are N_{p} transiting planets, the relative flux of the star is

$$F(t) = 1 - \sum_{j=1}^{N_{\mathrm{p}}} \lambda_j(\delta, r_{\mathrm{p}}). \tag{2.72}$$
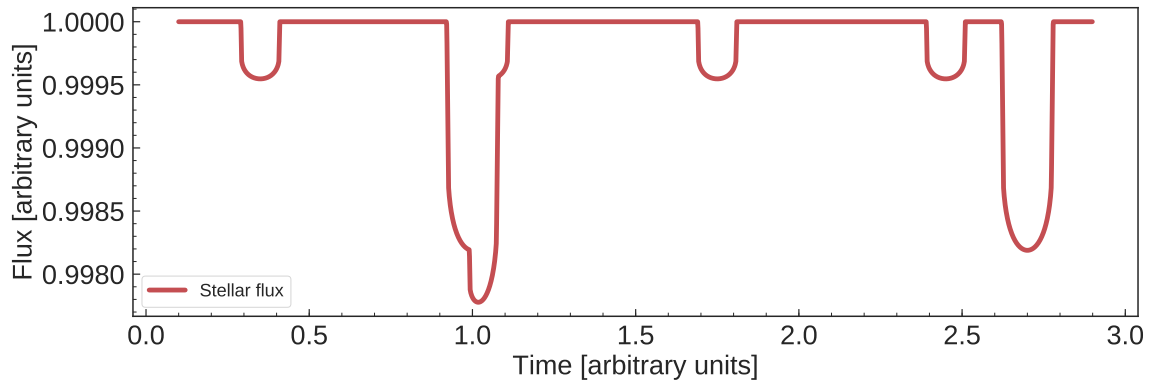
Figure 2.10: Synthetic light curve of a star with two exoplanets. Two different signals with different depth and period are present in the light curve. A multi-transit event is observed at time 1.

According to eq. (2.72), $F(t) = 1$ if no planet transits the star; it reduces to the one-transiting-planet case when there is a single planet crossing the stellar disc. Equation (2.72) takes also into account multi-planet transit events. We note that this approach does not take into account occultations between planets that may occur.

Figure 2.10 shows an example of the flux computed with eq. (2.72) for a star with two transiting exoplanets. From this figure we can see that the two planets have different period and radii. A multiple transit event is visible for the second planet of the smaller signal.

2.3.5   Planet radius and orbital parameters

Transits can reveal the presence of exoplanets orbiting stars. However, we can also learn about the physical properties of them. In section 2.3.1 we discuss how the transit depth is directly related with the planet-star ratio $r_\mathrm{p} = R_\mathrm{p}/R_\star$. Therefore, we can estimate the planet physical radius if we know the stellar size from an independent method, such as spectroscopy or astereoseismology. Even in the non-uniform disc case, the planet radius can be determined from the implemented limb darkening model.

Seager & Mallén-Ornelas (2003) showed that in the case of a planet in a circular orbit around an uniform source, there exist analytic relations to obtain the orbital parameters of the system. In a realistic case, in which limb darkening effects are present and the orbits may not be circular, we can compare theoretical models with data to estimate system's parameters (See Chapter 5).

Equation (2.68) shows that the light dimming depends on the scaled projected distance between the planet and star centres δ. This quantity depends on $a/R_\star$, e, ω, i and ν. Observations are given as photometric time-series, for instance, the dependence on ν has to be changed to the temporal parameters T_p and P. For a transiting planet, the time of minimum conjunction is also the mid-transit time T_0. Therefore, in transit analysis is common to estimate T_0 instead of the time of periastron T_p. They both are related via the true anomaly as $\nu(T_0) = \nu(T_\mathrm{p}) + \pi/2 - \omega_\star$. If this planet has a Keplerian orbit, it will cross T_0 each period P. This implies that a time-series with multiple transits of the same planet lead to a precise determination of T_0 and P.

If we have a estimation of the stellar temperature $T_\star$, we can compute the planet equilibrium temperature as

$$T_\mathrm{eq} = T_\star \left(1 - \alpha\right)^{1/4} \sqrt{\frac{R_\star}{2a}}, \tag{2.73}$$

where α is the planet *albedo*. We can also estimate the insolation received at the planet as

$$F_{\rm p} = \left(\frac{R_\star}{R_\odot}\right)^2 \left(\frac{T_\star}{T_\odot}\right)^4 \left(\frac{\rm AU}{a}\right)^2 F_\oplus \tag{2.74}$$

where $T_\odot = 5772\,{\rm K}$ and $R_\odot = 6.957 \times 10^8\,{\rm m}$ are Sun's equilibrium temperature and radius, respectively (Prša et al., 2016); a is the orbit semi-major axis in astronomical units AU; and $F_\oplus$ is the insolation Flux received at Earth.

2.3.6   Stellar density from transits

Transits also provide the stellar mean density. If we divide Kepler's third law (Eq. (2.28)) by the stellar volume $V_\star = 4/3\pi R_\star^3$ we obtain

$$\rho_\star + r_{\rm p}^3 \rho_{\rm p} = \frac{3\pi}{\rm G}\frac{1}{P^2}\left(\frac{a}{R_\star}\right)^3, \tag{2.75}$$

where $\rho_\star$ and $\rho_{\rm p}$ are the stellar and planetary densities, respectively. The term $r_{\rm p}^3$ is of the order of 10^{-3} for a Jupiter-size planet around a Sun-size star, and 10^{-6} for an Earth-size planet around a Sun-like star. Therefore, we can assume that the second term of the left-hand part of Eq. (2.75) is negligible. This gives

$$\rho_\star \approx \frac{3\pi}{\rm G}\frac{1}{P^2}\left(\frac{a}{R_\star}\right)^3. \tag{2.76}$$

Equation (2.76) can be used as a diagnostic tool in photometric transit surveys given that a planetary transit signal should yield a value of $\rho_\star$ that is consistent with the spectroscopically-derived stellar density (Winn, 2010). Alternatively, a high signal-to-noise ratio transit light curve can be used to better constraint the fundamental parameters of the host star (Sozzetti et al., 2007).

2.4   Science with transit light curve and radial velocity measurements

The transit and RV methods are powerful tools to detect exoplanets. They also allow us to estimate planetary and orbital parameters. When both methods are used together, they provide valuable and unique information about planetary systems.

2.4.1   Planet surface gravity

If we have transit photometry and RV measurements, we are able to extract eight important parameters, namely, T_0 (or $T_{\rm p}$), P, e, $\omega_\star$ (or ω), $r_{\rm p} = R_{\rm p}/R_\star$, $a/R_\star$, i and K. If we combine these parameters, we can estimate the planet surface gravity as (Southworth et al., 2007)

$$g_{\rm p} = \frac{2\pi}{P}\frac{\sqrt{1-e^2}\,K}{R_{\rm p}^2/a^2\,\sin i}. \tag{2.77}$$

The surface gravity can also be calculated as

$$g_{\rm p} = \frac{{\rm G}m_2}{R_{\rm p}^2}, \tag{2.78}$$

where m_2 and R_p are the planet mass and radius, respectively, calculated assuming a given set of stellar parameters. We can compare the two estimates of the gravity derived using equations (2.77) and (2.78) to verify that the stellar parameters have been correctly derived (Southworth et al., 2007).

2.4.2 Planet's true mass

In Sect. 2.2.2 we discussed how the RV method can provide only the planet's minimum mass (if the stellar mass is known). This is because the method does not allow us to measure the inclination of the orbit with respect to the line of sight.

The orbit inclination is well constrained by the transit method. For systems for which we have both RV and transit data, we can use the orbit inclination obtained from the modeling of the transit to estimate the planet's *true* mass.

2.4.3 Planet composition and structure

The transit method allows us to measure the planet's radius. Doppler spectroscopy yields the planet's true mass if combined with the orbit inclination derived from the transit modeling. The mass and radius can be used to derive the planet's mean density. By comparing the position of the planet on a mass-radius diagram with composition models, we can infer the planet's composition and internal structure (see Sect. 1.5.2).

CHAPTER 3

K2 TIMES-SERIES PHOTOMETRY

A clear night gives us an instantaneous snapshot of the Universe. At first sight celestial bodies seem immutable, but they are not. Their apparent immutability disappears if we measure the intensity of their emitted or reflected light as a function of time. The variability of their light – the so-called *light curve* – carries a wealth of precious information about the physical phenomena happening in faraway astronomical bodies. In Sect. 1.4.2 we discussed how the periodic stellar flux drop caused by the passage of a planet in front of the parent star can be used to detect "alien" worlds. In the following sections we will describe the challenges of detecting planetary transits in stellar light curves. We will also talk about the exquisite photometry of the space-based telescope *Kepler*.

3.1 Transits in stellar light curves

In order to detect transiting exoplanets in stellar light curves, two important "ingredients" are needed: high-precision photometry and continuous observations (Cameron, 2016). The required photometric precision depends on the depth of the transit we want to detect. Figure 3.1 displays the transit depth *vs.* the planet-to-star radius ratio for different stellar radii. To detect a Jupiter-size planet transiting a Sun-size star, we need a photometric precision of $\approx 1\%$ (10^4 ppm; Fig. 3.1). This precision was only reached at the end of the last century, when the first transit of the extrasolar planet HD 209458 b was discovered (Henry et al., 1999; Charbonneau et al., 2000). The required photometric precision increases for Earth-size planets transiting Sun-size stars, for which a precision better than 0.01% (100 ppm) is needed. The transit depth is inversely proportional to the square of the stellar radius. A planet transiting a very late-type M dwarf star ($R_\star \approx 0.1\,R_\odot$) produces a transit 100 times deeper than it would induce if it were transiting a G-type star ($R_\star \approx 1\,R_\odot$).

For ground-based transit observations, the photometric precision is ultimately limited by the Earth's atmosphere. The best photometric precision achievable from the ground is $\sim 0.1\%$ (1000 ppm; Fig. 3.1), owing to the atmospheric transparency fluctuations and scintillation noise (Cameron, 2016). Ground-based transit observations can easily detect gas-giant planets transiting Sun-like stars, but cannot detect the signal caused by an
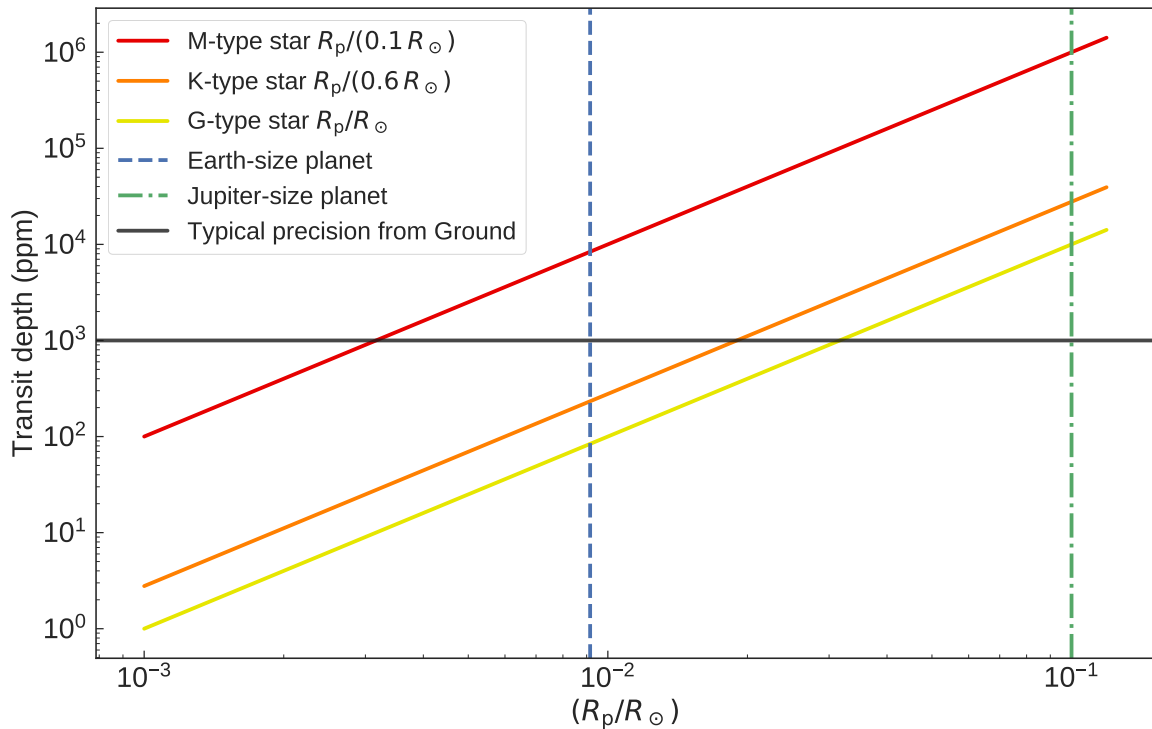
Figure 3.1: Transit depth *vs* planet-to-star radius ratio. Limb darkening effects have been neglected. The diagonal lines refer to different stellar radii (see the legend in the upper left corner). The vertical dashed and dash-dotted lines refer to the Earth's and Jupiter's size, respectively. The black horizontal line marks the best photometric precision (1000 ppm; 0.1%) achievable from the ground.

Earth-size planets passing in front of a G- or K-type star. Such planets can only be detect from the ground if they transit M-type stars.

Earth's rotation also limits the planet detections that are attainable from the ground. Long period transiting exoplanets have relatively long transit duration compared to the observing window of a star in a single night. The diurnal cycle of the Sun precludes reliable detection of transits of more than 5 or 6 h duration (Cameron, 2016).

While ground-based transit surveys have allowed us to detect short-period ($P < 10\,\mathrm{d}$) transiting giant planets ($R_\mathrm{p} \approx 10\,R_\oplus$) around relatively bright stars ($V < 13\,\mathrm{mag}$; see, e.g., Bakos et al., 2010; Pollacco et al., 2006), the discovery of small ($R_\mathrm{p} < 4\ R_\oplus$) and long-period ($P > 10\,\mathrm{d}$) transiting planets has been possible thanks to space-based transit search missions, such as *CoRoT* (Auvergne et al., 2009) and *Kepler* (Borucki et al., 2008).

The work presented here is based on time-series photometry collected during the so-called "*Kepler*'s second light", namely, the *K2* space-mission. We will therefore describe the *Kepler* space telescope, as well as the observations carried out during the nominal *Kepler* mission (2009 - 2013) and the extended *K2* mission (2014 - today).

3.2   The *Kepler* mission

In 2009 the *Kepler* spacecraft (Borucki et al., 2008) was launched to continue the search for transiting planets in our Galaxy – a hunt started in 2006 by the European space-telescope *CoRoT* (Auvergne et al., 2009), which was the first mission to demonstrate the pioneering science that would result from ultra-precise, long duration and continuous space-based photometric measurements. The primary science objective of the *Kepler* mission was the transit-driven exoplanet detection of small planets, with an emphasis on terrestrial

($R_p < 2\,R_\oplus$) planets located within the habitable zone of Sun-like stars (Borucki et al., 2008; Koch et al., 2010). In order to achieve this goal, *Kepler* collected high precision, continuous time-series photometry of more than 150,000 stars in the Cygnus-Lyra region.

3.2.1 The spacecraft

The *Kepler* spacecraft was built to obtaine high precision and continuous photometry of a large sample of stars (Koch et al., 2004, 2010). The *Kepler* telescope optical design consist of a 0.95 m Schmidt telescope with a field of view (FOV) of 116 square degrees, which allows for a simultaneous observation of more than 150,000 stars. The photometric detector consist of 42 charged coupled devices (CCDs) mounted in the focal plane of the telescope (Koch et al., 2004). Each CCD consists of arrays of 2200×1024 pixels, with a sky-projected pixel size of $3.98''$. The point-spread-function (PSF) for each star has 95% of its light within 2.5 to 5 pixels depending on its location in the FOV. Such CCDs detect visible light between 4200-9000 Å (the *Kepler* bandpass) with a median quantum efficiency of 40%. This allows for a dynamic range which goes from magnitude 9 to 15 in the *Kepler* bandpass. With this detector configuration, the telescope reached typical noise levels of $\sim$15 ppm in 6.5 h. for a $V = 12$ mag solar-like star.

An important aspect of the *Kepler* spacecraft is the telescope stability needed to reach high precision photometry. The spacecraft was built with four reaction wheels and twelve thrusters which can be shoot to ensure correct pointing. Such instrumentation was designed to roll the spacecraft to optimise solar power and to correct for solar wind pressure (Koch et al., 2004). The spacecraft is also equipped with ten coarse Sun sensors, two star trackers, and two three-axes inertial measurement units for initial acquisition, roll manoeuvres and safe-survival modes (Koch et al., 2004).

3.2.2 *Kepler* observations

Kepler mission was launched on March 6, 2009 and started science operations on May 13 of the same year. The spacecraft was placed in an Earth-trailing orbit to ensure a thermal stability and to provide precise pointing towards the same FOV (Koch et al., 2010). The telescope was pointed towards the Cignus-Lyra region (the centre of the field had coordinates R.A. $= 19^{\mathrm{h}}\,22^{\mathrm{m}}\,40^{\mathrm{s}}$ and DEC $= 44°\,30'\,00''$) which is just off of the galactic plane and 55° above the ecliptic plane (Koch et al., 2010). *Kepler* observed this field for almost 4 continuous years with the objective of detecting at least three-four transits of an Earth-size planet with an orbital period of one year in the habitable zone of a Sun-like star (Koch et al., 2010).

3.2.3 *Kepler*'s light curves

Kepler's detector[1] acquires one exposure every 6.5 s. Such exposures are integrated and stored in *long* and *short cadence* formats. Long cadence corresponds to a summed integration of 1765.5 s (29.4 min), while short cadence refers to 58.89 s (1 min). *Kepler*'s recorder can store only 5.4 million of the 95 million pixels available. Therefore, postage stamps have to be chosen strategically to collect data centred on targets of interests. The average number of postage stamps was around 166,000 targets per month for *Kepler*. Each target pixel file (TPF) packages these pixels as a time series of images in a binary flexible image transport system (FITS) file (Thompson et al., 2016).

Light curves are derived from TPFs files. There is a one-to-one correspondence between the files and timestamps and quality flags within the two products are identical. The

---

[1]The information about *Kepler* light curves are taken from https://keplerscience.arc.nasa.gov/data-products.html.
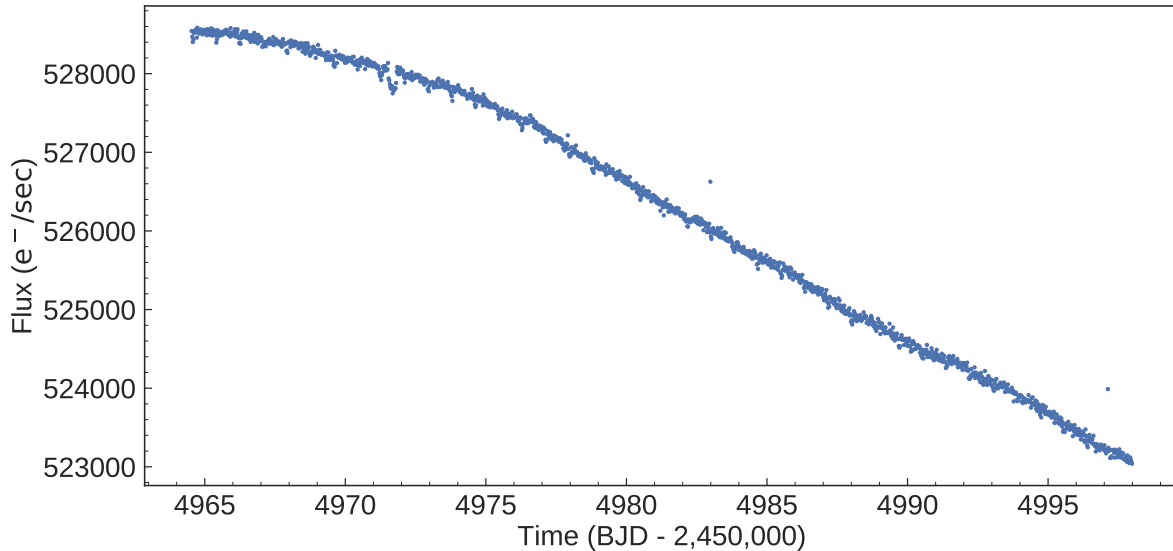
Figure 3.2: Light curve of Kepler-10 (KOI-72) observed by *Kepler* between May 13 and June 15, 2009 in long-cadence mode ($T_{\exp} = 1765.5\,\mathrm{s}$). The photometry has been downloaded from the MAST archive.

primary data within the light curve file is Simple Aperture Photometry - a summation of the calibrated pixels in the TPF. These light curves have intrinsic artefacts due to the spacecraft drift of typically 20 mas (milli-arcsec) over 6.5 hours and artefacts coming from the spacecraft itself, such as temperature changes. The *Kepler* team offered as final data products light curves coming from a pipeline designed to mitigate all these artefacts.

The spacecraft had to roll 90 degrees every three months to optimise solar panel efficiency. Whence, the spacecraft operations were divided in four sections each year called *quarters*. *Kepler* long cadence images and light curves are stored in files that span one quarter, i.e. three months. While short cadence data are saved in files that contain one month time-series.

The TPFs are the rawest form of target-specific data available from the *Kepler* archives. TPFs files together with light curves are available at the Mikulski Archive for Space Telescopes (MAST, https://archive.stsci.edu/kepler/). Figure 3.2 shows paer of the light curve of Kepler-10 as observed by *Kepler*. The shallow transit signals occurring every 0.84 d are caused by the the transiting planet Kepler-10 b (Batalha et al., 2011). The long term photometric variation is due to intrinsic flux changes of the star (see Appendix. A.1 for more details).

3.3   The *K2* mission

Kepler observed the Cignus-Lyra region for almost 4 years until May 11, 2013, when the second reaction wheel failed[2], causing the end of *Kepler*'s primary mission.

In 2014 the *Kepler* project team proposed a new mission concept named *K2* (Howell et al., 2014). The *K2* mission entails a series of sequential observing *Campaigns* of fields distributed around the ecliptic plane and offers a photometric precision approaching that of the original *Kepler* mission. Operating in the ecliptic plane minimises the torque exerted on the spacecraft by solar wind pressure, reducing pointing drift to the point where spacecraft attitude can effectively be controlled through a combination of thrusters and the two remaining reaction wheels. Each campaign is therefore limited by Sun angle

---

[2]On July 14, 2012, one of the four reaction wheels used for fine pointing of the spacecraft failed. As for any other spacecraft, three reaction wheels are needed to point the telescope.

constraints to a duration of approximately 80 days. *K2* campaigns last approximately 80 days observing towards the same sky region in the ecliptic plane. The details of each campaign are given in the *Kepler* science web-page (https://keplerscience.arc.nasa.gov/k2-fields.html).

3.3.1 *K2* light curves

As for the nominal *Kepler* mission, on board storage and bandwidth are limited. Constraints imposed by onboard storage and communications dictate that at most 6 per cent of the data from the full focal plane are saved and downloaded. Therefore, data for specific pre-selected targets is stored and transmitted to Earth. Such targets are proposed by the community via the NASA's Guest Observer program[3]. Each Campaign observe between 10,000 to 20,000 long cadence and between 50 and 100 short cadence targets. Each target is identified with an unique number stored in the Ecliptic Plane Input Catalog (EPIC). Final data products available to the community include original and calibrated pixel files, and light curves for each individual target.

The light curves from *K2* contain larger systematics than the original *Kepler* mission, due to the reduction in pointing precision as a result of having to rely on only two reaction wheels. The nominal *Kepler* pipeline is not able to remove all the artefacts of the light curve, such as those caused by the thruster firing. Vanderburg & Johnson (2014) created a technique to correct for the pointing-dependent nature of the pixel-level fluxes. The basic idea is to correlate the non uniform pixel response of the detectors with the spacecraft's pointing. In this way it is possible to remove the artefacts due to the spacecraft "shaking". Vanderburg & Johnson (2014) demonstrated this correction improves the photometric precision by typical factors of 2-5, and results in median photometric performance of *K2* targets to within a factor of two of the original, four-wheeled mission. Figure 3.3 shows the raw and corrected *K2* light curve of the target EPIC 218916923, that was observed by *K2* in campaign 7. The raw light curve (red points) exhibits abrupt changes of flux caused by the spacecraft thurster firing. Once the photometric data are corrected (blue points), the light curve shows flux variations due to physical effects (planetary transits and magnetic activity; see Barragán et al., 2018a, and Section 6.2).

As of September 2018, there are a handful of public pipelines that provides corrected light curves, such as K2SC (Aigrain et al., 2016), EVEREST (Luger et al., 2016) and K2SFF (Vanderburg & Johnson, 2014). The data are made available to the community through the MAST web-page.

3.3.2 Follow-up observations of *K2* targets

The nominal *Kepler* mission targets were typically faint stars ($13 < V < 15$). This was done with the propose of building a large sample of stars to check for long period planets. This helped us to understand planetary populations in the galaxy. However, such targets are not easy to follow-up from ground-base observations, which are required to perform further exoplanet characterisations.

K2 focuses on stars brighter than the nominal *Kepler* mission ($V < 13$). Transiting exoplanets detected around bright stars observed by *K2* can be monitored with ground-base instruments. Between them are ground-base spectrographs to perform high-precision spectroscopy (see Chapter 4). This allows us to measure the induced Doppler effect on the stellar light caused by the orbiting planets, hence to estimate the planet true mass and density. This give us hints on the planet composition. Another advantage about observing

---

[3]See https://keplerscience.arc.nasa.gov/k2-observing.html.
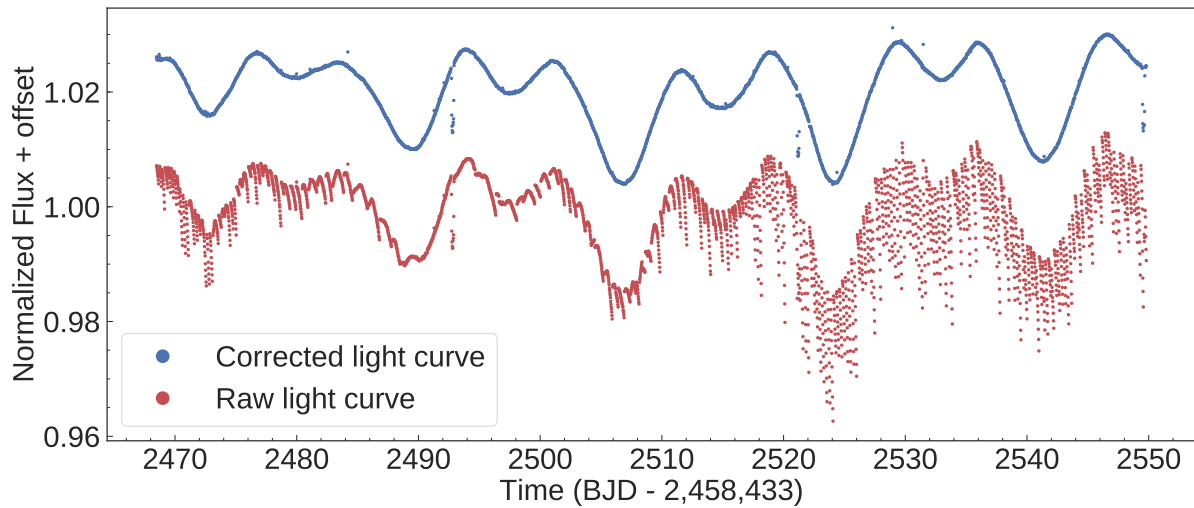
Figure 3.3: Raw (red dots) and corrected (blue dots) light curves of the *K2* target EPIC 218916923 (K2-139). This plot was created using data from Vanderburg & Johnson (2014, https://www.cfa.harvard.edu/~avanderb/k2c7/ep218916923.html).

K2 bright stars is that they can be characterised better that faint ones. High resolution spectroscopy and imaging, parallaxes, proper motion, among other techniques, allow for precise stellar characterisations. This has a direct consequence a better characterisation of the hosted exoplanets. Our results on radial velocity follow-up of *K2* targets are presented in Chapter 6.

CHAPTER 4

HIGH-PRECISION RADIAL VELOCITY MEASUREMENTS

Spectroscopy is the study of the interaction between electromagnetic waves and matter. The intensity of the light emitted/reflected from/by a body at different wavelengths is called *spectrum*. Astrophysics was born when humankind started to use the spectra of astronomical objects to understand their physical and chemical nature. The elements in the atmospheres of cool stars absorb and remit the light at specific wavelengths, producing a forest of spectral lines. Given its wave behaviour, light experiences the *Doppler effect*. If we are able to measure the Dopper shift $\Delta\lambda$ of the atmospheric absorption lines, we can measure the radial velocity of a star and search for the tiny signal induced by an orbiting planet.

4.1 Planet-induced radial velocity variation

The equations that describes the RV variation of a star orbited by a second body are known since more than a century (see, e.g., Vogel, 1873). However, the first detection of an exoplanet made via the RV method is relatively recent (Mayor & Queloz, 1995). This is because of the small RV variation induced by planets. Figure 4.1 shows the expected reflex motion for a Sun-mass star induced by planets with different masses as a function of the semi-major axis (see Eq. 2.59). As already briefly described in Sect. 1.4.1, the Sun's RV variation due to the presence of Jupiter ($P = 11.9$ years, a $= 5.2$ AU) is only $11.2 \, \mathrm{m\,s^{-1}}$. However, Jupiter would induce a stronger Doppler shift if its orbit were closer and/or the Sun were less massive. An Earth-mass planet with an Earth-like orbit causes a reflex motion of a mere $\sim 10 \, \mathrm{cm\,s^{-1}}$. The same planet would induce a RV variation of $1 \, \mathrm{m\,s^{-1}}$ if its orbit had a radius of 0.05 AU. Therefore, in order to detect exoplanets with the RV method we need spectrographs with exquisite RV precision and long-term stability (Hatzes, 2016).
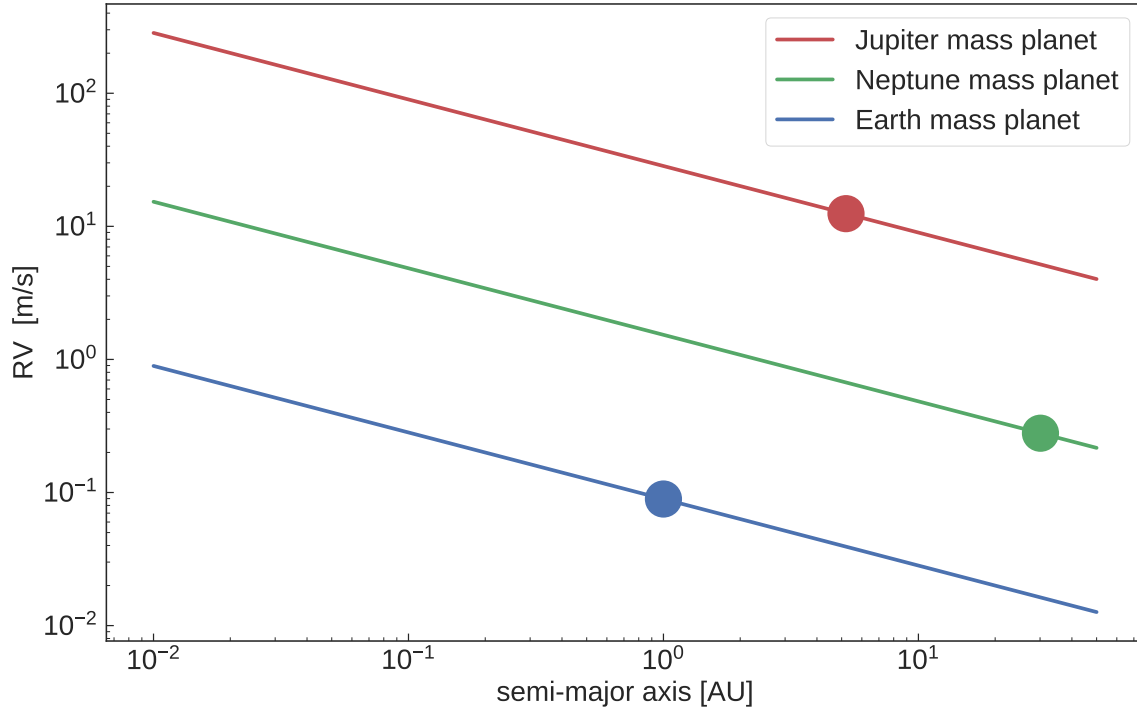
Figure 4.1: Sun's RV semi-amplitudes induced by Earth-, Neptune-, and Jupiter-mass planets at different orbital radii. The RV amplitudes are calculated assuming an inclination of 90 deg. RV variation induced by the Earth, Neptune and Jupiter are marked with blue, green, and red circles, respectively.

4.2 Spectrographs

A spectrograph is an instrument which breaks the light into its component wavelengths and spreads them apart (dispersion) using a dispersing element, such as a prism or a diffraction grating (Hatzes, 2016). In order to obtain spectra of astronomical bodies, the spectrograph has to be combined with a telescope – the light collector. Typically, the light from the telescope mirror converges to a focus at the entrance slit (or fibre) of the spectrograph. The light is then collimated, directed onto the dispersing element, and dispersed into its wavelength components. Finally, the dispersed light can be stored on photographic plates or in electronic detectors.

Most RV measurements are made at optical wavelengths using charge coupled devices (CCDs) detectors. We note that a spectrograph does not produce directly wavelength *vs* flux data. It does produce an image of the stellar spectrum, i.e., electron counts in a 2D pixel array. Details on the data reduction to convert CCD data into spectra are out of the scope of this work. For more details we refer the reader to more specific literature (see, e.g., Hatzes, 2016, and references therein).

The spectral resolution $\Delta\lambda$ of a spectrograph is defined as the smallest difference in wavelengths that can by resolved by the instrument at a given wavelength λ. It sets "the size" of the smallest spectral features that can be studied in the spectrum. The resolving power is defined as

$$R = \frac{\lambda}{\Delta\lambda}. \tag{4.1}$$

Following Hatzes (2016), the RV precision that can be achieved using a spectrograph of resolving power R is given by the following equation

$$\sigma_{\text{tot}}[\text{m s}^{-1}] \propto (\text{S/N})^{-1} \text{R}^{-3/2} \text{N}_{\text{lines}}^{-1/2} \sigma \qquad (4.2)$$

where (S/N) is the signal-to-noise ratio of the spectrum, N_{lines} the number of spectral lines, and σ the Doppler shift error of a single line. We note that the RV precision depends also on the spectral type of the observed star, as well as on its projected rotational velocity $v \sin i_\star$ (see Sect. 1.3.2 of Hatzes, 2016).

Equation (4.2) tells us that in order to achieve high-precision RV measurements it is necessary to use spectrographs with a large range of wavelengths and high-spectral resolution. *Echelle* spectrographs are designed with this propose. They disperses the light in two orthogonal directions using two dispersion stages (see, e.g., Gray, 2005; Hatzes, 2016).

4.3 High-precision spectrographs

The development of precise and stable high-resolution spectrographs is at the heart of the success of the RV method to detect extra solar planets. Nowadays, many spectrographs allow us to achieve the 1-5 m s^{-1} precision. In this Chapter we will briefly describe the three spectrographs that have significantly contributed to the success of our *K2* RV follow-up program. Results will be presented in Chapter 6.

4.3.1 FIES

The Fibre-fed Echelle Spectrograph (FIES, Frandsen & Lindberg, 1999; Telting et al., 2014) is mounted at the 2.56 m Nordic Optical Telescope, which is located at the Roque de los Muchachos observatory in the Canary Island of La Palma (Spain).

The spectrograph is fed by an octagonal fibre. This improves the light scrambling inside the fibre link and reduces the effects of illumination variations of the fibre pupil (Bouchy et al., 2013). In order to ensure long-term stability of the spectrograph, FIES is installed in a heavily insulated building separate from, and adjacent to, the telescope dome. The instrument is kept to a constant temperature within 0.02 °C. FIES has a high efficiency and can reach an RV precision of less than 2-3 m s^{-1} on slowly rotating late-type stars with V=9 mag in $T_{\text{exp}} = 20$ min (Gandolfi et al., 2017).

FIES covers the wavelength range from 3700 to 8300 Å without gaps in a single, fixed setting. The instrument allows for three different resolving powers of $R = 25,000, 46,000$ and $67,000$ called `LOW-RES`, `MED-RES`, and `HIGH-RES`, respectively.

The detector consists of one CCD of 2k × 2k 15μm pixels. Data are stored as flexible image transport system (FITS) files containing the CCD data. The observing strategy and data reduction techniques for FIES are described in Buchhave et al. (2010) and Gandolfi et al. (2013, 2015). Briefly, the observing strategy consists of taking three consecutive exposures per observation epoch – to remove cosmic ray hits – and acquire long-exposed ($T_{\text{exp}} \approx 30\text{-}60$ s) ThAr spectra immediately before and after the three sub-exposures – to trace the RV drift of the instrument. The spectra are reduced using standard procedures specifically designed for Echelle spectrographs. The radial velocity measurements are derived via multi-order cross-correlation with the spectrum of an RV standard star observed with the same instrument set-up as the target of interest.

4.3.2 HARPS

The High Accuracy Radial velocity Planet Searcher spectrograph (HARPS, Mayor et al., 2003) is mounted at the ESO-3.6 m telescope at La Silla observatory (Chile). The instru-

ment is a fibre-fed cross-dispersed Echelle spectrograph, providing a resolving power of $R \approx 115\,000$ in the wavelength range $\sim 3800 - 6900$ Å. The detector consists of two CCDs with pixel size of 15μm. The spectrograph is fed by two fibres (A and B): fibre A is the target fibre, while fibre B is the reference fibre that can be fed by a wavelength calibration unit, such as a Th-Ar or Fabry-Perot lamp. Alternatively, it can be used to monitor the sky background. (Hatzes, 2016).

The most important characteristic about HARPS is its stability. The spectrograph is placed inside a vacuum vessel in an insulated room below the telescope, enabling very accurate control of its temperature (within 0.01 °C). HARPS is kept in vacuum with a pressure always below 0.01 mbar. This ensures that the daily instrument RV drift is well below 1 ms. This makes HARPS is a state-of-the-art spectrograph in terms of RV precision, a fundamental requirement for RV planet search surveys.

HARPS data products consist of FITS files with extensions containing the data from both CCDs. The HARPS acquisition software is connected with the Data Reduction Software (DRS) at the telescope to perform an almost instantaneous data reduction. Every HARPS frame is processed by the online DRS pipeline, which delivers the extracted spectra. The RV measurements are measured by cross-correlating the observed spectra with numerical masks.

4.3.3   HARPS-N

The HARPS-N spectrograph (Cosentino et al., 2012) is mounted at the 3.6 m Telescopio Nazionale Galileo (TNG) of Roque de los Muchachos Observatory (La Palma island, Spain). HARPS-N is a copy of the HARPS spectrograph. It has been designed to be the most precise spectrograph in the Northern hemisphere. The instrument characteristics, including, the achieved RV stability, spectral resolution, and spectral coverage, are very similar to those of HARPS. The HARPS-N data are reduced using a dedicated HARPS-N pipeline. Radial velocities are extracted by cross-correlating the observed spectra with numerical masks.

4.4   RV observations conducted as part this thesis

As part of the work presented in this thesis, I performed high-resolution spectroscopic observations of *K2* bright stars ($V \lesssim 13$ mag). Specifically, the FIES RV follow-up was conducted on five nights, from January 30 to February 2, 2016, and from February 3 to February 5, 2018. Additional FIES spectra were collected in service mode, and in visitor mode by collaborators.

I also conduced intensive follow-up observations with the HARPS spectrograph. I carried a total of 33 nights of observations as follows: April 29 - May 3, 2016; November 21-29, 2016; August 18-27, 2017; March 13-17, 2018; April 10-14, 2018; May 10-14, 2018.

The HARPS-N observations were performed in service-mode.

The data collected during these observing have been published in Barragán et al. (2016, 2018a,b); Dai et al. (2017); Gandolfi et al. (2017); Guenther et al. (2017); Johnson et al. (2018); Palle et al. (2018); Prieto-Arranz et al. (2018); Persson et al. (2018); Trifonov et al. (2018); Van Eylen et al. (2018b).

CHAPTER 5

DATA ANALYSIS

In this chapter we describe the software suite `pyaneti`[1], which was developed in the course of this thesis project. `pyaneti` is a powerful and robust tool to perform multi-planet fit to RV and/or transit data sets. It combines the MCMC technique with the computational power of `FORTRAN` and the versatility of `PYTHON`. The code `pyaneti` is stored in the web repository `github` at https://github.com/oscaribv/pyaneti and is also indexed in the Astrophysical Source Code Library with the registration number 1707.003. Details about `pyaneti` can be found in Barragán et al. (2019).

This code has already been used for the analysis of several planetary systems (see, e.g., Barragán et al., 2016, 2018a,b; Chakraborty et al., 2018; Fridlund et al., 2017; Gandolfi et al., 2017, 2018; Guenther et al., 2017; Li et al., 2017; Livingston et al., 2018; Palle et al., 2018; Persson et al., 2018; Prieto-Arranz et al., 2018).

5.1 Bayesian analysis

The aim of data analysis is to extract information from experiments and/or observations. In this work, we are interested in extracting planetary physical parameters by comparing parametric models with astronomical observations. From a probabilistic point of view, we want to estimate the probability that a physical parametric model $M = M(\vec{\phi})$, function of some parameters $\vec{\phi}$, describes the data D. Such probability is called the conditional probability of M given D and it can be written as $P(M|D)$.

Bayes' theorem (Bayes & Price, 1763) provides a simple and robust mathematical framework to compute $P(M|D)$ as

$$P(M|D) = \frac{P(D|M)P(M)}{P(D)}.$$ (5.1)

In a context of a fixed data set, $P(D|M)$ is a function of the model called the likelihood of observing the data set D if the model M is true, while $P(M)$ is the prior probability

---

[1]From the Italian word *pianeti*, which means *planets*.

associated to the model M, and $P(D)$ is the model evidence. $P(M|D)$ is called the joint posterior distribution and it gives the probability that a model M is true given D is true.

5.1.1 Likelihood

For a given data set D composed of N measurements $D_{1,...,N}$, we can generate a set of N predicted points $M_{1,...,N}$ from a parametric model. The likelihood of a point D_i being described by a point M_i is written as $P(D_i|M_i)$. The likelihood of the whole data set D to be described by the model M is given by the product of each probability $P(D_i|M_i)$ as

$$P(D|M) = \prod_{i=1}^{N} P(D_i|M_i). \tag{5.2}$$

In order to compute $P(D|M)$ using eq. (5.2), we need to find out which likelihood functions describes better our data. If we assume that our measurements are normally distributed, independent, and that only contain uncorrelated noise σ_i, the likelihood of the data point D_i being true, assuming M_i is also true, is written as

$$P(D_i|M_i) = \frac{1}{\sqrt{2\pi(\sigma_i^2 + \sigma_j^2)}} \exp\left\{-\frac{1}{2}\frac{(D_i - M_i)^2}{\sigma_i^2 + \sigma_j^2}\right\}, \tag{5.3}$$

where the terms σ_j are used to normalise the likelihood in the case the nominal uncertainties σ_i are underestimated (see e.g., Sharma, 2017). If we use eq. (5.3) for a data set, its likelihood is given by using eq. (5.2) as

$$P(D_i|M_i) = \prod_{i}^{N} \left[\frac{1}{\sqrt{2\pi(\sigma_i^2 + \sigma_j^2)}}\right] \exp\left\{-\frac{1}{2}\chi^2\right\}, \tag{5.4}$$

where

$$\chi^2 = \sum_{i=1}^{N} \frac{(D_i - M_i)^2}{\sigma_i^2 + \sigma_j^2}. \tag{5.5}$$

`Pyaneti` uses the likelihood given by eq. (5.4), but we acknowledge that more general likelihoods exist, in which possible correlated noise between data points is taken into account (see, e.g., Parviainen, 2017; Sharma, 2017). We also note that for numerical reasons, it is better to treat $P(M|D)$ in a logarithmic way (See Sect. 5.3.3).

5.1.2 Priors

Priors contain previously known information about a given model parameter, e.g., some physical range in which a parameter has equal probability to lie. Alternatively, the parameter's probability can be given by a distribution based on previous estimates. Widely used priors are the uniform and Gaussian priors.

A *uniform prior* is called a weakly informative or uninformative prior. It is used when the only available information about a given parameter ϕ_i is that it lies inside a range $[a, b]$. For example, we know that the eccentricity of an elliptical orbit ranges between 0 and 1. If the parameter ϕ_i lies between a and b with equal probability, its uniform prior is given by
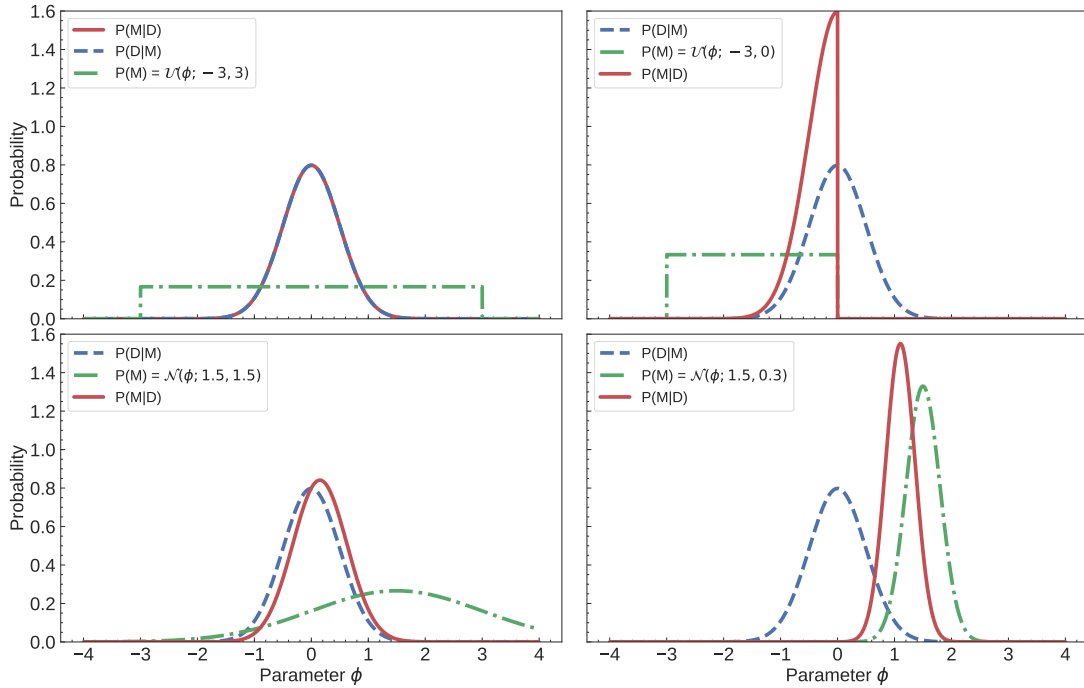
Figure 5.1: Posterior distributions (solid red line) for a fixed likelihood (blue dashed lines) and different priors (green dot-dashed lines). All quantities have been normalised for comparison purpose. *Upper left:* Uniform prior with limits $[-3, 3]$. *Upper right:* Uniform prior with limits $[-3, 0]$. *Lower left:* Gaussian prior with mean 1.5 and standard deviation 1.5. *Lower right:* Gaussian prior with mean 1.5 and standard deviation 0.3.

$$\mathcal{U}(\phi_i; a, b) = \left\{ \begin{array}{ll} (b-a)^{-1} & : a < \phi_i < b \\ 0 & : \text{otherwise} \end{array} \right. \tag{5.6}$$

A *Gaussian prior* is called an informative prior. This prior is useful when, for a given parameter, we have a previous measurement and its 1-σ uncertainty, and we want to use this information to weight the probability. For instance, if we have asteroseismology-derived mass and radius of a star hosting a transiting planet, we can use these quantities together with the orbital period to set a Gaussian prior on the semi-major axis of the planet's orbit through Kepler third law.

A Gaussian prior of a given parameter ϕ_i with median a and standard deviation b is given as

$$\mathcal{N}(\phi_i; a, b) = \frac{1}{\sqrt{2\pi b^2}} \exp\left[-\frac{(\phi_i - a)^2}{2b^2} \right]. \tag{5.7}$$

In this work we describe only the uniform and Gaussian priors, as those are currently implemented in `pyaneti`. We acknowledge the existence of other priors in the literature (see, e.g., Díaz, 2018; Sharma, 2017). Figure 5.1 shows how priors can affect the final posterior distribution for a fixed likelihood. For instance, the upper and lower limits of a flat prior may truncate or exclude the maximum of the likelihood function. The influence of a Gaussian prior on the posterior distribution depends on the prior's centre and width, as well as on the number of data points (e.g., Gelman et al., 2004).

5.1.3 Model evidence

The term $P(D)$ in equation (5.1) is called model evidence or marginal likelihood. It has the function to normalise the posterior distribution. By definition $P(D)$ is calculated by integrating the likelihood and prior distributions in the parameter space as

$$P(D) = \int P(D|M(\vec{\phi}))P(M(\vec{\phi}))d\vec{\phi}. \tag{5.8}$$

5.1.4 Marginal posterior distribution

We now have a mathematical description of all the components to calculate $P(M|D)$ from equation (5.1). In order to derive the parameters, we are interested on the shape of the posterior distribution of each parameter ϕ_i more than in its normalised probability. The parameter estimation can be extracted from the non-normalised posterior distribution, i.e. the term $P(D|M)P(M)$, ignoring the evidence term $P(D)$. We note that the evidence term has an important role when doing Bayesian comparison between different models (see, e.g., Gelman et al., 2004). Since M is a parametric model, we can marginalise the parameter ϕ_i by integrating $P(D|M)P(M)$ over the remaining $\phi_{j\neq i}$ parameters. This leads to a marginal posterior distribution for each parameter ϕ_i from which we can infer the model parameters.

5.2 Markov chain Monte Carlo

The calculation of a marginal posterior distribution can be done analytically or numerically. However, in some cases it may not have an analytic solution. For instance, numerical iterative methods are widely used to sample the parameter space in order to generate marginal posterior distributions from a collection of data points.

An efficient method to generate a set of data points in a parameter space is by using a *Markov chain*. Following the definition of Sharma (2017), a Markov chain is a sequence of random variables $X_1, \ldots, X_n$ such that, given the present state, the future and past are independent. If random numbers are used to generate the Markov chains, this method is called Markov chain Monte Carlo (MCMC). These random variables can be the points $\vec{\phi}$ in the parameter space that we want to sample. For instance, if we start a point in the parameter space $\vec{\phi}_1$, we can generate a set of different models $\vec{\phi}_i$ via Markov chains. In this way, we can create a set of N models from an initial $\vec{\phi}_1$.

There is a large variety of MCMC sampling methods, which ensure that the Markov chains converge to the optimal solution where the posterior has a static solution. For a basic MCMC algorithm, we refer the reader to the Metropolis-Hastings algorithm (Metropolis et al., 1953; Hastings, 1970). In the next section we will describe the ensemble sampler algorithm (Goodman & Weare, 2010) that is used by `pyaneti` for the parameter estimations. This algorithm was first used by Hou et al. (2012) to infer parameters from time-series RV measurements.

5.2.1 Ensemble sampler algorithm

The *ensemble sampler* algorithm uses a group of Markov chains to explore the parameter space. Each chain j starts with a point in the parameter space $\vec{\phi}_{j,t}$ and is evolved using the complementary chains of the ensemble.

Christen (2007) found that it is possible to evolve the chain $\phi_{j,t}$ to the state $t+1$ via a *walk move* using a complementary chain of the ensemble. Goodman & Weare (2010)

used the idea of the walk move to construct an affine invariant move called *stretch move*. The stretch move for the chain $\vec{\phi}_{j,t}$ is defined as

$$\vec{\Phi}_j = \vec{\phi}_{k,t} + z\left(\vec{\phi}_{j,t} - \vec{\phi}_{k,t}\right), \tag{5.9}$$

where $\vec{\phi}_{k,t}$ is a complementary chain of the ensemble, such that $j \neq k$ and z is a scaling variable that regulates the step. This scaling variable has to come from a density distribution g with the symmetry condition (Christen, 2007)

$$g\left(\frac{1}{z}\right) = z\,g(z). \tag{5.10}$$

A distribution that follows this condition is

$$g(z) \propto \begin{cases} \frac{1}{\sqrt{z}} & : z \in \left[\frac{1}{a}, a\right] \\ 0 & : \text{otherwise,} \end{cases} \tag{5.11}$$

where $a > 1$. There is no optimal value for a, but we set $a = 2$ to be consistent with ensemble sampler algorithms in the literature (e.g., Goodman & Weare, 2010; Hou et al., 2012). To ensure the invariant distribution we have to compute the ratio

$$q = z^{N-1}\frac{P(M(\vec{\Phi})|D)}{P(M(\vec{\phi}_{j,t})|D)}. \tag{5.12}$$

The term z^{N-1} ensures detailed balance (for more details see Goodman & Weare, 2010). To decide whether we accept or not the proposed state we use

$$\begin{aligned}
\vec{\phi}_{j,t+1} &= \vec{\Phi}_j & : q > U \\
\vec{\phi}_{j,t+1} &= \vec{\phi}_{j,t} & : q \leq U,
\end{aligned} \tag{5.13}$$

where U is a random number between $[0, 1]$. After a number N of iterations and L chains, we will have $N \times L$ samples for each parameter from which we can create posterior distributions. A general overview of a single step of the ensemble sampler method is given in Algorithm 1.

Figure 5.2 shows an example of the evolution of an ensemble sampler algorithm using six chains. The latter start at a different point in the parameter space. After a finite number of iterations (in this case a few hundreds), the chains converges to a stable region of the parameter space. Details on how we create marginal posterior distributions from chain's samples are provided in Section 5.2.3.

Another advantage of this approach is that, since each Markov chain evolves independently, this algorithm can be parallelized (Foreman-Mackey et al., 2013).

5.2.2 Convergence

In order to infer the parameter values based on a MCMC sampling we need to use chains that have converged. A widely used convergence test has been developed by Gelman & Rubin (1992). This test compares the "between-chain" B and "within-chain" W variance via the scaled potential factor $\hat{R} = \sqrt{[W(n-1)/n + B/n]/W}$, where n is the length of each chain. We define convergence as when chains have $\hat{R} < 1.02$ for all the parameters (Gelman et al., 2004).

---

input   : Initial ensemble of N states $\vec{\phi}_{j,t}$
output: Ensemble of N states $\vec{\phi}_{j,t+1}$

1 for $j = 1$ **to** N **do**
2 $\quad$ Select a complementary state from the ensemble such that $j \neq k$
3 $\quad$ Sample the scaled variable z from the density distribution g
4 $\quad$ Propose the new state via a walk move $\vec{\Phi}_j = \vec{\phi}_{k,t} + z\left(\vec{\phi}_{j,t} - \vec{\phi}_{k,t}\right)$
5 $\quad$ Compute q from eq. (5.12) using likelihood and priors for the states $\vec{\phi}_{j,t}$ and $\vec{\Phi}_j$
6 $\quad$ Sample an uniform random variable U between 0 and 1
7 $\quad$ **if** $q > U$ **then**
8 $\quad\quad$ $\vec{\phi}_{j,t+1} = \vec{\Phi}_j$
9 $\quad$ **else**
10 $\quad\quad$ $\vec{\phi}_{j,t+1} = \vec{\phi}_{j,t}$
11 $\quad$ **end**
12 end

Algorithm 1: One iterations of the ensemble sampler algorithm.

5.2.3   Marginal posterior distribution from parameter sampling

Chains that have converged to a static solution represent a sample of the marginal posterior distribution from which they were sampled. The frequencies of the chains can be used to create the posterior distribution of the sampled parameters. A common way to draw the sampling frequency is with a histogram, as shown in Figure 5.2. The final marginal posterior distribution for each parameter is also called *credible interval.*

The median and the 68% limits of the credible interval are commonly used to define the parameter's best estimate and its uncertainty (see, e.g., Hogg & Foreman-Mackey, 2018). When the marginal posterior distribution follows a Gaussian distribution, the median and the 68% limits of the credible interval correspond to the mean and standard deviation of a normal distribution. When the posterior distribution is skewed, the 68% limits are not symmetric with respect to the median, and they give an "first-order" idea of the shape of the marginal posterior distribution that describes a given parameter.

5.3   `pyaneti`

In Chapters 3 and 4 we describe how we can obtain transit and RV measurements. These measurements are the data D that we can compare with the parametric models M described in Chapter 2 using the Bayesian analysis and MCMC techniques previously discussed in this Chapter. The implementation of these ideas were put together in the code `pyaneti` (Barragán et al., 2019) which we will describe in this section.

5.3.1   Parametric models

The planet effects on the stellar light can be described by analytical functions which depends on a set of parameters. The general parametric function $f_{\mathrm{RV}}(\vec{\phi}; t)$ which describes the induced RV of a star orbited for multi-planets has the form (see eq. (2.58))

$$f_{\mathrm{RV}}(\vec{\phi}; t) = f(\{T_0, P, e, w_\star, K\}_\alpha, \gamma_\beta; t), \tag{5.14}$$

in which the set of parameters $\{T_0, P, e, w_\star, K\}$ repeats for each planet α and γ_β is for each instrument β. While the general parametric function $f_{\mathrm{tr}}(\vec{\phi})$ which describes transit events in a light curve is (see eq. (2.72))
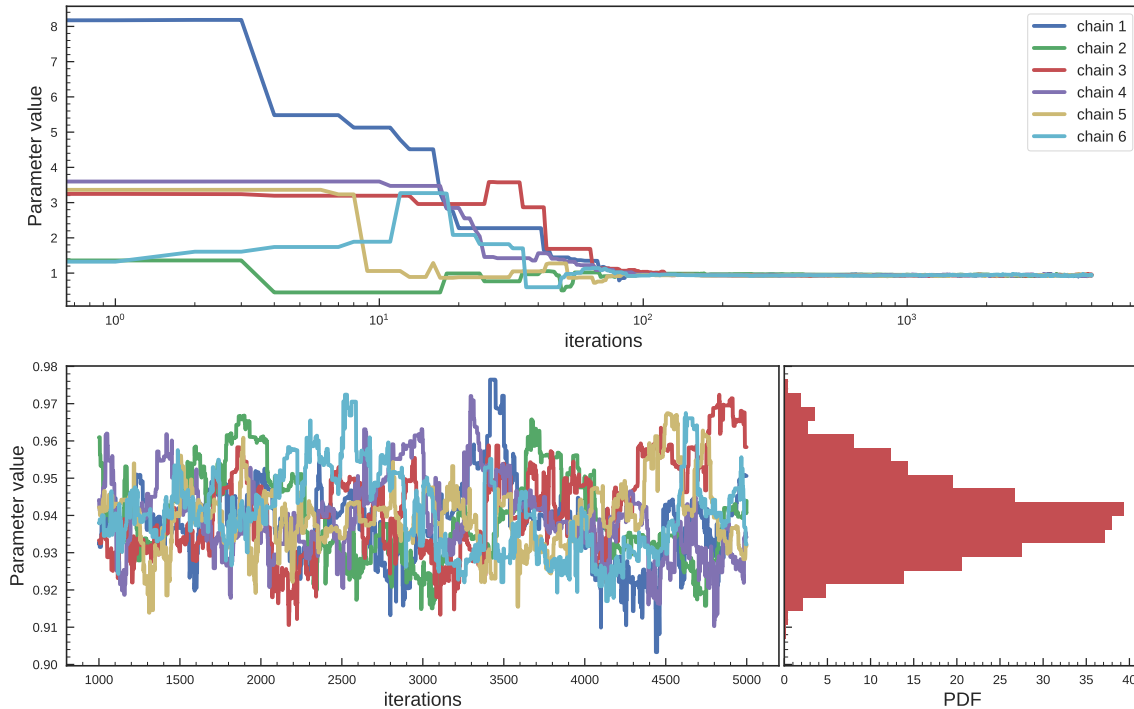
Figure 5.2: Example of the evolution of an ensemble sampler algorithm using six chains. *Upper panel:* Parameter value for each chain from iteration 0 to 5000 in logarithmic scale. *Lower left panel*: Chains behaviour for the last 4000 iterations. *Lower right panel:* Histogram created using all the information contained in all the chains the last 4000 iterations.

$$f_{\text{tr}}(\vec{\phi}; t) = f(\{T_0, P, e, w_\star, R_{\text{p}}/R_\star, a/R_\star, i\}_\alpha, \{u_1, u_2\}_\epsilon; t). \tag{5.15}$$

The set of parameters $\{T_0, P, e, w_\star, R_{\text{p}}/R_\star, a/R_\star, i\}$ repeats for each planet α. Each $\{u_1, u_2\}$ repeats for each band ϵ of the light curve.

For cases where RV and light curve data of a system are available, the best approach to perform the analysis is via a joint fit. By comparing equations (5.14) and (5.15) we see that T_0, P, e and $\omega_\star$ are shared parameters between RV and transit equations. For this case the orbital parameters of the planet will be fitted simultaneously for the RV and transit data. Generally speaking, transit data improves the values of T_0 and P while RV data constrains better e and $\omega_\star$. The parameters involved in a joint fit are then

$$\vec{\phi} = (\{T_0, P, e, w_\star, R_{\text{p}}/R_\star, a/R_\star, i, K\}_\alpha, \gamma_\beta, \{u_1, u_2\}_\epsilon), \tag{5.16}$$

Where $\{T_0, P, e, w_\star, R_{\text{p}}/R_\star, a/R_\star, i, K\}$ repeats for each planet α, $\{u_1, u_2\}$ for each band ϵ and γ for each instrument β. Equations (5.14), (5.15) and (5.16) can be used in eq. (5.4) to compare with a given data set D composed of RV, transit of a joint data set. Together with priors for the parameters of eq. (5.16), we can estimate a posterior distribution for each parameter using MCMC methods.

5.3.2 Parametrizations

Equation (5.16) defines the general set of parameters that can be extracted by modelling RV and photometry measurements. It is possible to use a set of convenient parametrizations to improve the exploration of the parameter space and avoid biases due to priors. In the following sub-sections we provide a brief description of the parametrizations used in `pyaneti`.

Eccentricity and angle of periastron

The posterior distribution of the eccentricity is not well sampled for orbits with small eccentricities (Lucy & Sweeney, 1971). A practical solution is to define e and $\omega_\star$ using a polar form. pyaneti adopts the parametrization proposed by Anderson et al. (2011)

$$ew_1 = \sqrt{e}\sin\omega_\star, \quad ew_2 = \sqrt{e}\cos\omega_\star. \tag{5.17}$$

This parametrization has two advantages: a) it is not truncated when the eccentricity is close to zero; b) uniform priors on ew_1 and ew_2 imply uniform priors on the eccentricity.

Impact factor

As presented in Sect. 2.3, the transit of a planet can described using the scaled projected distance between the planet and star centres. It is then convenient to parametrize the stellar inclination using a parameter that takes into account the projected distance. A practical approach is via the impact parameter defined as (Winn, 2010)

$$b = \frac{a}{R_\star}\cos i\left(\frac{1-e^2}{1+e\sin\omega_\star}\right). \tag{5.18}$$

The advantage of using the impact factor is that b can be compared directly with the projected distance δ (eq. (2.65)). In this way it is easy to set priors to exclude orbits for which there are no transits, i.e., when $b > 1 + r_{\mathrm{p}}$.

Limb Darkening coefficients

For the limb darkening coefficients pyaneti uses the parametrization proposed by Kipping (2013), who showed that an optimal way to sample the parameter space for the Mandel & Agol (2002)'s limb darkening coefficients is via the parametrization

$$q_1 = (u_1 + u_2)^2, \quad q_2 = \frac{u_1}{2(u_1 + u_2)}. \tag{5.19}$$

The advantage of this approach is that it fully accounts for our ignorance about the intensity profile and explores physical solutions by sampling uniformly q_1 and q_2 between 0 and 1. This yields robust and realistic uncertainty estimates. It is possible to recover the original u_1 and u_2 coefficients via

$$u_1 = 2q_1\sqrt{q_2}, \quad u_2 = \sqrt{q_1}(1 - 2q_2). \tag{5.20}$$

Stellar density

From Kepler's third law we obtain that

$$\rho_\star + r_{\mathrm{p}}^3\rho_{\mathrm{p}} = \frac{3\pi}{GP^2}\left(\frac{a}{R_\star}\right)^3. \tag{5.21}$$

where $\rho_\star$ is the star's mean density, ρ_p the planet's mean density, r_{p} the planet-to-star radius ratio, P the orbital period, $R_\star$ the star's radius, and a the semi-major axis of the relative orbit. Since r_{p}^3 is relatively small, the second term of the left side of eq. (5.21) can be neglected (Winn, 2010). There is thus a relation between the stellar density and the orbital parameters P and $a/R_\star$ that can be used to compare stellar density derived from the modelling of the transit light curves with an independent determination (e.g., from spectroscopy).

It is convenient to parametrize $a/R_\star$ with $\rho_\star$. If precise stellar parameters have been calculated, it is possible to set tight priors on the stellar density and hence on $a/R_\star$. For a multi-planet system, it is convenient to parametrize the scaled semi-major axis $a_j/R_\star$ of all planets j using the same stellar density. In this way the stellar density is constrained for all planets and Kepler's third law is not violated within planets orbiting the same star. `pyaneti` uses the parametrization $\rho_\star^{1/3}$ instead of $\rho_\star$ because $a/R_\star$ and $\rho_\star^{1/3}$ are linearly related assuming $r_\mathrm{p} \approx 0$ (eq. 5.21).

5.3.3 Numerical treatment of the posterior

Equation (5.4) may lead to very small/big numbers which generate numerical overflows. Therefore it is convenient to use the logarithmic of probability densities. Bayes' theorem is rewritten as

$$\ln P(M|D) = \ln P(D|M) + P(M) - P(D). \tag{5.22}$$

We note that this treatment of the posterior does not affect the MCMC method. Since the ratio between the actual and proposed states can be calculated easily as

$$\frac{P(D|\vec{\Phi})P(\vec{\Phi})}{P(D|\vec{\phi})P(\vec{\phi})} = \exp\left[\ln P(D|\vec{\Phi}) + \ln P(\vec{\Phi}) - \ln P(D|\vec{\phi}) - \ln P(\vec{\phi})\right] \tag{5.23}$$

By following this approach, the general form of the Gaussian likelihood for an RV and transit fit is given using eq. (5.4) as

$$P(D|M) = \prod_i^{N_\mathrm{RV}} \left[\frac{1}{\sqrt{2\pi(\sigma_i^2 + \sigma_\mathrm{j}^2)}}\right]_\mathrm{RV} \times \prod_i^{N_\mathrm{LC}} \left[\frac{1}{\sqrt{2\pi(\sigma_i^2 + \sigma_\mathrm{j}^2)}}\right]_\mathrm{LC} \times \exp\left\{-\frac{1}{2}\chi_\mathrm{Tot}^2\right\}, \tag{5.24}$$

where

$$\chi_\mathrm{Tot}^2 = \sum_i^{N_\mathrm{RV}} \frac{(D_{i,\mathrm{RV}} - M_{i,\mathrm{RV}})^2}{\sigma_i^2 + \sigma_\mathrm{j}^2} + \sum_i^{N_\mathrm{LC}} \frac{(D_{i,\mathrm{LC}} - M_{i,\mathrm{LC}})^2}{\sigma_i^2 + \sigma_\mathrm{j}^2}. \tag{5.25}$$

The RV and LC sub-indexes refers to RV and light curve data and models, respectively. The logarithmic form of the likelihood given in eq. (5.4) is rewritten as

$$\ln P(D|M) = -\frac{1}{2}\left[\sum_i^{N_\mathrm{RV}} \ln 2\pi(\sigma_i^2 + \sigma_\mathrm{j}^2) + \sum_i^{N_\mathrm{LC}} \ln 2\pi(\sigma_i^2 + \sigma_\mathrm{j}^2) + \chi_\mathrm{Tot}^2\right]. \tag{5.26}$$

We note that eq. (5.26) can be used too model pure RV or transit data.

5.3.4 Code's algorithm

Light curve and RV time-series can be passed to computational programs as arrays. This brings the advantage to manipulate data numerically. RV and transit equations can be used to compute models at the same time stamps of the time-series. This can be exploited to iterate MCMC methods using computers to perform parameter's estimation.

If we combine the MCMC analysis described in Sect. 5.1 along with the multi-planet equations presented in Chapter 2, we can develop a powerful tool to estimate planet parameters from Doppler and transit observations. We used this approach together with the computational speed of `FORTRAN` and the versatility of `PYTHON` to write the software

suite `pyaneti`. The computation-demanding routines, such as orbital solutions, likelihood calculations, etc., are calculated by `FORTRAN` subroutines. The input and output routines, such as data preparation, plot creations, etc., are handled by `PYTHON`. `FORTRAN` subroutines are wrapped to `PYTHON` using F2PY inside the `numpy` package (Van Der Walt et al., 2011)[2]. The code make use of `FORTRAN`, `PYTHON`, and `OpenMP` to run in parallel. It requires the `PYTHON` libraries `MATPLOTLIB` (Hunter, 2007), `NUMPY` (Van Der Walt et al., 2011), and `SEABORN`.

One of the main advantages of `pyaneti` is that all the code controls are given inside a `PYTHON`-based input file. Priors, fitted parameters, and data files are controlled via flags and python objects. This allows one to run the code with only one command line. A general overview of the algorithm of the code is given in Algorithm 2.

---

    input : RV and/or light curve time-series, correct input file for `star-name`
    output: Posterior distributions, plots, parameter inference of RV and/or transit models from
            data

1 `./pyneti.py star-name` (start of the run)
2 Read initial files (functions, default values)
3 Read input file with parameters for the current run (number of planets, priors, flags)
4 Read time-series data
5 Pass data and variables to `FORTRAN` routines
6 Start `FORTRAN` execution
7 Create random chains inside the prior ranges
8 Calculate likelihoods and priors for the initial state
9 Set iteration control variable `continua` to `True`
10 Initialise iterations count variable `i=0`
11 **while** *continua* **do**
12   Evolve chains following Algorithm 1   ! This line can also run in parallel
13   check for convergence after N iterations   !N is calculated as `niter` $\times$ `thin_factor`
14   **if** $i == N$ **then**
15   Check convergence using Gelman & Rubin (1992) criteria
16   **if** *chains converged == False* **then**
17   `continua = True`   !Chains have not converged: Keep iterating
18 $i = 0$! restart iteration counter
19   **else**
20   `continua = False`   !Chains have converged: save posteriors
21   **end**
22   **end**
23 **end**
24 Write posterior distributions with the converged chains taking into account the thin factor
25 End of `FORTRAN` execution
26 Run `PYTHON` output routines
27 Read posterior from posterior file
28 Automatic calculation of parameters and creation of plots
29 Save data in the `outpy/star-name_out` directory
30 End of run for `star-name`

Algorithm 2: General algorithm of `pyaneti`.

The advantage of using the ensemble sampler algorithm described in section 5.2.1 is that it can be parallelized. This speed-up the global solution of the MCMC run. The parallelization is done following the procedure described in Foreman-Mackey et al. (2013), in which we divide the ensemble in two sub-samples and evolve each group taking a chain from the complementary set of chains. We use Open Multi-Processing (`OpenMP`) to perform the parallelization inside the `FORTRAN` routines.

---

[2]More documentations are available at http://www.f2py.com/.

There are some physical effects that are not included in the current version of the code. Transit timing variations (TTVs), mutual interaction between planets, multi-band photometry, Rossiter-McLaughlin effect, planet's occultations, planet's phase curve fitting have not been implemented yet. `pyaneti` currently uses likelihood and priors as described in Sect. 5.1. More general likelihoods, such as Gaussian Process, have not been included yet. Nevertheless, the code is written in a modular way making it easy and straightforward to implement additional physical effects or equations. We plan to keep maintaining and upgrading `pyaneti`.

5.4 Code's tests

5.4.1 A toy model

Setup

We created a set of synthetic RV and transit data to check the performance of `pyaneti`. The simulated planetary system includes three planets: the two innermost planets transit the star, whereas the outer planet can only be seen in the RV data set.

Synthetic data points were created assuming a star with a mass of $0.66\,M_\odot$ and radius of $0.67\,R_\odot$. The planets have periods of 1.21321, 5.61122, and 12.12349 days with conjunction times of 1.0, 2.21529, and 4.63963 days, respectively. Their radii and masses are 1.5, 3.0, and $7\,R_\oplus$, and 5, 10, and $62\,M_\oplus$, respectively. The orbits of the two innermost planets are circular, whereas the outer planet has a non-zero eccentricity of $e_c = 0.1$ with the star's argument of periastron $\omega_{\star,c} = 204\,\mathrm{deg}$. We assumed inclinations of $i_b = 87$ deg, $i_c = 88$ deg, and $i_d = 84$ deg, so that the two innermost planets transit the star while planet d does not. We assumed that gravitational interaction between the three planets is negligible. We imposed limb darkening coefficients of $u_1 = 0.43$ and $u_2 = 0.31$. We used these values to calculate the scaled parameters used by `pyaneti`. Details of the whole set of fitted parameters are given in Table 5.1.

The synthetic light curve covers a range of 30 days starting at an arbitrary 0 point. We created the instantaneous normalised flux due to the transiting planets using eq. (2.72) with continuous time stamps separated by 5 minutes. We added Gaussian noise at the 5×10^{-5} level to simulate high precision photometry, such as that provided by *Kepler*. The synthetic light curve is displayed in the upper panel of Fig. 5.3.

The simulated RV measurements cover the 30 days simultaneous to the light curve data. Time stamps were taken from a random uniform distribution and the corresponding RVs were calculated using eq. (2.60). We simulated data for two spectrographs called instrument A and B. For spectrograph A, we created 50 absolute RVs with Gaussian noise of $1\,\mathrm{m\,s^{-1}}$ assuming a systemic velocity of $10\,\mathrm{km\,s^{-1}}$. For instrument B, we simulated 50 time stamps with Gaussian noise of $5\,\mathrm{m\,s^{-1}}$, but we assigned error bars of $3\,\mathrm{m\,s^{-1}}$ to each point to simulate a jitter term of $\sigma_j = (5^2 - 3^2)^{1/2}\,\mathrm{m\,s^{-1}} = 4\mathrm{m\,s^{-1}}$. We assumed that the RVs of instrument B are relative and arbitrarily centred around $0\,\mathrm{km\,s^{-1}}$. The lower panel of Fig. 5.3 shows the synthetic data-points following the correction for the RV offset between the two instruments.

We performed a joint fit setting uniform priors for all the parameters (details are given in Table 5.1). We used 100 independent Markov chains started randomly inside the uniform prior ranges. Once all chains converged, we used the last 5000 iterations and saved the chains' states every 10 iterations. This approach generated a posterior distribution of 50,000 points for each parameter.
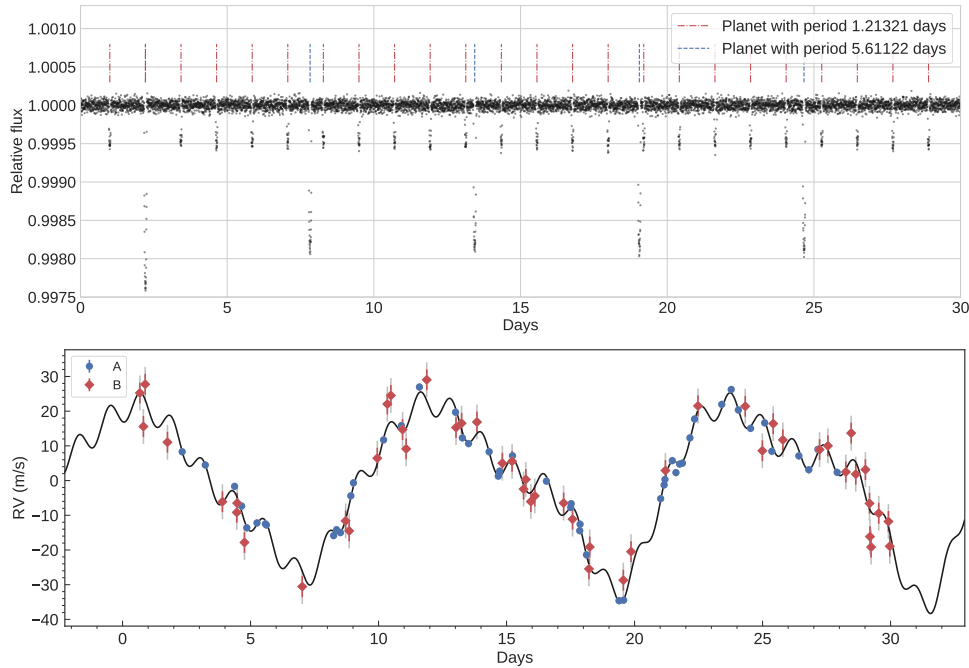
Figure 5.3: *Upper panel:* Thirty-day-long synthetic light curve. We assumed a relative flux of 1 with no trends. There are two transiting planets with different periods and sizes, marked with dashed lines. *Lower panel:* Synthetic RV measurements. The RV signal consists of three planets with different masses and periods. Instrument A (blue circles) has a precision of 1 m s^{-1}, whereas instrument B (red squares) has a precision of 5 m s^{-1}. The nominal error bars of instrument B were set to 3 m s^{-1} to simulate a jitter term (gray extensions to the nominal error bars). The best fitting model is shown as a thick black line. Offsets were subtracted to both data sets.

Results

Table 5.1 contains the medians and 68% credible intervals of the posterior distributions of the fitted parameters. We note that the system parameter's true values are inside the posterior distribution of each parameter. In most cases, the true values are inside the 68% credible interval. This shows the power of `pyaneti` to infer real parameters from data.

The lower panel of Fig. 5.3 shows the simulated RV data and the inferred best-fitting three-planet model. Figure. 5.4 displays the phase-folded transit and RV curves. Figure 5.5 displays the posterior distributions of some of the fitted parameters. These histograms are useful diagnostic plots to check the goodness of the MCMC output. We note that our analysis provides unimodal posterior distributions. Their shapes are either Gaussian ($T_{0,b}$ and P_b), or skewed ($\rho_\star^{1/3}$ and $R_{p,c}/R_\star$). The 68% credible intervals are over plotted on each histogram; they corresponds to the error bars reported in Table 5.1.

5.4.2 The multi-planet system K2-38

Setup

We also tested `pyaneti` with a real planetary system. We modelled the transit photometry and radial velocities of K2-38 and compared our results with those published by Sinukoff et al. (2016). K2-38 is G2 V star transited by two planets whose masses have been measured via Doppler spectroscopy. The inner planet, K2-38 b, orbits the star every 4 days. It has a mass of 12 $M_\oplus$ and a radius of 1.55 $R_\oplus$. The outer transiting planet, K2-38 b, has an orbital period of 10.5 days, a mass of 9.8 $M_\oplus$, and a radius of 2.4 $R_\oplus$.

K2-38 was photometrically observed by the K2 mission (Howell et al., 2014) during its

Table 5.1: System parameters.

Parameter	Real value	Prior[a]	Inferred value
Model Parameters planet b			
Orbital period P_{orb} (days)	1.21321	$\mathcal{U}[1.2122, 1.2142]$	1.2132028 ± 0.0000097
Transit epoch T_0	1.0	$\mathcal{U}[0.9965, 1.0035]$	1.00010 ± 0.00012
Scaled planet radius $R_{\mathrm{p}}/R_\star$	0.020525	$\mathcal{U}[0, 0.1]$	$0.0204479^{+0.00027}_{-0.00015}$
Impact parameter, b	0.33	$\mathcal{U}[0, 1]$	$0.25^{+0.13}_{-0.15}$
e	0	$\mathcal{F}[0]$	0
$\omega_\star$	0	$\mathcal{F}[0]$	0
RV semi-amplitude variation K (m s^{-1})	3.95	$\mathcal{U}[0, 50]$	4.16 ± 0.23
Model Parameters planet c			
Orbital period P_{orb} (days)	5.61122	$\mathcal{U}[5.6012, 5.6212]$	5.611254 ± 0.000041
Transit epoch T_0	2.21529	$\mathcal{U}[2.2143, 2.2163]$	2.21530 ± 0.00010
Scaled planet radius $R_{\mathrm{p}}/R_\star$	0.04105	$\mathcal{U}[0, 0.1]$	$0.04058^{+0.00057}_{-0.00030}$
Impact parameter, b	0.60	$\mathcal{U}[0, 1]$	$0.57^{+0.06}_{-0.03}$
e	0	$\mathcal{F}[0]$	0
$\omega_\star$	0	$\mathcal{F}[0]$	0
RV semi-amplitude variation K (m s^{-1})	4.74	$\mathcal{U}[0, 50]$	4.86 ± 0.33
Model Parameters planet d			
Orbital period P_{orb} (days)	12.12349	$\mathcal{U}[11.8235, 12.4235]$	12.142 ± 0.028
Transit epoch T_0	4.640	$\mathcal{U}[4.1396, 5.1396]$	4.592 ± 0.052
e	0.1	$\mathcal{U}[0, 1]$	0.096 ± 0.012
$\omega_\star$	3.57	$\mathcal{U}[0, 2\pi]$	3.60 ± 0.14
RV semi-amplitude variation K (m s^{-1})	22.75	$\mathcal{U}[0, 50]$	22.99 ± 0.24
Other Parameters			
Cubic root of stellar density $\rho_\star^{1/3}$	1.458	$\mathcal{U}[0.05, 2]$	$1.496^{+0.039}_{-0.072}$
Systemic velocity γ_{A} (km s^{-1})	10	$\mathcal{U}[9, 11]$	9.99991 ± 0.00017
Systemic velocity γ_{B} (km s^{-1})	0	$\mathcal{U}[-1, 1]$	0.00107 ± 0.00084
Jitter term σ_{A} (m s^{-1})	0	$\mathcal{U}[0, 100]$	$0.25^{+0.24}_{-0.18}$
Jitter term σ_{B} (m s^{-1})	4	$\mathcal{U}[0, 100]$	$4.09^{+0.77}_{-0.68}$
Parametrized limb-darkening coefficient q_1	0.55	$\mathcal{U}[0, 1]$	0.60 ± 0.05
Parametrized limb-darkening coefficient q_2	0.29	$\mathcal{U}[0, 1]$	$0.25^{+0.05}_{-0.04}$

Note – [a] $\mathcal{U}[a, b]$ refers to uniform priors between a and b and $\mathcal{F}[a]$ to a fixed value a.
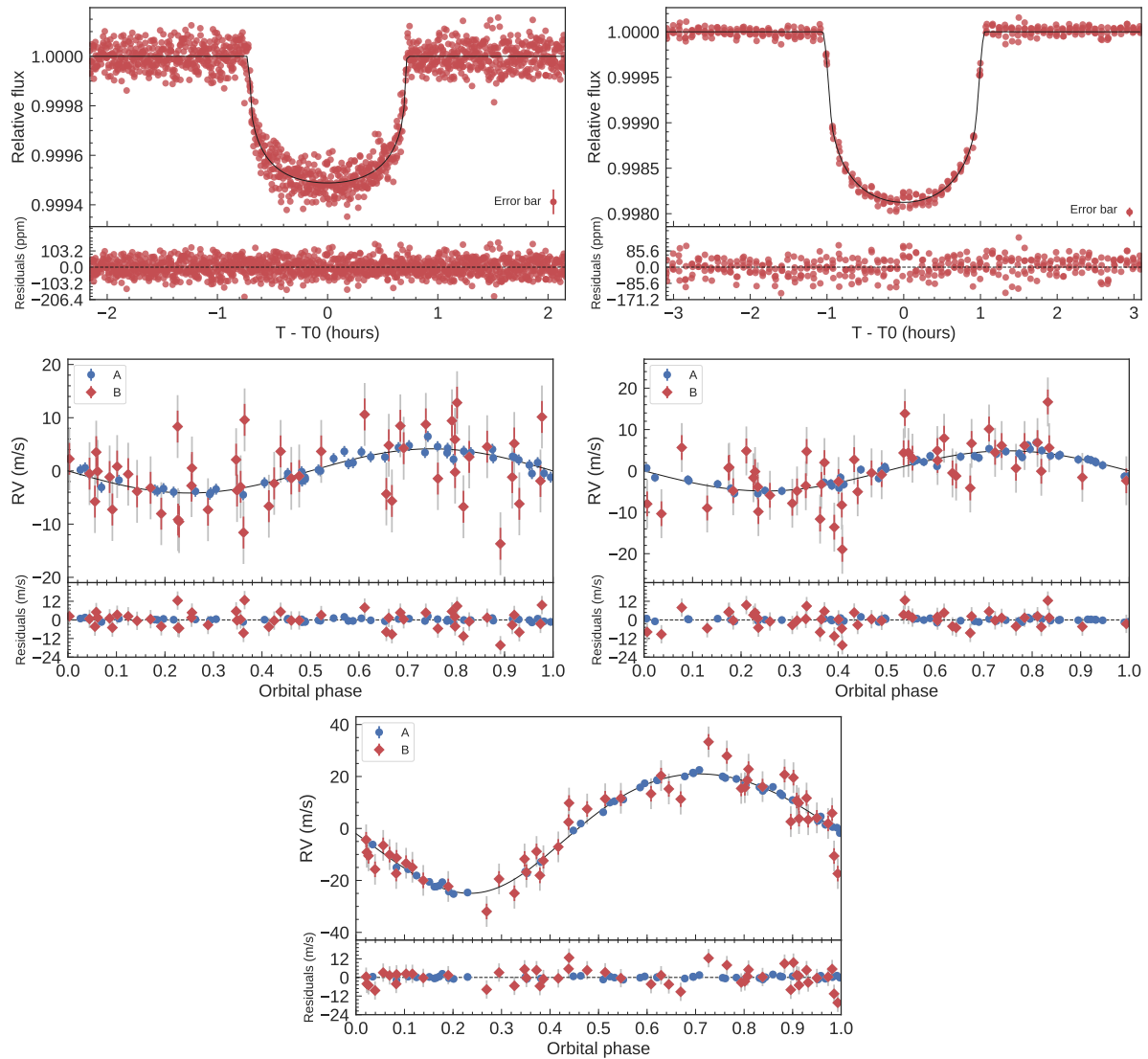
Figure 5.4: *Upper panels:* Phase-folded light curves for planet b and c of the simulated planetary system. Synthetic data points are plotted with the red circles. The best fitting transit models are over-plotted with thick black lines. *Middle and lower panels:* Phase-folded RV curves for planet b, c and d of the simulated planetary model. Synthetic data for instrument A is shown with blue circles, whereas for instrument B with red diamonds. The best fitting RV models are over-plotted with thick black lines. Gray error bars account for the jitter term for each instrument.
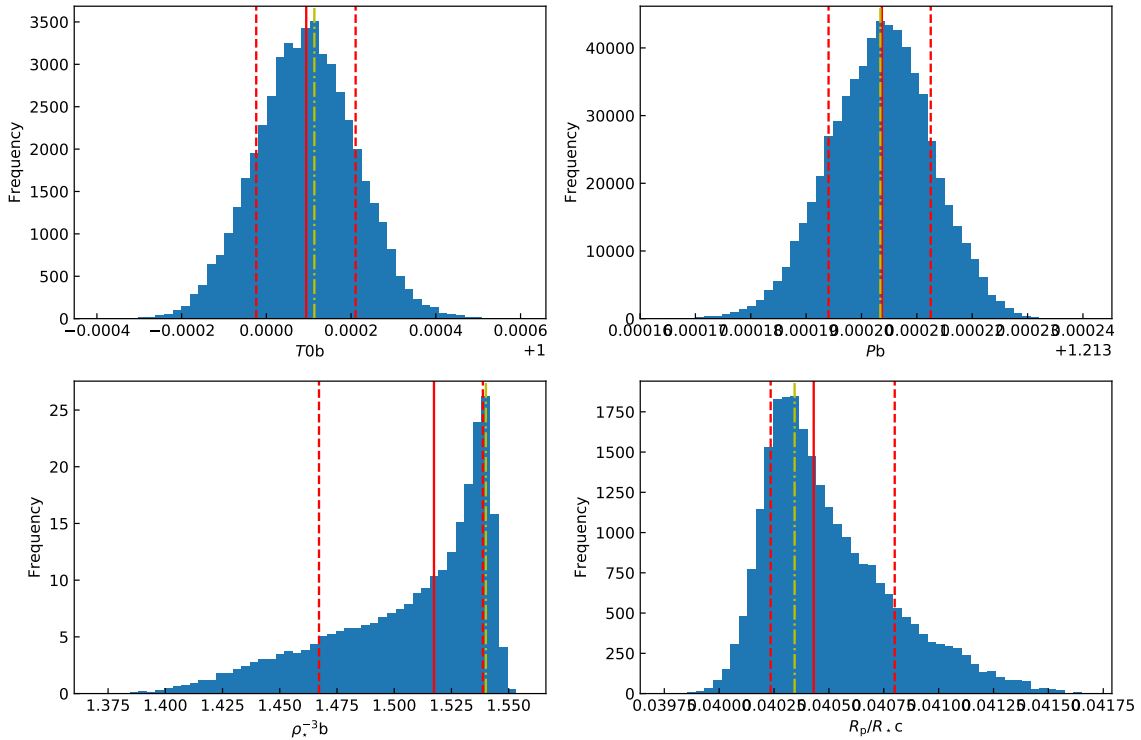
Figure 5.5: Posterior distributions for $T_{0,b}$ (upper left), P_b (upper right), $\rho_\star^{1/3}$ (lower left), and $R_{p,c}/R_\star$ (lower right) of the toy model fit. The solid red lines mark the medians of the distributions, whereas the dashed red lines mark the limits of the 68% credible intervals. The mode are shown with the dot-dashed yellow lines.

campaign 2. The RV measurements were gathered with the `HIRES` spectrograph (Vogt et al., 1994) mounted at the Keck I 10 m telescope, at Keck Observatory (Mauna Kea, Hawai'i). Sinukoff et al. (2016) detected a linear trend in the RV measurements, indicative of the presence of an additional companion in the system. While modelling the RV data, the authors added a jitter term to the nominal uncertainties to account for instrumental velocity noise not included in the nominal uncertainties and/or possible sources of stellar variability. Because of its complexity, this system is an ideal test-bench for `pyaneti`.

We used the `EVEREST` processed light curve (Luger et al., 2016) to perform the transit light curve analysis. We de-trended the `K2` data with `exotrending` (Barragán & Gandolfi, 2017, see Appendix A.1) by fitting a second-order polynomial function to the 5-hour out-out-transit data centred around each transit. The RV measurements were taken from Sinukoff et al. (2016).

We used the general form of the likelihood given in eq. (5.3) to account for the RV jitter term. We added a linear trend term $\dot{\gamma}$ to equation (2.60) taking as zero point the time of conjunction of planet b. We super-sampled the transit model by a factor of 10 to account for the *K2* long-cadence data (Kipping, 2010, see Appendix A.2). We fixed q_2 to 0.5 to recover the linear limb darkening case and set Gaussian priors on q_1 with 1-σ uncertainty of 0.1. We set uniform priors for the remaining parameters (details are provided in Table 5.2) and assumed circular orbits as adopted by Sinukoff et al. (2016). The sampling of the parameter space follows the procedure described in Sect. 5.4.1. Briefly, we initialised 100 independent chains created randomly inside the prior ranges. Once all chains converged, we created posterior distributions with 50,000 independent points for each parameter.

Table 5.2: System parameters.

Parameter	Sinukoff et al. (2016)	Prior[a]	Fitted value
Model Parameters planet b			
Orbital period P_{orb} (days)	4.01593 ± 0.00050	$\mathcal{U}[4.0134, 4.0184]$	$4.01632^{+0.00032}_{-0.00034}$
Transit epoch T_0 (BJD - 2,450,000)	6896.8786 ± 0.0054	$\mathcal{U}[6896.8486, 6896.9086]$	$6896.8734^{+0.0038}_{-0.0034}$
Scaled semi-major axis $a/R_\star$	$10.7^{+1.3}_{-3.7}$	$\mathcal{U}[1.1, 50]$	$11.3^{+1.0}_{-2.3}$
Scaled planet radius $R_{\mathrm{p}}/R_\star$	$0.01281^{+0.00105}_{-0.00064}$	$\mathcal{U}[0, 0.1]$	$0.01247^{+0.00087}_{-0.00045}$
Impact parameter, b	0.48 ± 0.30	$\mathcal{U}[0, 1]$	$0.35^{+0.33}_{-0.25}$
e	0	$\mathcal{F}[0]$	0
$\omega_\star$ (deg)	90	$\mathcal{F}[90]$	90
RV semi-amplitude variation K (m s^{-1})	4.6 ± 1.1	$\mathcal{U}[0, 100]$	4.6 ± 1.1
Model Parameters planet c			
Orbital period P_{orb} (days)	10.56103 ± 0.00090	$\mathcal{U}[10.5565, 10.5655]$	10.56155 ± 0.00049
Transit epoch T_0 (BJD - 2,450,000)	6900.4752 ± 0.0033	$\mathcal{U}[6900.4552, 6900.4952]$	6900.4740 ± 0.0018
Scaled semi-major axis $a/R_\star$	$26.3^{+5.4}_{-16.1}$	$\mathcal{U}[1.1, 50]$	$31.3^{+2.1}_{-5.1}$
Scaled planet radius $R_{\mathrm{p}}/R_\star$	$0.02004^{+0.0024}_{-0.0013}$	$\mathcal{U}[0, 1]$	$0.01841^{+0.0010}_{-0.0005}$
Impact parameter, b	$0.64^{0.23}_{-0.41}$	$\mathcal{U}[0, 1]$	$0.34^{+0.27}_{-0.25}$
e	0	$\mathcal{F}[0]$	0
$\omega_\star$ (deg)	90	$\mathcal{F}[90]$	90
RV semi-amplitude variation K (m s^{-1})	2.8 ± 1.3	$\mathcal{U}[0, 1000]$	2.8 ± 1.3
Other Parameters			
RV value at $T_{0,1}$ γ (m s^{-1}) [b]	-1.7 ± 0.9	$\mathcal{U}[-1000, 1000]$	0.034 ± 0.010
Linear trend slope $\dot{\gamma}$ (km s^{-1} d^{-1})	-0.101 ± 0.030	$\mathcal{U}[-1, 1]$	-0.103 ± 0.029
HIRES jitter term σ_{HIRES} (m s^{-1})	$2.4^{+1.0}_{-0.7}$	$\mathcal{U}[0, 1000]$	$2.4^{+1.0}_{-0.7}$
Parametrized LDC q_1	0.38 ± 0.1 [c]	$\mathcal{N}[0.38, 0.1]$	0.42 ± 0.1
Parametrized LDC q_2	0.5 [c]	$\mathcal{F}[0.5]$	0.5

Note – [a] $\mathcal{U}[a, b]$ refers to uniform priors between a and b, $\mathcal{N}[a, b]$ to Gaussian priors with median a and standard deviation b, and $\mathcal{F}[a]$ to a fixed value a. [b] Our results and Sinukoff et al. results do not agree because the instant at which the intercept is calculated is not the same. [c] We transform the values reported by Sinukoff et al. to the q_1 and q_2 parametrization to perform the comparison.

Results

The final estimates and their 1-σ uncertainties are taken as the median and the 68 % of the credible interval of the posterior distributions. Values are reported in Table 5.2. Photometric and RV data, along with the best fitting transit and RV models are displayed in Figure 5.6.

We compare our results with those from Sinukoff et al. (2016) in Table 5.2. The parameter estimates agree well within their 1-σ uncertainties. However, we note that the largest discrepancies are found for the parameters derived from the K2 data. This is very likely due to the different extracted light curve used in our analysis, as well as on the different transit de-trending algorithm. As for the RV-derived parameters, our results are in excellent agreement with those reported by Sinukoff et al. (2016).

This test confirms the correct implementation of the MCMC method and multi-planet equations. Sinukoff et al. (2016) used the widely used ensemble sampler package `emcee` (Foreman-Mackey et al., 2013).

5.5   Execution performance

We show here that `pyaneti` is able to produce scientific results within a few minutes in a personal laptop. We ran the test case presented in section 5.4.2 (2 planet system, 435 data points, 10 000 iterations with 100 independent Markov chains) with different CPU configurations. We used a machine with an Intel i7-6500U CPU (Four 2.50GHz cores) and
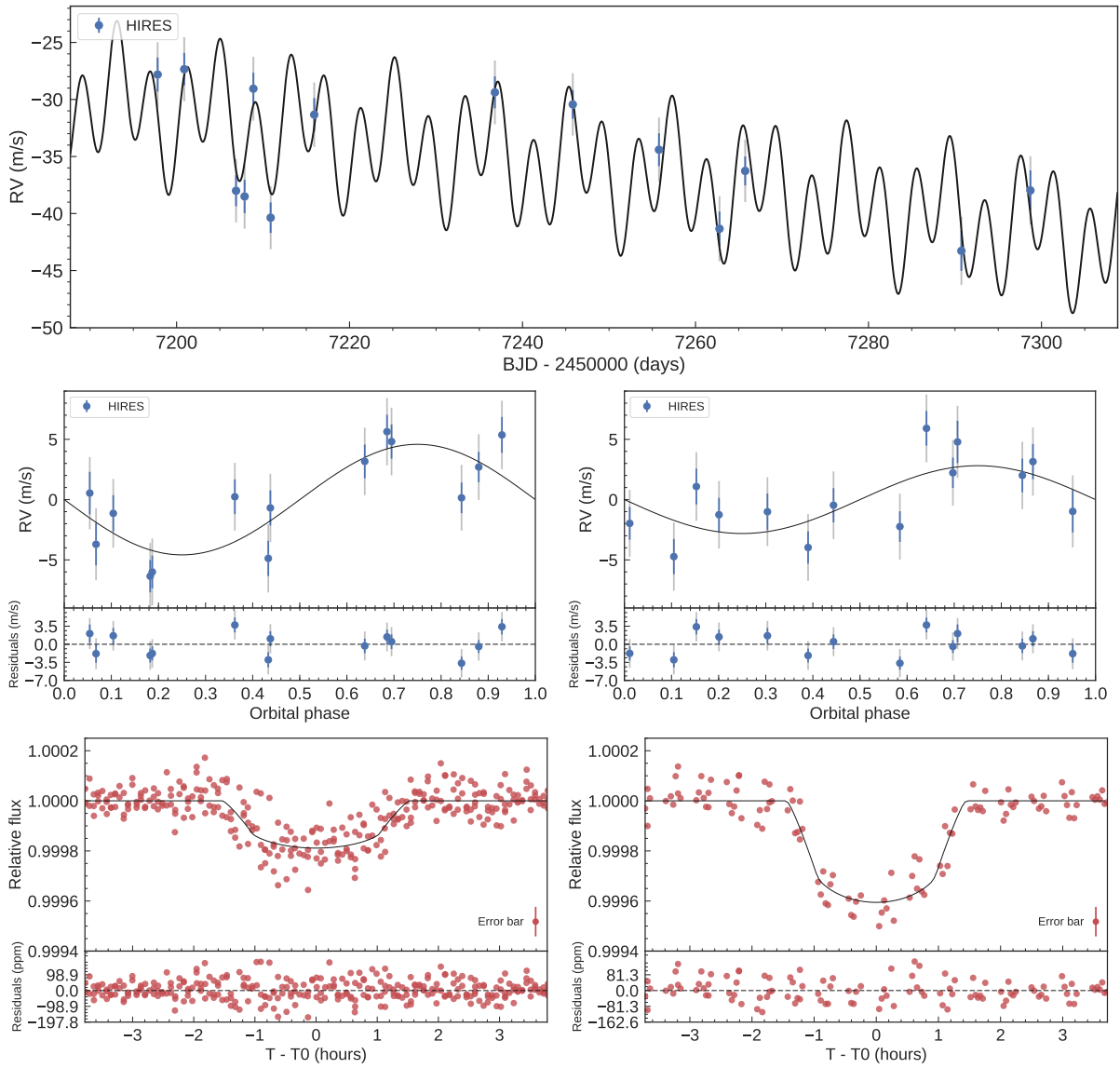
Figure 5.6: *Upper panel*: HIRES RV measurements of K2-38 (blue circles). The best-fitting solution is shown with a thick black line. A linear trend is visible in the data. The fitted stellar jitter is shown as a gray extension to the nominal error bars. *Middle panels*: Phase-folded RV curves for K2-38 b (left) and K2-38 c (right). *Lower panels*: Transit light curve folded to the orbital period of K2-38 b (left) and K2-38 c (right), and residuals. The red points are `K2` data. The thick black lines mark the best fitting transit models.

with Linux (Fedora 64-bit) operating system. We compiled the code with `gfortran` 8.1.1 and used 1, 2, and 4 CPUs. The respective execution times were 10m 11s, 5m 56s and 4m 22s. These results prove the power of the code to perform a full run in a personal laptop. However, we stress that the execution time depends on the analysed data set. Based on our experience with `pyaneti`, the modelling of only RV data is carried withing a few minutes. For demanding fits requiring longer execution time (e.g., long time-series photometry), `pyaneti` can be ran in parallel in a server machine equipped with more than one CPU.

CHAPTER 6

CHARACTERISATION OF EXOPLANETS

In this chapter we present the planetary systems that have been characterised in the course of this thesis project. They are:

- K2-98 b: A doomed Neptunian world (Barragán et al., 2016).

- K2-139: An active star hosting a warm Jupiter (Barragán et al., 2018a).

- K2-141 b: A lava world with a "short year" (Barragán et al., 2018b).

- K2-111 b: A very old world (Fridlund et al., 2017).

- K2-19: Two worlds in resonance (Nespral et al., 2017).

- K2-106 b and c: Two worlds with different densities (Guenther et al., 2017).

- HD 3167 b and c: Two worlds with different densities II (Gandolfi et al., 2017).

- GJ 9827: The different nature of three neighbouring worlds (Niraula et al., 2017; Prieto-Arranz et al., 2018).

- 44 Validated Planets from K2 Campaign 10 (Livingston et al., 2018).

- π Mensae c: A world transiting a naked-eye star (Gandolfi et al., 2018).

6.1   K2-98 b: A doomed Neptunian world

We announced the discovery and mass measurement of K2-98 b in Barragán et al. (2016). K2-98 b is a transiting Neptune-size planet monitored by the *K2* mission during its Campaign 5. We combined the *K2* time-series data with ground-based photometric and spectroscopic follow-up observations to confirm the planetary nature of the object and derive its mass, radius, and orbital parameters. K2-98 b is a warm Neptune-like planet in a 10-day orbit around a V=12.2 mag F-type star with $M_\star = 1.074 \pm 0.042\ M_\odot$, $R_\star = 1.311 \pm 0.083\ R_\odot$, and age of $5.2^{+1.2}_{-1.0}$ Gyr. We derived a planetary mass and radius of $M_{\rm p} = 33 \pm 12 M_\oplus$ and $R_{\rm p} = 4.36^{+0.31}_{-0.30} R_\oplus$. We estimated that the planet will be engulfed by its host star in ∼3 Gyr, due to the evolution of the latter towards the red giant branch. K2-98 b joins the still relatively small number of Neptune-size planets (∼20 objects) whose mass and radius have been determined with a precision better than 33 %.

6.1.1   Detection

The transit detection an validation were done with the `DST` (Cabrera et al., 2012) and the `EXOTRANS` pipelines (Grziwa et al., 2012) using Vanderburg & Johnson (2014) light curves. Both, `DST` and `EXOTRANS`, identified a planet-like signal associated with the star EPIC 211391664 (K2-98). The candidate passed standard test which validated the planetary nature of the transiting object (Barragán et al., 2016). The Vanderburg & Johnson (2014) light curve for K2-98 is displayed in Figure 6.1.

6.1.2   Ground-based imaging

The photometric follow-up of K2-98 (EPIC 211391664) was done on 17 May 2016 with the `FASTCAM` lucky imaging camera (Oscoz et al., 2008) mounted on the 1.5m Carlos Sánchez Telescope of Teide Observatory in Tenerife (Spain). Data were processed using the `COELI` algorithm (Cagigal et al., 2016). The final image shows the target to be isolated except for the detection of an object located 1.9" South-East of K2-98 (see Fig. 1 of Barragán et al., 2016). We estimated that the light from the faint object contributes with a fraction of 1/(50±10) to the measured flux of K2-98 and correct the *K2* light curve accordingly prior to performing the joint analysis.

6.1.3   Spectroscopic follow-up

The RV data consist of 12 data points taken with three different instruments (4 from FIES, 4 from HARPS and 4 from HARPS-N, see Sect. 4.3 for details about these instruments). The full list of RV measurements are presented in (Barragán et al., 2016). Figure 6.1 shows the RV time-series for the three instruments following the subtraction of the instrumental offsets.

6.1.4   Stellar parameters

The stellar parameter estimation was done using co-added spectra for each instrument. The derived values for $T_{\rm eff}$, $\log g_\star$, [M/H], and $v \sin i_\star$ are listed in Table 6.1. The stellar mass, radius, and age were determined by combining the effective temperature $T_{\rm eff}$ and metallicity [M/H] with the mean density $\rho_\star$ obtained from the transit light curve modelling (see Sect. 6.1.5). The final adopted stellar parameters are reported in Table 6.1.
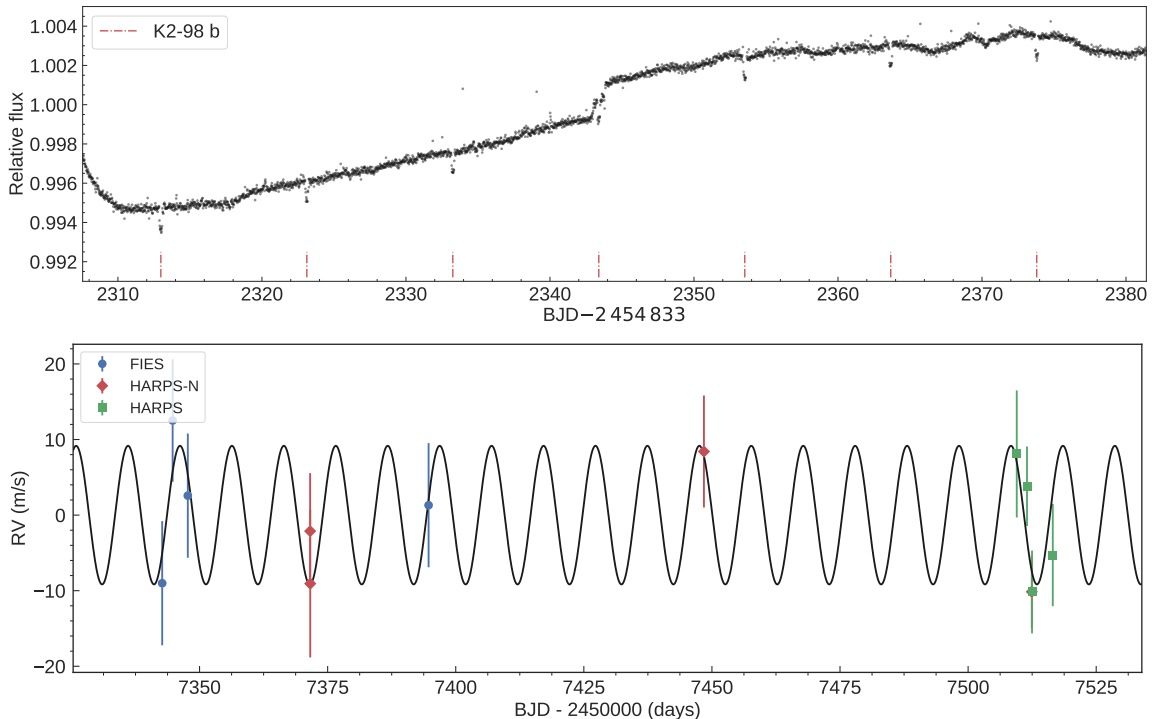
Figure 6.1: *Upper panel: K2* Light curve for K2-98 as extracted by Vanderburg & Johnson (2014). The positions of the transit signals are marked with vertical red dot-dashed lines. *Lower panel:* Top: FIES (blue circles), HARPS-N (red diamonds) and HARPS (green squares) RV measurements versus time, following the subtraction of the systemic velocities for each instrument. The 1-σ uncertainties are marked using the same colour used for each data set. The solid line represents the inferred RV model.

6.1.5   Joint RV-transit data analysis

We perform the joint modelling of the photometric and spectroscopic data using the code `pyaneti` (Barragán et al., 2019, see also Sect. 5.3). The photometric data included in the joint analysis are subsets of the whole *K2* light curve extracted by Vanderburg & Johnson (2014). We select $\sim$13 hours of data-points centred on each of the 7 transits[1] observed by *K2*. We detrended the individual transits using a second-order polynomial locally fitted to the $\sim$16 out-of-transit points per transit (8 points per side). The final data-set contains 180 photometric points. The modelled RV data-set contains the 12 measurements listed in (Barragán et al., 2016).

The fitted parameters are the transit epoch T_0, the orbital period P, the eccentricity e, the argument of periastron of the star's orbit $\omega_\star$, the scaled semi-major axis $a/R_\star$, planet-to-star radius ratio $R_p/R_\star$, impact parameter b, the RV semi-amplitude variation K, the systemic velocity γ_j for three different instruments and the LDC parametrization q_1 and q_2. The prior details for all the parameters are given in Table 6.1. We account for the *K2* long integration ($T_{\rm exp}$=29.425 minutes) by super-sampling the transit model with 10 sub-samples (Kipping, 2010, see Appendix A.2).

The joint modelling is carried out running 500 independent chains. Once chains converged, we ran 5000 additional iterations with a thin factor of 10, leading to a final number of 500 independent points for each chain, i.e., 250 000 independent points for each fitted parameter.

We noted than an initial global fit to the data yields the parameterized limb darkening coefficients $q_1 = 0.33^{+0.30}_{-0.16}$ and $q_2 = 0.38^{+0.35}_{-0.24}$, which corresponds to $u_1 = 0.43 \pm 0.23$ and

---

[1]The transit duration is $\sim$5 hours.
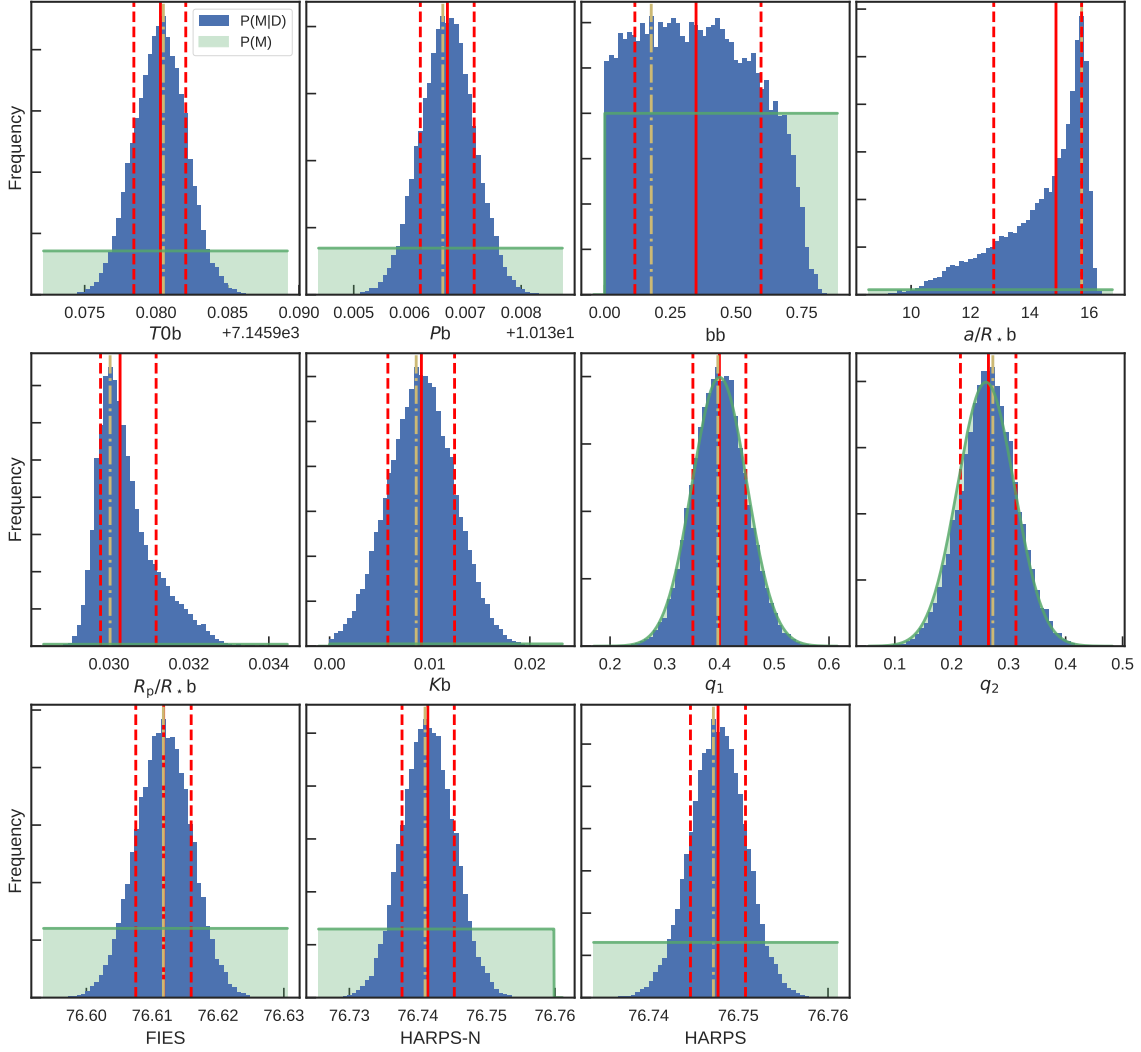
Figure 6.2: Posterior distributions of the K2-98's parameters as obtained from the final analysis performed with `pyaneti`. The blue region corresponds to the marginalised posterior $P(M|D)$, whereas the shaded green region mark the shape of the prior $P(M)$. Median (solid red line), 68% credible interval (dashed red line), and mode (dash-dotted yellow line) are also shown.

$u_2 = 0.14^{+0.39}_{-0.33}$. As described in Csizmadia et al. (2013), the large uncertainties arise from the shallow transit depth ($\sim 0.1\%$), the small number of data points (~ 180) and transits (7), and the *K2* long integration time (~ 30 minutes). We thus choose to constrain the limb darkening coefficient interpolating the table of Claret & Bloemen (2011) and assuming conservative 0.05 error bars. We stress that the system parameters derived with uniform priors on the limb darkening coefficients are consistent to within 1-σ uncertainties with those obtained by setting the Gaussian prior.

The inferred posterior distributions from the MCMC analysis are shown in Figure 6.2. The parameter estimates and error bars are listed in Table 6.1. They are taken as the median and the 68% central interval of the final posterior distributions. Our results are consistent with the transit parameters derived by Barros et al. (2016) and Pope et al. (2016). Figure 6.3 shows the folded transit light curve and phase-folded RV curve, along with their inferred models.

Table 6.1: K2-98 system parameters.

Parameter	Prior[a]	Final value
Stellar parameters		
Star mass $M_\star$ ($M_\odot$)	$\cdots$	1.074 ± 0.042
Star radius $R_\star$ ($R_\odot$)	$\cdots$	1.311 ± 0.083
Star density $\rho_\star$ (from spectroscopy, $\mathrm{g\,cm^{-3}}$)	$\cdots$	$0.67^{+0.15}_{-0.12}\mathrm{g\,cm^{-3}}$
Star density $\rho_\star$ (from light curve, $\mathrm{g\,cm^{-3}}$)	$\cdots$	$0.60^{+0.12}_{-0.22}\mathrm{g\,cm^{-3}}$
Effective Temperature $\mathrm{T_{eff}}$ (K)	$\cdots$	6120 ± 80
Surface gravity $\log g_\star$ (cgs)	$\cdots$	$4.23^{+0.03}_{-0.05}$
Iron abundance [Fe/H] (dex)	$\cdots$	-0.2 ± 0.1
Star distance d (pc)	$\cdots$	435^{+30}_{-15}
Model parameters of K2-98		
Orbital period P_{orb} (days)	$\mathcal{U}[10.1331, 10.1403]$	10.13669 ± 0.00047
Transit epoch T_0 ($\mathrm{BJD_{TDB}} - 2\,450\,000$)	$\mathcal{U}[7145.9667, 7145.9947]$	7145.9803 ± 0.0018
Scaled semi-major axis $a/R_\star$	$\mathcal{U}[5, 100]$	$14.8^{+0.9}_{-2.1}$
Planet-to-star radius ratio $R_{\mathrm{p}}/R_\star$	$\mathcal{U}[0, 0.2]$	$0.03038^{+0.00098}_{-0.00071}$
Impact parameter, b	$\mathcal{U}[0, 1.0]$	$0.35^{+0.25}_{-0.24}$
$\sqrt{e}\sin\omega$	$\mathcal{F}[0]$	0
$\sqrt{e}\cos\omega$	$\mathcal{F}[0]$	0
Radial velocity semi-amplitude variation K ($\mathrm{m\,s^{-1}}$)	$\mathcal{U}[0, 1000]$	9.3 ± 3.2
Additional model parameters		
Parameterized limb-darkening coefficient q_1	$\mathcal{N}[0.40, 0.05]$	0.40 ± 0.05
Parameterized limb-darkening coefficient q_2	$\mathcal{N}[0.26, 0.05]$	0.26 ± 0.05
Systemic velocity γ_{FIES} ($\mathrm{km\,s^{-1}}$)	$\mathcal{U}[76.5927, 76.6343]$	76.6114 ± 0.0042
Systemic velocity γ_{HARPS} ($\mathrm{km\,s^{-1}}$)	$\mathcal{U}[76.7276, 76.7658]$	76.7478 ± 0.0032
Systemic velocity $\gamma_{\mathrm{HARPS-N}}$ ($\mathrm{km\,s^{-1}}$)	$\mathcal{U}[76.7213, 76.7599]$	76.7416 ± 0.0037
Derived parameters of K2-98		
Planet mass M_{p} ($M_\oplus$)	$\cdots$	33 ± 12
Planet radius R_{p} ($R_\oplus$)	$\cdots$	$4.36^{+0.31}_{-0.30}$
Planet mean density ρ_{p} ($\mathrm{g\,cm^{-3}}$)	$\cdots$	$2.17^{+0.99}_{-0.82}$
Semi-major axis of the planetary orbit a (AU)	$\cdots$	$0.089^{+0.009}_{-0.013}$
Orbit eccentricity e	$\cdots$	0
Orbit inclination i_{p} (degrees)	$\cdots$	$88.6^{+0.9}_{-1.3}$
Transit duration τ_{14} (hours)	$\cdots$	$5.061^{+0.099}_{-0.086}$
Equilibrium temperature[b] T_{eq} (K)	$\cdots$	1062^{+83}_{-38}

Note – [a] $\mathcal{U}[a, b]$ refers to uniform priors between a and b, $\mathcal{N}[a, b]$ means Gaussian priors with mean a and standard deviation b and $\mathcal{F}[a]$ to a fixed a value. [b] Assuming albedo $= 0$.
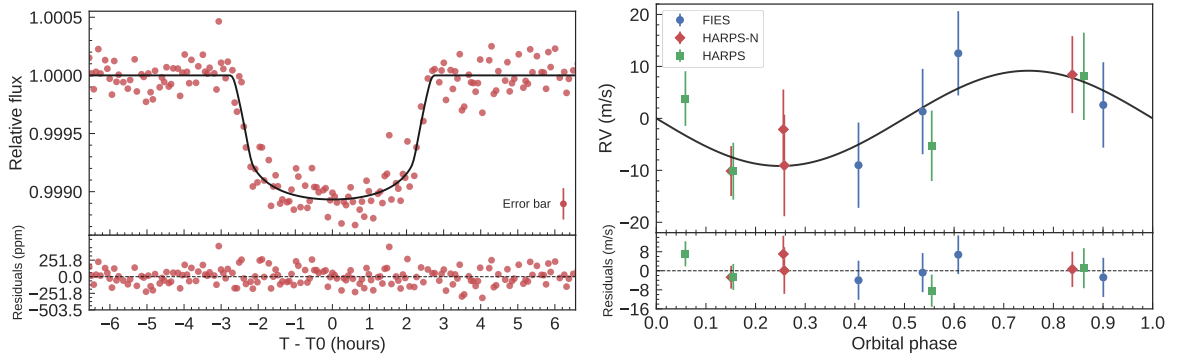
Figure 6.3: Left panel: transit light curve folded to the orbital period of K2-98 b and residuals. The red points are the *K2* data. The solid line marks the re-binned best-fitting transit model. Right panel: phase-folded FIES (blue circles), HARPS-N (red diamonds), and HARPS (green squares) RV measurements of K2-98b and best-fitting circular orbit (solid line), following the subtraction of the systemic velocities as measured from each instrument.

6.1.6 Orbital eccentricity

A fit for an eccentric orbit yields $e = 0.24^{+0.30}_{-0.18}$ with a significance of only about 1-σ. In order to further check whether the non-zero eccentricity solution is significant or not, we run an F-test and calculate the p-value, i.e., the probability that the apparent eccentricity could have arisen if the underlying orbit were circular (Lucy & Sweeney, 1971). In doing so we take into account the number of fitted parameters – both for the circular and eccentric model –, the number of measurements and their uncertainties, and the residuals from the best fitting circular and eccentric solution. We find a p-value of 0.87, which is much higher than the 0.05 significance threshold suggested by Lucy & Sweeney (1971) to prefer $e \neq 0$ over $e = 0$. We therefore conclude that the non-zero best fitting eccentricity obtained with models where e is allowed to vary is not significant. Moreover, we find that the circular (DOF=153) and eccentric (DOF=151) models provide very similar minimum χ^2 values of $\sim$152. The difference of the Bayesian information criterion is ΔBIC=10 between the two models, implying that the circular model is favoured. We therefore adopt the circular model as the one that better describes our data. We note that the derived system parameters for a non-zero eccentricity are consistent to within 1-σ uncertainties with those derived assuming a circular orbit.

6.1.7 K2-98 b's composition

K2-98 b has a mass of $M_{\mathrm{p}} = 33 \pm 12 M_{\oplus}$ and a radius of $R_{\mathrm{p}} = 4.36^{+0.31}_{-0.30} R_{\oplus}$ consistent with a density of $2.17^{+0.99}_{-0.82}$ g cm^{-3}. These parameters are calculated adopting the stellar mass and radius listed in Table 6.1.

Figure 6.4 shows the position of K2-98 b in the mass-radius diagram for Neptune-size planets. The plot includes only those objects whose both mass and radius have been estimated with a precision of at least $\sim$25 %. K2-98 b joins the family of intermediate mass ($20 < M_{\mathrm{p}} < 50 M_{\oplus}$) Neptune-size planets. Whereas its radius is slightly larger than that of Neptune ($3.9 R_{\oplus}$), the mass of K2-98 b is almost twice as large as the mass of Neptune. This implies that a solid massive core surrounded by a large atmosphere is expected (see, e.g., Weiss & Marcy, 2014).

6.1.8 K2-98 b's formation and migration

Assuming a minimum mass solar nebula (MMSN), the isolation mass (Schlichting, 2014) of a planet at 0.093 AU is $\sim$0.004 $M_{\oplus}$, which is significantly lower than the mass of K2-98 b. In order to form K2-98 b *in situ*, a disc surface density $\sim$5500 times larger than the MMSN is required. This value would generate gravitational instabilities in the disc, because its Toomre parameter would be $Q \approx 0.03 \ll 1$ (Schlichting, 2014). This scenario does not support the *in situ* formation of K2-98 b.

Valsecchi et al. (2014) proposed that Neptune-mass planets may form via migration of hot Jupiters that come so close to their host stars as to fill their Roche lobe and start conservative mass transfer to the star. This may reverse the direction of migration and increase the orbital period. However, it seems very difficult to reach a final orbital period of about 10 days, as in the case of K2-98 b. Moreover, this formation scenario cannot easily account for the measured relatively low density of the planet. Therefore, we argue that K2-98 b likely formed in the outer region of the protoplanetary disc and then migrated inwards to its current position (see, e.g. Kley & Nelson, 2012).

We integrate the equations of tidal and rotational evolution as in Lanza & Mathis (2016) assuming a constant modified tidal quality factor $Q'_{\star}$ for the star. Given that the stellar rotation period is close to the orbital period (see Barragán et al., 2016, Sect. 5),
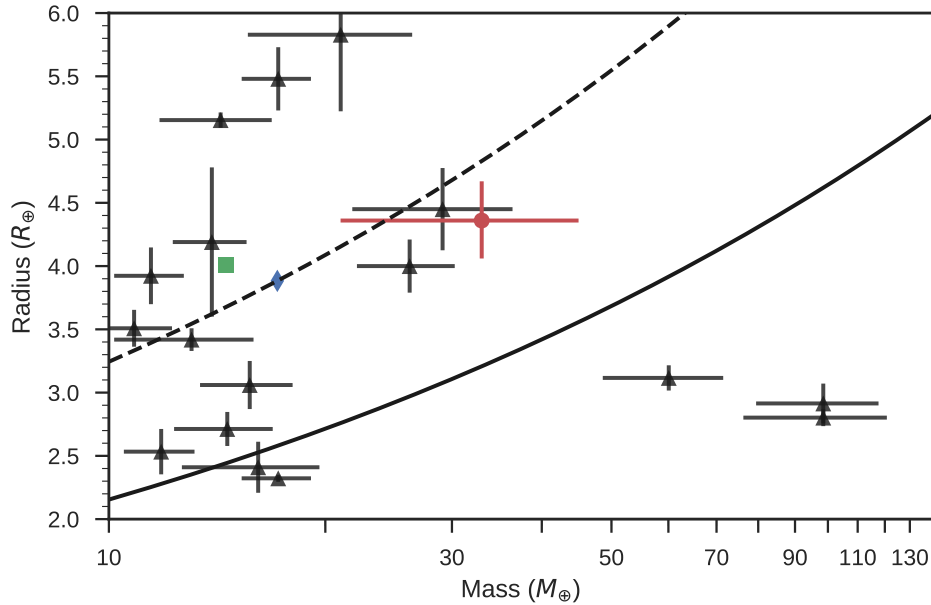
Figure 6.4: Mass-radius diagram for Neptune-size planets ($2.0 \lesssim R_{\mathrm{p}} \lesssim 6.0\,R_{\oplus}$) whose both mass and radius have been determined with a precision of at least $\sim 33\,\%$ (Exoplanet Orbit Database, as of June 2016; Han et al., 2014). The red circle marks the position of K2-98 b. The green diamond and blue square show the position of Neptune and Uranus, respectively. The solid and dashed lines mark the Earth ($5.5\,\mathrm{g\,cm^{-3}}$) and Neptune ($1.6\,\mathrm{g\,cm^{-3}}$) isodensity curves.

tidal dissipation by inertial waves inside the star is considered leading to a remarkably stronger tidal interaction than in the case of the equilibrium tide (Ogilvie & Lin, 2007). Therefore, we explore the evolution for three fixed values of $Q'_{\star}$, i.e., 10^5, 10^6, and 10^7, from the stronger to the weaker coupling. Following Lanza et al. (2011), we include the loss of angular momentum produced by the stellar magnetised wind considering a saturation regime for an angular velocity greater than $8\,\Omega_{\odot}$, where $\Omega_{\odot}$ is the present solar angular velocity. We assume that the orbit of the planet is circular, although the tidal interaction is so weak that any initial eccentricity could survive up to the present stage of the system evolution (see below).

Fig. 6.5 shows the evolution of the rotation period of the star (upper panel), semi-major axis of the planet's orbit (middle panel), and stellar radius (lower panel) as obtained from the evolutionary models (see Barragán et al., 2016, Sect. 5). Tidal interaction is so weak that there is virtually no evolution of the orbital separation since the planet arrived at the present semi-major axis (Fig. 6.5, middle panel). The rotation of the star is braked solely by the stellar wind with a completely negligible tidal exchange between the orbital and the spin angular momenta, and no dependency on the stellar tidal quality factor $Q'_{\star}$, owing to the small mass of the planet and large separation. (Fig. 6.5, upper panel). Under our model assumptions, we estimate that the star reached the zero age main sequence (ZAMS) with a rotation period of about 1.5 days.

The tidal evolution of the planet will become important in the future – after ~ 3 Gyr from now – due to the increase of the stellar radius and rotational period of the star, leading to a rapid decay of the planet's orbit (Fig. 6.5, middle panel).

The amount of angular momentum in the orbit is insufficient to synchronise the rotation of the star, so the present approximately synchronous state cannot be maintained. Damiani & Lanza (2015) showed that other systems having host stars with an effective temperature around 6100 K show a rather wide distribution of the ratio of the orbital
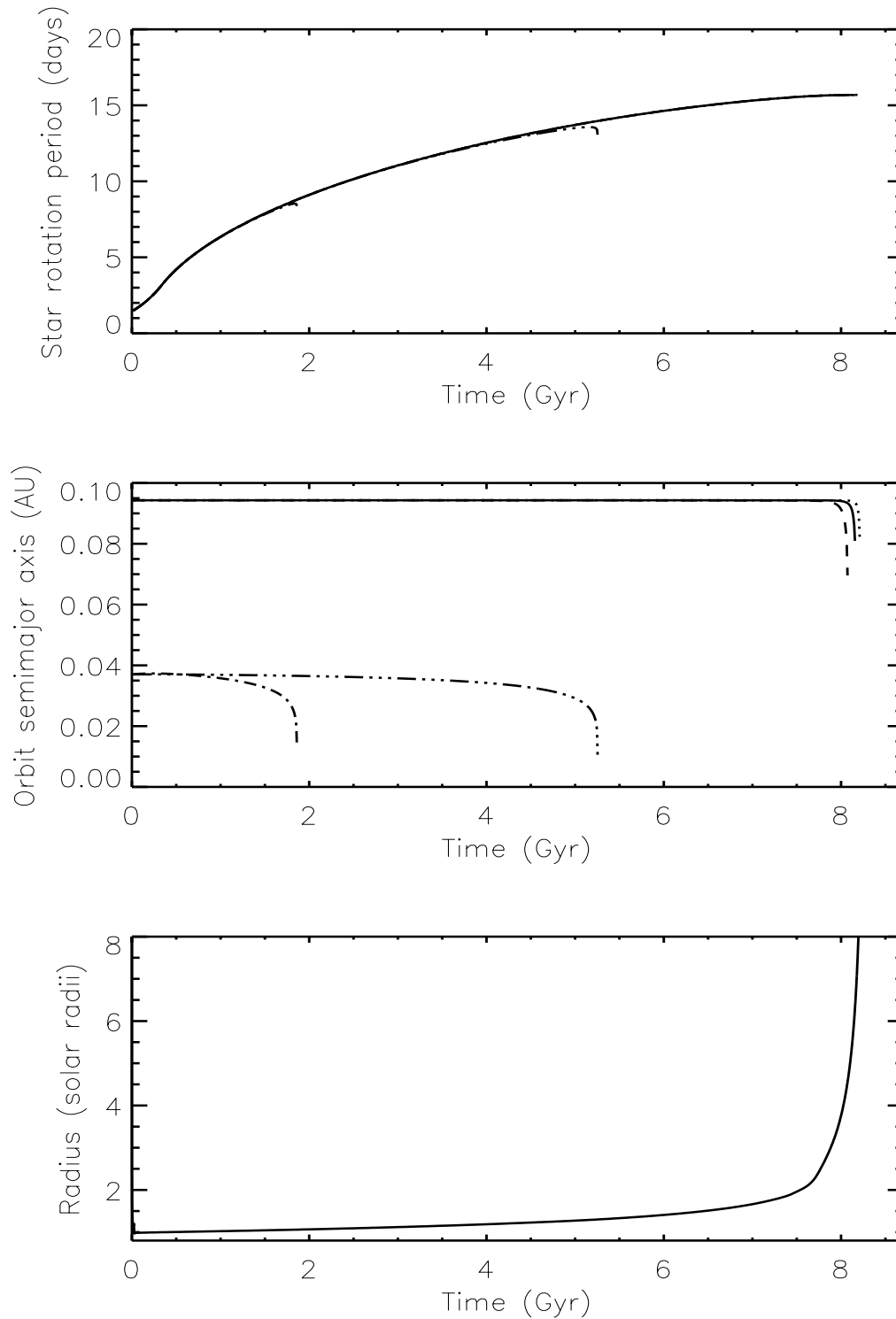
Figure 6.5: Rotational period of the star (upper panel), semi-major axis of the planet orbit (middle-panel), and stellar radius (lower panel) versus time. Different line styles refer to different initial semi-major axis a_0 and tidal quality factor of the star $Q'_\star$ as follows: solid line: $Q'_\star = 10^6$, $a_0 = 0.0943$ AU; dotted line: $Q'_\star = 10^7$, $a_0 = 0.0943$ AU; dashed line: $Q'_\star = 10^5$, $a_0 = 0.0943$ AU; dash-dotted: $Q'_\star = 10^5$, $a_0 = 0.037$ AU (corresponding to an orbital period of 2.5 days); dash-triple-dotted: $Q'_\star = 10^6$, $a_0 = 0.037$ AU. This figure was made by A. F. Lanza to appear in Barragán et al. (2016).

period to the stellar spin period, even in the case of more massive planets, thus supporting the conclusion that the present approximate synchronicity is probably coincidental.

Finally, we consider the possibility that the planet was initially significantly closer to the star when the latter reached the ZAMS and was pushed outwards by the action of tides because angular momentum was transferred from the stellar spin to the orbit, provided that the rotational period of the star was shorter than the orbital one. We find that also this scenario is unlikely. As an illustrative case, we show in Fig. 6.5 two integrations for the planet initially at an orbital period of 2.5 days, corresponding to a semi-major axis of 0.037 AU. This is the minimum orbital period for observed Neptune-mass planets around main-sequence stars (cf. Fig. 4 of Valsecchi et al., 2014) that we choose in order to maximise the strength of the tidal interaction. Since the star was initially rotating faster than the planet, the tidal interaction was initially pushing the planet outwards, in particular for $Q'_\star = 10^5$ (Fig. 6.5, middle panel). However, the fast rotational braking of the star led soon to a rotation period longer than the orbital period. Since the amount of orbital angular momentum was too small to maintain the synchronous state, the final fate of the planet was to fall towards the star under the action of tides within a few Gyrs[2]. This scenario would account for the significant dearth of Neptune-like planets with orbital periods below 2-4 days (see, e.g., Mazeh et al., 2016; Szabó & Kiss, 2011).

The tidal evolution of the system further supports an inward migration scenario for K2-98 b, from the outer region of the system to its current position.

---

[2]We note that assuming a different initial orbital period leads to qualitatively similar scenarios. If the initial orbital period of the planet is shorter than 2.5 days (i.e., $a_0 < 0.037$ AU), tidal push is stronger, but for a shorter time interval before the rotation period of the star becomes longer than the orbital period, after which the orbit decays faster. If the planet is further out ($P_{0,\mathrm{orb}} > 2.5$ days and $a_0 > 0.037$ AU), tides are weaker, but they can act longer before the direction of the evolution of the semi-major axis is reversed and the planet falls into the star.

6.2   K2-139: An active star hosting a warm Jupiter

We announced the discovery and mass measurement of the exoplanet K2-139 b in Barragán et al. (2018a). This discovery is part of a series of *K2* exoplanet discoveries made by the KEST collaboration. K2-139 b is a transiting warm-Jupiter on a 29-day orbit around an active ($\log R'_{\mathrm{HK}} = -4.46 \pm 0.06$) K0 V star in *K2* Campaign 7. We derived the system's parameters by combining the *K2* photometry with ground-based follow-up observations. With a mass of $M_{\mathrm{p}} = 0.387^{+0.083}_{-0.075} M_{\mathrm{J}}$ and radius of $R_{\mathrm{p}} = 0.808^{+0.034}_{-0.033} R_{\mathrm{J}}$, K2-139 b is one of the transiting warm Jupiters with the lowest mass known to the date. The planetary mean density of $\rho_{\mathrm{p}} = 0.91^{+0.24}_{-0.20} \,\mathrm{g\,cm^{-3}}$ can be explained with a core of $\sim$50 $M_{\oplus}$. Given the brightness of the host star ($V = 11.653$ mag), the relatively short transit duration ($\sim$5 hours), and the expected amplitude of the Rossiter-McLaughlin effect ($\sim$25 m s^{-1}), K2-139 is an ideal target to measure the spin-orbit angle of a planetary system hosting a warm Jupiter.

6.2.1   Detection

We use the transit detection algorithms `DST` (Cabrera et al., 2012) and `EXOTRANS` (Grziwa et al., 2012) to search for transit signals in *K2* Campaign 7 light curves extracted by Vanderburg & Johnson (2014). Both codes detected a periodic transit-like signal associated with the star EPIC 218916923 (K2-139). The target passed all the tests which validated the planetary nature of the transiting object (see Barragán et al., 2018a, for more details). As a sanity check, we downloaded the EVEREST light curve of EPIC 218916923 (Luger et al., 2016) and detected the same signal. The EVEREST light curve of K2-139 b is shown in Figure 6.6.

6.2.2   ALFOSC imaging

K2 Campaign 7 is projected close to the galactic centre and thus in a relatively crowded stellar region. In order to estimate the contamination factor arising from sources whose light leaks into the photometric masks used by Vanderburg & Johnson (2014) and Luger et al. (2016), we observed K2-139 on 13 September 2016 (UT) with the ALFOSC camera mounted at the Nordic Optical Telescope (NOT) of Roque de los Muchachos Observatory (La Palma, Spain). The sky conditions were photometric with excellent seeing conditions ($\sim$0.6"). We used the Bessel R-filter and acquired 16 images of 6 sec, 2 images of 20 sec, and 1 image of 120 sec. The data were bias subtracted and flat-fielded using dusk sky flats. Aperture photometry was then performed on all stars within the mask used in the extraction of the light curve by Vanderburg & Johnson (2014) and Luger et al. (2016).

Several fainter stars can be identified inside the photometric mask (see Fig. 2 of Barragán et al., 2018a), of which the two brightest sources are also in the EPIC catalogue with Kepler band magnitudes of 16.8 and 18.4. The closest detected source is a 6.8-mag fainter star at 3.8" South of K2-139. We can exclude stars as faint as $\sim$20 mag at an angular distance larger than $\sim$0.6" from K2-139. It is worth noting that the faintest star whose flux could account for the $\sim$1% deep transit of K2-139 cannot be more than $\sim$5 mag fainter than our target. The summed flux of these faint stars amounts to 1.4±0.3 % of the total off-transit flux within the aperture. We subtracted this contamination flux from the EVEREST *K2* light curve prior to performing the joint analysis presented in Sect. 6.2.5.
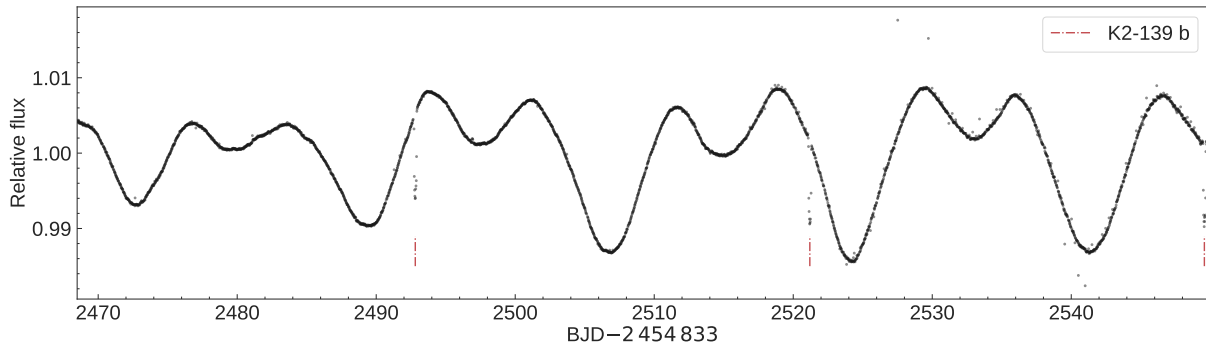
Figure 6.6: *K2* Light curve for EPIC 218916923 (K2-139) as extracted by Luger et al. (2016). The positions of the 3 observed transits are marked with vertical red dot-dashed lines. The quasi-periodic modulation is very likely caused by Sun-like spots appearing and disappearing from the visible stellar disc as the star rotates around its axis (see Sect. 6.2.4).

6.2.3 Spectroscopic follow-up

The high-precision radial velocity follow-up of K2-139 was started in June 2016 with the FIES spectrograph. The observations were carried out as part of the OPTICON and CAT observing programs 16A/055, P53-201, and P53-203. The data acquisition and reduction methods are similar to the ones described in Section 4.3.1. We also observed K2-139 in July, August, and September 2016 with the HARPS and HARPS-N spectrographs. Data were reduced using the dedicated HARPS and HARPS-N pipelines and extracted the RVs by cross-correlation with a G2 numerical mask. The full list of FIES (10 measurements), HARPS (6 measurements), and HARPS-N (3 measurements) RVs are listed in Barragán et al. (2018a).

6.2.4 Stellar parameters

Spectral analysis

We derived the spectroscopic parameters of K2-139 from the co-added FIES spectra. The stacked FIES data have a S/N ratio of ∼110 per pixel at 5500 Å. The estimated spectroscopic values for K2-139 are $T_{\mathrm{eff}} = 5340 \pm 110$ K, $\log g_\star = 4.50 \pm 0.09$ (cgs), [Fe/H] $= 0.22 \pm 0.08$ dex, $v_{\mathrm{mic}} = 0.9 \pm 0.1$ km s^{-1}, $v_{\mathrm{mac}} = 2.5 \pm 0.6$ km s^{-1} and $v \sin i_\star = 2.8 \pm 0.6$ km s^{-1}. The details of the approach to estimate those values are given in Barragán et al. (2018a). As a sanity check, we also analysed the HARPS and HARPS-N data and obtained consistent results but with larger error bars, owing to the lower S/N ratio of the co-added HARPS and HARPS-N spectra compared to that of the co-added FIES data. Using the Boyajian et al. (2013)'s calibration (see their Table 6), the effective temperature of K2-139 defines the spectral type of the host star as K0 V.

Interstellar extinction

We measured the visual reddening (A_{V}) of K2-139 following the technique described in Gandolfi et al. (2008). We fitted the spectral energy distribution of the star to synthetic colors extracted from the `BT-NEXTGEN` model spectrum (Allard et al., 2011) with the same photospheric parameters as the star. We adopted the extinction law of Cardelli et al. (1989) and assumed a normal value for the total-to-selective extinction, i.e., $R_{\mathrm{V}} = A_{\mathrm{V}}/E(B-V) = 3.1$. We measured a visual extinction of $A_{\mathrm{V}} = 0.07 \pm 0.05$ mag. This value is below the upper limit of $A_{\mathrm{V}} \lesssim 0.3$ mag extracted from the Schlegel et al. (1998)'s all-sky extinction map, corroborating our result.

Rotational period

The *K2* light curve of K2-139 displays periodic and quasi-periodic variations with a peak-to-peak photometric amplitude of $\sim 2\%$ (see Fig. 6.6). The late-type spectral type of the star suggests that the observed variability is due to Sun-like spots appearing and disappearing from the visible stellar disc as the star rotates around its axis. This is corroborated by the fact that K2-139 is a chromospherically active star. The HARPS and HARPS-N spectra show clear emission components in the cores of the Ca II H&K lines, from which we measured an average activity index of $\log R'_{\mathrm{HK}} = -4.46 \pm 0.06$[3].

The out-of-transit photometric variability observed in the light curve of K2-139 is mainly due to two active regions located at opposite stellar longitudes, whose lifetime is longer than the duration of the *K2* observations. Using the spots as tracers of stellar rotation and following the auto correlation function (ACF) technique described in McQuillan et al. (2014), we estimated that the rotational period of the star is $P_{\mathrm{rot}} = 17.24 \pm 0.12$ days. The Lomb-Scargle periodogram of the light curve shows its strongest peak at the same period confirming our results.

It is worth noting that the rotation period ($P_{\mathrm{rot}} = 17.24 \pm 0.12$ days) and radius ($R_\star = 0.862 \pm 0.032\,R_\odot$; see next section) of the host star translate into a maximum value for the projected rotational velocity of $v \sin i_{\star,\mathrm{max}} = 2.53 \pm 0.10\ \mathrm{km\,s^{-1}}$, which agrees with the spectroscopically derived $v \sin i_\star = 2.8 \pm 0.6\ \mathrm{km\,s^{-1}}$, suggesting that the star is seen nearly equator-on ($i_\star \approx 90\,\mathrm{deg}$) and that the system might be aligned along the line-of-sight.

Stellar mass, radius and age

We derived the stellar mass, radius, and age using the on-line interface for Bayesian estimation of stellar parameters available at http://stev.oapd.inaf.it/cgi-bin/param. Briefly, the web tool interpolates onto `PARSEC` model isochrones (Bressan et al., 2012), the V-band apparent magnitude, effective temperature, metal content, and parallax. We used the V-band magnitude reported in Table 1 of Barragán et al. (2018a) – after correcting for interstellar reddening (Sect 6.2.4) – along with the effective temperature and metal content we derived in Sect. 6.2.4. The parallax was retrieved from the *Gaia*'s first data release ($\mathrm{px} = 6.56 \pm 0.43\,\mathrm{mas}$, $d = 152 \pm 10$ pc Fabricius et al., 2016). We adopted the log-normal initial mass function from Chabrier (2001).

K2-139 has a mass of $M_\star = 0.919 \pm 0.033\,M_\odot$ and radius of $R_\star = 0.862 \pm 0.032\,R_\odot$, corresponding to a surface gravity of $\log g_\star = 4.503 \pm 0.035$ (cgs), in excellent agreement with the spectroscopically derived value of $\log g_\star = 4.50 \pm 0.09$ (cgs). The derived mean density $\rho_\star = 2.02 \pm 0.24\ \mathrm{g\,cm^{-3}}$ of K2-139 is also consistent within 1-σ with the density estimated by the modelling of the transit light curve ($\rho_\star\ 2.11^{+0.74}_{-0.81}\ \mathrm{g\,cm^{-3}}$; see Sect. 6.2.5).

The isochrones provide an age of 3.6 ± 3.4 Gyr for K2-139. Using the equations given in Barnes & Kim (2010) and Barnes (2010), the rotation period of 17.3 days implies a gyrochronological age of 1.8 ± 0.3 Gyr.

6.2.5 Joint RV-transit data analysis

We performed the joint fit to the photometric and RV data using the `pyaneti` software (Barragán et al., 2019, see also Sect. 5.3). The photometric data included in the joint analysis are subsets of the whole EVEREST *K2* light curve. We used the EVEREST light curve because it provides a slightly better rms over the Vanderburg & Johnson (2014)'s data. We selected ~ 10 hours of data-points around each of the 3 transits, which have a

---

[3]This value is corrected for the interstellar medium absorption, following the procedure described in Fossati et al. (2017) and using the measured stellar parameters and reddening. The correction is +0.06. The star is therefore slightly more active than what measured from the spectra.

duration of $\sim$5 hours. We de-trended each individual transits with the code `exotrending` (Barragán & Gandolfi, 2017, see Appendix A.1), using a second-order polynomial fitted to the out-of-transit points. The fitted data include 12 points immediately before and after each transit, with the exception of the last transit for which only 9 data points are available. We removed the data points that are affected by stellar spot crossing events (see Sect. 6.2.6 for more details).

We fitted the RV data using a Keplerian model for the planet, along with two sine-like curves to account for the activity-induced RV (see Section 6.2.6 for details). We adopted the limb-darkened quadratic law of Mandel & Agol (2002) for the transit model. Following Kipping (2010, see Appendix A.2), we super-sampled the light curve model using 10 sub-samples per *K2* exposure to account for the long-cadence acquisition. Details on the fitted parameters and adopted priors are given in Table 5.1. We use the same approach as in Sect. 6.1.5 to generate 250,000 independent points for each fitted parameter.

6.2.6 Stellar activity modeling

A simple Keplerian model provides a poor fit to the RV measurements with $\chi^2/\mathrm{dof} = 6.1$ (Table 6.2), suggesting that additional signals might be present in our Doppler data. Activity-induced RV variation is expected given the 2 % peak-to-peak photometric variability observed in the *K2* light curve of K2-139 (Fig. 6.6) and the Ca II H & K activity index of $\log R'_{\mathrm{HK}} = -4.46 \pm 0.06$. The *K2* photometric variation corresponds to a spot filling factor of approximately 2 %, if this variation is due to cool starspots. We can use the empirical relationship relating spot coverage to RV amplitude from Saar & Donahue (1997) or Hatzes (2002) to estimate the RV amplitude expected from spots. Using the projected rotational velocity of 2.8 km s^{-1} results in an RV semi-amplitude of $\approx$20–30 m s^{-1}. The code `SOAP2` (Dumusque et al., 2014), designed to estimate the effect of active regions on photometric and spectroscopic measurements, provides consistent results.

In order to look for additional signals in our Doppler data, we performed a frequency analysis of the RV measurements and activity indicators. The full details are described in Barragán et al. (2018a). We concluded that we cannot exclude the existence of spot-induced signals in our RV measurements.

Photometric and radial velocity variations due to rotational modulation can be complex with not only the rotational period P_{rot} present, but also its harmonics, e.g., $P_{\mathrm{rot}}/2$, $P_{\mathrm{rot}}/3$. Assuming that the surface structures responsible for this modulation (e.g., cool spots) are not evolving rapidly, then the simplest representation of the rotational modulation is through the Fourier components defined by the rotation period and its harmonics.

Figure 6.6 shows that the evolution time-scale of the active regions in the stellar surface is longer than the 80-day duration of the *K2* campaign. Since our RV follow-up spans 55 days, we can assume that any activity-induced RV signal is coherent within our observing window. This approach has been used previously for other planetary systems orbiting active stars (e.g., Pepe et al., 2013, see Appendix B).

The Fourier analysis of the *K2* light curve is the best way to measure the contribution of the rotation period and its harmonics to the quasi-periodic photometric variability of the star. We therefore analysed the *K2* light curve using a pre-whitening procedure. That is, the dominant period was found, a sine-fit made to the data and subtracted, and additional periods searched in the residual data. We used the program `Period04` (Lenz & Breger, 2005) for this procedure.

The dominant periods are $\sim$17.2 days, i.e., the rotation period of the star (Sect. 6.2.4), and roughly the first four harmonics (i.e., 8.6, 5.7, 4.3, and 3.4 days). The 17.2- and 8.6-day periods have about the same amplitude, while the 5.7-day period ($P_{\mathrm{rot}}/3$) has

Table 6.2: Model comparison for K2-139 RV data.

Model	Comment	$N_{\rm pars}$	$K_{\rm b}$ (m s^{-1})	$\chi^2/{\rm dof}^{(a)}$	$\ln P(D\vert M)$	AIC$^{(b)}$
P0	Planet	6	29.1 ± 2.0	6.1	35.6	-60
P1	Planet + 1 sine-curve at $P_{\rm rot}$	9	29.4 ± 2.4	3.4	58.1	-98
P2	Planet + 2 sine-curves at $P_{\rm rot}$ and $P_{\rm rot}/2$	11	$27.3^{+2.6}_{-2.5}$	3.8	60.1	-98
P3	Planet + 3 sine-curves at $P_{\rm rot}$, $P_{\rm rot}/2$, and $P_{\rm rot}/3$	13	$27.8^{+2.7}_{-2.6}$	5.3	59.3	-93
NP1	1 sine-curve at $P_{\rm rot}$ (No planet signal)	6	0	18.5	-44.8	101
NP2	2 sine-curves at $P_{\rm rot}$ and $P_{\rm rot}/2$ (No planet signal)	8	0	15.9	-12.0	40

Note – $^{(a)}$ χ^2 value assuming no jitter. $^{(b)}$ We used the Akaike Information Criteria (AIC = $2N_{\rm pars} - \ln 2P(D\vert M)$) instead of the widely used Bayesian information criteria (BIC) because our RV data sample is small (19 data points), and BIC performs better for large samples (Burnham & Anderson, 2002).

10% of the main amplitude. The $P_{\rm rot}/4$ signal has only about 4% of the main amplitude. The light curve analysis indicates that the signal due to rotational modulation can largely be represented by the rotational period ($P_{\rm rot}$) and its first harmonic ($P_{\rm rot}/2$).

In order to test if the addition of RV sinusoidal signals at the stellar rotation period and its harmonics can account for the additional variation seen in our RV measurements, we compared different models by adding signals one by one. The first model (P0) includes only the planet signal, i.e., a Keplerian model fitted to the RV data using the same priors given in Table 6.3, but fixing epoch and period to the values derived by the transit modelling. The next model (P1) is obtained from P0 by adding a sinusoidal signal at the rotation period of the star ($P_{\rm rot}$). Models P2 includes the first harmonic of the rotation period ($P_{\rm rot}/2$), whereas model P3 account for the first ($P_{\rm rot}/2$) and second ($P_{\rm rot}/3$) harmonics. While adding sinusoidal signals, we fitted for their amplitudes, phases and periods. We used flat priors for the phases and amplitudes (details in Table 6.3). We used a Gaussian prior for $P_{\rm rot}$ using the value and its uncertainty derived in Sect. 6.2.4. The periods of the harmonic signals were left free to vary depending on the value assumed by $P_{\rm rot}$ at each step of the MCMC chains. In order to check if the RV variation induced by the planet is significant in our data set, we also performed the fit using models where the planetary signal was not included (models NP1 and NP2; see Table 6.2).

Table 6.2 shows the goodness of the fit for each model. The preferred model is P2 (planet plus 2 sinusoidal signals at $P_{\rm rot}$ and $P_{\rm rot}/2$) with the lowest Akaike Information Criteria (AIC) and maximum likelihood. This result is consistent with the Fourier analysis of the *K2* light curve, which suggests that the major contribution to the photometric variations arises from the stellar rotation period and its first harmonic. Our analysis provides also additional evidence that the Doppler motion induced by the planet is present in our RV data set. First, the planet signal does not significantly vary for the P0, P1, P2 and P3 models (Table 6.2). Second, the models with no planetary signal (NP1 and NP2) provide a poor fit to the RV measurements (Table 6.2).

To account for additional instrumental noise not included in the nominal RV error bars and/or imperfect treatment of the various sources of RV variations, we fitted for a jitter term for each instrument. The final parameter estimates and their error bars are listed in Table 6.3. They are defined as the median and the 68% credible interval of the final posterior distributions displayed in Figure 6.7). The best fitting transit and RV models are displayed in Figure 6.8 along with the photometric and RV data points.

Table 6.3: K2-139 system parameters.

Parameter	Prior[a]	Final value
Stellar parameters		
Star mass $M_\star$ ($M_\odot$)	$\cdots$	0.919 ± 0.033
Star radius $R_\star$ ($R_\odot$)	$\cdots$	0.862 ± 0.032
Star density $\rho_\star$ (from spectroscopy, $\mathrm{g\,cm^{-3}}$)	$\cdots$	$2.02^{+0.25}_{-0.22}$
Star density $\rho_\star$ (from light curve, $\mathrm{g\,cm^{-3}}$)	$\cdots$	$2.11^{+0.74}_{-0.81}$
Effective Temperature T_{eff} (K)	$\cdots$	5340 ± 110
Surface gravity $\log g_\star$ (cgs)	$\cdots$	4.50 ± 0.09
Iron abundance [Fe/H] (dex)	$\cdots$	0.22 ± 0.08
Microturbulent velocity v_{mic} ($\mathrm{km\,s^{-1}}$)	$\cdots$	0.9 ± 0.1
Macroturbulent velocity v_{mac} ($\mathrm{km\,s^{-1}}$)	$\cdots$	2.5 ± 0.6
Projected rotational velocity $v \sin i_\star$ ($\mathrm{km\,s^{-1}}$)	$\cdots$	2.8 ± 0.6
Rotational period P_{rot} (days)	$\cdots$	17.24 ± 0.12
Activity index[b] $\log R'_{\mathrm{HK}}$	$\cdots$	-4.46 ± 0.06
Gyrochronological age (Gyr)	$\cdots$	1.8 ± 0.3
Interstellar extinction A_{V} (mag)	$\cdots$	0.07 ± 0.05
Star distance d (pc)	$\cdots$	152 ± 10
Model parameters of K2-139 b		
Orbital period P_{orb} (days)	$\mathcal{U}[28.3773, 28.3873]$	28.38236 ± 0.00026
Transit epoch T_0 ($\mathrm{BJD_{TDB}} - 2\,450\,000$)	$\mathcal{U}[7325.8120, 7325.8220]$	7325.81714 ± 0.00033
Scaled semi-major axis $a/R_\star$	$\mathcal{U}[1.2, 100]$	$44.8^{+4.7}_{-6.7}$
Planet-to-star radius ratio $R_{\mathrm{p}}/R_\star$	$\mathcal{U}[0, 0.2]$	$0.0961^{+0.0023}_{-0.0015}$
Impact parameter, b	$\mathcal{U}[0, 1.2]$	$0.30^{+0.21}_{-0.19}$
$\sqrt{e}\sin\omega$	$\mathcal{U}[-1, 1]$[c]	$0.10^{+0.29}_{-0.30}$
$\sqrt{e}\cos\omega$	$\mathcal{U}[-1, 1]$[c]	$0.06^{+0.24}_{-0.27}$
Radial velocity semi-amplitude variation K ($\mathrm{m\,s^{-1}}$)	$\mathcal{U}[0, 200]$	$27.7^{+6.0}_{-5.3}$
Model parameters of RV sinusoidal signal at P_{rot}		
Period P_{rot} (days)	$\mathcal{N}[17.24, 0.12]$	17.26 ± 0.12
Epoch T_0 ($\mathrm{BJD_{TDB}} - 2\,450\,000$)	$\mathcal{U}[7324.0, 7341.3]$	$7332.4^{+5.5}_{-5.1}$
Radial velocity semi-amplitude variation K ($\mathrm{m\,s^{-1}}$)	$\mathcal{U}[0, 200]$	$7.1^{+7.5}_{-5.0}$
Model parameters of RV sinusoidal signal at $P_{\mathrm{rot}}/2$		
Period P_{orb} (days)	$\mathcal{F}[P_{\mathrm{rot}}/2]$	8.63 ± 0.06
Epoch T_0 ($\mathrm{BJD_{TDB}} - 2\,450\,000$)	$\mathcal{U}[7317.0, 7325.7]$	7321.3 ± 2.2
Radial velocity semi-amplitude variation K ($\mathrm{m\,s^{-1}}$)	$\mathcal{U}[0, 200]$	$10.6^{+7.7}_{-6.9}$
Additional model parameters		
Parameterised limb-darkening coefficient q_1	$\mathcal{U}[0, 1]$	$0.37^{+0.18}_{-0.13}$
Parameterised limb-darkening coefficient q_2	$\mathcal{U}[0, 1]$	$0.48^{+0.24}_{-0.16}$
Systemic velocity γ_{FIES} ($\mathrm{km\,s^{-1}}$)	$\mathcal{U}[-32.3913, -30.2990]$	-31.3575 ± 0.0064
Systemic velocity γ_{HARPS} ($\mathrm{km\,s^{-1}}$)	$\mathcal{U}[-32.2217, -30.1633]$	-31.1970 ± 0.0093
Systemic velocity $\gamma_{\mathrm{HARPS-N}}$ ($\mathrm{km\,s^{-1}}$)	$\mathcal{U}[-32.2141, -30.1683]$	$-31.1950^{+0.0122}_{-0.0128}$
Jitter term σ_{FIES} ($\mathrm{m\,s^{-1}}$)	$\mathcal{U}[0, 100]$	$9.6^{+9.8}_{-6.5}$
Jitter term σ_{HARPS} ($\mathrm{m\,s^{-1}}$)	$\mathcal{U}[0, 100]$	$15.4^{+11.0}_{-7.6}$
Jitter term $\sigma_{\mathrm{HARPS-N}}$ ($\mathrm{m\,s^{-1}}$)	$\mathcal{U}[0, 100]$	$10.2^{+15.8}_{-7.3}$
Derived parameters of K2-139 b		
Planet mass M_{p} (M_{Jup})	$\cdots$	$0.387^{+0.083}_{-0.075}$
Planet radius R_{p} (R_{Jup})	$\cdots$	$0.808^{+0.034}_{-0.033}$
Planet mean density ρ_{p} ($\mathrm{g\,cm^{-3}}$)	$\cdots$	$0.91^{+0.24}_{-0.20}$
Semi-major axis of the planetary orbit a (AU)	$\cdots$	$0.179^{+0.021}_{-0.027}$
Orbit eccentricity e	$\cdots$	$0.12^{+0.12}_{-0.08}$
Argument of periastron of stellar orbit $\omega_\star$ (degrees)	$\cdots$	124^{+175}_{-79}
Orbit inclination i_{p} (degrees)	$\cdots$	$89.62^{+0.25}_{-0.36}$
Transit duration τ_{14} (hours)	$\cdots$	$4.89^{+0.08}_{-0.22}$
Equilibrium temperature[d] T_{eq} (K)	$\cdots$	565^{+48}_{-32}

Note – [a] $\mathcal{U}[a, b]$ refers to uniform priors between a and b, $\mathcal{N}[a, b]$ means Gaussian priors with mean a and standard deviation b and $\mathcal{F}[a]$ to a fixed a value. [b] Corrected for interstellar reddening following Fossati et al. (2017). The correction is $+0.06$. [c] The code always ensures that $e < 1$. [d] Assuming albedo $= 0$.
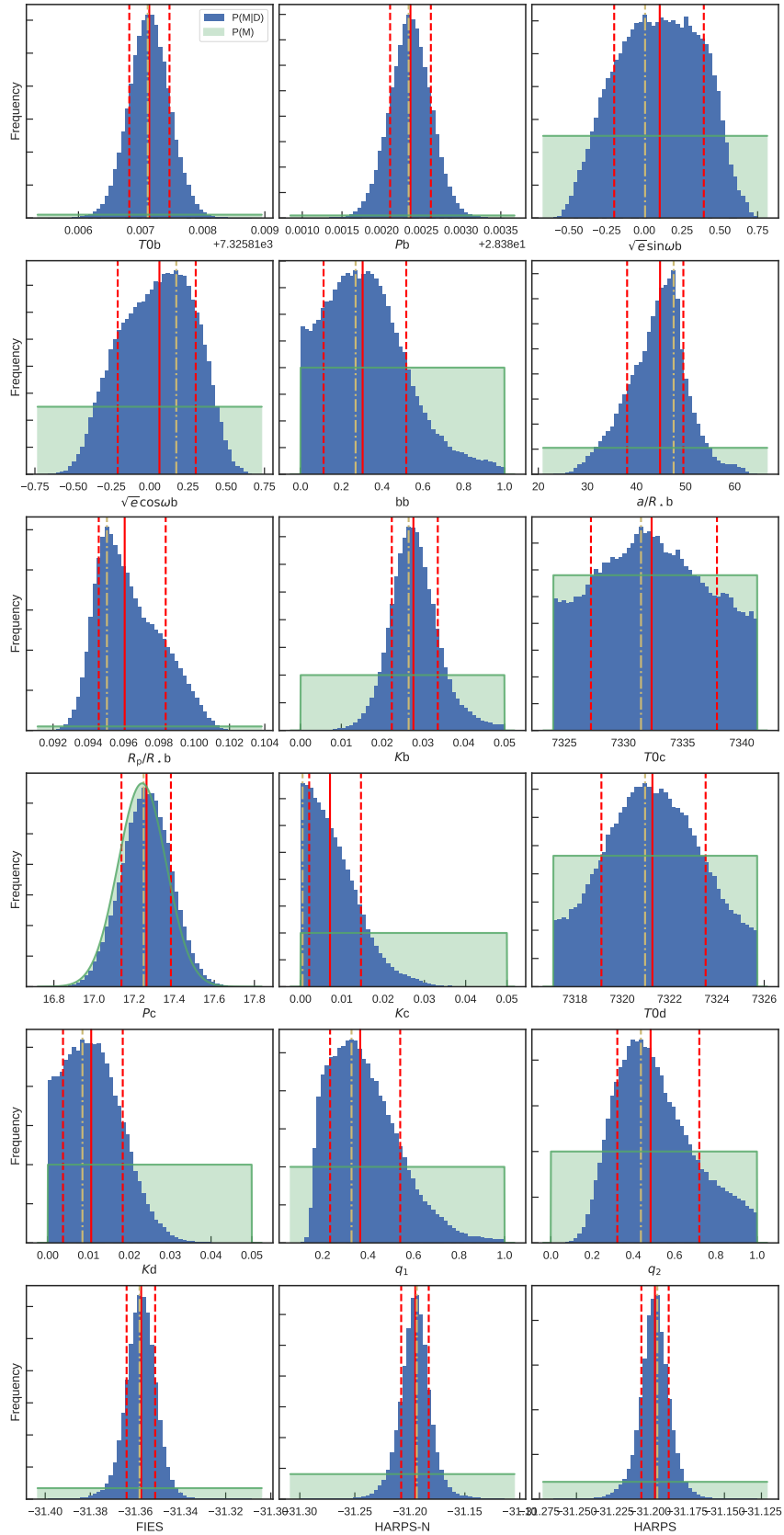
Figure 6.7: Posterior distributions of the K2-139 b's parameters as obtained from the final analysis performed with `pyaneti`. The blue region corresponds to the marginalised posterior $P(M|D)$, whereas the shaded green region mark the shape of the prior $P(M)$. Median (solid red line), 68% credible interval (dashed red line), and mode (dash-dotted yellow line) are also shown.
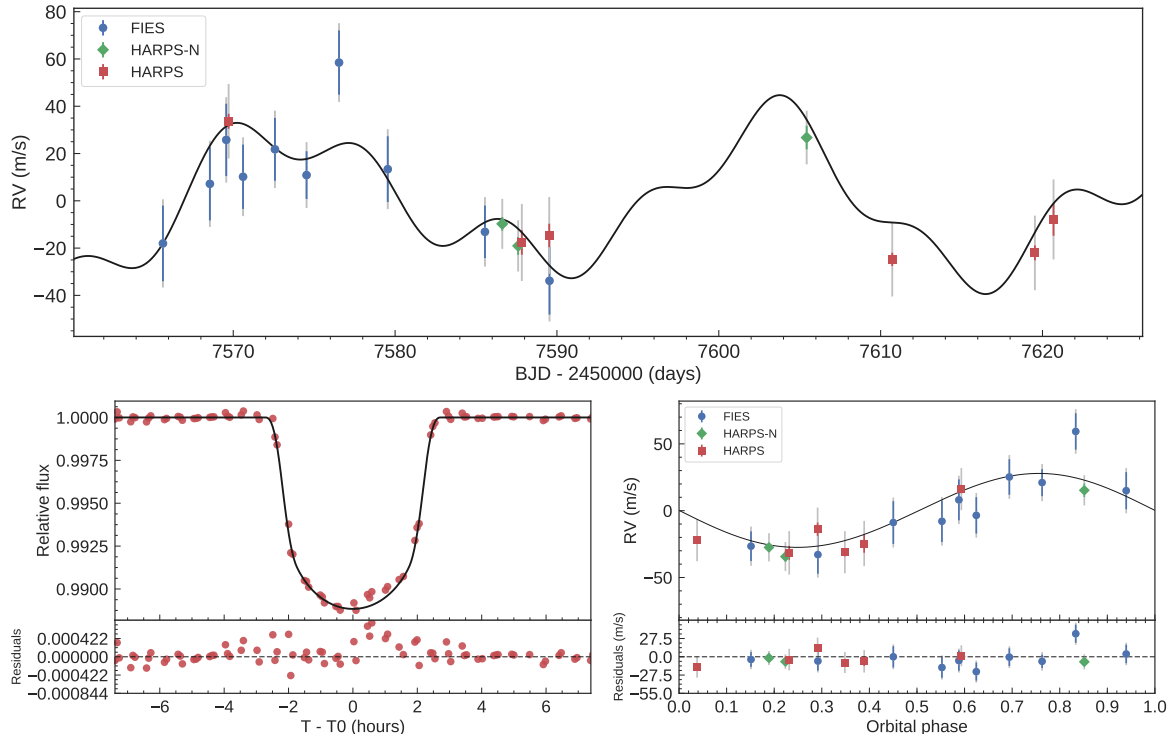
Figure 6.8:   *Top*: FIES (blue circles), HARPS-N (green diamonds) and HARPS (red squares) RV measurements *versus* time, following the subtraction of the systemic velocities for each instrument. The 1σ uncertainties are marked using the same colour used for each data-set. The vertical grey lines mark the error bars including jitter. The solid line represents the best fitting RV model, which includes the planet signal, and the activity signal at the stellar rotation period and its first harmonic. *Lower left panel*: Transit light curve folded to the orbital period of K2-139 b and residuals. The red points mark the *K2* data and their error bars. The solid line mark the re-binned best-fitting transit model.   *Lower right panel*: Phase-folded RV curve of K2-139 b and best fitting Keplerian solution (solid line), following the subtraction of the two additional sinusoidal signals used to account for the stellar activity. The FIES, HARPS, and HARPS-N are corrected for the instrument offsets as derived from the global analysis.

6.2.7   Additional companion

Huang et al. (2016) found that warm Jupiters with low eccentricities ($e \lesssim 0.4$) have inner low-mass companions. They used this evidence as an argument in favour of the *in situ* formation, since the planet migration would have cleaned the warm Jupiter neighbour-hood. We searched the light curve for additional transit signals but found no evidence for an additional transiting planet in the system. The periodogram of the RV residuals show no significant peak with false alarm probability lower than 5 %.

6.2.8   Spot-crossing events

The passage of a planet in front of a spot can be detected as a bump in the transit light curve (see, e.g., Sanchis-Ojeda & Winn, 2011). Spot-crossings events are clearly visible in the EVEREST transit light curves (Fig. 6.8). The same features appear at the same times and with consistent amplitudes in the Vanderburg & Johnson (2014) data, confirming that the bumps are real and not due to systematics. To assess whether the bumps significantly affect the parameter estimates, we performed the joint analysis as described in Sect 6.2.5 including all the transit data points. We found that the final parameters are consistent within 1-σ with those reported in Table 6.3.
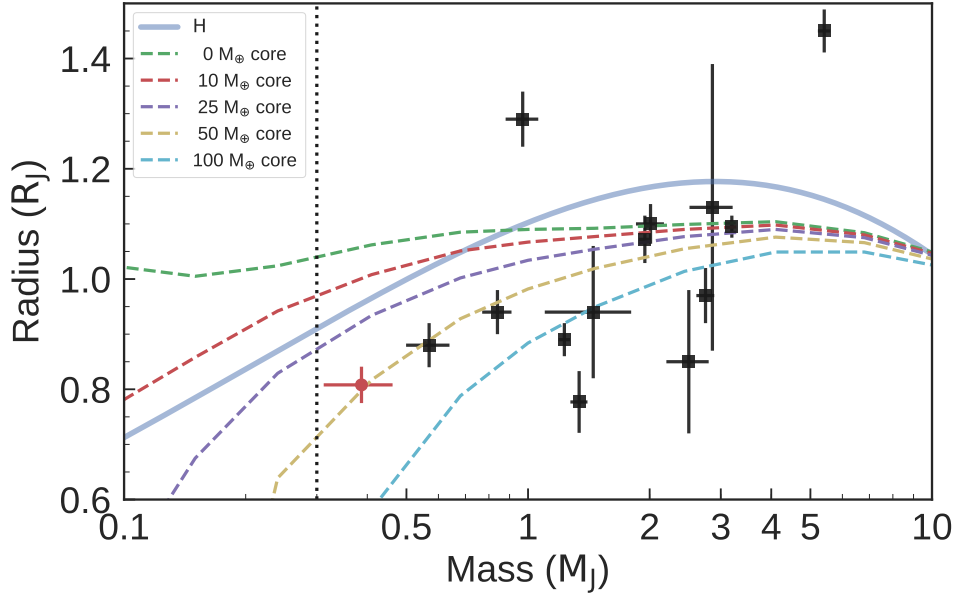
Figure 6.9: Warm Jupiters (black squares; $M_\mathrm{p} \geq 0.3\ M_\mathrm{Jup}$ and $10 \leq P_\mathrm{orb} \leq 100$ days) whose mass and radius have been estimated with a precision of at least 25 % (as of January 2017, exoplanet.eu). K2-139 b is shown with a filled red circle. The solid line corresponds to a planet with a pure hydrogen composition (Seager et al., 2007). The dashed lines represent the Fortney et al. (2007) models for planet core masses of 0, 10, 25, 50 and 100 $M_\oplus$. The vertical dotted line marks the giant planet lower limit as defined by Hatzes & Rauer (2015).

6.2.9 Planet's composition and formation scenario

With a mass of $M_\mathrm{p} = 0.387^{+0.083}_{-0.075}\ M_\mathrm{J}$ and radius of $R_\mathrm{p} = 0.808^{+0.034}_{-0.033}\ R_\mathrm{J}$ (resulting in a mean density of $\rho_\mathrm{p}=0.91^{+0.24}_{-0.20}\ \mathrm{g\,cm^{-3}}$), K2-139 b joins the small group of well characterised warm Jupiters. Fig. 6.9 shows the position of K2-139 b in the mass-radius diagram for warm Jupiters ($M_\mathrm{p} \geq 0.3\ M_\mathrm{Jup}$; $10 \leq P_\mathrm{orb} \leq 100$ days) whose mass and radius have been determined with a precision better than 25 % (14 objects). Notably, K2-139 b is the transiting warm Jupiter with the lowest mass known to the date in which the discovery was announced, if the definition of giant planets given by Hatzes & Rauer (2015) is adopted. Fig. 6.9 displays also the planetary models of Fortney et al. (2007) for different core masses and age between 1.0 and 4.5 Gyrs. The planet radius of K2-139 b can be explained if the planet has a core[4] of $49^{+19}_{-17}\ M_\oplus$, containing $\sim$40 % of the total planetary mass. We expect that K2-139 b has a solid core surrounded by a gaseous envelope.

Rafikov (2006) found that a core of mass $5-20\ M_\oplus$ at a semi-major axis between 0.1 and 1.0 AU would be able to start the runaway accretion phase to form a gas giant planet *in situ*. However, according to his models, these kind of cores are unlikely to form, owing to the high irradiation coming from the star. Boley et al. (2016) suggested instead that more massive cores ($M_\mathrm{core} \gtrsim 20 M_\oplus$) can be built up from the merging of tightly packed inner planets formed at the early stages of the circumstellar disc. Batygin et al. (2016) found a similar result and argued that the massive core of HD 149026b ($M_\mathrm{core} \approx 100 M_\oplus$) could be explained by one or more super-Earths which merged and accreted the surrounding gas to form a gas-giant planet. Huang et al. (2016) suggested that these cores can initiate runaway accretion if they are formed in a region with enough gas around them, while those without enough volatiles remain super-Earths and represent the population of massive rocky planets unveiled by *Kepler* around solar-like stars (e.g., Demory, 2014). Based on

---

[4]Calculated by interpolating Fortney et al. (2007)'s models.

these studies and given the semi-major axis of $0.179^{+0.021}_{-0.027}$ AU, the $48 \pm 14\,M_{\oplus}$ core of K2-139 b could have formed the planet *in situ*. We note that the metallicity of K2-139 is relatively high ([Fe/H] $= 0.21 \pm 0.05$), suggesting that the primordial circumstellar disc had a relatively high content of dust, which would have enhanced the formation of the core of K2-139 b (see, e.g. Johnson & Li, 2012). Alternatively, the planet might have formed beyond the snow line and migrated inwards via planet-disc interaction (see, e.g., Baruteau et al., 2014).

6.2.10 Orbit inclination

The spin-orbit angle, i.e., the angle between the spin axis of the star and the angular momentum vector of the orbit, can provide us with valuable information on the migration mechanisms of exoplanets (see, e.g. Albrecht et al., 2012; Gandolfi et al., 2012; Morton & Johnson, 2011; Winn, 2010). Currently, there are only 4 warm Jupiters ($M_{\mathrm{p}} \geq 0.3\,M_{\mathrm{Jup}}$ and $10 \leq P_{\mathrm{orb}} \leq 100$ days) with measured obliquity[5]. From this perspective, K2-139 is an ideal target to measure the sky-project spin-orbit angle via observations of the Rossiter-McLaughlin (RM) effect. Assuming spin-orbit alignment, the expected amplitude of the RM anomaly is $\Delta \mathrm{RV} \approx \sqrt{1 - b^2}\,(R_{\mathrm{p}}/R_{\star})^2\,v \sin i_{\star} \approx 25\,\mathrm{m\,s^{-1}}$ (Winn, 2010). Given the brightness of the host star ($V = 11.653$ mag), this amplitude can easily be measured using state-of-the-art spectrographs such as HARPS@ESO-3.6m. Moreover, the transit duration ($\sim$5 hours) is shorter than the visibility of K2-139, which is $\sim$9 hours from La Silla observatory (altitude higher than 30 deg above the horizon).

Alternatively, the spin-orbit angle could be measured from the analysis of the spot-crossing events as described in Sanchis-Ojeda et al. (2011) and Sanchis-Ojeda et al. (2012). Anomalies ascribable to the passage of K2-139 b in front of stellar spots are visible in the 3 transit light curves observed by *K2*. Unfortunately, the limited number of transits and the *K2* long cadence data do not allow us to perform a meaningful quantitative analysis of the spot-crossing events. Given the amplitude of the detected anomalies ($\sim$0.1 %), space-based high-precision photometry is needed to detect the spot-crossing events. Observations performed with the upcoming CHaracterising ExOPlanets Satellite (CHEOPS; Broeg et al., 2013) would allow us to photometrically determine the spin-orbit angle of this system.

---

[5]Source: http://www2.mps.mpg.de/homes/heller/content/main_HRM.html, as of January 2017.

6.3   K2-141 b: A lava world with a "short year"

We announced the discovery and characterisation of K2-141 b in Barragán et al. (2018b). This paper is part of a series of *K2* exoplanet characterisations made by the KESPRINT consortium. K2-141 b is an ultra-short-period super-Earth on a 6.7-hour orbit transiting an active K7 V star based on data from *K2* campaign 12. We confirmed the planet's existence and measured its mass with a series of follow-up observations: seeing-limited MuSCAT imaging, NESSI high-resolution speckle observations, and FIES and HARPS high-precision radial-velocity monitoring. K2-141 b has a mass of $M_\mathrm{p} = 5.31 \pm 0.46\ M_\oplus$ and radius of $R_\mathrm{p} = 1.54^{+0.10}_{-0.09}\ R_\oplus$, yielding a mean density of $\rho_\mathrm{p} = 8.00^{+1.83}_{-1.45}\ \mathrm{g\,cm^{-3}}$ and suggesting a rocky-iron composition. Models indicate that iron cannot exceed $\sim$70% of the total mass. With an orbital period of only 6.7 hours, K2-141 b is the shortest-period planet known to date (October 2017) with a precisely determined mass.[6]

6.3.1   Detection

The search for planet candidates for *K2*'s Campaign 12 is the same approach described in Dai et al. (2017). This approach showed that the light curve of EPIC 246393474 (hereafter K2-141) shows significant periodic transit-like signal with a depth of $\sim$0.04% occurring every 0.28 days (6.7 hours). We searched for additional transiting planets in the system by re-running the BLS algorithm after removing the data within 1.5 hours of each transit of planet b. No transit signal was detected: the maximum SDE of the new BLS spectrum was 4.5. A visual inspection of the light curve did not reveal any additional transits, either. The target passed standard tests used to detect false positives due to eclipsing binaries: we did not detect any secondary eclipses or alternation of eclipse depths.

We show the *K2* light curve of K2-141 in Fig. 6.10. The *K2* light curve of K2-141 shows quasi-periodic variations with a peak-to-peak amplitude of about $\sim$1%, very likely the result of rotation and active regions on the host star. Using the auto-correlation method applied to the out-of-transit *K2* light curve (McQuillan et al., 2014), we measured a stellar rotation period of $P_\mathrm{rot} = 14.03 \pm 0.09$ days.

6.3.2   Ground-based photometric observations

Diffraction-limited imaging

On the night of August 9, 2017, UT, we conducted speckle imaging observations of the star K2-141 with the NASA Exoplanet Star and Speckle Imager (NESSI; Scott et al., 2017, PASP, in prep.), a new instrument for the WIYN 3.5 meter telescope, which uses high-speed electron-multiplying CCDs (EMCCDs) to capture sequences of 40 ms exposures simultaneously in two bands. We also observed nearby point source calibrator stars close in time to the science target. We observed simultaneously in the "blue" band centred at 562 nm with a width of 44 nm and the "red" band centred at 832 nm with a width of 40 nm. The pixel scales of the "blue" and "red" EMCCDs are 0.0175649 and 0.0181887 ″/pixel, respectively. The data reduction followed the same procedures described by Howell et al. (2011). Using the point source calibrator images, we computed reconstructed 256×256 pixel images in each band, corresponding to $4.6'' \times 4.6''$. No secondary sources were detected in the reconstructed images (see Fig. 2 of Barragán et al., 2018b). We measured the background sensitivity of the reconstructed images using a series of concentric annuli centred on the target star, resulting in 5σ sensitivity limits (in delta-magnitudes) as a function of angular separation.

---

[6] K2-141 b has also been independently discovered, confirmed, and characterised by Malavolta et al. (2018). Their results are in very good agreement with ours.
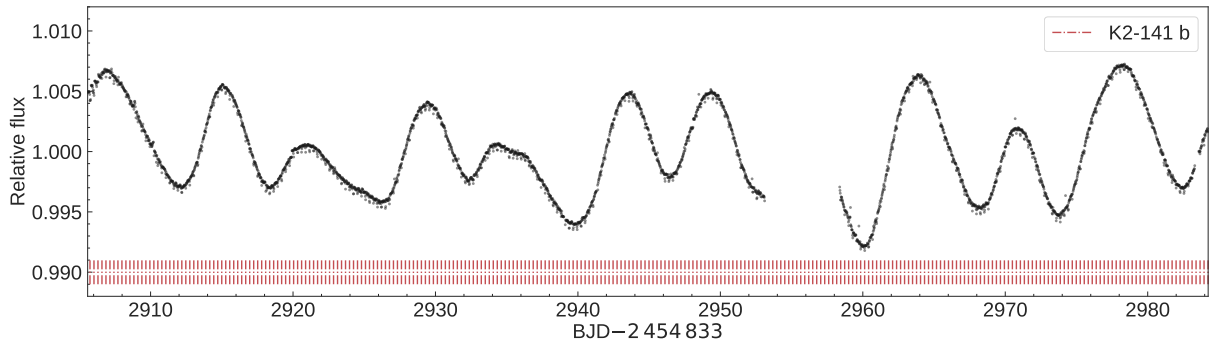
Figure 6.10: *K2* light curve of K2-141. Stellar activity is seen as the quasi-periodic, long period modulation. Transit positions are marked with red dash-doted vertical lines. The 5.3-day-long data gap, during which the telescope entered safe mode, is clearly visible at approximately two thirds of the way through the time series.

Seeing-limited imaging

In order to search for sources outside of the $4.6'' \times 4.6''$ field-of-view of our high-resolution NESSI images, but within the $16''$–wide circular aperture used to extract the light curve from the *K2* pixel files, we also obtained seeing-limited multi-band optical images using the MuSCAT (Narita et al., 2015) instrument on the 1.88m telescope at the Okayama Astrophysical Observatory. The pixel scale of MuSCAT's CCDs is $0.36''$/pixel. The instrument can observe in Sloan g'_2, r'_2, and $z_{s,2}$ bands simultaneously. The observations were performed on September 23, 2017 UT with seeing of $\sim$1.5$''$. To keep the peak count level at about 45,000 ADU, we took ten exposures of 15, 4, and 12 sec with the g'_2, r'_2, and $z_{s,2}$ bands, respectively. The frames were dark-subtracted and flat-fielded using standard routines. The five best on-focus frames were stacked together for each band.

We detected a companion located at 12.6 arcsec towards the East of K2-141. MuS-CAT's images show that this target is about 7.8 mag fainter than K2-141 (from the weighted averaged of the g'_2 and r'_2 filters). This accounts for a contamination factor of 1/1400 of the target brightness. This value does not have a measurable impact on the derived parameters.

6.3.3 High-precision Doppler observations

We obtained nine high-resolution spectra on five different nights with the FIES spectrograph (see Sect. 4.3.1), from August 15 to September 14, 2017, UTC, within observing programs 55-019, 55-202, and 55-206. Since the 6.7-hour period is short enough to allow a significant fraction of the orbit to be sampled in one night, we obtained two spectra per night during three of the five FIES observing nights. The reduction procedures are similar to the ones described in Sect. 4.3.1.

We also acquired 27 spectra with the HARPS spectrograph as part of the observing program 099.C-0491. We adopted the same observing strategy as the FIES observations, acquiring between two and five spectra per night on seven different nights, from August 19 to 27, 2017, UTC. We reduced the data using the dedicated off-line HARPS pipeline and extracted the RVs via cross-correlation with a K5 numerical mask.

The full set of RV data are listed in Barragán et al. (2018b) and they are accessible via the CDS portal at http://cdsarc.u-strasbg.fr/viz-bin/qcat?J/A+A/612/A95.

6.3.4   Stellar fundamental parameters

We derived the spectroscopic parameters of K2-141 from the co-added HARPS spectrum, which has a S/N per pixel of ∼250. The details about the spectral analysis are described in Barragán et al. (2018b). We report the adopted effective temperature $T_{\rm eff}$, iron abundance [Fe/H], and projected velocity $v \sin i_\star$ in Table 6.4. The stellar radius and surface gravity were re-determined using a different method, as described in the next paragraphs.

We derived the stellar radius $R_\star$ and reddening $A_{\rm v}$ using the K2-141's spectral energy distribution as described in (Gandolfi et al., 2008). Adopting the extinction law of Cardelli et al. (1989) and assuming a total-to-selective extinction of $R = A_{\rm v}/E_{B-V} = 3.1$, we found that the interstellar reddening is consistent with zero ($A_{\rm v} = 0.01 \pm 0.02$ mag). Using the distance of d $= 58.77 \pm 0.81$ pc from the *Gaia*'s first data release (Gaia Collaboration et al., 2016), we determined a stellar radius of $R_\star = 0.674 \pm 0.039\, R_\odot$.

We finally converted $T_{\rm eff}$, $R_\star$, and [Fe/H] into stellar mass $M_\star$ and surface gravity $\log g_\star$ using the empirical relations derived by Torres et al. (2010) coupled to Monte Carlo simulations. K2-141 is a K7 V star (Pecaut & Mamajek, 2013) with an effective temperature of $T_{\rm eff} = 4373 \pm 57$ K, a photospheric iron abundance of [Fe/H] $= +0.03 \pm 0.10$ dex, a mass of $M_\star = 0.662 \pm 0.022\, M_\odot$, and a radius of $R_\star = 0.674 \pm 0.039\, R_\odot$, yielding a surface gravity of $\log g_\star = 4.584 \pm 0.051$ (cgs). The final adopted values are given in Table 6.4. We used gyrochronology to estimate the age of K2-141 from the relations by Angus et al. (2015) and found 740 ± 360 Myr, suggesting that the star might be relatively young (Table 6.4).

6.3.5   Stellar activity and frequency analysis of the HARPS data

K2-141 is an active star. As presented in Sect. 6.3.1, the *K2* light curve of K2-141 displays quasi-periodic modulation with a peak-to-peak amplitude of about 1% (Fig. 6.10). The photometric variability is very likely caused by active regions (spots, faculae, and plages) carried across the visible hemisphere of the stellar disc as the star spins about its axis. This is corroborated by the detection of strong emission components in the cores of the Ca II H & K lines (see Fig. 4 of Barragán et al., 2018b), from which we derived an average S-index of 0.938 ± 0.074, indicative of a high level of magnetic activity.

The magnetic activity of K2-141 is expected to produce quasi-periodic signals in time-series RV data, commonly referred to as "stellar jitter". We used the code `SOAP2` (Dumusque et al., 2014) to estimate the RV variation induced by stellar activity. From the amplitude of the photometric variability, the spectroscopic parameters, and the rotation period of the star, we calculated an expected RV semi-amplitude variation of ∼5-10 m s^{-1}.

We performed a frequency analysis of our RV measurements to look for the signature of the transiting planet and search for possible activity-induced signals. For this purpose, we did not include the FIES RVs because of the higher uncertainties, the relatively small number of data points, and the need to account for an offset between the FIES and HARPS data-sets. The analysis was done using `Period04` (Lenz & Breger, 2004). A discrete Fourier transform (DFT) analysis of the HARPS RV measurements shows a peak at 3.57 c/d, that is, the orbital frequency of K2-141 b (0.28 days) with an amplitude of (∼7 m s^{-1}).

An additional trend is visible in the RV data after the signal of the transiting planet has been subtracted from the HARPS measurements. We found a Spearman's rank correlation coefficient of -0.80 with a p-value of 1.4×10^{-6}, strongly suggesting the existence of an additional source of RV variation in our data[7]. To assess if the source of this additional

---

[7]Following Fisher (1925), we adopted a significance level of $p = 0.05$.

signal is induced by stellar activity, we looked for possible correlations between the RV residuals and the activity indexes, namely, the Ca II H & K S-index, and the FWHM and bisector span (BIS) of the cross-correlation function (see Fig. 6 of Barragán et al., 2018b). Although the RV residuals and the BIS do not show a significant anti-correlation (-0.30 with $p = 0.13$), we found significant correlations between the RV residuals and the FWHM (0.73 with $p = 3.3 \times 10^{-5}$), and the RV residuals and the S-index (0.72 with $p = 4.8 \times 10^{-5}$). We concluded that the long-term trend observed in the HARPS data is likely caused by the presence of active regions on the photosphere of the star. We will present our approach to filtering out the stellar jitter in Section 6.3.6.

6.3.6 Data analysis and results

In order to arrive at a robust measurement of the planetary mass despite the additional RV variations induced by stellar activity (see Sect. 6.3.5), we used three different approaches to fit the data as described below.

Floating chunk offset method

The first method (hereafter M1) is based on the floating chunk offset (FCO) technique pioneered by Hatzes et al. (2011, see Appendix B), which works well when the orbital period is much shorter than the timescales associated with the signals induced by stellar activity and any additional planets (A description of the method is given in Sect. B). From this point of view, K2-141 b is an ideal target to apply the FCO method and remove long-term signals coming from outer companions and stellar activity (see, e.g., Hatzes et al., 2011; Gandolfi et al., 2017). Our observing strategy was tailored to use this technique by acquiring multiple spectra per night (Sect. 6.3.3).

We performed a Markov chain Monte Carlo (MCMC) joint analysis of the transit and RV data using the code `pyaneti` (Barragán et al., 2019, see Sect. 5.3). We fitted a Keplerian orbit to the RV data and used the limb-darkened quadratic model by Mandel & Agol (2002) for the transit light curves. We integrated the light curve model over ten steps to account for the *Kepler* long-cadence observation (Kipping, 2010, see Appendix A.2). We used flat uniform priors for all parameters. Details are given in Table 6.4. We explored the parameter space with 500 Markov chains to generate a posterior distribution of 250,000 independent points for each parameter. The inferred parameter value and its uncertainty is given by the median and 68.3% credible interval of the posterior distribution. We did not account for additional jitter terms because $\chi^2/\text{dof} \approx 1$.

When fitting for an eccentric orbit, the posterior distribution of the eccentricity has a median of 0.06 and a 99%-confidence upper limit of 0.20. The Bayesian Information Criterion (BIC) favours a circular orbit with a $\Delta\,\text{BIC} = 8$. Our result is consistent with a circular orbit, as expected for a planet with such a short period. All further analyses were carried out fixing the orbit to be circular.

The inferred single-planet model together with the RV time-series following the subtraction of the offset for each night is shown in Fig. 6.11. This figure shows how the FCO method removes the activity, yielding only the RV signal induced by the planet. We measured a Doppler semi-amplitude of 6.74 ± 0.56 m s^{-1}, which corresponds to a mass of $5.31 \pm 0.46\ M_\oplus$.

Sinusoidal activity signal modelling

In the second method (hereafter M2), the RV signal associated with stellar activity is modelled as a coherent sinusoidal signal (e.g., Pepe et al., 2013; Barragán et al., 2018a,

see also Appendix. B). The *K2* light curve shows the presence of long-lived active regions whose evolution time scale is longer that the rotation period of the star. Since our RV follow-up lasted only ∼30 days, that is, two stellar rotation periods, we can reasonably assume that the activity-induced RV signal remained coherent within our observing window.

For this method we used `pyaneti` and performed an MCMC analysis similar to M1. To account for the activity-induced signal at the rotation period of the star, we included an additional sinusoidal signal whose period was constrained with a Gaussian prior centred at $P_{\rm rot} = 14.03$ d with a standard deviation of 0.09 d (see Sect. 6.3.5). For the phase and amplitude of the activity signal we adopted uniform priors.

We first performed a fit including only the planetary signal. This analysis produces a RV $\chi^2/$dof ≈ 5. When including the extra sinusoidal signal, M2 gives an RV $\chi^2/$dof ≈ 1.3 and a Δ BIC $= 130$ over the previous model. This further proves that RV data cannot be explained by only the planetary signal (cfr. Sect. 6.3.5). To account for imperfect treatment of the activity-induced variation, we added RV jitter terms to the equation of the likelihood for the FIES and HARPS RV data.

The final inferred Doppler amplitude induced by stellar activity is $5.05^{+0.72}_{-0.66}$ m s^{-1}, which agrees with the prediction made with `SOAP2` (Sect. 6.3.5). The RV semi-amplitude variation induced by the planet is 6.71 ± 0.63 m s^{-1}, which translates to a planetary mass of 5.23 ± 0.50 $M_{\oplus}$. Figure 6.11 displays the two-signal model together with the RV measurements for both instruments following the subtraction of the instrumental offsets.

Gaussian process

The third method (hereafter M3) models the correlated noise associated with stellar activity with a Gaussian Process (GP); GP describes stochastic processes with a parametric description of the covariance matrix. GP regression has proven to be successful in modelling the effect of stellar activity for several other exoplanetary systems (see, e.g., Haywood et al., 2014; López-Morales et al., 2016, see Appendix B).

We used the same GP model that was described in detail by Dai et al. (2017). The list of parameters includes the RV semi-amplitude K, the orbital period $P_{\rm orb}$ and the time of conjunction $t_{\rm c}$. The model also includes the so-called hyperparameters of the quasi-periodic kernel: the covariance amplitude h, the correlation timescale τ, the period of the covariance T, and Γ which specifies the relative contribution between the squared exponential and periodic part of the kernel.

We sampled the parameter posterior distribution with MCMC using the procedure described in Dai et al. (2017). The RV semi-amplitude for planet b was found to be $6.48^{+0.73}_{-0.71}$ m s^{-1}. This translates into a planetary mass of $5.05^{+0.57}_{-0.55}$ $M_{\oplus}$. Fig. 6.11 shows the measured RV variation of K2-141 and the GP model. We found that the amplitude of the correlated noise is $h_{\rm rv} = 4.0^{+2.2}_{-1.2}$ m s^{-1}, which agrees with the value inferred by M2 and `SOAP2`.

6.3.7   K2-141 b mass and radius

The three techniques used to determine the mass of K2-141 b give results that are consistent to within $\sim 0.5\sigma$. While we have no reason to prefer one method over the other, we adopted the results of M1 (FCO method), which gives a planetary mass of $M_{\rm p} = 5.31 \pm 0.46$ $M_{\oplus}$ ($\sim 11\sigma$ significance). Figure 6.12 shows the posterior distributions calculated with `pyaneti` for the fitted parameters. The parameter estimates are given in Table 6.4. Figure 6.13 displays the *K2* and RV measurements along with the inferred transit and Keplerian models from the FCO method folded to the orbital period of the planet.
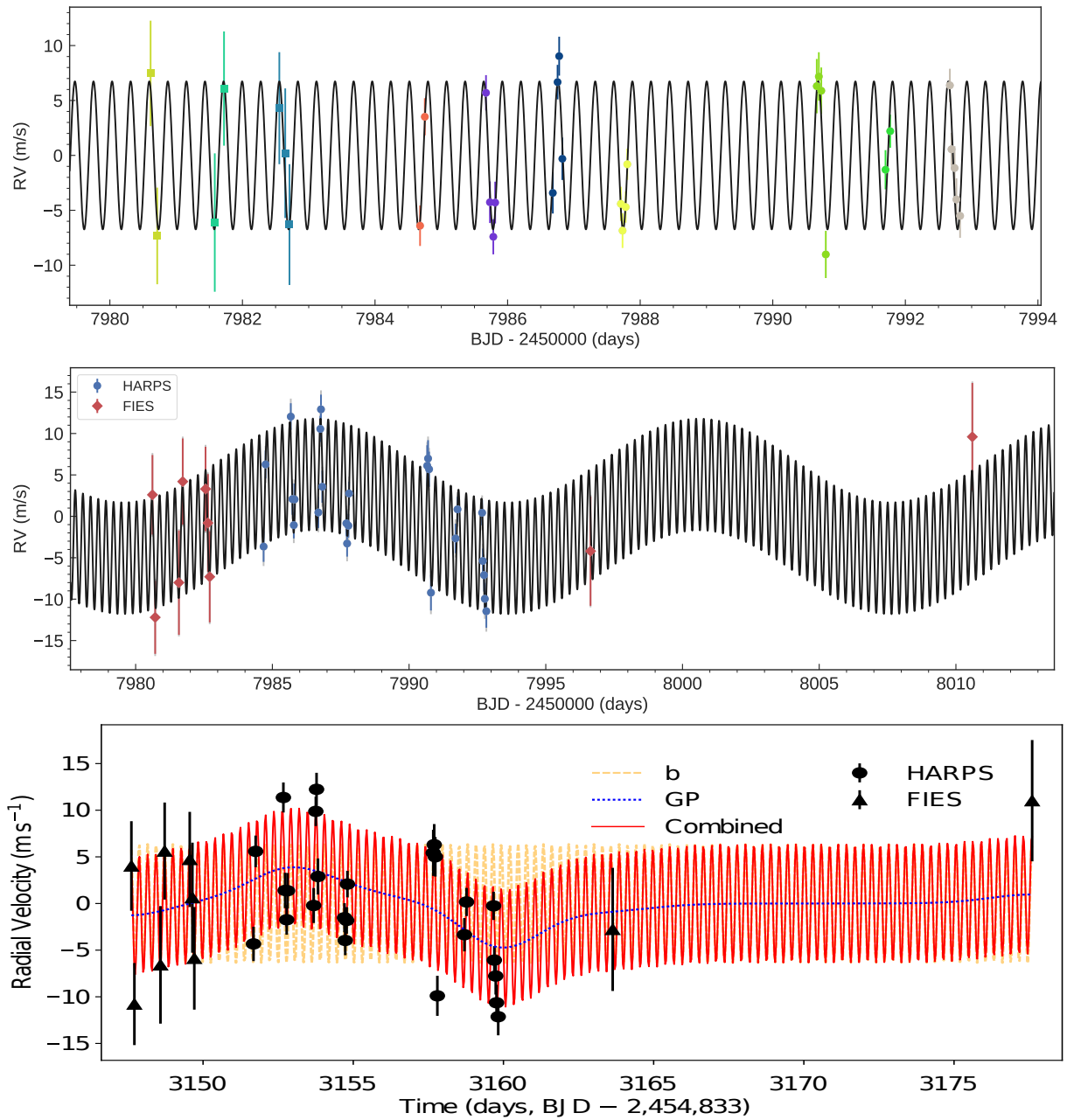
Figure 6.11: *Upper panel*: RV curve of K2-141 as obtained using the FCO method. The best fitting circular solution is marked with a solid black line. HARPS and FIES data are shown with filled circles and squares, respectively. Different colours refer to different nights. *Middle panel:* HARPS (blue circles) and FIES (red diamonds) measurements for K2-141 following the extraction of the instrumental offsets. The inferred RV model (black solid lines) was obtained from the planet signal plus a coherent sinusoidal signal which accounts for the stellar activity. *Lower panel:* The measured radial velocity variation of K2-141 from HARPS (circles) and FIES (triangles). The red solid line is the best-fit model including the signal of planet b and the GP model of the correlated stellar noise. The yellow dashed line shows the signal of planet b. The blue dotted line shows the GP. This plot was created by F. Dai (see Barragán et al., 2018b).
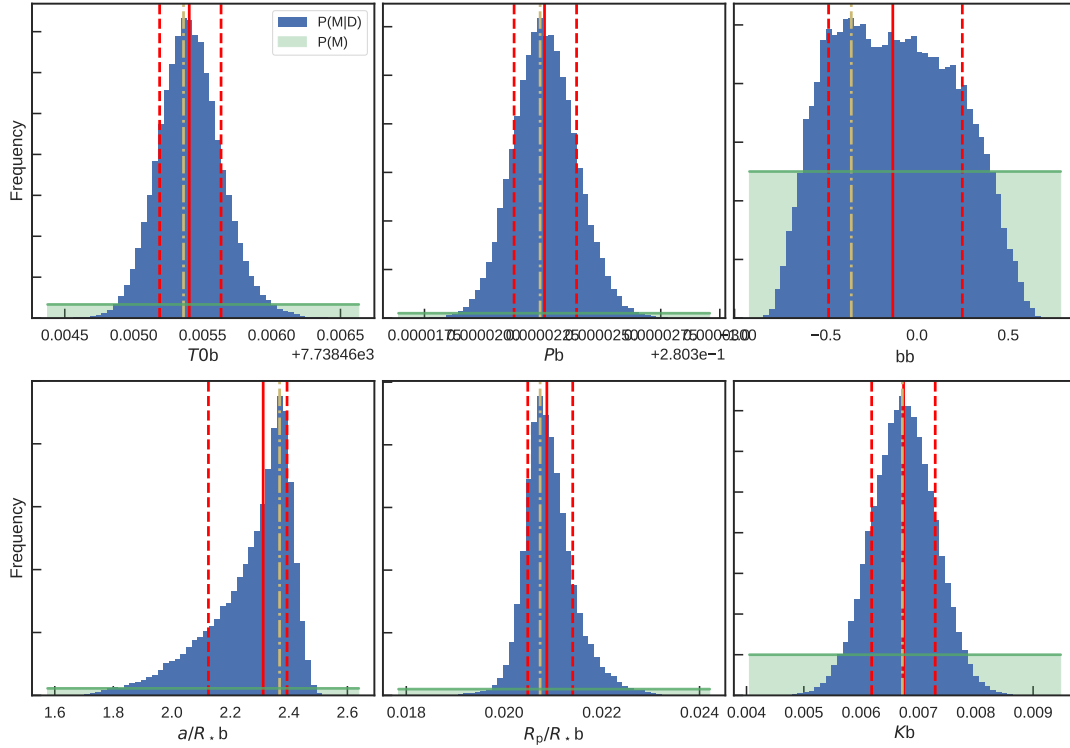
Figure 6.12: Posterior distributions of the K2-141's fitted parameters as obtained using the code `pyaneti`. The posterior distributions of the night offsets are not shown. The blue region corresponds to the posterior $P(M|D)$, whereas the green shaded area marks the prior shape $P(M)$. Median (red solid line), 68% credible interval (red dashed line) and mode (yellow dash-dotted line) are also shown.
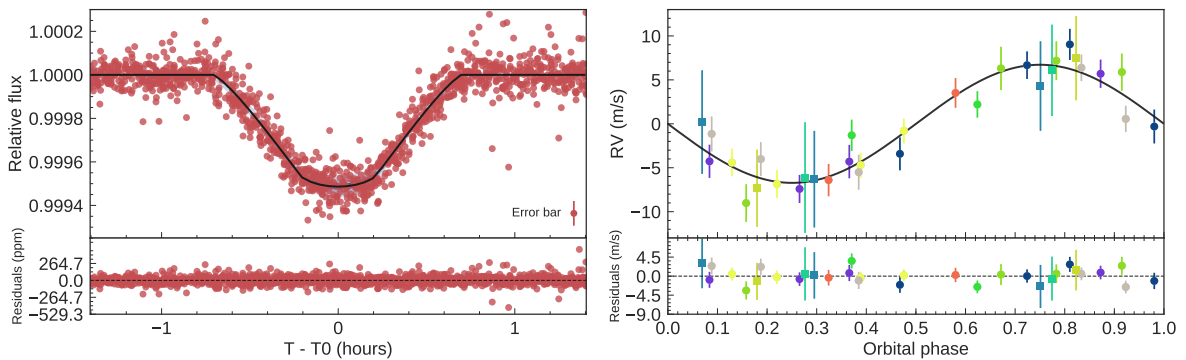
Figure 6.13: *Left panel.* Transit light curve folded to the orbital period of K2-141 b and residuals. The red points mark the *K2* data, whereas the thick black line the re-binned best-fitting transit model. *Right panel.* Phase-folded RV curve of K2-141 folded to the orbital period of the planet, as obtained using the FCO method. The best fitting circular solution is marked with a solid black line. HARPS and FIES data are shown with filled circles and squares, respectively. Different colors refer to different nights. The lower panel shows the residuals to the best fitting model.

Table 6.4: Stellar and planetary parameters.

Parameter	Prior[a]	Final value
Stellar parameters		
Star mass $M_\star$ ($M_\odot$)	$\cdots$	0.662 ± 0.022
Star radius $R_\star$ ($R_\odot$)	$\cdots$	0.674 ± 0.039
Stellar density $\rho_\star$ (g cm^{-3})	$\cdots$	$3.05^{+0.61}_{-0.48}$
Stellar density $\rho_\star$ (from light curve, g cm^{-3})	$\cdots$	$2.98^{+0.33}_{-0.67}$
Effective Temperature T_{eff} (K)	$\cdots$	4373 ± 57
Surface gravity $\log g_\star$ (cgs)	$\cdots$	4.584 ± 0.051
Iron abundance [Fe/H] (dex)	$\cdots$	0.03 ± 0.10
Projected rotational velocity $v \sin i_\star$ (km s^{-1})	$\cdots$	3.0 ± 1.7
Rotational period P_{rot} (days)	$\cdots$	14.03 ± 0.09
Gyrochronological age (Myr)	$\cdots$	740 ± 360
Interstellar extinction A_{V} (mag)	$\cdots$	0.01 ± 0.02
Star distance d (pc)	$\cdots$	58.77 ± 2.81
Model Parameters		
Orbital period P_{orb} (days)	$\mathcal{U}[0.2802, 0.2804]$	0.2803226 ± 0.0000013
Transit epoch T_0 (BJD$_{\mathrm{TDB}} - 2\,450\,000$)	$\mathcal{U}[7738.45, 7738.47]$	$7738.46540^{+0.00023}_{-0.00021}$
Scaled semi-major axis $a/R_\star$	$\mathcal{U}[1.1, 20]$	$2.31^{+0.08}_{-0.19}$
Scaled planet radius $R_{\mathrm{p}}/R_\star$	$\mathcal{U}[0.0, 0.1]$	$0.02088^{+0.00053}_{-0.00039}$
Impact parameter, b	$\mathcal{U}[-1, 1]$	$-0.01^{+0.38}_{-0.35}$
$\sqrt{e}\sin \omega_\star$	$\mathcal{F}[0]$	0
$\sqrt{e}\cos \omega_\star$	$\mathcal{F}[0]$	0
Parameterized limb-darkening coefficient q_1	$\mathcal{U}[0, 1]$	$0.54^{+0.29}_{-0.25}$
Parameterized limb-darkening coefficient q_2	$\mathcal{U}[0, 1]$	$0.29^{+0.32}_{-0.19}$
Doppler semi-amplitude variation K (m s^{-1})	$\mathcal{U}[0, 50]$	6.74 ± 0.56
Derived Parameters		
Planet mass M_{p} ($M_\oplus$)	$\cdots$	5.31 ± 0.46
Planet radius R_{p} ($R_\oplus$)	$\cdots$	$1.54^{+0.10}_{-0.09}$
Planet density ρ_{p} (g cm^{-3})	$\cdots$	$8.00^{+1.83}_{-1.45}$
Semi-major axis of the planetary orbit a (AU)	$\cdots$	$0.00716^{+0.00055}_{-0.00065}$
Eccentricity e	$\cdots$	0
Orbit inclination along the line-of-sight i_{p} ($^\circ$)	$\cdots$	90 ± 10
Transit duration τ_{14} (hours)	$\cdots$	0.94 ± 0.02
Equilibrium temperature[b] T_{eq} (K)	$\cdots$	2039^{+87}_{-48}
Linear limb-darkening coefficient u_1	$\cdots$	$0.43^{+0.27}_{-0.26}$
Quadratic limb-darkening coefficient u_2	$\cdots$	$0.31^{+0.36}_{-0.43}$

Note – [a] $\mathcal{U}[a, b]$ refers to uniform priors between a and b, $\mathcal{F}[a]$ to a fixed a value. [b] Assuming albedo = 0.

The upper left panel of Fig. 6.14 shows the mass-period diagram for all the USP planets with directly measured masses. We included 55 Cnc e, CoRoT-7 b, HD 3167 b, K2-106 b, Kepler-10 b, Kepler-78 b and EPIC 228732031 b (K2-131 b) using the planetary masses and radii reported in the TEPCat database (Southworth, 2011)[8]. With a period of 0.28 d (6.7 h), K2-141 b is the shortest-period planet with a measured mass among all planets known to date. As of October 2017, there are only three transiting exoplanets known to have orbital periods shorter than K2-141 b, namely, Kepler 70 b, KOI-1843 b, and EPIC 228813918 b. However, their masses have not yet been measured. The mass of Kepler 70 b ($P = 0.24$ d; Charpinet et al., 2011) was estimated based on the radius and an assumed mean density. For KOI-1843 b ($P = 0.18$ d), the mass was constrained based on the lower limit of the planet's mean density calculated from the requirement that the planet must orbit outside the star's Roche limit (Rappaport et al., 2013). For EPIC 228813918 b ($P = 0.18$ d) Smith et al. (2017) reported a lower limit for the planetary mass based on Rappaport et al. (2013), as well as a 3σ upper limit based on RV

---

[8]http://www.astro.keele.ac.uk/jkt/tepcat/.
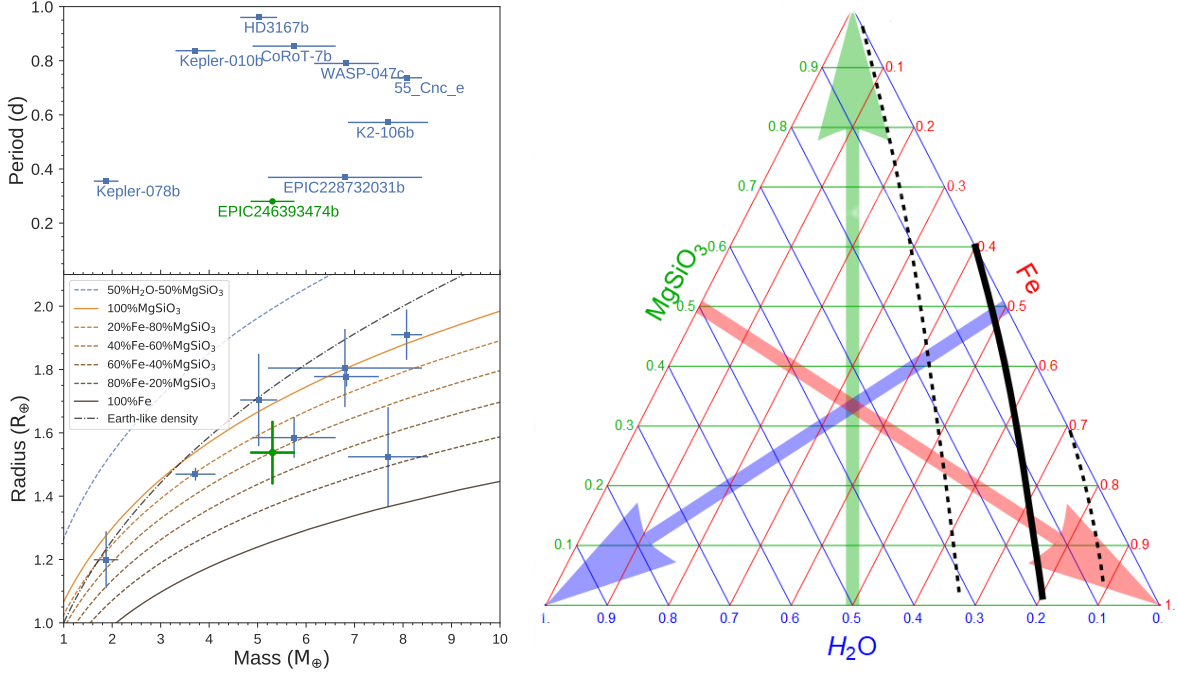
Figure 6.14: Mass-period (*upper left panel*) and mass-radius (*lower left panel*) diagram for USP planets ($P_{orb} < 1$ day, $R_p < 2R_\oplus$) with measured masses. The solid green circle marks the position of K2-141 b. USP planets in the literature are marked with blue squares. The composition models from Zeng et al. (2016) are displayed with different lines and colours. The Earth-like density curve is also shown with a dot-dashed black line. *Right panel:* Ternary plot for different planetary compositions. We show different combinations of water, rock and iron for possible solid planet compositions. The solid and dashed black lines mark the possible position of K2-141 b and the 68 % credible intervals. This plot was created using the applet available at `https://www.cfa.harvard.edu/~lzeng/manipulateplanet.html`.

measurements.

6.3.8   K2-141 b's composition

The mass of $M_p = 5.31 \pm 0.46$ $M_\oplus$ and radius of $R_p = 1.54^{+0.10}_{-0.09}$ $R_\oplus$ yield a mean density of $\rho_p = 8.00^{+1.83}_{-1.45}$ g cm^{-3}. The lower left panel of Fig. 6.14 shows the mass-radius diagram for USP small transiting planets ($P_{orb} < 1$ day, $R_p < 2R_\oplus$), along with Zeng et al. (2016)'s theoretical models for different compositions. Dressing et al. (2015) suggested that planets with masses between 1 and 6 $M_\oplus$ are consistent with a composition of 17% Fe and 83% MgSiO$_3$ (rock). Their sample included three USP planets (Kepler-78 b, Kepler-10 b and CoRoT-7 b), two planets with periods 4.3 and 13.8 days, and the solar system planets Earth and Venus. Figure 6.14 shows a 20% Fe and 80% MgSiO$_3$ composition line, similar to the values found by Dressing et al. (2015). Given its mass and radius, K2-141 b lies close to the 40%Fe-60% MgSiO$_3$ compositional model. Within the 1σ uncertainties, K2-141 b lies between the 20%Fe-80% MgSiO$_3$ and 60%Fe-40% MgSiO$_3$ models. If we consider only the five USP planets with $M_p < 6$ $M_\oplus$, we found that no single theoretical curve is consistent with them all. At face value this shows that there is some dispersion in the composition of USP planets.

We further inferred the composition of K2-141 b using a ternary plot (right panel of Figure 6.14) for planetary compositions comprising different abundances of H$_2$O, MgSiO$_3$ and Fe (Zeng & Sasselov, 2013; Zeng et al., 2016). The dashed lines mark the allowed region for K2-141 b, given the 1σ uncertainty on the planetary mass and radius. We first analysed a water-free model (right-hand side of the triangle). If the planet does not

contain H_2O, K2-141 b has a composition comprising $\sim$5-70% iron and $\sim$30-95% rocks. If the planet does contain H_2O, then the maximum water abundance (1σ upper limit) cannot exceed $\sim$30% of the total mass.

Rappaport et al. (2013) pointed out that for planets with orbital periods $\lesssim 6$ h, the mere requirement that the planet is outside the Roche limit leads to an astrophysically relevant lower limit on the planet's mean density. Assuming a constant density, a planet with a period of 6.7 h would need a minimum density of $\sim 3.5\,\mathrm{g\,cm^{-3}}$ to avoid tidal destruction by the star. This value is smaller than K2-141 b's density lower limit of $5.2\,\mathrm{g\,cm^{-3}}$. In this case the RV data are more powerful than the Roche-limit consideration, for determining the planet's composition.

6.3.9   K2-141b in the radius gap

According to the theoretical models, the radius gap found by Fulton et al. (2017) is caused by photo-ionising radiation (see Sect., 1.5.3). In this context, K2-141 b receives a stellar radiation of about 2900 $F_{\oplus}$ (where $F_{\oplus}$ refers to insolation received on Earth), which is more than four times the threshold of 650 $F_{\oplus}$ needed for planets to undergo photo-evaporation of H/He envelopes (Lundkvist et al., 2016). This implies that if K2-141 b had an atmosphere, it was lost due to the vicinity to its host star.

6.4 K2-111 b: A very old world

Fridlund et al. (2017) reported the validation and characterisation of a transiting super-Earth around the star EPIC 210894022 (K2-111), that was observed by *K2* in its Campaign 4. By combining the *K2* photometry with high-spatial resolution imaging and high-precision RV measurements, we confirmed that the transit signal is caused by a super-Earth orbiting the star K2-111. The planet has a mass of $M_{\rm p} = 8.6 \pm 3.9\ M_{\oplus}$ and radius of $R_{\rm p} = 1.92^{+0.21}_{-0.20}\ R_{\oplus}$. A second more massive object with a period longer than about 120 days is indicated by a long term radial velocity drift. With an age of $\gtrsim 11$ Gyrs this system is one of the oldest where planets is hitherto detected. Further studies of this planetary system is important since it contains information about the planetary formation process during a very early epoch of the history of our Galaxy.

6.4.1 Light curve and RV data

The *K2* photometry are subsets of the K2-111's light curve extracted by Vanderburg & Johnson (2014). Here we selected ∼7 hours of data points around each of the 13 transits observed by *K2* and de-trended each transit using a second order polynomial fitted to the out-of-transit data points with `exotrending` (Barragán & Gandolfi, 2017, see Appendix A.1). The RV data set includes 6 FIES and 12 HARPS-N measurements presented in Sect. 3.1 of Fridlund et al. (2017).

6.4.2 Joint RV and transit modelling

We performed the joint fit of the photometric and RV data using the code `pyaneti` Barragán et al. (2019). We used the equations of Mandel & Agol (2002) to fit the transit light curves and a Keplerian orbit to model the RV measurements. We adopted a quadratic limb darkening law and followed the parametrization described in Kipping (2013). To account for the *K2* long integration time (∼30 minutes), we integrated the transit models over 10 steps (Kipping, 2010, see Appendix A.2).

We set uniform priors for all the parameters with some exceptions. Given the limited number of available RV measurements and their error bars, we assumed a circular orbit ($e = 0$). The shallow transit and *K2*'s long cadence data do not enable a meaningful determination of the scaled semi-major axis ($a_{\rm p}/R_{\star}$) and limb darkening coefficients u_1 and u_2. We thus set Gaussian priors for the scaled semi-major axis using Kepler's third law and the derived stellar parameters (see Sect. 3.2 of Fridlund et al., 2017). We also used the on-line applet[9] written by Eastman et al. (2013) to interpolate Claret & Bloemen (2011)'s limb darkening tables to the spectroscopic parameters of the host star (see Sect. 3.2 of Fridlund et al., 2017) and set Gaussian priors for the limb darkening coefficients u_1 and u_2 adopting 0.1 conservative error bars. Details about the fitted parameters and priors are given in Table 6.5.

We explore the parameter space with 500 chains created randomly inside the prior ranges. We created a posterior distribution of each parameter with $250,000$ independent data points.

We searched for evidence of an outer companion in the RV measurements by adding a linear trend $\dot{\gamma}$ to the Keplerian model fitted to the RV data. The best fitting solution provide a linear trend of $\dot{\gamma} = -0.217 \pm 0.077\ {\rm m\,s^{-1}\,d^{-1}}$ with a ∼3-σ significance level. The $\ln \mathcal{L}_{\rm RV}$ and ${\rm BIC}_{\rm RV}$ of the models with and without linear trend are 77.6 and -144, and 73.7 and -139, respectively. We therefore conclude that the model with a linear trend is favoured.

---

[9]Available at `http://astroutils.astronomy.ohio-state.edu/exofast/limbdark.shtml`.

Table 6.5: Stellar and planetary parameters.

Parameter	Prior[a]	Final value
Stellar parameters		
Star mass $M_\star$ ($M_\odot$)	$\cdots$	1.0 ± 0.07
Star radius $R_\star$ ($R_\odot$)	$\cdots$	1.4 ± 0.14
Effective Temperature T_{eff} (K)	$\cdots$	4373 ± 57
Model Parameters		
Orbital period P_{orb} (days)	$\mathcal{U}[5.3489, 5.3528]$	5.35117 ± 0.00055
Transit epoch T_0 (BJD$_{\text{TDB}} - 2\,450\,000$)	$\mathcal{U}[7067.9568, 7067.9926]$	$7067.9704^{+0.0044}_{-0.0039}$
Scaled semi-major axis $a/R_\star$	$\mathcal{N}[9.6, 1.0]$	$9.59^{+0.98}_{-0.95}$
Scaled planet radius $R_{\text{p}}/R_\star$	$\mathcal{U}[0.0, 0.1]$	$0.01255^{+0.00050}_{-0.00048}$
Impact parameter, b	$\mathcal{U}[0, 1]$	$0.633^{+0.091}_{-0.128}$
$\sqrt{e}\sin\omega_\star$	$\mathcal{F}[0]$	0
$\sqrt{e}\cos\omega_\star$	$\mathcal{F}[0]$	0
Parameterized limb-darkening coefficient q_1	$\mathcal{N}[0.42, 0.1]$	$0.4240523^{-0.09}_{-0.09}$
Parameterized limb-darkening coefficient q_2	$\mathcal{N}[0.29, 0.1]$	$0.2879764^{+0.09}_{-0.09}$
Doppler semi-amplitude variation K (m s^{-1})	$\mathcal{U}[0, 50]$	3.1 ± 1.4
Radial acceleration $\dot{\gamma}$ (m s^{-1} d^{-1})	$\mathcal{U}[-1, 1]$	-0.217 ± 0.077
Derived Parameters		
Planet mass M_{p} ($M_\oplus$)	$\cdots$	5.31 ± 0.46
Planet radius R_{p} ($R_\oplus$)	$\cdots$	$1.92^{+0.21}_{-0.20}$
Planet density ρ_{p} (g cm^{-3})	$\cdots$	$6.6^{+4.53}_{-3.2}$
Semi-major axis of the planetary orbit a (AU)	$\cdots$	$0.0621^{+0.0092}_{-0.0085}$
Eccentricity e	$\cdots$	0
Orbit inclination along the line-of-sight i_{p} ($^\circ$)	$\cdots$	86.2 ± 1.0
Transit duration τ_{14} (hours)	$\cdots$	0.94 ± 0.02
Equilibrium temperature[b] T_{eq} (K)	$\cdots$	1309^{+71}_{-63}
Linear limb-darkening coefficient u_1	$\cdots$	0.38 ± 0.08
Quadratic limb-darkening coefficient u_2	$\cdots$	0.28 ± 0.08

Note – [a] $\mathcal{U}[a, b]$ refers to uniform priors between a and b, $\mathcal{N}[a, b]$ means Gaussian priors with mean a and standard deviation b and $\mathcal{F}[a]$ to a fixed a value. [b] Assuming albedo $= 0$.

The final parameters are given in Table 6.5. They are defined as the median and 68 % credible interval of the posterior distribution for each parameter. Posterior distributions are shown in Figure 6.15. We show the folded transit light curve, and the RV curves in Figs. 6.16.

6.4.3 Orbital Dynamics

The mass, orbital period and eccentricity of the body responsible for the RV trend can be constrained by requiring that the system is dynamically stable. Bodies too close, too massive, and on too eccentric orbits would result in an unstable system. If the outer body is on a circular orbit, it must be a gas giant planet or more massive, and the system is stable even for stellar-mass companions. If it is on a highly-eccentric orbit, gas giant planets at P ~ 1 yr are ruled out by dynamical stability. In this case, the outer planet may be a lower-mass planet on a close orbit (P ~ 1 yr) or a gas giant on a wider orbit (P $\gtrsim 2$ yr). Note that an eccentric orbit permits lower masses for the outer body, but this requires a specific alignment of the orbit with respect to the observer (edge-on orbit and pericentre pointing along the line of sight). In general, one can also place limits on what additional planets could be in a system between two known ones. For example, if the second planet is a Jupiter at 1 AU on a circular orbit, the separation is roughly 20 mutual Hill radii, meaning that one (or more) additional planets could be accommodated between the two planets.
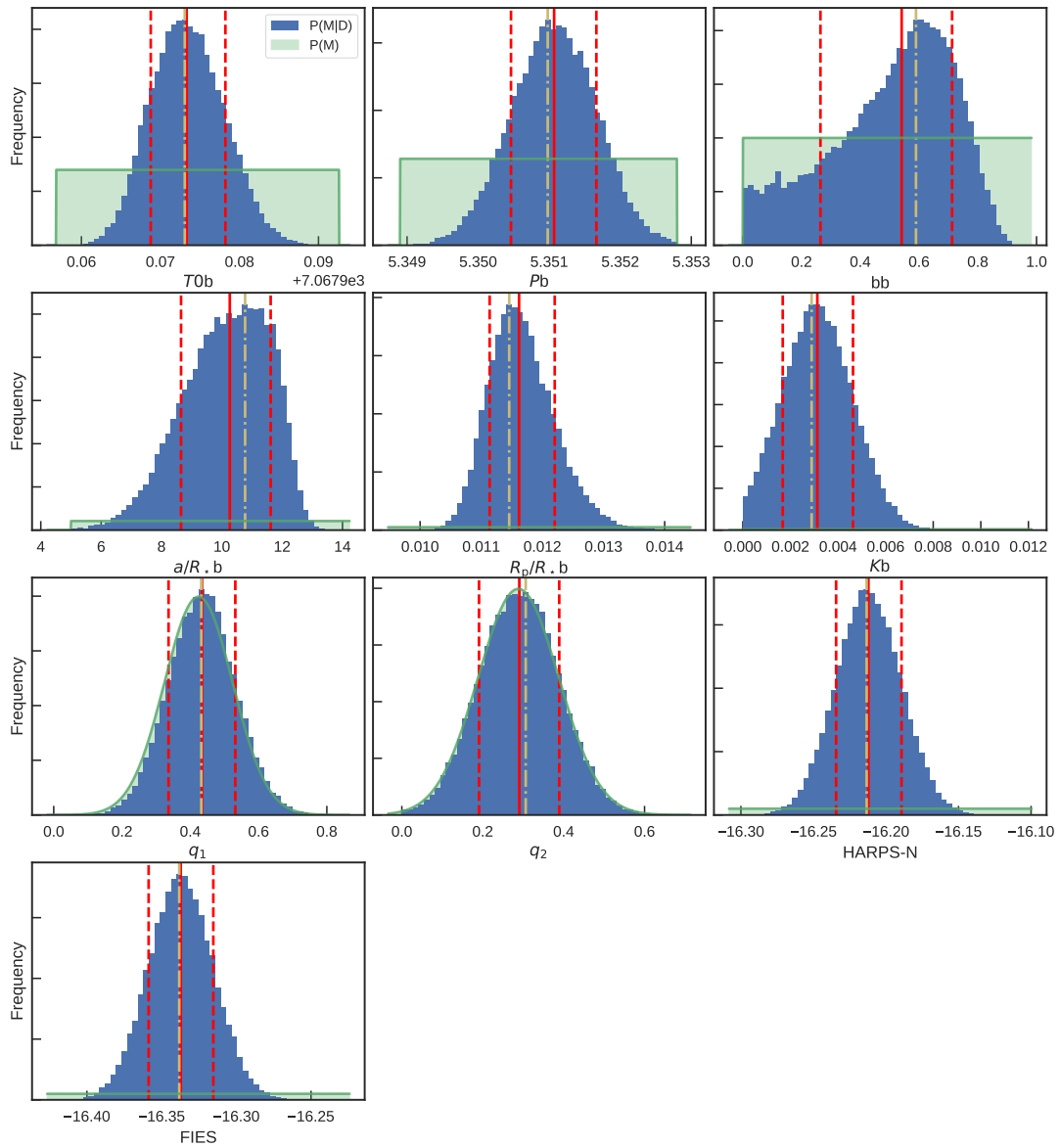
Figure 6.15: Posterior distributions of the K2-111's fitted parameters as obtained using the code `pyaneti`. The blue region corresponds to the posterior $P(M|D)$, whereas the green shaded area marks the prior shape $P(M)$. Median (red solid line), 68% credible interval (red dashed line) and mode (yellow dash-dotted line) are also shown.
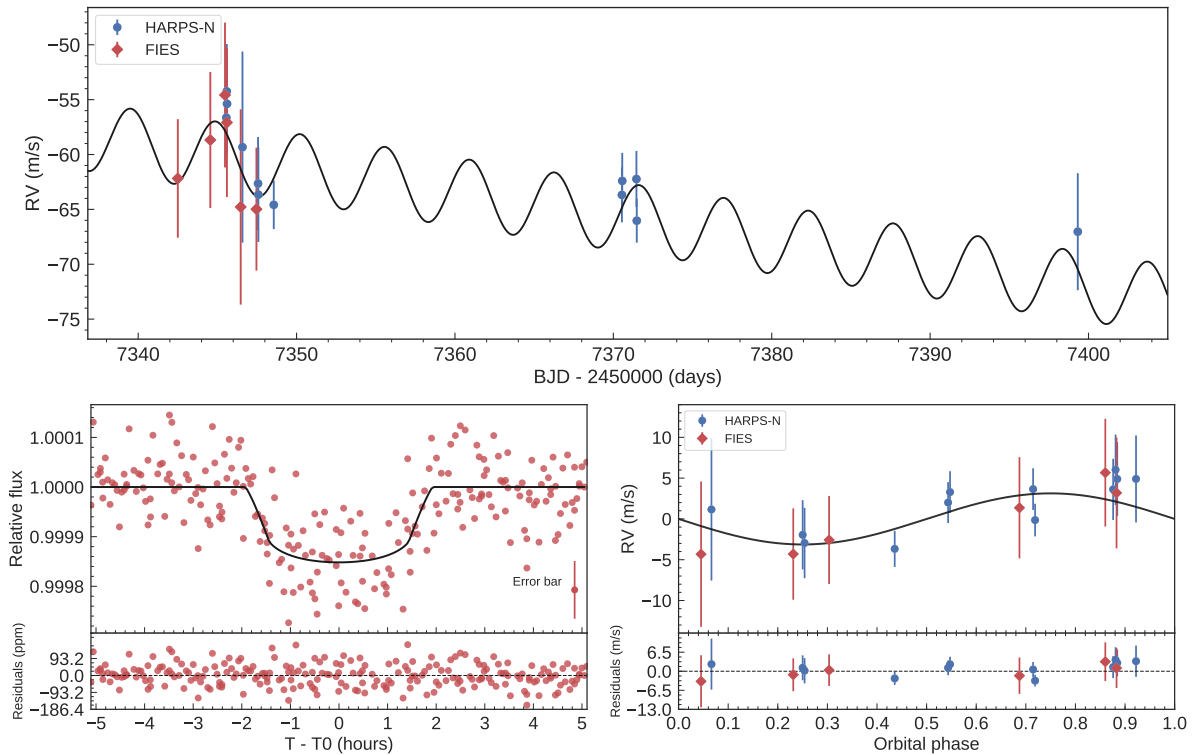
Figure 6.16:   Upper panel: FIES (red diamonds) and HARPS-N (blue circles) RV measurements versus time, following the correction for instrument offset. The best fitting Keplerian model with a linear trend is over-plotted with a thick line. *Lower left panel.* Transit light curve folded to the orbital period of K2-111 b and residuals. The red points mark the *K2* data, whereas the thick black line the re-binned best-fitting transit model. *Lower right panel.* Phase-folded RV curve of K2-111 folded to the orbital period of the planet. The best fitting circular solution is marked with a solid black line. HARPS-N and FIES data are shown with filled circles and diamonds, respectively. The lower panel shows the residuals to the best fitting model.

6.4.4   Planet mass, radius and age

The K2-111 system is demonstrated to be a rare and important object among the plethora of transiting exoplanets that has been discovered by space missions in the last decade. Using adaptive optics imaging and statistical methods, and also detecting the RV signature of this planet we have confirmed the presence of a $1.92^{+0.21}_{-0.20}$ $R_{\oplus}$ planet in a 5.35d orbit, as giving rise to the *K2* transit signature. We find that the planet has a mass of 8.6 ± 3.9 $M_{\oplus}$. The periodic RV signal is overlaid on a trend that we identify with a second more massive planet. The evidence for the planet K2-111 are strong enough for us to say that it is confirmed, while we would require more data in order to confirm also the -c planet.

    We believe this planet to be extremely old. The reasons for this is as follows: *a*) The low but α-rich metal content of K2-111. *b*) This star has a very high space velocity of 157.2 ± 3 km s^{-1} making it a likely member of the thick disk population. *c*) The measurement of the stellar density, the low $\log g_{\star}$ for a star of ≤ 0.9 $M_{\odot}$, as well as the luminosity of 1.9 $L_{\odot}$ is highly suggestive of an evolved object and we argue in Sect. 5 of Fridlund et al. (2017) that the system is $\gtrsim$ 10 Gyrs old and that the host star has begun to move off the main-sequence.

    Together with the 5 planets in the Kepler-444 system K2-111 and its possible companion are among the oldest planets known to date. Assuming a radius of $1.92^{+0.21}_{-0.20}$ $R_{\oplus}$ the planet has an average density of $6.6^{+4.53}_{-3.2}$ g cm^{-3} placing it in the same class as Corot-7 b and Kepler-10b. In this context it is indeed "Earth-like" with similar density to Venus and the Earth itself. It would have formed together with a star having a low metallicity, and more importantly at a very early epoch of our Galaxy. Although K2-111 is also iron-poor it is moderately α-rich, in common with the planet host Kepler-444, which could be favourable for the formation of an Earth-like body. But we also have tentative indications for a more massive planet in the same system. A number of studies so far have pointed out a correlation where metal-rich stars are more likely to harbour gas-giants (e.g., Valenti & Fischer, 2005), while the correlation appear to be missing for the sample of small planets discovered by Kepler (Buchhave et al., 2012). Having formed $\sim$ 5-6 Gyrs before the birth of the Solar System in what is known as the galactic thick disk population, K2-111 and its planet(s) carries information about the early stages of stellar and planetary formation in the Galaxy. It would therefore be very interesting to continue to study this system, primarily to confirm the presence of the second more massive planet and finding also its period. Finding more systems, similar to K2-111 and Kepler-444, would allow us to begin to determine what the implications for planetary formation as a function of galactic age is.

6.5   K2-19: Two worlds in resonance

K2-19 (also known as EPIC 201505350) is a V=13 mag late-type star observed by the K2 space mission during its Campaign 1. K2-19 is a compact planetary system hosting three planets, of which the two larger ones, K2-19b and K2-19c, are close to the 3:2 mean motion resonance.

Several attempts have been made to determine the masses of K2-19 b and K2-19 c. Armstrong et al. (2015) combined *K2* data with ground-based transit photometry of K2-19 b and used the observed TTVs to put some constraints on the mass of the two planets. Barros et al. (2015) used a more sophisticated approach to derive the masses of the planets based on a photo-dynamical model that considers transit timings and durations from transits observed by the *K2* mission, as well as two additional K2-19 b transits observed from the ground. They also included radial velocities obtained with SOPHIE at the Observatoire de Haute Provence (OHP) 1.9 m telescope in their analysis, although they realized that the precision of these RVs prevented the detection of the Doppler reflex motion induced by the planets.

In Nespral et al. (2017) we presented radial velocity follow-up observations of K2-19. As part of this thesis, we performed an analysis of the radial velocity measurements. We detected K2-19 b, the larger and more massive planet in the system, with a mass of 54.8 ± 7.5 M$_\oplus$ and we provided a marginal detection of K2-19 c, with a mass of M$_c = 5.9^{+7.6}_{-4.3}$ M$_\oplus$. The details of this analysis are presented in the next subsections.

Nespral et al. (2017) also used the `TRADES` code to simultaneously model both, the RV measurements and the existing transit timing measurements. This was done in order to provide a comparison between RV and TTV methods to derive exoplanet masses. `TRADES` code derived a mass of 54.4 ± 8.9 M$_\oplus$ for K2-19b and of $7.5^{+3.0}_{-1.4}$ M$_\oplus$ for K2-19c. For K2-19b, these masses are consistent with a previous determination that was principally based on a photodynamical analysis of the K2-19 light curve. Differences remain mainly in the mass determination of the more lightweight planet, driven likely by the limited precision of the RV measurements and possibly some as yet unrecognised systematics.

6.5.1   RV data

The Doppler monitoring of K2-19 is presented in Nespral et al. (2017). The RV data-set contains 10 measurements taken with FIES, 9 with HARPS-N, and 5 with HARPS.

6.5.2   Two-planet RV modeling

We fitted one-planet and two-planet Keplerian models to the FIES, HARPS-N, and HARPS RV data. In the first case, we assumed that the observed Doppler shift is caused *entirely* by the largest transiting planet K2-19 b; in the second case we assumed that both planets contribute to the observed RV variation. The RV analysis was done using `pyaneti` (Barragán et al., 2019, see Sect. 5.3). We set Gaussian priors on the orbital periods and mid-times of first transit for both planets using the values given by Armstrong et al. (2015). For the remaining parameters we used flat priors. The list of fitted parameters and prior details are given in Table 6.6.

We evolved 1 000 independent chains and ran 50 000 additional iterations, with a thinning factor of 50, once convergence was reached. The final parameter estimates were obtained by combining the points from all the chains, leading to a total number of 10^6 points for each parameter.
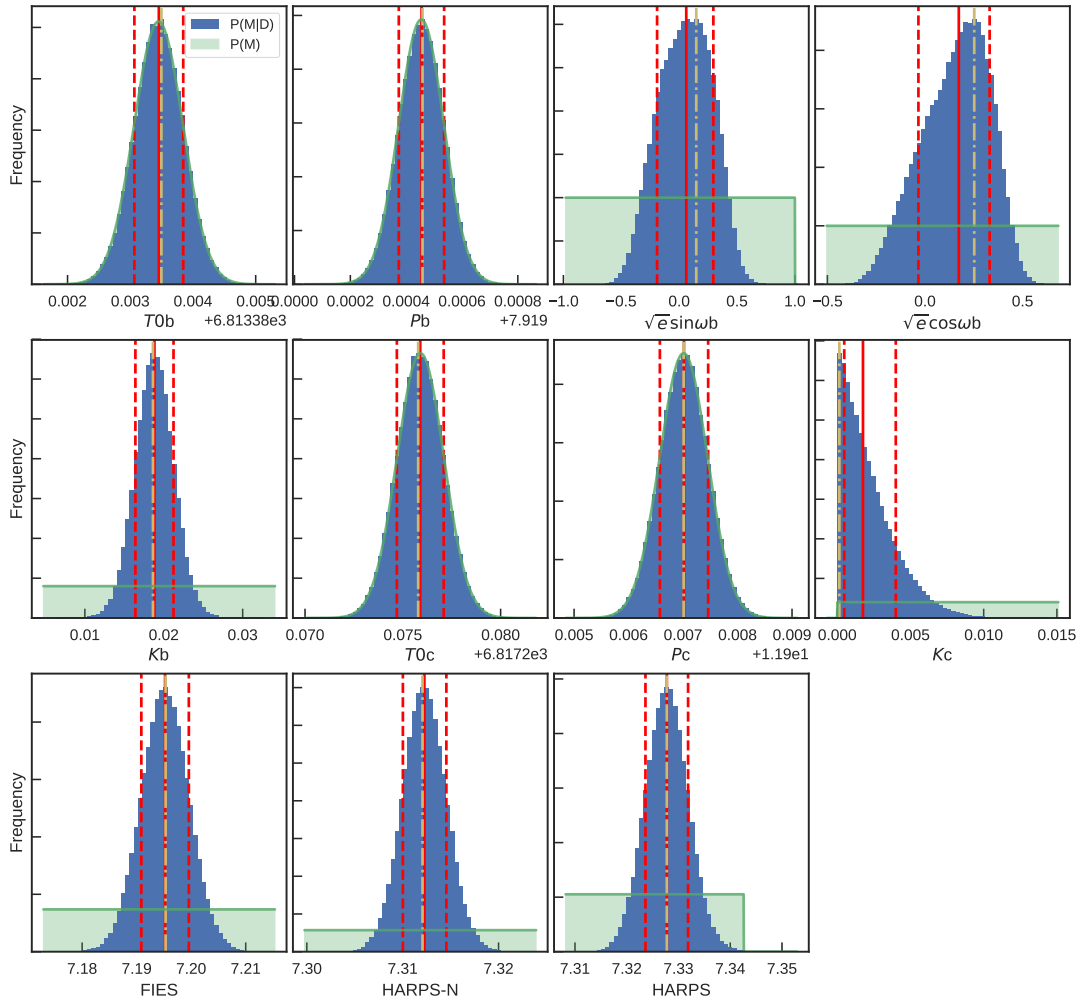
Figure 6.17: Posterior distributions of the K2-19's fitted parameters as obtained using the code `pyaneti`. The blue region corresponds to the posterior $P(M|D)$, whereas the green shaded area marks the prior shape $P(M)$. Median (red solid line), 68% credible interval (red dashed line) and mode (yellow dash-dotted line) are also shown.

6.5.3   Inferred planet parameters

Figure 6.17 shows the inferred posterior distribution for each fitted parameter obtained with `pyaneti`. They all are unimodal, but we note that there is a truncation effect in the lower prior limit for K_c (see Sect. 6.5.4 for more details). Considering the known difficulties of quantifying the contribution from stellar activity to RV amplitudes on the $1\,\mathrm{m\,s^{-1}}$ level, we expect that the RV amplitudes have larger uncertainties than those derived in this analysis.

We see that for planets, the posterior distributions for T_0 and P matches the prior distribution. This shows how the fit to the RV data does not modify the T_0 and P values coming from a transit fit. The parameter estimates, defined as the median values of the posterior probability distributions, are given in Table 6.6 along with the 68% credible interval. The inferred models for both planets are shown in Figure 6.18.

6.5.4   Planet masses

Assuming a stellar mass of $M_\star = 0.918 \pm 0.064\ M_\odot$ (Table 6.6, see Sect. 3 of Nespral et al., 2017), modelling the RV data with only one Keplerian orbit gives a mass of

Table 6.6: K2-19 system parameters.

Parameter	Prior[a]	Final value
Stellar parameters[b]		
Star mass $M_\star$ $(M_\odot)$	$\cdots$	0.918 ± 0.064
Star radius $R_\star$ $(R_\odot)$	$\cdots$	0.8810000 ± 0.111
Effective Temperature $T_{\rm eff}$ (K)	$\cdots$	5250 ± 70
Model parameters of K2-19 b		
Orbital period $P_{\rm orb}$ (days)	$\mathcal{N}[7.9195, 0.0001]$	7.9195 ± 0.0001
Transit epoch T_0 (BJD$_{\rm TDB}$$-2\,450\,000$)	$\mathcal{N}[6813.3835, 0.0004]$	6813.3835 ± 0.0004
$\sqrt{e}\sin\omega$	$\mathcal{U}[-1, 1]$	$0.07^{+0.23}_{-0.25}$
$\sqrt{e}\cos\omega$	$\mathcal{U}[-1, 1]$	$0.17^{+0.16}_{-0.21}$
Radial velocity semi-amplitude variation K (m s^{-1})	$\mathcal{U}[0, 100]$	18.8 ± 2.4
Model parameters of K2-19 c		
Period $P_{\rm rot}$ (days)	$\mathcal{N}[11.9070, 0.0004]$	11.9070 ± 0.0004
Epoch T_0 (BJD$_{\rm TDB}$$-2\,450\,000$)	$\mathcal{N}[6817.2759, 0.0012]$	6817.2759 ± 0.0012
$\sqrt{e}\sin\omega$	$\mathcal{F}[0]$	0
$\sqrt{e}\cos\omega$	$\mathcal{F}[0]$	0
Radial velocity semi-amplitude variation K (m s^{-1})	$\mathcal{U}[0, 100]$	$1.8^{+2.3}_{-1.3}$
Additional model parameters		
Systemic velocity $\gamma_{\rm FIES}$ (km s^{-1})	$\mathcal{U}[7.1628, 7.2307]$	7.1951 ± 0.0044
Systemic velocity $\gamma_{\rm HARPS}$ (km s^{-1})	$\mathcal{U}[7.2832, 7.3533]$	7.3278 ± 0.0041
Systemic velocity $\gamma_{\rm HARPS-N}$ (km s^{-1})	$\mathcal{U}[7.2951, 7.3426]$	7.3122 ± 0.0023
Derived parameters of K2-19 b		
Planet mass $M_{\rm p}$ $(M_\oplus)^{[c]}$	$\cdots$	54.8 ± 7.5
Orbit eccentricity e	$\cdots$	$0.09^{+0.09}_{-0.07}$
Argument of periastron of stellar orbit $\omega_\star$ (degrees)	$\cdots$	100^{+37}_{-70}
Derived parameters of K2-19 c		
Planet mass $M_{\rm p}$ $(M_\oplus)^{[c]}$	$\cdots$	$5.9^{+7.6}_{-4.3}$
Orbit eccentricity e	$\cdots$	0

Note – [a] $\mathcal{U}[a, b]$ refers to uniform priors between a and b, $\mathcal{N}[a, b]$ means Gaussian priors with mean a and standard deviation b and $\mathcal{F}[a]$ to a fixed a value. [b] Details about the stellar parameter estimation are given in Nespral et al. (2017). [c] The true masses were calculated using the orbit inclinations given by Armstrong et al. (2015).
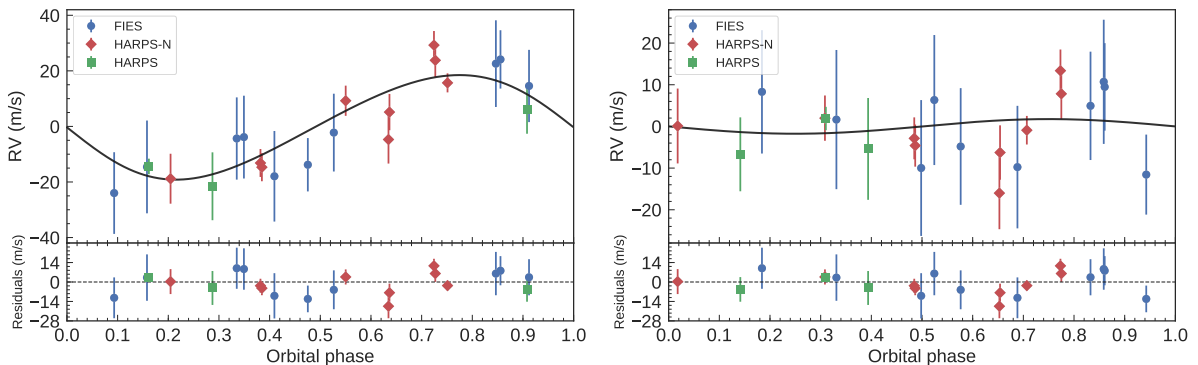
Figure 6.18: FIES (blue circles), HARPS-N (red diamonds), and HARPS (green triangles) RV measurements of K2-19 and Keplerian fits (solid line), phase folded to the orbital period and time of first transit of K2-19b (left figure) and K2-19c (right figure). For K2-19c, the fitted RVs from K2-19b have been removed. All RVs, fits and residuals (in smaller subpanels) are shown following the subtraction of the systemic velocities from the three instruments.

$M_b = 58.6 \pm 4.6\,M_\oplus$ for K2-19 b, with a χ^2 value of 15.6 (dof = 14). The two-planet modelling gives a similar value of $M_b = 54.8 \pm 7.5\,M_\oplus$ for K2-19 b, and a mass of $M_c = 5.9^{+7.6}_{-4.3}\,M_\oplus$ for K2-19 c, with a chi-square value of 17.5 (dof = 11). We conclude that the RV data do not allow us to significantly detect the Doppler reflex motion induced by K2-19 c. Nevertheless, two planets are known to be in this system and given the marginal RV detection of K2-19 c, the two-planet fit is the preferred one.

Figure 6.17 shows that the posterior distribution for K_c, the RV semi-amplitude of planet, is truncated at zero. For instance, we can only draw a maximum mass for planet c. With a 99% of confidence, the maximum RV semi-amplitude induced by K2-19 c is $7.0\,\mathrm{m\,s^{-1}}$ which translates to a maximum mass of $23.8\,M_\oplus$.

6.6 K2-106 b and c: Two worlds with different densities

Adams et al. (2017) reported the discovery of two small planets transiting the star K2-106 (EPIC 220674823), which was observed by *K2* in its campaign 8. Intensive radial velocity follow-up observations were presented in Guenther et al. (2017), as part of follow-up program carried out by the KESPRINT consortium to determine the masses, radii, and mean densities of the two transiting planets orbiting K2-106. The parameter estimation of both planets was done as part of this thesis. This analysis will be described in the present section. Details about the detection, validation, photometric follow-up, and stellar characterisation are given in Guenther et al. (2017).

We found that although the two planets have similar masses, their densities are very different. For K2-106 b we derived a mass of $8.44^{+0.96}_{-0.94}$ $M_\oplus$, a radius of 1.52 ± 0.16 $R_\oplus$, and a high density of $12.8^{+5.3}_{-3.5}$ g cm^{-3}. For K2-106 c, we found a mass, radius and radius of $8.4^{+4.8}_{-4.3}$ $M_\oplus$, $2.53^{+0.28}_{-0.27}$ $R_\oplus$, and $2.8^{+2.2}_{-1.5}$ g cm^{-3}, respectively. Since the system contains two planets of almost the same mass, but different distances from the host star, it is an excellent laboratory to study atmospheric escape. In agreement with the theory of atmospheric-loss processes, it is likely that the outer planet has a hydrogen-dominated atmosphere. The mass and radius of the inner planet is in agreement with theoretical models predicting an iron core containing 80^{+20}_{-30} % of its mass. Such a high metal content is surprising, particularly given that the star has a solar metal abundance.

6.6.1 RV and light curve data

We used the *K2* photometry provided by Vanderburg & Johnson (2014), and detrended and cleaned the transit light curves using the code `exotrending` (Barragán & Gandolfi, 2017, see Appendix A.1). We show the light curve of K2-106 in Figure 6.19.

The RV measurements were collected using 5 different spectrographs (Guenther et al., 2017). Between August 14, 2016, and January 14, 2017, we obtained 13 spectra of K2-106 with the Carnegie Planet Finder Spectrograph (PFS; Crane et al., 2008, 2010). We also obtained 3 RV measurements of K2-106 with the High Dispersion Spectrograph (HDS; Noguchi et al., 2002) on the 8.2 m Subaru Telescope. We also obtained 6 RV measurements with the FIES spectrograph, 12 RV measurements with the HARPS-N spectrograph, and 20 RVs with the HARPS spectrograph. The RV measurements are listed in Tables 1 and 2 of Guenther et al. (2017). The data-set is also accessible through the CDS portal at `http://cdsarc.u-strasbg.fr/viz-bin/qcat?J/A+A/608/A93`.

While the paper from Guenther et al. (2017) was being refereed, we learned that Sinukoff et al. (2017) had also undertaken RV measurements of K2-106 and uploaded their article on the preprint arXiv server. Their work included 35 relative RV measurements obtained with Keck-HIRES, which we also included in our analysis.

6.6.2 Orbital solution of K2-106b

K2-106 b is an ultra-short period planet ideal to measure the mass via the floating chunk offset (FCO) method (Hatzes et al., 2011, see also section B). We selected the HARPS, HARPS-N and HIRES measurements for which at least two data points were taken the same night. This leads to a number of 8, 3, and 5 chunks of nightly HARPS, HARPS-N and HIRES RV data, respectively.

We modeled the HIRES, HARPS and HARPS-N RV measurements with `pyaneti` (Barragán et al., 2019). We fixed the ephemeris to the values given by our joint analysis of the data (see §6.6.3). We fitted for the RV semi-amplitude for planet b, K_b, and the 16 nightly offsets.
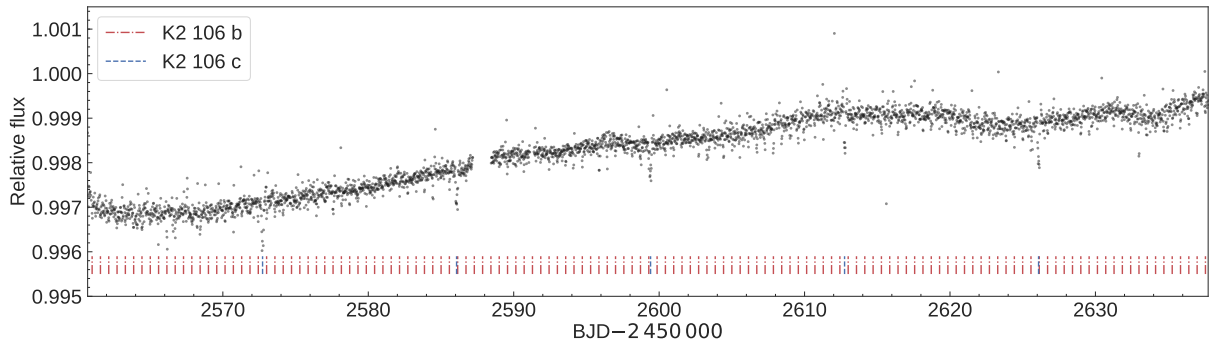
Figure 6.19: *K2* light curve of K2-106 extracted by Vanderburg & Johnson (2014). Stellar activity is seen as the quasi-periodic, long period modulation. Transits of both planets are marked with vertical lines.
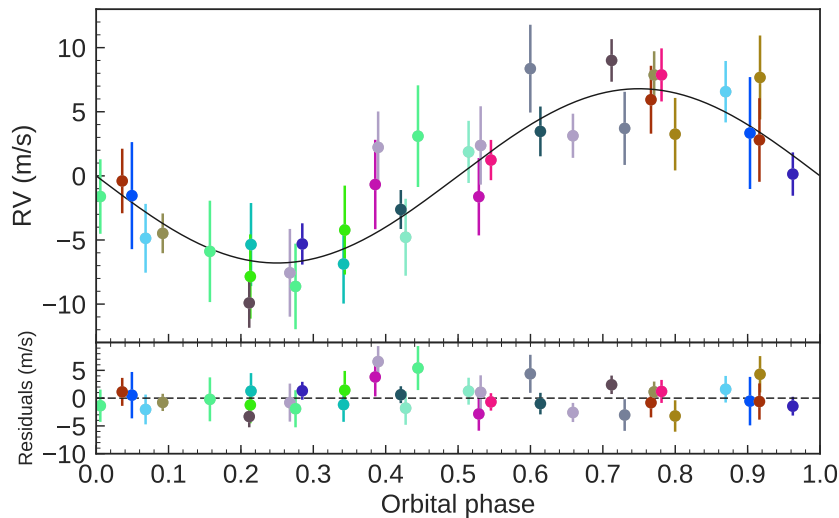
Figure 6.20: The RV curve of K2-106 phase-folded to the orbital period of planet b, as derived using the FCO method and residuals. The best fitting circular solution is marked with a thick line. Different colours represent measurements from different observing nights.

We adopted uniform priors within a wide range for each parameter and ran 500 independent Markov chains. We ran the code in order to create posterior distributions of 250 000 independent data points for each fitted parameter once chains converged.

The final estimates and their 1-σ uncertainties were taken as the median and the 68 % of the credible interval of the posterior distributions. Figure 6.20 shows the RV data together with the inferred model once all the night offsets were subtracted. We found a radial velocity semi-amplitude variation of $K_b = 6.80 \pm 0.67$ ms which translates into a mass of $M_b = 8.48 \pm 0.92 \, M_\oplus$ for K2-106 b.

6.6.3   Multi-planet joint analysis

We performed the multi-planet joint analysis using the code `pyaneti` (Barragán et al., 2019, see also Sect. 5.3). We fitted the RV and light curve data assuming two planets orbiting the star. Since the stellar activity was negligible, we did not add extra sinusoidal signals (see Sect. 3.2 of Guenther et al., 2017, for more details). We also fit for a jitter term for each spectrograph. Given the very short orbital period, we assumed a circular orbit for K2-106 b, but included eccentricity orbit in the case of K2-106 c. Details for fitted parameters and priors are given in Table 6.7. Following Kipping (2010, see

Appendix A.2), we super-sampled the light curve model using 10 sub-samples per *K2* exposure to account for the long-cadence acquisition. We used a similar approach to the one presented in Sect. 6.1.5 to generate posterior distributions with 250, 000 independent points for each fitted parameter once chains converged.

Posterior distributions for each fitted parameters are displayed in Figure 6.21. We report our results in Table 6.7 as the median and the 68 % credible interval of the final posterior probability distribution of each parameter. Fig. 6.22 shows the *K2* transit light curves and best fitting transit models, as well as the RV data together with the best fitting Keplerian models of K2-106 b and c. In figure 6.23 we show a multi-transit event that occurred at the fifth transit of K2-106 c.

6.6.4 Planets' masses, radii, and composition

Given the stellar parameters derived by Guenther et al. (2017) (see Table 6.7), the planet masses are $8.44^{+0.96}_{-0.94}$ $M_\oplus$ and $8.4^{+4.8}_{-4.3}$ $M_\oplus$ for K2-106 b and K2-106 c, respectively. The radius of the inner planet is 1.52 ± 0.16 $R_\oplus$ and the outer planet is $2.53^{+0.28}_{-0.27}$ $R_\oplus$. With these values, the mean densities of both planets are $12.8^{+5.3}_{-3.5}$ g cm^{-3} and $2.8^{+2.2}_{-1.5}$ g cm^{-3}. We note that our derived planet radii are consistent with the values reported by Adams et al. (2017).

Figure 6.24 shows the mass-radius relation for low-mass planets together with various compositions taken from Zeng et al. (2016). The filled symbols are the values for K2-106 b and K2-106 c using our stellar parameters. K2-106 b is located between the lines with 50% and 100% iron composition. How robust is this conclusion that K2-106 b is metal rich? When we use models published by Fortney et al. (2007) or Wurm et al. (2013), we obtain the same results. Thus, regardless of which set of stellar parameters we use, whether we include the jitter term, and regardless of which models we use, in all cases we reach the conclusion that the iron core contains more than half of the mass of the planet. The conclusion that this planet is metal rich is therefore robust. The composition is Mercury-like rather than Earth-like. This is very interesting because other ultra-short planets seem to have an Earth-like composition. The high metal content of the planet is particularly surprising because the host star has solar metallicity (see Table 3 of Guenther et al., 2017). The unusual composition of K2-106 b also shows that rocky planets are more diverse than previously thought, and it can provide important clues of how such metal-rich planets form

Another interesting aspect of the K2-106 system is that the masses of the two planets are relatively similar, but the densities are very different. Since the mass and radius measurements for both planets might be affected in the same way by the systematic uncertainties of the stellar parameters, the diversity of exoplanets (e.g., Hatzes & Rauer, 2015) cannot be entirely explained by problems in the determination of the stellar parameters. As shown in Fig. 6.24, the density of K2-106 c is consistent with a planet composed of 100 % water. However, other planets like K2-106 c have compositions suggesting a rocky core with a hydrogen atmosphere (Chen et al., 2017). Since the mass is $8.4^{+4.8}_{-4.3}$ $M_\oplus$ and the ratio of the stellar flux received by the planet compared to Earth is $F_p/F_\oplus \sim 52$, there is no reason why K2-106 c could not have a hydrogen atmosphere. The difference in atmospheric loss rates (see Sect. 3.5 of Guenther et al., 2017) explains why the inner planet has no hydrogen atmosphere, while the other planet is likely to have one. K2-106 c is an ideal target for future studies of atmospheric escape.
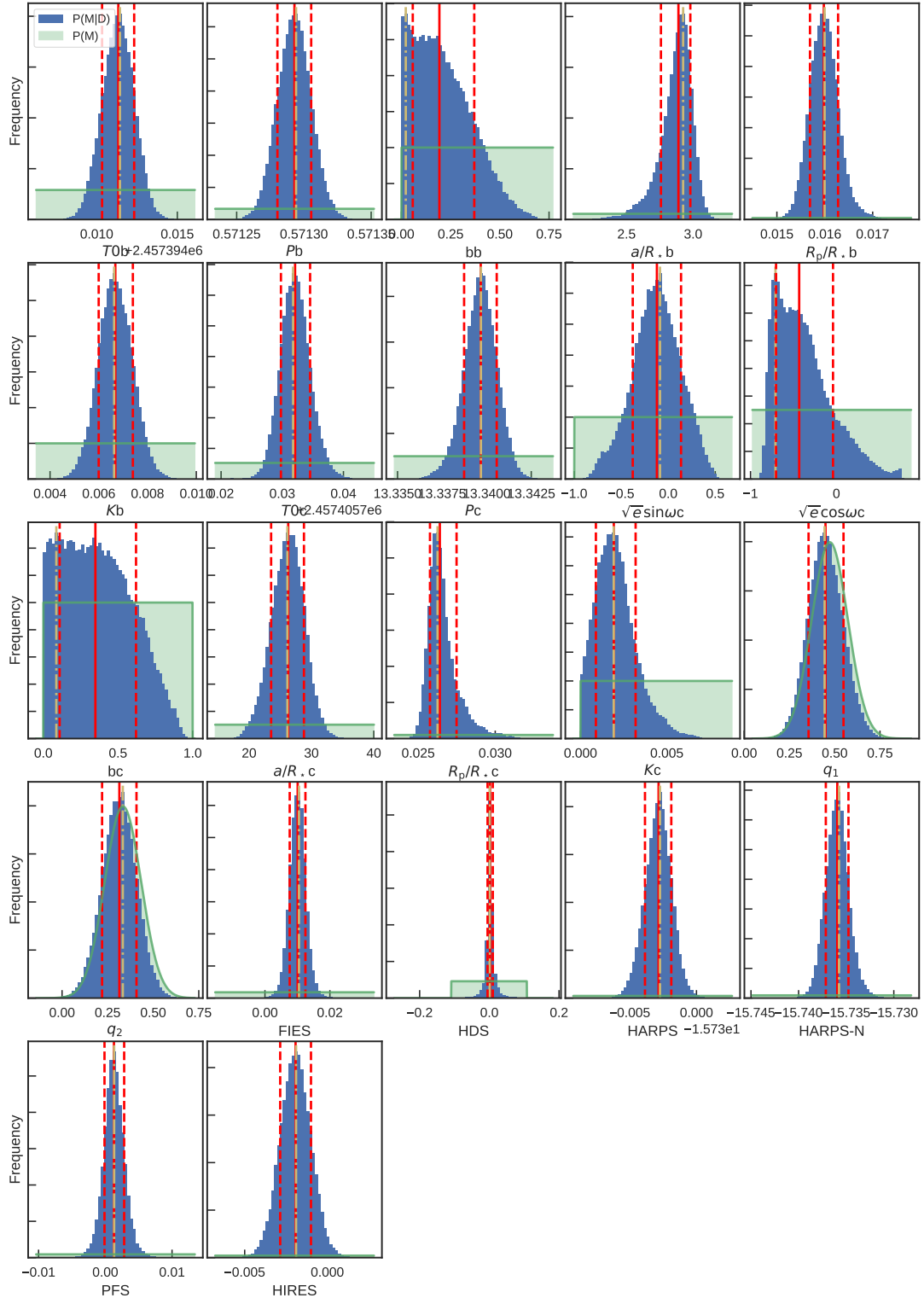
Figure 6.21: Posterior distributions of the K2-106's fitted parameters as obtained from the final analysis performed with `pyaneti`. The blue region corresponds to the posterior $P(M|D)$, whereas the green shaded area marks the prior shape $P(M)$. Median (red solid line), 68% credible interval (red dashed line), and mode (yellow dash-dotted line) are also shown.

Table 6.7: K2-106 system parameters.

Parameter	Prior[a]	Final value
Stellar parameters[b]		
Star mass $M_\star$ ($M_\odot$)	$\cdots$	0.945 ± 0.063
Star radius $R_\star$ ($R_\odot$)	$\cdots$	0.869 ± 0.088
Effective Temperature $T_{\rm eff}$ (K)	$\cdots$	5470 ± 30
Model parameters of K2-106 b		
Orbital period $P_{\rm orb}$ (days)	$\mathcal{U}[0.5710, 0.5716]$	0.571292 ± 0.000012
Transit epoch T_0 (BJD$_{\rm TDB}-2\,450\,000$)	$\mathcal{U}[7394.0039, 7394.0211]$	7394.0114 ± 0.0010
Scaled semi-major axis $a/R_\star$	$\mathcal{U}[1.2, 10]$	$2.79^{+0.14}_{-0.33}$
Planet-to-star radius ratio $R_{\rm p}/R_\star$	$\mathcal{U}[0, 0.1]$	$0.01611^{+0.00052}_{-0.00036}$
Impact parameter, b	$\mathcal{U}[0, 1]$	$0.3223883^{+0.26}_{-0.23}$
$\sqrt{e}\sin\omega$	$\mathcal{F}[0]$	0
$\sqrt{e}\cos\omega$	$\mathcal{F}[0]$	0
Radial velocity semi-amplitude variation K (m s^{-1})	$\mathcal{U}[0, 10]$	6.67 ± 0.69
Model parameters of K2-106 c		
Orbital period $P_{\rm orb}$ (days)	$\mathcal{U}[13.3312, 13.3512]$	$13.33966^{+0.00092}_{-0.00099}$
Transit epoch T_0 (BJD$_{\rm TDB}-2\,450\,000$)	$\mathcal{U}[7405.6932, 7405.7692]$	$7405.73156^{+0.0025}_{-0.0023}$
Scaled semi-major axis $a/R_\star$	$\mathcal{U}[1.2, 100]$	$23.9^{+6.7}_{-6.2}$
Planet-to-star radius ratio $R_{\rm p}/R_\star$	$\mathcal{U}[0, 0.1]$	$0.0264^{+0.0013}_{-0.0007}$
Impact parameter, b	$\mathcal{U}[0, 1]$	$0.3223883^{+0.26}_{-0.23}$
$\sqrt{e}\sin\omega$	$\mathcal{U}[-1, 1]$	$0.04^{+0.29}_{-0.41}$
$\sqrt{e}\cos\omega$	$\mathcal{U}[-1, 1]$	$-0.49^{+0.32}_{-0.19}$
Radial velocity semi-amplitude variation K (m s^{-1})	$\mathcal{U}[0, 10]$	6.67 ± 0.69
Additional model parameters		
Parameterized limb-darkening coefficient q_1	$\mathcal{N}[0.47, 0.1]$	0.46 ± 0.10
Parameterized limb-darkening coefficient q_2	$\mathcal{N}[0.33, 0.1]$	0.32 ± 0.10
Systemic velocity $\gamma_{\rm FIES}$ (km s^{-1})	$\mathcal{U}[-0.0102, 0.0306]$	$0.0102^{+0.0024}_{-0.0026}$
Systemic velocity $\gamma_{\rm HDS}$ (km s^{-1})	$\mathcal{U}[-0.0195, 0.0178]$	0.0013566 ± 0.0055
Systemic velocity $\gamma_{\rm PFS}$ (km s^{-1})	$\mathcal{U}[-0.0143, 0.0255]$	0.0014 ± 0.0015
Systemic velocity $\gamma_{\rm HIRES}$ (km s^{-1})	$\mathcal{U}[-0.0348, 0.0207]$	$-0.00186^{+0.00094}_{-0.00097}$
Systemic velocity $\gamma_{\rm HARPS}$ (km s^{-1})	$\mathcal{U}[-15.7531, -15.7125]$	$-15.73301^{+0.00090}_{-0.00095}$
Systemic velocity $\gamma_{\rm HARPS-N}$ (km s^{-1})	$\mathcal{U}[-15.7530, -15.7179]$	-15.7361 ± 0.0012
RV jitter term $\sigma_{\rm FIES}$ (m s^{-1})	$\mathcal{U}[0, 100]$	$2.4^{+3.0}_{-1.7}$
RV jitter term $\sigma_{\rm HDS}$ (m s^{-1})	$\mathcal{U}[0, 100]$	$6.3^{+9.4}_{-4.4}$
RV jitter term $\sigma_{\rm PFS}$ (m s^{-1})	$\mathcal{U}[0, 100]$	$4.2^{+1.7}_{-1.3}$
RV jitter term $\sigma_{\rm HIRES}$ (m s^{-1})	$\mathcal{U}[0, 100]$	$4.8^{+0.7}_{-0.6}$
RV jitter term $\sigma_{\rm HARPS}$ (m s^{-1})	$\mathcal{U}[0, 100]$	$2.0^{+1.3}_{-1.2}$
RV jitter term $\sigma_{\rm HARPS-N}$ (m s^{-1})	$\mathcal{U}[0, 100]$	$1.8^{+1.5}_{-1.2}$
Derived parameters of K2-106 b		
Planet mass $M_{\rm p}$ ($M_{\rm Jup}$)	$\cdots$	$8.44^{+0.96}_{-0.94}$
Planet radius $R_{\rm p}$ ($R_{\rm Jup}$)	$\cdots$	1.52 ± 0.16
Planet mean density $\rho_{\rm p}$ (g cm^{-3})	$\cdots$	$12.8^{+5.3}_{-3.5}$
Semi-major axis of the planetary orbit a (AU)	$\cdots$	$0.0110^{+0.0014}_{-0.0016}$
Orbit eccentricity e	$\cdots$	0
Argument of periastron of stellar orbit $\omega_\star$ (degrees)	$\cdots$	90
Orbit inclination $i_{\rm p}$ (degrees)	$\cdots$	$83.4^{+4.8}_{-7.0}$
Equilibrium temperature[c] $T_{\rm eq}$ (K)	$\cdots$	2451^{+157}_{-81}
Derived parameters of K2-106 c		
Planet mass $M_{\rm p}$ ($M_{\rm Jup}$)	$\cdots$	$8.4^{+4.8}_{-4.3}$
Planet radius $R_{\rm p}$ ($R_{\rm Jup}$)	$\cdots$	$2.53^{+0.28}_{-0.27}$
Planet mean density $\rho_{\rm p}$ (g cm^{-3})	$\cdots$	$2.8^{+2.2}_{-1.5}$
Semi-major axis of the planetary orbit a (AU)	$\cdots$	$0.096^{+0.030}_{-0.026}$
Orbit eccentricity e	$\cdots$	$0.36^{+0.20}_{-0.21}$
Argument of periastron of stellar orbit $\omega_\star$ (degrees)	$\cdots$	176^{+54}_{-36}
Orbit inclination $i_{\rm p}$ (degrees)	$\cdots$	$89.2^{+0.6}_{-1.3}$
Equilibrium temperature[c] $T_{\rm eq}$ (K)	$\cdots$	835^{+134}_{-99}

Note – [a] $\mathcal{U}[a, b]$ refers to uniform priors between a and b, $\mathcal{N}[a, b]$ means Gaussian priors with mean a and standard deviation b and $\mathcal{F}[a]$ to a fixed a value. [b] Details about the stellar parameter estimation are given in Guenther et al. (2017). [c] Assuming albedo $= 0$.
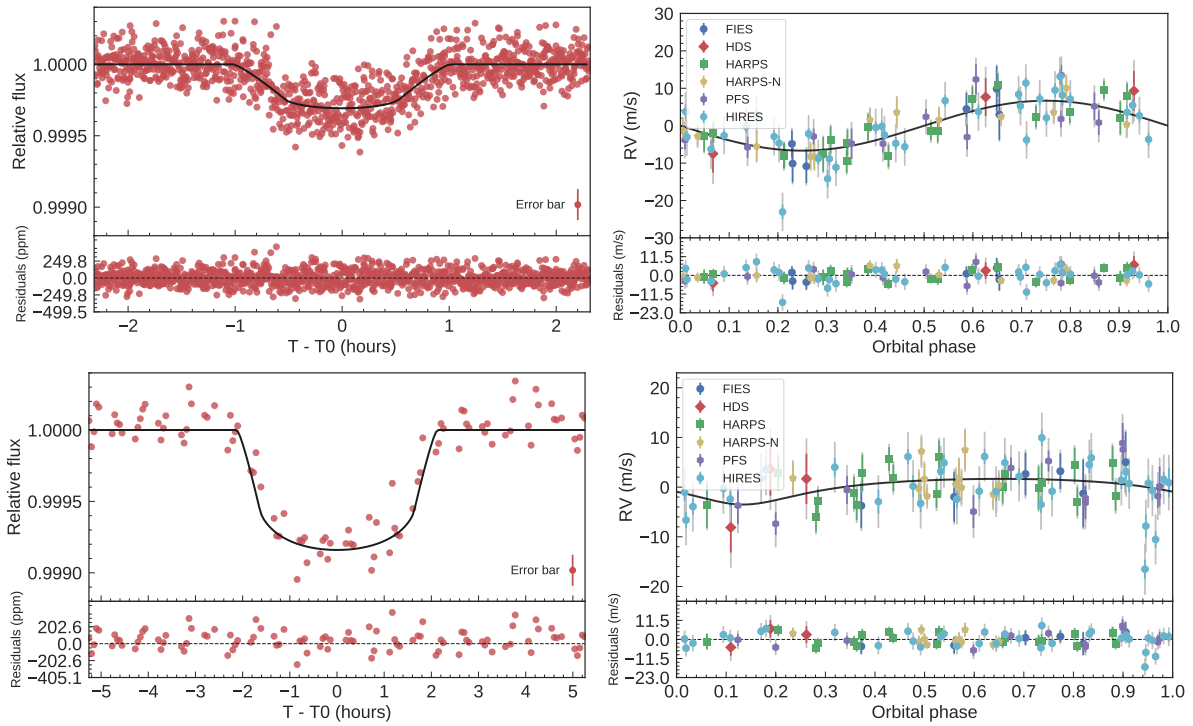
Figure 6.22: Transit light curves and RV curves of K2-106 due to planet b (upper panels) and c (lower panels). The best fitting transit and Keplerian models are overplotted with thick black lines. The *K2* data points are shown with red circles (left panels). The HARPS and HARPS-N RV measurements are plotted with red circles and blue diamonds, respectively, along with their nominal uncertainties (right panels). The RV curves are phase-folded to the orbital period of the two planets, following the subtraction of the systemic velocities and other signals, except planet b (upper right panel) and c (lower right panel).
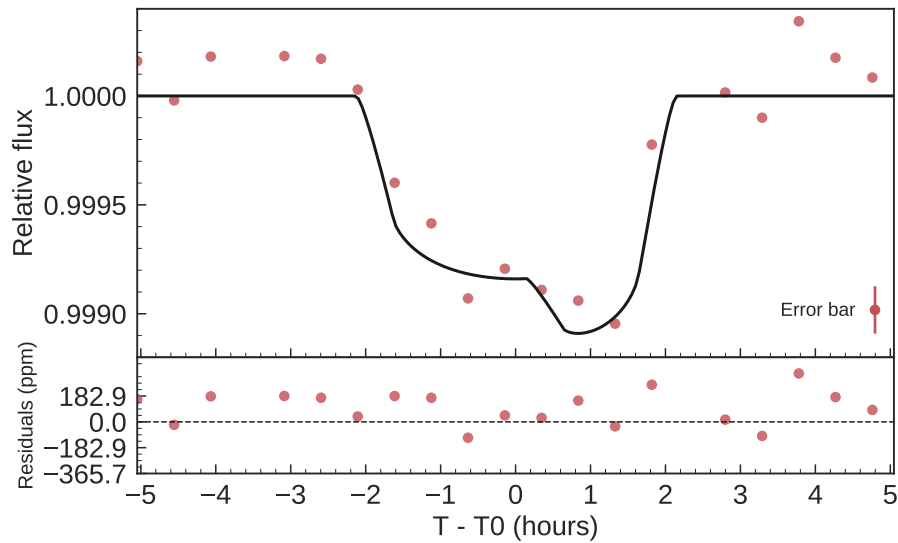
Figure 6.23: Multi-transit event for K2-106. The *K2* data points are shown with red circles. The best-fitting transit model is overplotted with a thick black line. The data and the model show the simultaneous transit of K2-106 b and K2-106 c.
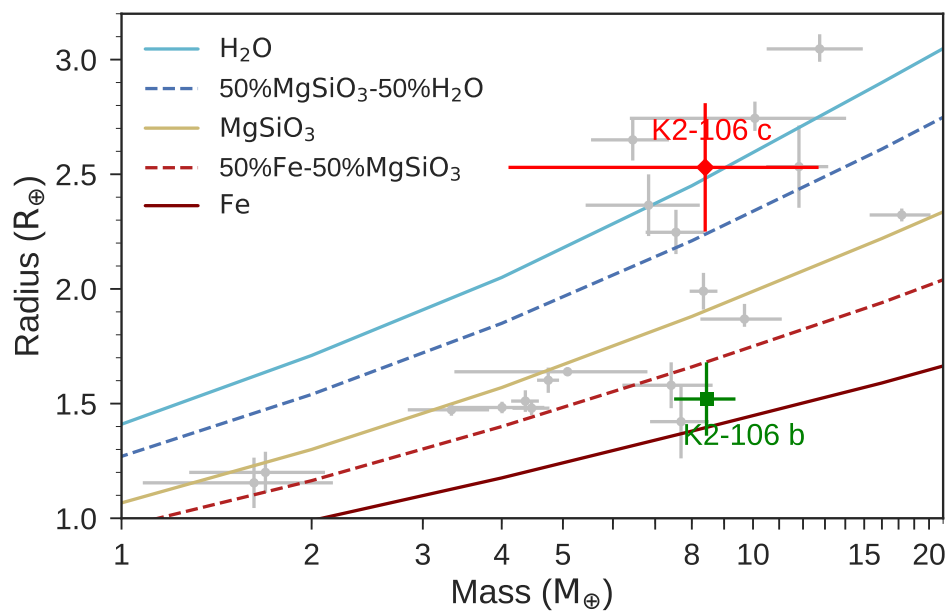
Figure 6.24: Mass-radius diagram for well-characterised (5-σ precision level or better) super-Earths and Neptunes. From bottom to top, the solid curves are theoretical models (Zeng et al., 2016) for planets with a composition of 100% iron (brown), 50% silicate and 50% iron (dashed red), 100% silicate (beige), 50% silicate and 50% water (dashed blue), water (light blue). K2-106 b & K2-106 c are highlighted with different symbols and colours.

6.7   HD 3167 b and c: Two worlds with different densities II

Using time-series photometric data from *K2*'s Campaign 8, Vanderburg et al. (2016) announced the discovery of two small transiting planets around the bright (V=8.9 mag) K0 dwarf star HD 3167. The inner planet, HD 3167 b, has a radius of $R_{\rm p}$=1.6 $R_{\oplus}$ and transits the host star every 0.96 days. HD 3167 b qualifies as an ultra-short period planet. The outer planet, HD 3167 c, has a radius of 2.9 $R_{\oplus}$ and an orbital period of 29.85 days. The brightness of the host star makes the system amenable to follow-up observations such as high-precision RV measurements for planetary mass determination.

Gandolfi et al. (2017) presented an intensive radial velocity follow-up of HD 3167 performed with the FIES@NOT, HARPS@ESO-3.6m, and HARPS-N@TNG spectrographs. The data analysis presented in Gandolfi et al. (2017) was done as part of this thesis. We revised the system parameters and determined radii, masses, and densities of the two transiting planets by combining the *K2* photometry with our spectroscopic data.

With a mass of 5.69 ± 0.44 $M_{\oplus}$, radius of 1.574 ± 0.054 $R_{\oplus}$, and mean density of $8.00^{+1.10}_{-0.98}$ g cm^{-3}, HD 3167 b joins the small group of ultra-short period planets known to have a rocky terrestrial composition. HD 3167 c has a mass of $8.33^{+1.79}_{-1.85}$ $M_{\oplus}$ and a radius of $2.740^{+0.106}_{-0.100}$ $R_{\oplus}$, yielding a mean density of $2.21^{+0.56}_{-0.53}$ g cm^{-3}, indicative of a planet with a composition comprising a solid core surrounded by a thick atmospheric envelope. The rather large pressure scale height ($\sim$350 km) and the brightness of the host star make HD 3167 c an ideal target for atmospheric characterisation via transmission spectroscopy across a broad range of wavelengths. We found evidence of additional signals in the radial velocity measurements but the currently available data set does not allow us to draw any firm conclusion on the origin of the observed variation.

Details about the detection and the validation are given in Vanderburg et al. (2016). Ground-based follow-up and stellar characterisation are described in Gandolfi et al. (2017). In this section we will present the different analyses that were performed to model the transit and radial velocity signals. We note that Christiansen et al. (2017) presented an independent mass determination of HD3167 b and c using a different RV data-set. Their results are consistent with ours.

6.7.1   RV and light curve data

For our analysis we used the light curve (Fig. 6.25) extracted following the technique described in Vanderburg & Johnson (2014). The fitted photometric data-set includes 6 and 15 hours of *K2* data-points centred around each transit of HD 3167 b and c. We de-trended the segments using the program `exotrending` (Barragán & Gandolfi, 2017, see Appendix A.1). Briefly, we fitted a second order polynomial to the out-of-transit data and removed outliers using a 3-sigma-clipping algorithm applied to the residuals of the preliminary best fitting transit models derived using the formalism of Mandel & Agol (2002) coupled to a non-linear least square fitting procedure.

The description of the Doppler follow-up of HD 3167 is given in Gandolfi et al. (2017). The RV data-set contains 37 measurements taken with FIES, 32 with HARPS-N, and 50 with HARPS. The RV measurements are accessible through the CDS portal at `http://cdsarc.u-strasbg.fr/viz-bin/Cat?cat=J%2fAJ%2f154%2f123`.

6.7.2   Orbital solution of HD 3167 b

We performed a Keplerian fit of the FIES, HARPS, and HARPS-N RV data following the floating chunk offset (FCO) method described in Hatzes et al. (2011, see Appendix B). The ultra-short period planet HD 3167 b is well suited for application of the FCO method.
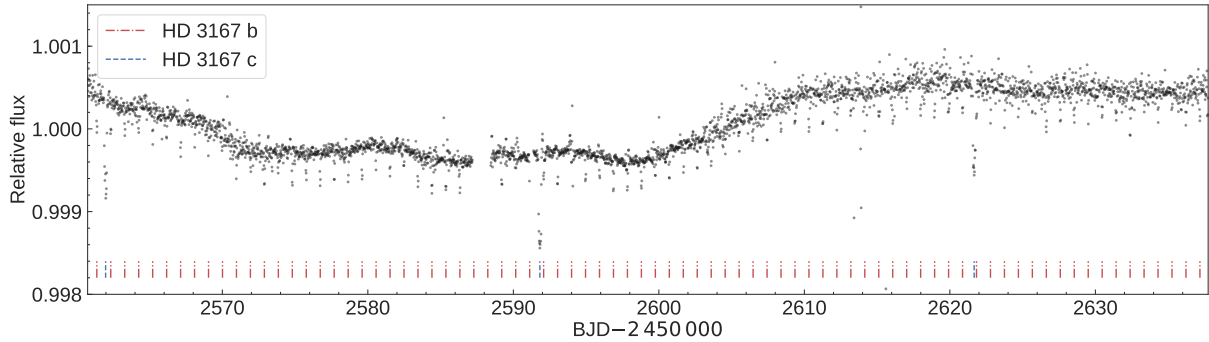
Figure 6.25: *K2* light curve of HD 3167 as extracted by Vanderburg & Johnson (2014). Transits of both planets are marked with vertical lines.

This technique is particularly effective at filtering out the long term RV variation due to magnetic activity coupled with stellar rotation. The star has an estimated rotation period of about 23.5 days (Gandolfi et al., 2017, see §4.3), which is longer than the orbital period of HD 3167 b. HD 3167 c has an orbital period of about 29.95 days, which results in a change of less than 0.01 in phase within the nightly visibility window of the target ($\sim$5-6 hours). The RV of the star due to the outer transiting planet does not change significantly during an observing night. Moreover, each of the three data sets has its own zero-point offset, which is naturally taken into account by the method. Finally, the FCO technique also removes – or at least greatly minimises – any long term systematic errors, such as the night-to-night RV drifts of FIES.

We modelled the FIES, HARPS and HARPS-N RV measurements with `pyaneti` (Barragán et al., 2019, see Sect. 5.3). Following Hatzes et al. (2011), we divided the RVs into three subsets of nightly measurements – one per instrument – and analysed only those radial velocities for which multiple measurements were acquired on the same night, leading to a total of 12, 15, and 11 chunks of nightly FIES, HARPS, and HARPS-N RVs, respectively. The best fitting orbital solution of HD 3167 b was found keeping period and transit ephemeris fixed to the values derived by our joint analysis described in §6.7.3, but allowing the RV semi-amplitude variation $K_{\rm b}$ and the 38 nightly offsets to vary. We also fitted for $\sqrt{e_{\rm b}}\sin\omega_{\star,\rm b}$ and $\sqrt{e_{\rm b}}\cos\omega_{\star,\rm b}$, where $e_{\rm b}$ is the eccentricity and $\omega_{\star,\rm b}$ is the argument of periastron of the star. We also fitted for a constant white noise term – commonly referred to as RV "jitter" term – to account for instrumental velocity noise not included in the nominal uncertainties and/or possible sources of short term stellar variability – such as granulation – not removed by the FCO method. Three independent jitters were added in quadrature to the formal error bars of each instrument. We super-sampled the light curve model using 10 sub-samples per *K2* exposure to account for the long-cadence acquisition (Kipping, 2010, see Appendix A.2).

We adopted uniform priors within a wide range for each parameter and ran 500 independent Markov chains. Once chains converged, we took 25000 iterations using a thin factor of 50, leading to a posterior distribution of 250 000 independent data points for each fitted parameter. The final estimates and their 1-σ uncertainties were taken as the median and the 68 % of the credible interval of the posterior distributions.

We obtained a best fitting non-zero eccentricity of $e_{\rm b} = 0.12 \pm 0.05$. We also fitted the RV data assuming a circular orbit ($\sqrt{e_{\rm b}}\sin\omega_{\star,\rm b} = \sqrt{e_{\rm b}}\cos\omega_{\star,\rm b} = 0$). Figure 6.26 displays our FIES, HARPS, and HARPS-N measurements along with the best fitting circular model. Different symbols refer to different instrument, whereas different colours represent different nights. In order to assess the significance of our result we created 10^5 sets of synthetic RVs that sample the best fitting circular solution at the epochs of our real
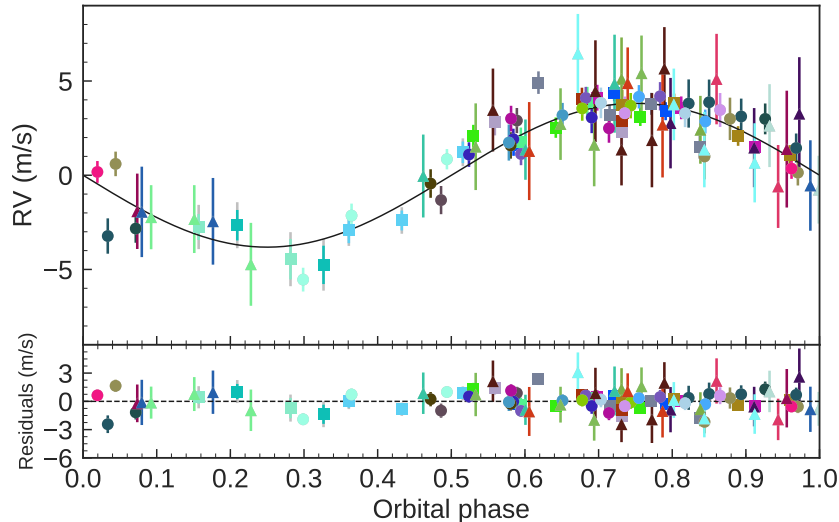
Figure 6.26: The RV curve of HD 3167 phase-folded to the orbital period of planet b, as derived using the FCO method and residuals. The best fitting circular solution is marked with a thick line. The FIES, HARPS, and HARPS-N RV measurements are plotted with triangles, circles, and squares, respectively, along with their formal error bars. Different colours represent measurements from different observing nights.

observations. We added Gaussian noise at the same level of our measurements and fitted the simulated data allowing for an eccentric solution. We found that there is a $\sim 18\%$ probability that a best fitting eccentric solution with $e \geq 0.12$ could have arisen by chance if the orbit were actually circular. As this is above the 5% significance level suggested by Lucy & Sweeney (1971), we decided to conservatively assume a circular model.

We found a radial velocity semi-amplitude variation of $K_\mathrm{b} = 3.81 \pm 0.50 \mathrm{~m\,s^{-1}}$ which translates into a mass of $M_\mathrm{b} = 5.39 \pm 0.72 \, M_\oplus$ for HD 3167 b. We note that the eccentric solution provides a planetary mass that is consistent within 1-σ with the result from the circular model.

6.7.3   Transit and RV joint analysis

We performed a joint modelling of the *K2* and RV measurements with `pyaneti`. We modelled the RV data with two Keplerian signals and fitted the transit light curves using the Mandel & Agol (2002)'s model with a quadratic limb darkening law. We parametrized the limb darkening coefficients following Kipping (2013). To account for the *K2* long cadence data, we integrated the transit models over 10 steps. For each planet i we fitted for the orbital period P, i, time of first transit $T_{0,i}$, scaled semi-major axis $a_i/R_\star$, impact parameter b_i, planet-to-star radius ratio $R_\mathrm{i}/R_\star$, and RV semi-amplitude variation K_i. To account for the RV offset between HARPS and HARPS-N, we fitted also for a systemic velocity for each instrument. We assumed a circular orbit for the inner planet and fitted for $\sqrt{e_c}\sin\omega_{\star,c}$ and $\sqrt{e_c}\cos\omega_{\star,c}$ for the outer planet.

The 30-minute integration time of *K2* smears out the shape of planetary transits increasing the degeneracy between the scaled semi-major axis $a/R_\star$ and the impact parameter b (Csizmadia et al., 2011). We therefore set Gaussian priors for $a_\mathrm{i}/R_\star$ for both planets using the stellar mass and radius (Sect., 4 of Gandolfi et al., 2017) and constrained and the orbital period of both planets through Kepler's third law. We did not add RV jitter terms at this stage of our analysis.

We explored the parameter space with 500 independent chains created randomly inside

the prior ranges for each parameter, as listed in the second column of Table 6.8. Once all chains converged, we ran 25000 more iterations with a thin factor of 50. This led to a posterior distribution of 250000 independent points for each fitted parameter.

The two-planet model provides a poor fit to the HARPS and HARPS-N measurements with a RV χ^2 of 597 and $\chi^2/\mathrm{dof} = 8.7$, suggesting that additional signals might be present in the data, as discussed in the next section.

Gandolfi et al. (2017) found two additional signals with periods of 6.0 and 10.7 days in the HARPS and HARPS-N measurements. However, the sampling of the observations, as well as the limited number of RVs and their noise level do not allow us to assess whether the two signals are due to activity, or are rather induced by two additional orbiting planets. We thus include the two signals in our analysis to account for these extra sinusoidal signals, but warn the reader that more observations are needed to unveil their true nature.

6.7.4   Joint two-planet and stellar activity modelling

We used `pyaneti` to perform the final joint modelling of the *K2* and RV measurements. We fitted the transit and RV curves of HD 3167 b and c following the guidelines presented in § 6.7.3, and incorporated the modelling of the two additional RV signals at 6.0 and 10.7 days using two sinusoidal curves (see Appendix B). We set uniform priors for the periods of the two additional signals – using a 2-day range centred around the values found by the frequency analysis presented in Gandolfi et al. (2017) – and adopted uniform priors for the corresponding phases and amplitudes (details in Table 6.8). To account for additional instrumental noise not included in the nominal RV error bars and/or imperfect treatment of the various sources of RV variations (e.g., stellar activity and/or additional planets), we added jitter terms to the equation of the likelihood for the HARPS and HARPS-N RV measurements.

We display the posterior distribution for each fitted parameter in Figure 6.27. The parameter estimates and their error bars were taken to be the median and the 68 % credible interval of the final posterior probability distribution of each parameter. We report our results in Table 6.8. Fig. 6.28 shows the *K2* transit light curves and best fitting transit models, as well as the HARPS and HARPS-N RVs and best fitting Keplerian models of HD 3167 b and c. The RV fits to the two additional signals at 6.0 and 10.7 days are shown in Fig. 6.29. Figure 6.30 shows two consecutive transits of HD 3167 b and HD 3167 c to show the difference in transit depth and duration for both planets.

6.7.5   Planet's masses

The mass of HD 3167 b is in very good agreement with the value we derived using the FCO method corroborating our analysis (cfr. § 6.7.2). Does the inclusion of the 6.0 and 10.7-day signals bias the mass determinations of HD 3167 b and HD 3167 c ? A two-planet model fit that includes only planet b and c gives RV semi-amplitude variations of $K_\mathrm{b} = 3.74 \pm 0.39\ \mathrm{m\,s^{-1}}$ and $K_\mathrm{c} = 2.29 \pm 0.45\ \mathrm{m\,s^{-1}}$, respectively. By adding only the 10.7-day signal we get $K_\mathrm{b} = 4.06 \pm 0.37\,\mathrm{m\,s^{-1}}$ and $K_\mathrm{c} = 2.04 \pm 0.43\,\mathrm{m\,s^{-1}}$. By adding both the 10.7-day and the 6.0-day signal we obtain $K_\mathrm{b} = 4.02 \pm 0.31\,\mathrm{m\,s^{-1}}$ and $K_\mathrm{c} = 1.88^{+0.40}_{-0.42}\,\mathrm{m\,s^{-1}}$, proving that the RV semi-amplitude variations – and thus the determination of the planetary masses of HD 3167 b and HD 3167 c – are not significantly affected by the inclusion of the two additional signals.
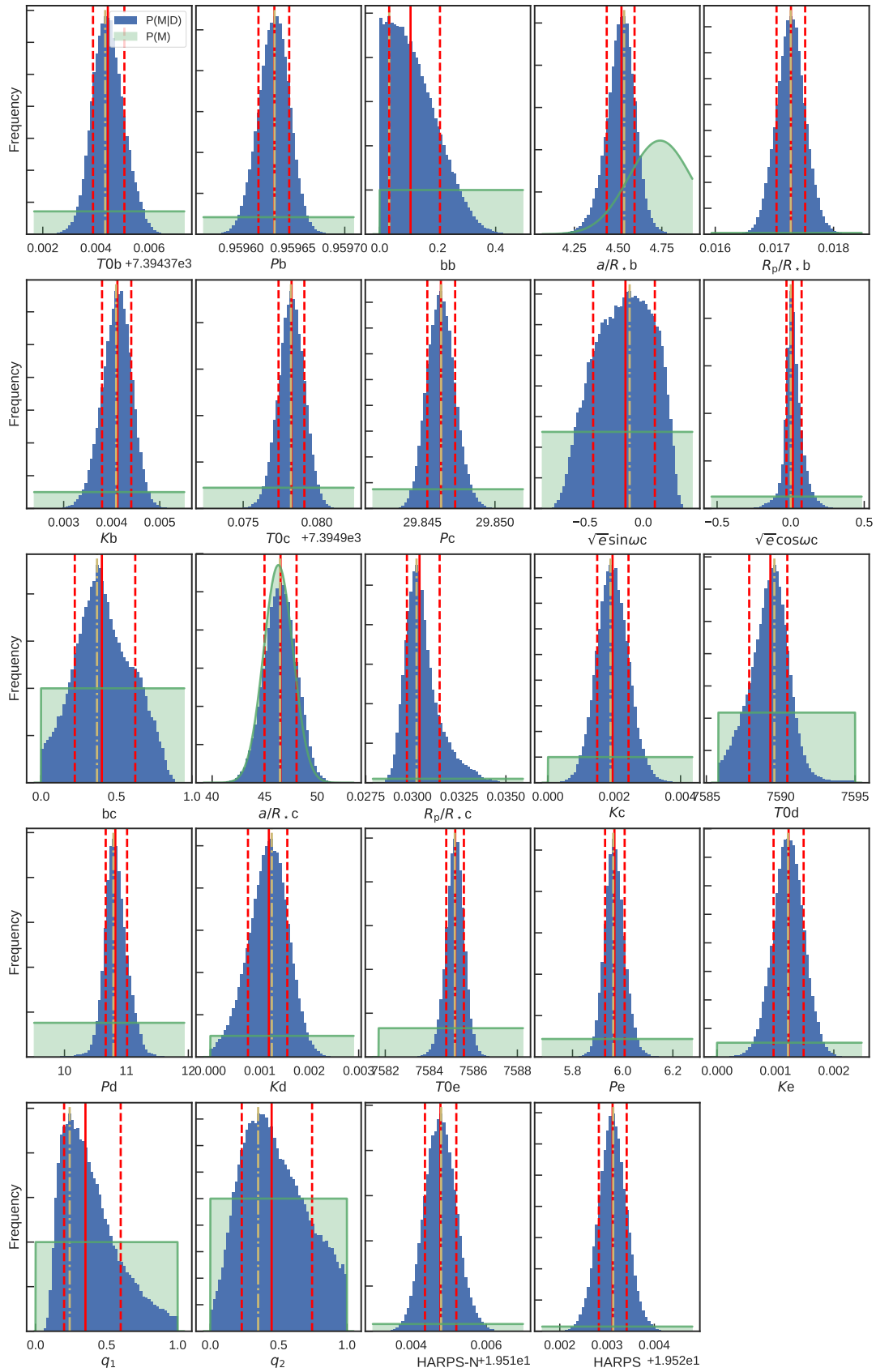
Figure 6.27: Posterior distributions of the HD 3167's fitted parameters as obtained from the final analysis performed with `pyaneti`. The blue region corresponds to the posterior $P(M|D)$, whereas the green shaded area marks the prior shape $P(M)$. Median (red solid line), 68% credible interval (red dashed line), and mode (yellow dash-dotted line) are also shown.

Table 6.8: HD 3167 system parameters.

Parameter	Prior[a]	Final value
Stellar parameters[b]		
Star mass $M_\star$ ($M_\odot$)	$\cdots$	0.877 ± 0.024
Star radius $R_\star$ ($R_\odot$)	$\cdots$	0.835 ± 0.026
Effective Temperature T_{eff} (K)	$\cdots$	5286 ± 40
Model Parameters for HD 3167 b		
Orbital period P_{orb} (day)	$\mathcal{U}[0.9596, 0.9598]$	0.959632 ± 0.000015
Transit epoch T_0 ($BJD_{TDB} - 2\,450\,000$)	$\mathcal{U}[7394.3675, 7394.3763]$	$7394.37442^{+0.00060}_{-0.00055}$
Scaled semi-major axis $a/R_\star$	$\mathcal{N}[4.74, 0.18]$	$4.516^{+0.076}_{-0.085}$
Scaled planet radius $R_p/R_\star$	$\mathcal{U}[0, 0.5]$	0.01728 ± 0.00025
Impact parameter, b	$\mathcal{U}[0, 1]$	$0.11^{+0.11}_{-0.08}$
Radial velocity semi-amplitude variation K (m s^{-1})	$\mathcal{U}[0, 100]$	4.02 ± 0.31
$\sqrt{e}\sin\omega$	$\mathcal{F}[0]$	0
$\sqrt{e}\cos\omega$	$\mathcal{F}[0]$	0
Model Parameters for HD 3167 c		
Orbital period P_{orb} (day)	$\mathcal{U}[29.8508, 29.8532]$	$29.84622^{+0.00098}_{-0.00091}$
Transit epoch T_0 ($BJD_{TDB} - 2\,450\,000$)	$\mathcal{U}[7394.9763, 7394.9787]$	7394.97831 ± 0.00085
Scaled semi-major axis $a/R_\star$	$\mathcal{N}[46.3, 1.4]$	46.5 ± 1.5
Scaled planet radius $R_p/R_\star$	$\mathcal{U}[0, 0.5]$	$0.03006^{+0.00065}_{-0.00055}$
Impact parameter, b	$\mathcal{U}[0, 1]$	$0.30^{+0.11}_{-0.18}$
Radial velocity semi-amplitude variation K (m s^{-1})	$\mathcal{U}[0, 100]$	$1.88^{+0.40}_{-0.42}$
$\sqrt{e}\sin\omega$	$\mathcal{U}[-1, 1]$	$0.00^{+0.17}_{-0.24}$
$\sqrt{e}\cos\omega$	$\mathcal{U}[-1, 1]$	$0.06^{+0.16}_{-0.17}$
Signal with period of 10.7 days		
Period P_{orb} (days)	$\mathcal{U}[9.4, 12.0]$	$10.77^{+0.15}_{-0.13}$
Radial velocity semi-amplitude variation K (m s^{-1})	$\mathcal{U}[0, 100]$	$1.34^{+0.27}_{-0.28}$
Signal with period of 6.0 days		
Period P_{orb} (days)	$\mathcal{U}[5.4, 6.5]$	$5.967^{+0.038}_{-0.035}$
Radial velocity semi-amplitude variation K (m s^{-1})	$\mathcal{U}[0, 100]$	1.26 ± 0.25
Other Parameters		
Systemic velocity γ_{HARPS} (km s^{-1})	$\mathcal{U}[19.4183, 19.6317]$	19.52311 ± 0.00029
Systemic velocity $\gamma_{HARPS-N}$ (km s^{-1})	$\mathcal{U}[19.4086, 19.6197]$	19.51471 ± 0.00036
RV jitter term σ_{HARPS} (m s^{-1})	$\mathcal{U}[0, 10]$	$1.44^{+0.24}_{-0.21}$
RV jitter term $\sigma_{HARPS-N}$ (m s^{-1})	$\mathcal{U}[0, 10]$	$0.95^{+0.24}_{-0.20}$
Parameterized limb-darkening coefficient q_1	$\mathcal{U}[0, 1]$	$0.34^{+0.26}_{-0.15}$
Parameterized limb-darkening coefficient q_2	$\mathcal{U}[0, 1]$	$0.47^{+0.29}_{-0.22}$
Derived Parameters for HD 3167 b		
Planet mass M_p ($M_\oplus$)	$\cdots$	5.69 ± 0.44
Planet radius R_p ($R_\oplus$)	$\cdots$	1.574 ± 0.054
Mean density ρ_b (g cm^{-3})	$\cdots$	$8.00^{+1.10}_{-0.98}$
Eccentricity e	$\cdots$	0 (fixed)
Semi-major axis of the planetary orbit a (AU)	$\cdots$	0.01752 ± 0.00063
Orbit inclination i_p ($^\circ$)	$\cdots$	$88.6^{+1.0}_{-1.4}$
Transit duration τ_{14} (hours)	$\cdots$	1.65 ± 0.03
Equilibrium temperature[c] T_{eq} (K)	$\cdots$	1759 ± 20
Derived Parameters for HD 3167 c		
Planet mass M_p ($M_\oplus$)	$\cdots$	$8.33^{+1.79}_{-1.85}$
Planet radius R_p ($R_\oplus$)	$\cdots$	$2.740^{+0.106}_{-0.100}$
Mean density ρ_c (g cm^{-3})	$\cdots$	$2.21^{+0.56}_{-0.53}$
Eccentricity e	$\cdots$	$0.05^{+0.07}_{-0.04}$
Argument of periastron $w_\star$ ($^\circ$)	$\cdots$	178^{+134}_{-136}
Semi-major axis of the planetary orbit a (AU)	$\cdots$	0.1806 ± 0.0080
Orbit inclination i_p ($^\circ$)	$\cdots$	89.6 ± 0.2
Transit duration τ_{14} (hours)	$\cdots$	$4.81^{+0.17}_{-0.09}$
Equilibrium temperature[c] T_{eq} (K)	$\cdots$	548 ± 10
Linear limb-darkening coefficient u_1	$\cdots$	$0.54^{+0.15}_{-0.17}$
Quadratic limb-darkening coefficient u_2	$\cdots$	$0.04^{+0.35}_{-0.27}$

Note – [a] $\mathcal{U}[a, b]$ refers to uniform priors between a and b, $\mathcal{N}[a, b]$ means Gaussian priors with mean a and standard deviation b and $\mathcal{F}[a]$ to a fixed a value. [b] Details about the stellar parameter estimation are given in Gandolfi et al. (2017). [c] Assuming albedo $= 0$.
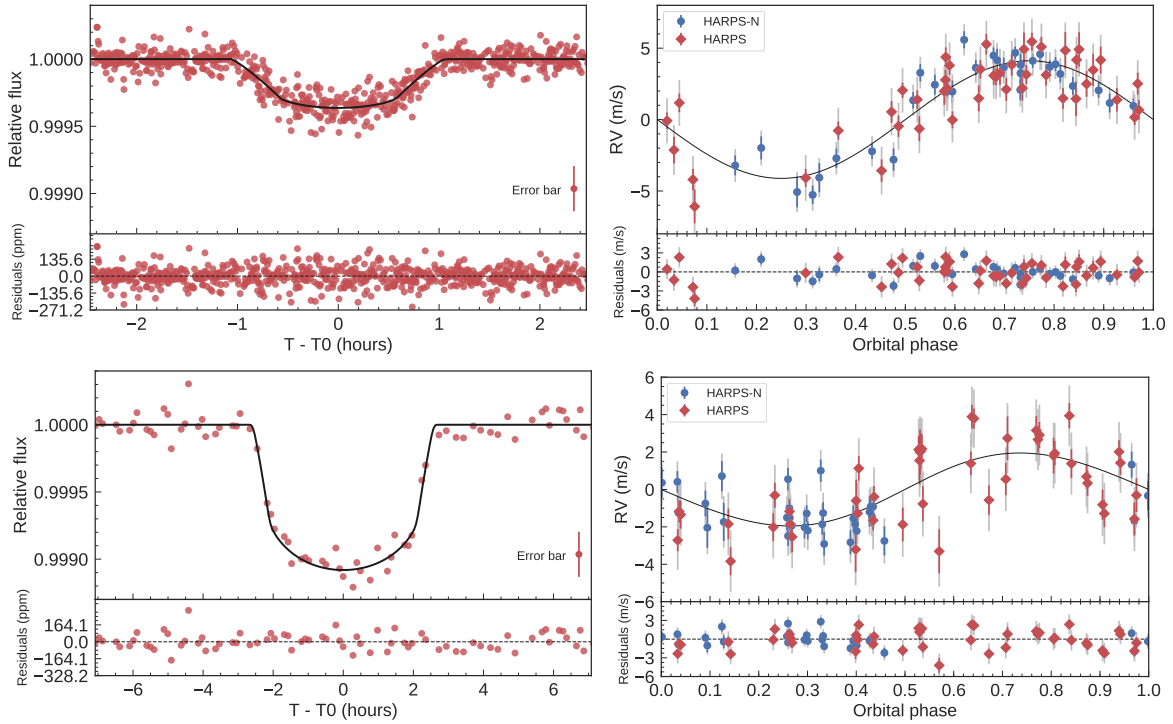
Figure 6.28: Transit light curves and RV curves of HD 3167 due to planet b (upper panels) and c (lower panels). The best fitting transit and Keplerian models are overplotted with thick black lines. The *K2* data points are shown with red circles (left panels). The HARPS and HARPS-N RV measurements are plotted with red circles and blue diamonds, respectively, along with their nominal uncertainties (right panels). The RV curves are phase-folded to the orbital period of the two planets, following the subtraction of the systemic velocities and other signals, except planet b (upper right panel) and c (lower right panel).
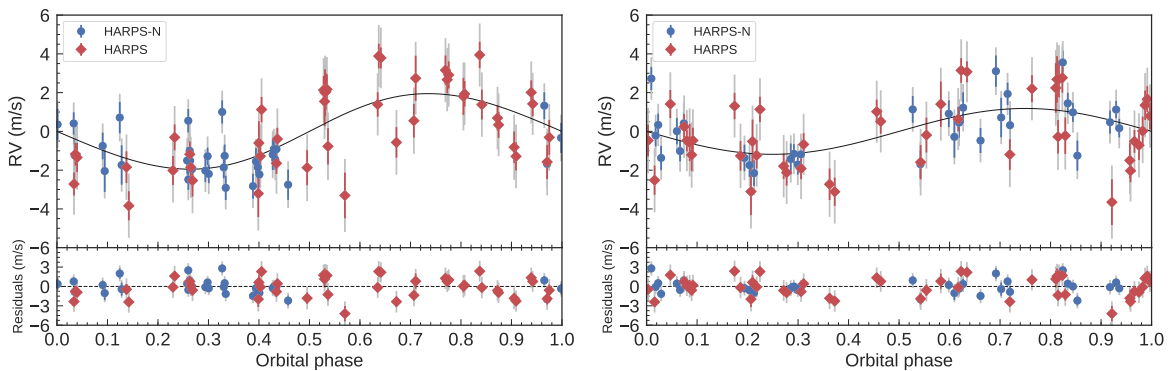
Figure 6.29: Radial velocity curves of the two signals at 10.7 days (left panel) and 6.0 days (right panel) and best-fitting models. The HARPS and HARPS-N RV measurements are plotted with red circles and blue diamonds, respectively, along with their nominal uncertainties.
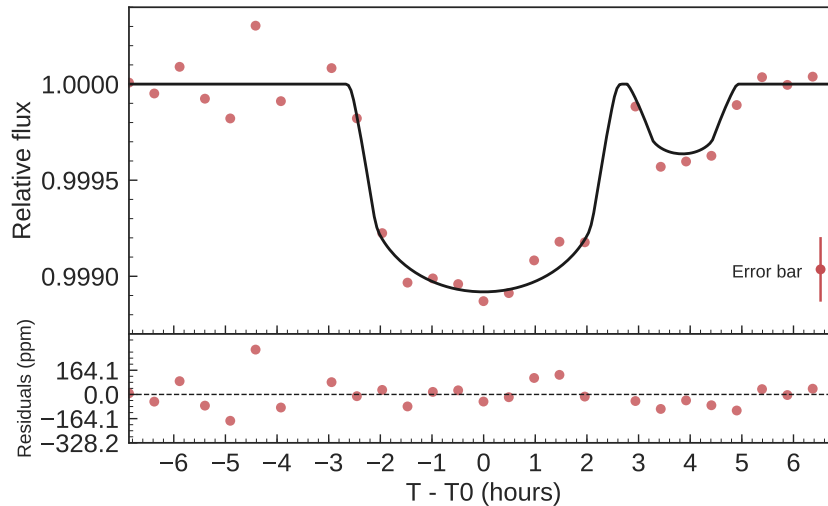
Figure 6.30: Consecutive transits of HD 3167 b and HD 3167 c. The *K2* data points are shown with red circles. The best fitting transit model is overplotted with thick black lines. Note the different depth and duration.

6.7.6   Planet's composition

The ultra-short period planet HD 3167 b has a mass of $M_b = 5.69 \pm 0.44\ M_\oplus$ and a radius of $R_b = 1.574 \pm 0.054\ R_\oplus$, yielding a mean density of $\rho_b = 8.00^{+1.10}_{-0.98}$ g cm^{-3}. Figure 6.31 displays the position of HD 3167 b on the mass-radius diagram compared to the sub-sample of small transiting planets ($R \leq 4\ R_\oplus$) whose masses and radii have been derived with a precision better than 20 %. Theoretical models from Zeng et al. (2016) are over-plotted using different lines and colours. The precision of our mass determination ($\sim 8\ \%$) allows us to conclude that HD 3167 b is a rocky terrestrial planet with a composition consisting of $\sim 50\ \%$ silicate and $\sim 50\%$ iron.

With a mass of $M_c = 8.33^{+1.79}_{-1.85}\ M_\oplus$ and a radius of $R_c = 2.740^{+0.106}_{-0.100}\ R_\oplus$ the outer planet HD 3167 c has a mean density of $\rho_b = 2.21^{+0.56}_{-0.53}$ g cm^{-3}, which is consistent with a com-position comprising a solid core surrounded by a thick atmosphere. HD 3167 c joins the small group of low-density mini-Neptunes with precise mass and radius determinations (see Fig. 6.31).

HD 3167 c is expected to have a completely different nature with respect to the inner planet b. Despite the lack of mass measurements, Vanderburg et al. (2016) noticed that HD 3167 c may be a primary target for transmission spectroscopy. The rather large pres-sure scale height of about 350 km and the brightness of the host star (V=8.9 mag) make HD 3167 c an ideal target for transmission spectroscopy observations across a wide range of wavelengths, from the far-ultraviolet to the infrared. One can expect the planet to have a rather large hydrogen-rich cloud made of gas escaping from the planetary upper atmosphere under the effect of the high-energy stellar radiation, similarly to GJ 436 b (Kulow et al., 2014; Ehrenreich et al., 2015). This cloud would be detectable at Lyα dur-ing primary transit. Such observations would then provide us with crucial information about the properties of the upper planetary atmosphere and its environment (e.g., stellar wind density and velocity). Observations at longer wavelengths would instead give us the opportunity to study the lower atmosphere and infer its chemical composition and physical properties. HD 3167 c appears to be one of the best candidates to investigate the atmosphere of a low-mass planet.
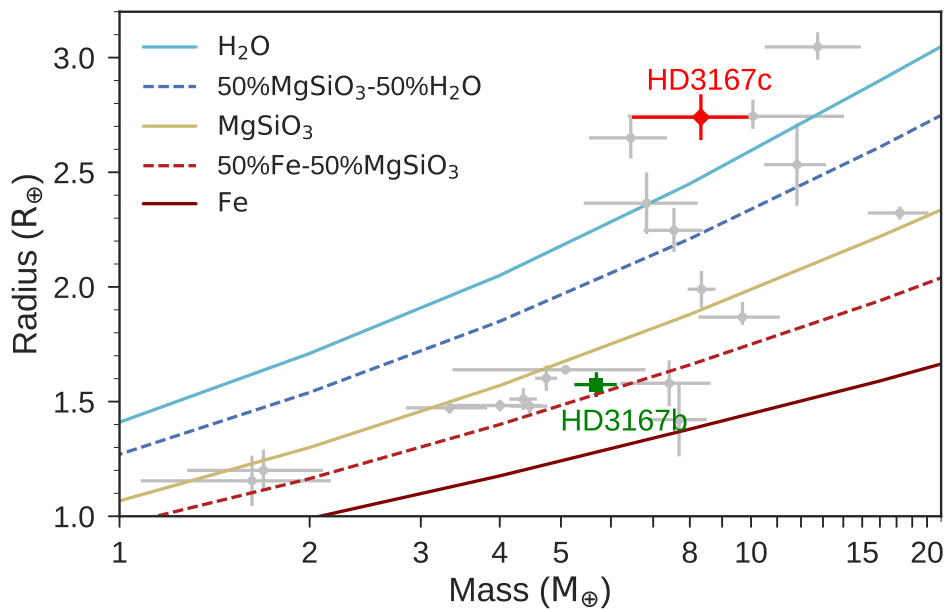
Figure 6.31: Mass-radius diagram for well-characterised (5-σ precision level or better) super-Earths and Neptunes. From bottom to top, the solid curves are theoretical models (Zeng et al., 2016) for planets with a composition of 100% iron (brown), 50% silicate and 50% iron (dashed red), 100% silicate (beige), 50% silicate and 50% water (dashed blue), water (light blue). HD 3167 b & HD 3167 c are highlighted with different symbols and colours.

6.8 GJ 9827: The different nature of three neighbouring worlds

GJ 9827 is a relatively bright ($V = 10.39$ mag) late K-dwarf star at 30 pc from the Solar system. Using data from *K2*'s Campaign 12, Niraula et al. (2017) reported on the discovery of 3 transiting planets around this star. As part of this thesis, we ran an independent MCMC analysis using `pyaneti` in order to corroborate the results reported in Table 1 of Niraula et al. (2017). This discovery was also announced independently by Rodriguez et al. (2018).

An intense ground-based follow up is presented by the KESPRINT team in Prieto-Arranz et al. (2018). Details about the observations and stellar characterisation are given in detail in Prieto-Arranz et al. (2018). The RV follow-up, and the parameter estimation from the light curve and RV data were carried out as part of this thesis. We provide details below.

6.8.1 Light curve and RV data

Figure 6.32 shows the *K2* light curve of GJ 9827 as extracted by Vanderburg & Johnson (2014). For the data analysis presented in Sect. 6.8.2 we used the light curve extracted and flattened from the *K2* raw target pixel files as in Dai et al. (2017).

The RV data are presented in Prieto-Arranz et al. (2018). The data consists of 35 HARPS RVs taken under programs 099.C-0491 and 0100.C-0808, and 23 HARPS-N RV measurements acquired under the programs OPT17A_64 and A36TAC_12. The HARPS spectra were gathered from August 19 to October 24 2017 UT, and the HARPS-N spectra from July 29 to December 9 2017 UT. We used the second fibre of both instruments to monitor the sky background. The HARPS and HARPS-N spectra were reduced and extracted using the dedicated data reduction software (DRS). The RVs were measured by cross-correlating the Echelle orders of the observed spectra with a K5 numerical mask (Baranne et al., 1996; Pepe et al., 2002) and by fitting a Gaussian function to the average cross-correlation function (CCF). The list of HARPS and HARPS-N measurements are presented in Prieto-Arranz et al. (2018).

6.8.2 Multi-planet joint analysis

We performed the joint analysis to the photometric and RV data with `pyaneti` (Barragán et al., 2019, see Sect. 5.3). We fitted Keplerian orbits to the RV data and used the limb-darkened quadratic transit model by Mandel & Agol (2002) for the *K2* transit light curves. In order to account for the *Kepler* long-cadence acquisition, we super-sampled the transit models using 10 subsamples per *K2* exposure (Kipping, 2010, see Appendix A.2).

We fitted for a transit and a RV signal for each of the three planets. We sampled for $\rho_\star^{1/3}$ and recovered the scaled semi-major axis ($a_{\rm p}/R_\star$) of the three planets using Kepler's third law. We used uniform priors for all the parameters, except for the limb darkening coefficients for which we set Gaussian priors as described in Niraula et al. (2017). Details about fitted parameters and priors are given in Table 6.10.

6.8.3 Stellar activity modelling

The RV data of GJ 9827 shows activity-induced RV at the stellar rotation frequency and its harmonics, with an estimated semi-amplitude of $\sim 3 \, \mathrm{m \, s^{-1}}$ (See Sect. 4 of Prieto-Arranz et al., 2018). The light curve of GJ 9827 (Fig. 6.32) suggests that the evolution time scale of active regions is longer than the *K2* observations (~ 80 days). Since our FIES, HARPS, and HARPS-N RV follow-up covers ~ 140 days, we can model the RV
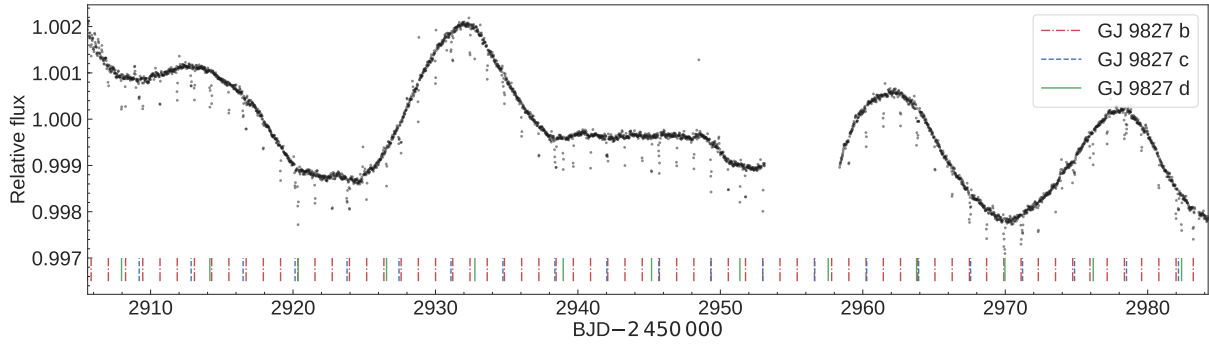
Figure 6.32: *K2* light curve of GJ 9827 extracted by Vanderburg & Johnson (2014). Stellar activity is seen as the quasi-periodic, long period modulation. Transit positions for the three planets are marked with vertical lines.

Table 6.9: Model comparison for GJ 9827.

Model	$K_{\rm b}$ (m s^{-1})	$K_{\rm c}$ (m s^{-1})	$K_{\rm d}$ (m s^{-1})	$K_{\rm rot}$ (m s^{-1})	$K_{\rm rot/2}$ (m s^{-1})	χ^2/dof	BIC
3P	2.86 ± 0.28	0.80 ± 0.24	1.26 ± 0.25	0	0	2.8	-500
3P + P$_{\rm rot}$	2.96 ± 0.30	1.11 ± 0.27	0.99 ± 0.26	5.68 ± 0.84	0	1.9	-539
3P + P$_{\rm rot/2}$	3.01 ± 0.28	0.85 ± 0.27	1.16 ± 0.27	0	3.18 ± 0.38	1.4	-564
3P + P$_{\rm rot}$ + P$_{\rm rot/2}$	2.98 ± 0.31	0.82 ± 0.27	1.25 ± 0.30	$0.64^{+1.10}_{-0.47}$	3.27 ± 0.50	1.7	-488

induced signal using a coherent sinusoidal signals at the stellar rotation frequency and its harmonics, similarly to the work described in, e.g., Pepe et al. (2013) and Barragán et al. (2018a, see Appendix B).

In order to check which Fourier components at the rotation frequency and its harmonics can better describe the activity signal, we tested different RV models. The first model (3P) includes only the three planetary signals. The second model (3P+P$_{\rm rot}$) is obtained from 3P by adding a sinusoidal signal at the rotation period of the star ($P_{\rm rot}$ ~30 days). The third model called 3P+P$_{\rm rot}$/2 includes three Keplerians and a sinusoidal signal at half the rotation period (~15 days). We also tested a model where two sinusoidal signals at both P$_{\rm rot}$ and P$_{\rm rot}$/2 were included. Since the stellar rotation period is not well constrained, we set uniform priors in the ranges $[P_{\rm rot} - 2 : P_{\rm rot} + 2]$ and $[P_{\rm rot/2} - 1 : P_{\rm rot/2} + 1]$.

Table 6.9 summarises the results of our test, showing the goodness of the fit for each model. With the lowest Bayesian information criteria (BIC), the preferred model is 3P+P$_{\rm rot}$/2 (3 planets plus one sinusoidal signal at ~15 days). Table 6.9 shows also that the semi-amplitudes of the three planetary signals do not change significantly when considering different models, providing evidence that the Doppler motion induced by the three planets is present in our RV data-set and does not depend on the Fourier components used to model the activity-induced RV signal.

We emphasise that our approach of treating the RV stellar signal as a coherent signal at the first harmonic of the rotation frequency relies on the fact that the *K2* light curve provides evidence that the evolution time-scale of active regions is longer than the duration of our RV follow-up. Unfortunately, the assumption of a coherent stellar signal does not hold for the RV measurements presented by Teske et al. (2018) because their follow-up spans ~7 years with average gaps of ~69 days.

Table 6.10: GJ 9827 fitted parameters.

Parameter	Prior[a]	Final value
Model Parameters for GJ 9827 b		
Orbital period $P_{\rm orb}$ (day)	$\mathcal{U}[1.2089, 1.2091]$	1.208966 ± 0.000012
Transit epoch T_0 (BJD$_{\rm TDB}$$-2\,450\,000$)	$\mathcal{U}[7738.8226, 7738.8289]$	7738.82646 ± 0.00043
Scaled planet radius $R_{\rm p}/R_\star$	$\mathcal{U}[0, 0.05]$	$0.02322^{+0.00058}_{-0.00037}$
Impact parameter, b	$\mathcal{U}[0, 1]$	$0.21^{+0.23}_{-0.14}$
RV semi-amplitude variation K (m s^{-1})	$\mathcal{U}[0, 50]$	3.00 ± 0.35
$\sqrt{e}\sin\omega$	$\mathcal{F}[0]$	0
$\sqrt{e}\cos\omega$	$\mathcal{F}[0]$	0
Model Parameters for GJ 9827 c		
Orbital period $P_{\rm orb}$ (day)	$\mathcal{U}[3.6477, 3.6493]$	3.64823 ± 0.00012
Transit epoch T_0 (BJD$_{\rm TDB}$$-2\,450\,000$)	$\mathcal{U}[7738.5380, 7738.5579]$	7738.5496 ± 0.0015
Scaled planet radius $R_{\rm p}/R_\star$	$\mathcal{U}[0, 0.05]$	$0.01820^{+0.00054}_{-0.00041}$
Impact parameter, b	$\mathcal{U}[0, 1]$	$0.25^{+0.21}_{-0.16}$
RV semi-amplitude variation K (m s^{-1})	$\mathcal{U}[0, 50]$	0.82 ± 0.32
$\sqrt{e}\sin\omega$	$\mathcal{F}[0]$	0
$\sqrt{e}\cos\omega$	$\mathcal{F}[0]$	0
Model Parameters for GJ 9827 d		
Orbital period $P_{\rm orb}$ (day)	$\mathcal{U}[6.2003, 6.2024]$	6.20142 ± 0.00013
Transit epoch T_0 (BJD$_{\rm TDB}$$-2\,450\,000$)	$\mathcal{U}[7740.9564, 7740.9684]$	7740.96198 ± 0.00086
Scaled planet radius $R_{\rm p}/R_\star$	$\mathcal{U}[0, 0.05]$	$0.02993^{+0.00101}_{-0.00078}$
Impact parameter, b	$\mathcal{U}[0, 1]$	$0.864^{+0.022}_{-0.013}$
RV semi-amplitude variation K (m s^{-1})	$\mathcal{U}[0, 50]$	1.11 ± 0.32
$\sqrt{e}\sin\omega$	$\mathcal{F}[0]$	0
$\sqrt{e}\cos\omega$	$\mathcal{F}[0]$	0
Extra sinusoidal signal		
Orbital period $P_{\rm orb}$ (day)	$\mathcal{U}[13.5, 15.5]$	14.46 ± 0.11
Transit epoch T_0 (BJD$_{\rm TDB}$$-2\,450\,000$)	$\mathcal{U}[7734.85, 7749.15]$	$7739.87^{+1.96}_{-1.92}$
RV semi-amplitude variation K (m s^{-1})	$\mathcal{U}[0, 50]$	3.15 ± 0.44
Other Parameters		
Stellar density parametrization $\rho_\star^{1/3}$ (g$^{1/3}$cm^{-1})	$\mathcal{U}[0.01, 2.3]$	$1.697^{+0.044}_{-0.128}$
Systemic velocity $\gamma_{\rm HARPS}$ (km s^{-1})	$\mathcal{U}[31.9310, 31.9621]$	$31.94794^{+0.00036}_{-0.00036}$
Systemic velocity $\gamma_{\rm HARPS-N}$ (km s^{-1})	$\mathcal{U}[31.9312, 31.9636]$	$31.94888^{+0.00035}_{-0.00034}$
Systemic velocity $\gamma_{\rm FIES}$ (km s^{-1})	$\mathcal{U}[31.7624, 31.7896]$	$31.7737^{+0.0014}_{-0.0014}$
RV jitter term $\sigma_{\rm HARPS}$ (m s^{-1})	$\mathcal{U}[0, 10]$	$0.96^{+0.37}_{-0.39}$
RV jitter term $\sigma_{\rm HARPS-N}$ (m s^{-1})	$\mathcal{U}[0, 10]$	$0.61^{+0.48}_{-0.40}$
RV jitter term $\sigma_{\rm FIES}$ (m s^{-1})	$\mathcal{U}[0, 10]$	$1.25^{+1.55}_{-0.89}$
Parameterized limb-darkening coefficient q_1	$\mathcal{N}[0.52, 0.1]$	$0.53^{+0.09}_{-0.09}$
Parameterized limb-darkening coefficient q_2	$\mathcal{N}[0.40, 0.1]$	$0.34^{+0.09}_{-0.09}$

Note – The derived parameters are shown in Table 6.11. [a] $\mathcal{U}[a, b]$ refers to uniform priors between a and b, $\mathcal{N}[a, b]$ means Gaussian priors with mean a and standard deviation b and $\mathcal{F}[a]$ to a fixed a value. [b] Details about the stellar parameter estimation are given in Gandolfi et al. (2017). [c] Assuming albedo $= 0$.

6.8.4   Joint three planet and stellar activity modelling

We performed the final joint analysis assuming that the RV data are described by the $3P+P_{rot/2}$ model. For the phase, amplitude, and period of the activity signal we adopted uniform priors (see Table 6.10). We included a jitter term for each spectrograph to account for additional instrumental noise not included in the nominal RV error bars and/or imperfect treatment of the various sources of RV variations. Since GJ 9827 hosts a short-period multi-planetary system, we assumed tidal circularisation of the orbits and fixed $e = 0$ for all three planets (Van Eylen & Albrecht, 2015).

We explored the parameter space with 500 Markov chains initialised at random positions inside the prior ranges. Once all chains converged, we ran 5000 iterations more. We used a thin factor of 10 to generate a posterior distribution of 250,000 independent points for each parameter.

The inferred posterior distributions for each fitted parameter are shown in Figure 6.33. We derived parameter values and uncertainties from the median and the 68.3% credible intervals of their posterior distributions. Fitted and derived parameters are reported in Tables 6.10 and 6.11, respectively. The inferred models for each planet for the light curve and RV data are shown in Fig. 6.34. Figure 6.35 shows the stellar activity induced RV signal together with the inferred sinusoidal model. In Fig. 6.36 we show simultaneous transits of the three planets to show explicitly the differences on transit depths and durations.

6.8.5   Planet masses

We determined masses, radii, and densities of the three planets known to transit GJ 9827. We found that GJ 9827 b has a mass of $M_b = 3.69 \pm 0.47 \, M_\oplus$ and a radius of $R_b = 1.58 \pm 0.14 \, R_\oplus$, yielding a mean density of $\rho_b = 5.11^{+1.74}_{-1.27} \, \mathrm{g \, cm^{-3}}$. GJ 9827 c has a mass of $M_c = 1.45 \pm 0.57 \, M_\oplus$, radius of $R_c = 1.24 \pm 0.11 \, R_\oplus$, and a mean density of $\rho_c = 4.13^{+2.31}_{-1.77} \, \mathrm{g \, cm^{-3}}$. For GJ 9827 d we derived $M_d = 2.35_{\pm}0.69 \, M_\oplus$, $R_d = 2.04 \pm 0.18 \, R_\oplus$, and $\rho_d = 1.51^{+0.71}_{-0.53} \, \mathrm{g \, cm^{-3}}$. GJ 9827 is the brightest (V=10.35 ± 0.10 mag) multiplanet system for which the masses of all transiting planets have been measured.

6.8.6   Planet composition

GJ 9827 hosts a canonical terrestrial planet, GJ 9827 c, and two planets close to the radius valley (§ 1.5.3) but from different sides: the super-Earth GJ 9827 b and the sub-Neptune GJ 9827 d. Fig. 6.37 shows the position of the three planets in the mass-radius diagram along with the Zeng et al. (2016)'s theoretical models for different internal compositions. Planets b and c may have rocky nuclei with traces of lighter elements. Given its radius, planet d is likely surrounded by a large gaseous H/He-rich envelope. Since the innermost planets lie on the same isocomposition line of $\sim 80\% \mathrm{MgSiO_3}$-$20\% \mathrm{H_2O}$ (Fig. 6.37), we can speculate that the outer planet might have a nucleus with similar composition too. According to Wolfgang & Lopez (2015), the atmosphere of GJ 9827 d would account for up to only $\sim 1\%$ of the total mass, yielding to a thickness of $\sim 0.6 \, R_\oplus$, that is, $\sim 30\%$ of the planet's radius.
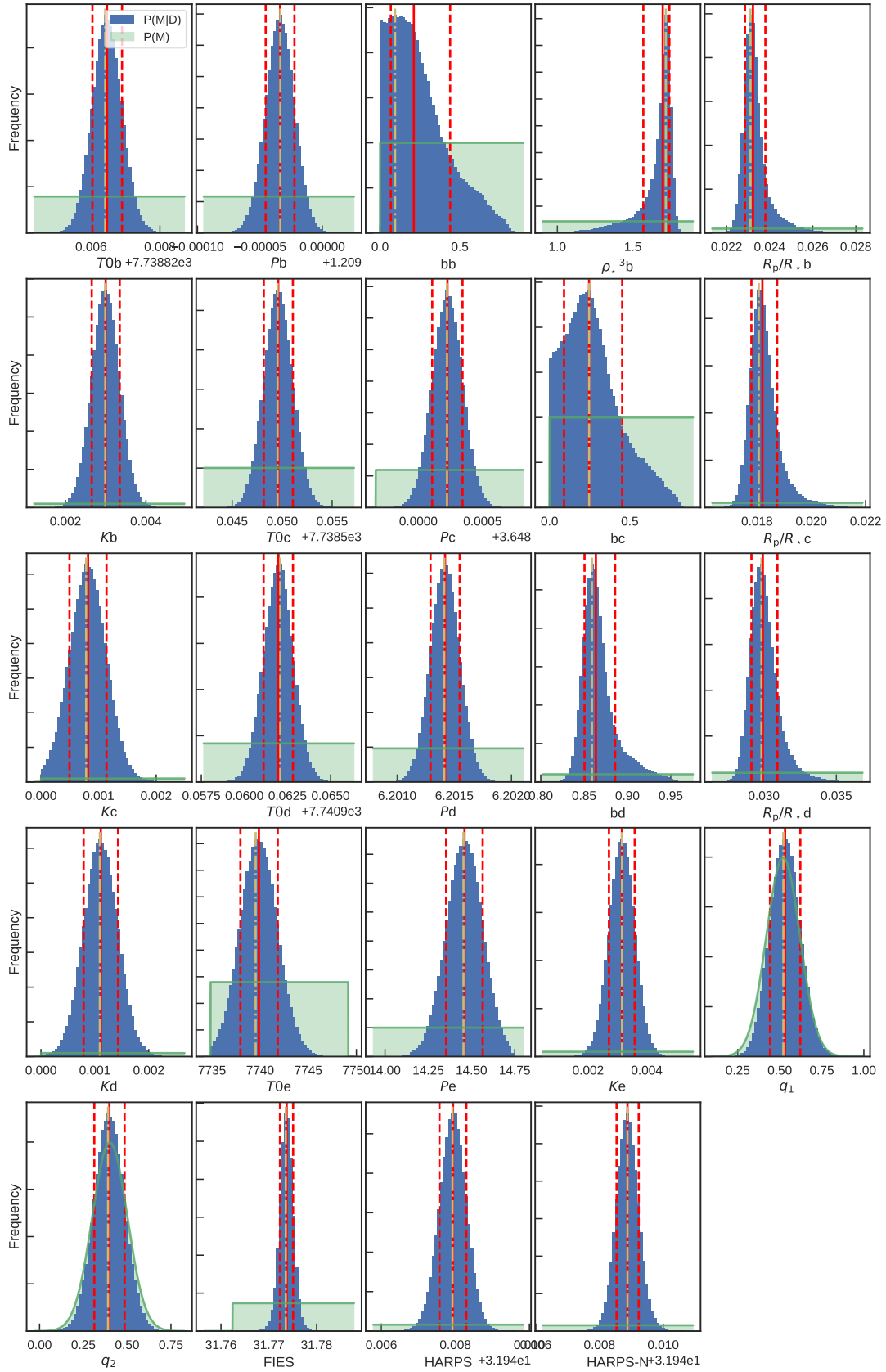
Figure 6.33: Posterior distributions of the GJ 9827's fitted parameters as obtained from the final analysis performed with `pyaneti`. The blue region corresponds to the posterior $P(M|D)$, whereas the green shaded area marks the prior shape $P(M)$. Median (red solid line), 68% credible interval (red dashed line), and mode (yellow dash-dotted line) are also shown.
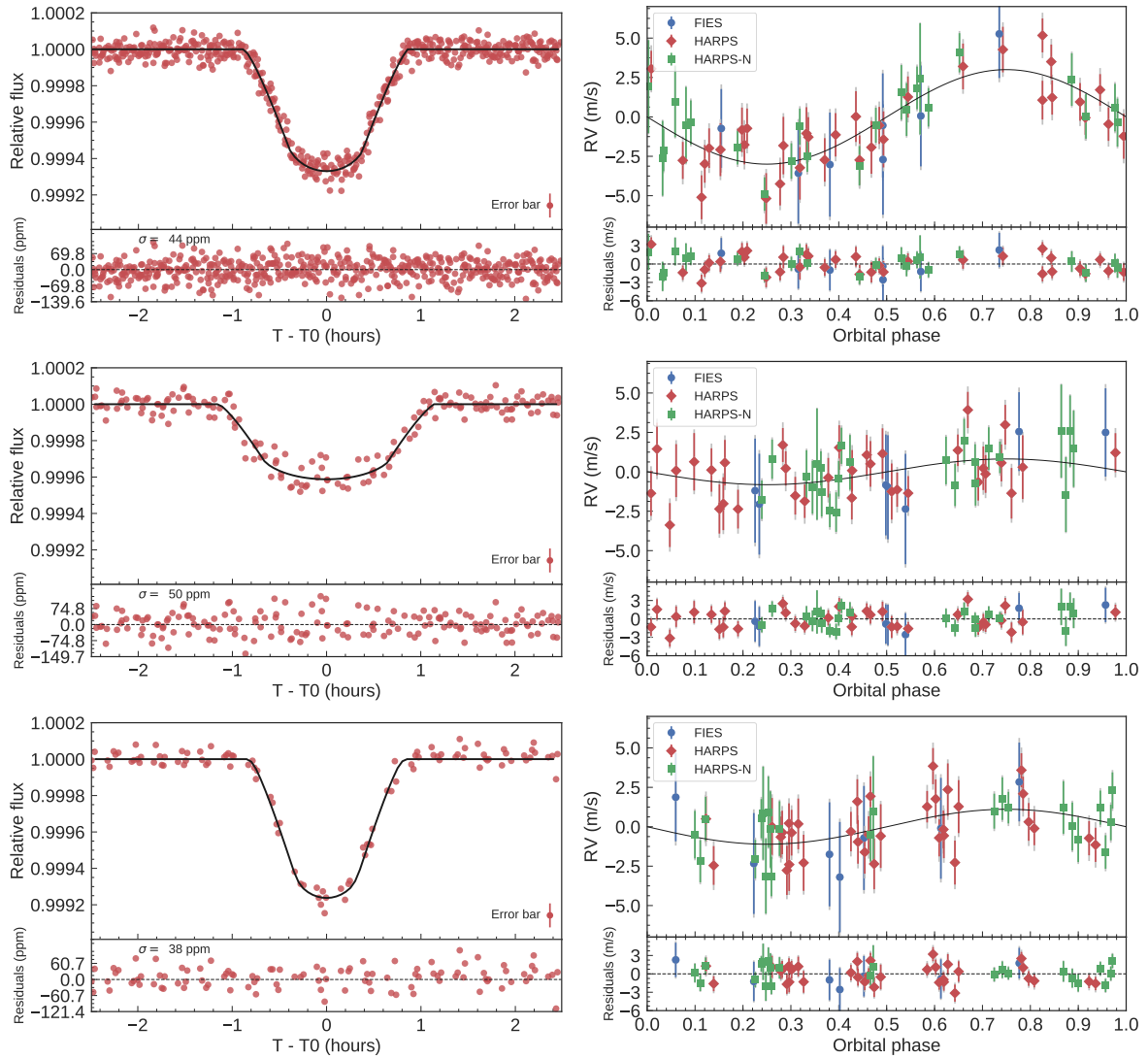
Figure 6.34: From top to bottom and left to right: transit fit and phase-folded RV curve of GJ 9827 b, GJ 9827 c, GJ 9827 d after removing the activity signal from the star and the signals from the other planets. The gray error bars account for additional instrumental noise and/or imperfect treatment of the various sources of RV variations.
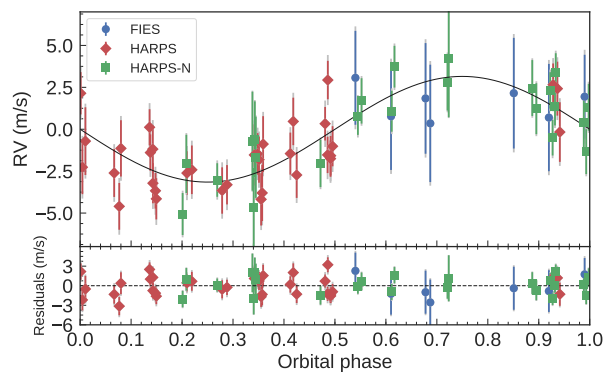
Figure 6.35: RV curve of GJ 9827 phase-folded to the first harmonic of the stellar rotation period ($P_{\rm rot}/2 = 15.1$ days) after removing the signals of the three transiting planets.
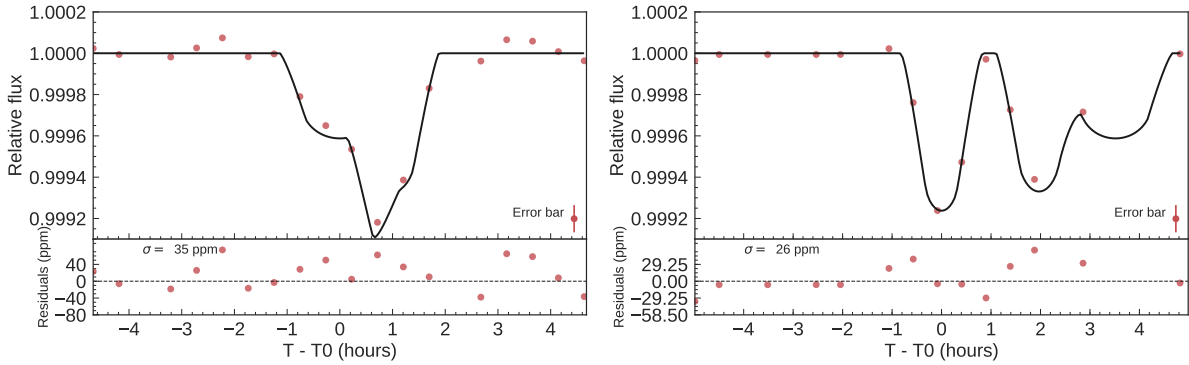
Figure 6.36: Multi-transit events for GJ 9827 at different times. The best fitting transit model is over-plotted with thick black lines. Left panel: simultaneous transit of planet c and d. Right panel: The transit of the three planets occur almost at the same time. The *K2* data points are shown with red circles.
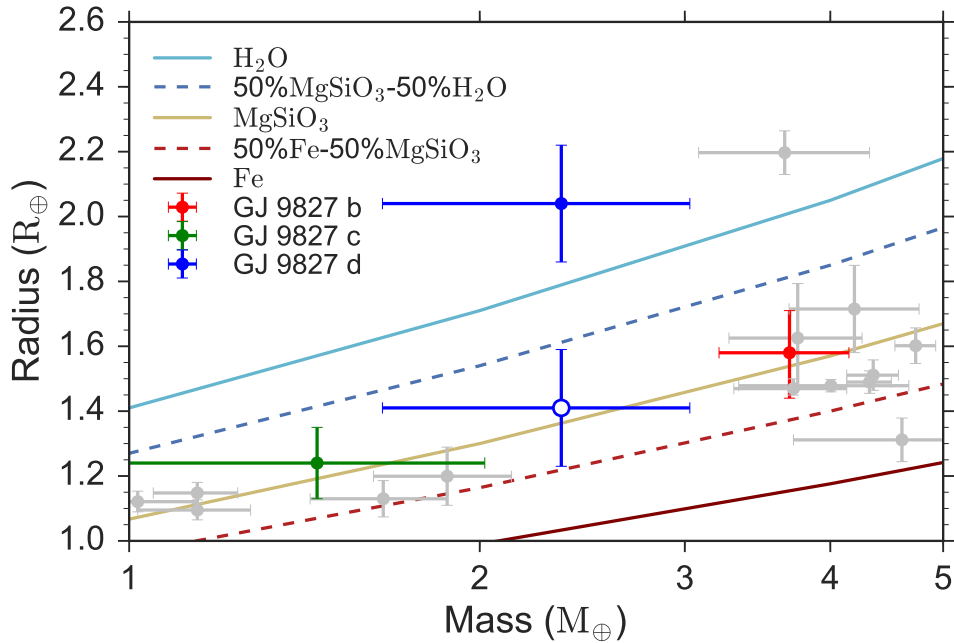
Figure 6.37: Mass-radius diagram for all rocky planets with masses between 1-5 $M_\oplus$ and radii between 1-2.6 $R_\oplus$, as registered in the TEPCat database. The solid circles indicate measurements of the mass and radius of the planets of GJ 9827. The empty circle shows the inferred mass y radius of the nucleus of the third planet under the assumptions made on section 6.8.6. This plot was created by J. Prieto-Arranz to appear in Prieto-Arranz et al. (2018) using the code available at https://github.com/oscaribv/fancy-massradius-plot.

Table 6.11: GJ 9827 derived parameters.

Parameter	Final value
Stellar parameters[a]	
Star mass $M_\star$ ($M_\odot$)	0.637 ± 0.051
Star radius $R_\star$ ($R_\odot$)	0.622 ± 0.051
Effective Temperature T_{eff} (K)	5286 ± 40
Derived Parameters for GJ 9827 b	
Planet mass M_{p} ($M_\oplus$)	3.69 ± 0.47
Planet radius R_{p} ($R_\oplus$)	1.58 ± 0.14
Mean density ρ_{b} ($\mathrm{g\,cm^{-3}}$)	$5.11^{+1.74}_{-1.27}$
Eccentricity e	0
Scaled semi-major axis $a/R_\star$	$7.23^{+0.19}_{-0.55}$
Semi-major axis of the planetary orbit a (AU)	$0.0206^{+0.0020}_{-0.0023}$
Orbit inclination i_{p} (°)	$88.33^{+1.15}_{-2.10}$
Transit duration τ_{14} (hours)	$1.281^{+0.020}_{-0.020}$
Equilibrium temperature[c] T_{eq} (K)	1114^{+46}_{-26}
Derived Parameters for GJ 9827 c	
Planet mass M_{p} ($M_\oplus$)	1.45 ± 0.57
Planet radius R_{p} ($R_\oplus$)	1.24 ± 0.11
Mean density ρ_{c} ($\mathrm{g\,cm^{-3}}$)	$4.13^{+2.31}_{-1.77}$
Eccentricity e	0
Scaled semi-major axis $a/R_\star$	$15.10^{+0.39}_{-1.14}$
Semi-major axis of the planetary orbit a (AU)	$0.0429^{+0.0042}_{-0.0048}$
Orbit inclination i_{p} (°)	$89.07^{+0.59}_{-0.92}$
Transit duration τ_{14} (hours)	$1.825^{+0.042}_{-0.042}$
Equilibrium temperature[b] T_{eq} (K)	771^{+31}_{-18}
Derived Parameters for GJ 9827 d	
Planet mass M_{p} ($M_\oplus$)	$2.35_{\pm}0.69$
Planet radius R_{p} ($R_\oplus$)	2.04 ± 0.18
Mean density ρ_{c} ($\mathrm{g\,cm^{-3}}$)	$1.51^{+0.71}_{-0.53}$
Eccentricity e	0
Scaled semi-major axis $a/R_\star$	$21.51^{+0.56}_{-1.63}$
Semi-major axis of the planetary orbit a (AU)	$0.0611^{+0.0060}_{-0.0068}$
Orbit inclination i_{p} (°)	$87.70^{+0.08}_{-0.25}$
Transit duration τ_{14} (hours)	$1.248^{+0.038}_{-0.033}$
Equilibrium temperature[b] T_{eq} (K)	646^{+26}_{-15}
Limb darkening coefficients	
Linear limb-darkening coefficient u_1	$0.58^{+0.12}_{-0.12}$
Quadratic limb-darkening coefficient u_2	$0.15^{+0.13}_{-0.13}$

Note – The fitted parameters are shown in Table 6.10. [a] Details about the stellar parameter estimation are given in Prieto-Arranz et al. (2018). [b] Assuming albedo = 0.

6.9   44 Validated Planets from K2 Campaign 10

K2 Campaign 10 was pointed towards a relatively high galactic latitude where blending within the photometric apertures is less significant than for other fields, and contamination from background eclipsing binaries is low. This makes of *K2* Campaign 10 an excellent opportunity to statistically validate exoplanets.

In Livingston et al. (2018) we presented the validation of 44 transiting exoplanets around stars observed by *K2* on its Campaign 10. As part of this thesis, we performed a MCMC analysis of the light curve candidates to provide an additional layer of confidence on the main analysis presented in Livingston et al. (2018).

6.9.1   Light curve data

We first downloaded the light curves of Vanderburg & Johnson (2014) from the MAST database for all the 72 targets listed in Table 1 of Livingston et al. (2018). We then detrended the light curves by fitting a second order polynomial to the out-of-transit data using `exotrending` (Barragán & Gandolfi, 2017, see Appendix A.1).

6.9.2   Transit fitting

To explore the transit model parameter space with MCMC, we used the code `pyaneti` (Barragán et al., 2019, see also § 5.3) to fit the detrended light curves with uniform priors for all parameters. For each system, we explored the parameter space with 500 independent Markov chains. We then created posterior distributions with 250,000 independent points for each fitted parameter (see Sect. 6.1.5).

6.9.3   Comparison with other pipeline in Livingston et al. (2018)

For the majority of candidates, the main transit parameters of interest (period P, planet-to-star radius rate $R_{\rm p}/R_{\star}$, impact parameter b, and scaled semi-major axis $a/R_{\star}$) are consistent within 1-σ between the two independent analyses, although there are some cases in which marginally significant differences were found. These differences are likely to be the result of different handling of the *K2* systematics and/or the stellar variability in the light curves. The overall good agreement between these two independently-derived sets of transit parameters provides an additional layer of confidence in the quality of the candidates. The results of this comparison are listed in Table 6.12.

Table 6.12: Comparison of parameters between both analysis presented in Livingston et al. (2018).

EPIC	$P_{\rm orb}$	ΔP	$R_{\rm p}$	$\Delta R_{\rm p}$	b	Δb	a	Δa
201092629.01	$26.809633^{+0.001327}_{-0.001235}$	3.7	$0.0263^{+0.0011}_{-0.0007}$	3.0	$0.25^{+0.28}_{-0.17}$	0.4	$48.0^{+2.0}_{-6.0}$	0.7
201102594.01	$6.513855^{+0.000534}_{-0.000660}$	0.0	$0.0656^{+0.0138}_{-0.0041}$	0.3	$0.54^{+0.37}_{-0.37}$	0.3	$23.0^{+4.3}_{-10.9}$	0.1
201110617.01	$0.813175^{+0.000032}_{-0.000032}$	0.5	$0.0163^{+0.0008}_{-0.0007}$	0.1	$0.39^{+0.33}_{-0.27}$	0.0	$4.6^{+0.5}_{-1.0}$	0.4
201111557.01	$2.302093^{+0.000127}_{-0.000133}$	0.8	$0.0143^{+0.0010}_{-0.0008}$	0.1	$0.40^{+0.34}_{-0.28}$	0.0	$12.0^{+1.5}_{-3.0}$	0.1
201127519.01	$6.178825^{+0.000030}_{-0.000030}$	0.6	$0.1080^{+0.0024}_{-0.0016}$	1.1	$0.24^{+0.15}_{-0.16}$	0.3	$17.7^{+0.4}_{-0.8}$	0.6
201128338.01	$32.652883^{+0.002143}_{-0.002309}$	0.6	$0.0418^{+0.0023}_{-0.0014}$	1.3	$0.40^{+0.32}_{-0.30}$	0.1	$57.0^{+4.8}_{-14.0}$	0.2
201132684.01	$5.898463^{+0.001803}_{-0.001503}$	1.5	$0.0135^{+0.0009}_{-0.0009}$	0.7	$0.30^{+0.23}_{-0.20}$	0.3	$13.3^{+1.3}_{-2.1}$	0.6
201132684.02	$10.062708^{+0.001114}_{-0.001122}$	1.3	$0.0271^{+0.0012}_{-0.0010}$	0.9	$0.43^{+0.22}_{-0.26}$	0.1	$18.9^{+1.9}_{-3.1}$	0.0
201164625.01	$2.713225^{+0.001656}_{-0.001971}$	0.6	$0.0090^{+0.0057}_{-0.0023}$	0.5	$0.47^{+0.37}_{-0.32}$	0.1	$18.8^{+48.6}_{-11.3}$	1.2
201166680.01	$11.540719^{+0.002151}_{-0.002063}$	0.4	$0.0136^{+0.0006}_{-0.0006}$	0.8	$0.43^{+0.16}_{-0.18}$	0.1	$21.0^{+1.0}_{-2.1}$	0.1
201166680.02	$24.942035^{+0.003282}_{-0.003280}$	0.6	$0.0147^{+0.0005}_{-0.0005}$	1.4	$0.22^{+0.26}_{-0.16}$	0.5	$35.0^{+1.7}_{-3.5}$	0.1
201180665.01	$17.773142^{+0.000122}_{-0.000123}$	1.1	$0.1879^{+0.0035}_{-0.0034}$	0.4	$0.67^{+0.02}_{-0.02}$	0.8	$33.6^{+0.5}_{-0.4}$	0.5
201211526.01	$21.073824^{+0.003409}_{-0.002816}$	1.2	$0.0164^{+0.0014}_{-0.0008}$	0.6	$0.40^{+0.35}_{-0.28}$	0.1	$38.0^{+5.9}_{-9.7}$	0.0
201225286.01	$12.420030^{+0.000967}_{-0.000768}$	1.0	$0.0249^{+0.0032}_{-0.0011}$	0.0	$0.40^{+0.37}_{-0.28}$	0.1	$25.8^{+2.2}_{-7.8}$	0.3
201274010.01	$13.008576^{+0.001302}_{-0.001295}$	0.6	$0.0278^{+0.0015}_{-0.0013}$	0.8	$0.42^{+0.34}_{-0.28}$	0.0	$27.7^{+2.9}_{-7.4}$	0.1
201352100.01	$13.383697^{+0.001049}_{-0.001031}$	0.1	$0.0307^{+0.0019}_{-0.0013}$	0.9	$0.41^{+0.33}_{-0.30}$	0.1	$36.4^{+3.6}_{-9.5}$	0.3
201357643.01	$11.893194^{+0.000420}_{-0.000420}$	0.2	$0.0318^{+0.0008}_{-0.0006}$	0.1	$0.36^{+0.32}_{-0.25}$	0.0	$17.7^{+1.1}_{-3.7}$	0.0
201386739.01	$5.768345^{+0.000696}_{-0.000597}$	0.8	$0.0370^{+0.0019}_{-0.0015}$	1.1	$0.38^{+0.29}_{-0.25}$	0.1	$11.2^{+0.9}_{-2.1}$	0.0
201390048.01	$9.456636^{+0.000964}_{-0.000971}$	1.6	$0.0177^{+0.0011}_{-0.0008}$	0.9	$0.43^{+0.34}_{-0.30}$	0.0	$24.3^{+2.7}_{-6.9}$	0.1
201390927.01	$2.637995^{+0.000129}_{-0.000132}$	0.0	$0.0290^{+0.0017}_{-0.0013}$	0.9	$0.44^{+0.32}_{-0.30}$	0.0	$10.6^{+1.2}_{-2.8}$	0.1
201392505.01	$27.363675^{+0.035237}_{-0.016303}$	2.9	$0.0160^{+0.0043}_{-0.0047}$	5.3	$0.56^{+0.32}_{-0.37}$	0.3	$68.6^{+20.6}_{-26.9}$	1.4
201437844.01	$9.553130^{+0.001159}_{-0.001060}$	2.4	$0.0152^{+0.0004}_{-0.0004}$	1.8	$0.22^{+0.26}_{-0.15}$	0.5	$19.4^{+0.9}_{-1.8}$	0.7
201437844.02	$21.057795^{+0.001448}_{-0.001458}$	0.0	$0.0308^{+0.0006}_{-0.0006}$	0.3	$0.40^{+0.16}_{-0.11}$	0.5	$32.9^{+1.5}_{-3.0}$	0.5
201595106.01	$0.877180^{+0.000040}_{-0.000041}$	1.2	$0.0129^{+0.0008}_{-0.0007}$	1.2	$0.42^{+0.32}_{-0.29}$	0.0	$6.1^{+0.8}_{-1.4}$	0.3
201598502.01	$7.514375^{+0.000687}_{-0.000779}$	0.5	$0.0385^{+0.0039}_{-0.0021}$	0.9	$0.45^{+0.36}_{-0.32}$	0.1	$21.9^{+2.8}_{-7.5}$	0.2
201615463.01	$8.527713^{+0.001707}_{-0.001639}$	0.2	$0.0139^{+0.0008}_{-0.0008}$	1.1	$0.41^{+0.31}_{-0.28}$	0.0	$10.9^{+1.0}_{-2.6}$	0.1
228707509.01	$15.349275^{+0.000298}_{-0.000302}$	3.7	$0.1631^{+0.0021}_{-0.0037}$	2.8	$0.68^{+0.04}_{-0.05}$	0.8	$24.1^{+0.8}_{-0.7}$	0.9
228720681.01	$15.781458^{+0.000245}_{-0.000243}$	0.3	$0.1019^{+0.0022}_{-0.0030}$	0.9	$0.74^{+0.04}_{-0.06}$	0.6	$24.3^{+1.7}_{-1.2}$	0.6
228721452.01	$0.505574^{+0.000052}_{-0.000054}$	1.0	$0.0076^{+0.0008}_{-0.0007}$	0.6	$0.74^{+0.10}_{-0.16}$	0.9	$2.9^{+0.2}_{-0.4}$	1.0
228721452.02	$4.564508^{+0.000318}_{-0.000320}$	2.1	$0.0121^{+0.0005}_{-0.0005}$	3.0	$0.28^{+0.27}_{-0.20}$	0.3	$12.6^{+0.8}_{-1.6}$	0.8
228724899.01	$5.202587^{+0.000348}_{-0.000379}$	0.0	$0.0348^{+0.0055}_{-0.0020}$	0.3	$0.52^{+0.37}_{-0.35}$	0.2	$21.0^{+3.4}_{-9.7}$	0.7
228725791.01	$2.250464^{+0.000209}_{-0.000225}$	0.6	$0.0308^{+0.0019}_{-0.0016}$	0.8	$0.48^{+0.21}_{-0.27}$	0.1	$8.6^{+1.0}_{-1.4}$	0.0
228725791.02	$6.492941^{+0.001399}_{-0.001910}$	0.5	$0.0313^{+0.0020}_{-0.0018}$	0.6	$0.30^{+0.27}_{-0.20}$	0.3	$17.4^{+1.9}_{-2.9}$	0.2
228725972.01	$4.478767^{+0.000622}_{-0.000596}$	0.2	$0.0183^{+0.0010}_{-0.0009}$	0.7	$0.58^{+0.12}_{-0.12}$	0.5	$12.4^{+0.6}_{-1.3}$	0.2
228725972.02	$10.095993^{+0.000753}_{-0.000740}$	0.8	$0.0259^{+0.0009}_{-0.0008}$	0.2	$0.25^{+0.26}_{-0.18}$	0.4	$21.3^{+1.1}_{-2.2}$	0.3
228729473.01	$16.769028^{+0.002673}_{-0.002826}$	1.0	$0.0390^{+0.0015}_{-0.0009}$	2.0	$0.31^{+0.24}_{-0.22}$	0.8	$8.4^{+0.4}_{-1.0}$	0.9
228732031.01	$0.369293^{+0.000007}_{-0.000007}$	1.2	$0.0199^{+0.0010}_{-0.0008}$	0.6	$0.38^{+0.30}_{-0.26}$	0.1	$2.9^{+0.2}_{-0.5}$	0.6
228734900.01	$15.871027^{+0.001990}_{-0.001782}$	0.3	$0.0195^{+0.0007}_{-0.0007}$	0.5	$0.39^{+0.32}_{-0.27}$	0.0	$19.0^{+1.6}_{-4.3}$	0.3
228735255.01	$6.569194^{+0.000037}_{-0.000036}$	0.3	$0.1134^{+0.0019}_{-0.0010}$	0.4	$0.21^{+0.15}_{-0.14}$	0.5	$14.8^{+0.3}_{-0.6}$	0.8
228736155.01	$3.270851^{+0.000334}_{-0.000373}$	0.4	$0.0154^{+0.0010}_{-0.0008}$	0.1	$0.44^{+0.32}_{-0.30}$	0.0	$10.6^{+1.3}_{-2.8}$	0.3
228739306.01	$7.172600^{+0.001126}_{-0.001120}$	0.0	$0.0277^{+0.0028}_{-0.0015}$	0.9	$0.45^{+0.36}_{-0.31}$	0.1	$16.1^{+2.1}_{-5.5}$	0.0
228748383.01	$12.402562^{+0.003191}_{-0.003055}$	1.5	$0.0180^{+0.0012}_{-0.0010}$	1.0	$0.42^{+0.34}_{-0.29}$	0.0	$14.1^{+1.7}_{-3.8}$	0.1
228748826.01	$4.014377^{+0.000317}_{-0.000304}$	0.3	$0.0303^{+0.0050}_{-0.0017}$	1.0	$0.49^{+0.39}_{-0.34}$	0.2	$12.0^{+1.7}_{-5.3}$	0.1
228753871.01	$18.693829^{+0.002443}_{-0.002428}$	0.5	$0.0293^{+0.0016}_{-0.0014}$	0.4	$0.40^{+0.31}_{-0.27}$	0.1	$62.1^{+7.1}_{-13.8}$	0.2

Table 6.12 – continued from previous page

EPIC	P_{orb}	ΔP	R_{p}	ΔR_{p}	b	Δb	a	Δa
228758778.01	$9.296632^{+0.002139}_{-0.002028}$	1.1	$0.0394^{+0.0045}_{-0.0028}$	0.7	$0.46^{+0.39}_{-0.31}$	0.0	$21.6^{+4.7}_{-8.3}$	0.1
228758948.01	$12.202002^{+0.000790}_{-0.000760}$	0.4	$0.0357^{+0.0019}_{-0.0013}$	0.6	$0.38^{+0.29}_{-0.26}$	0.0	$21.8^{+1.7}_{-4.3}$	0.1
228763938.01	$13.814364^{+0.002778}_{-0.002668}$	0.1	$0.0201^{+0.0016}_{-0.0012}$	0.3	$0.42^{+0.33}_{-0.29}$	0.0	$27.3^{+3.3}_{-7.4}$	0.2
228784812.01	$4.188426^{+0.000792}_{-0.000773}$	0.4	$0.0122^{+0.0011}_{-0.0009}$	0.1	$0.42^{+0.34}_{-0.29}$	0.3	$12.1^{+2.0}_{-3.3}$	0.2
228798746.01	$2.698349^{+0.000118}_{-0.000127}$	0.3	$0.0176^{+0.0008}_{-0.0008}$	0.4	$0.42^{+0.32}_{-0.28}$	0.0	$12.2^{+1.3}_{-3.0}$	0.0
228801451.01	$0.584253^{+0.000015}_{-0.000015}$	0.2	$0.0139^{+0.0005}_{-0.0005}$	0.7	$0.32^{+0.27}_{-0.22}$	0.2	$3.9^{+0.3}_{-0.5}$	0.9
228801451.02	$8.329889^{+0.000554}_{-0.000772}$	3.0	$0.0172^{+0.0012}_{-0.0011}$	4.8	$0.67^{+0.10}_{-0.08}$	0.9	$22.8^{+1.5}_{-3.1}$	0.4
228804845.01	$2.860187^{+0.000318}_{-0.000313}$	0.3	$0.0149^{+0.0010}_{-0.0007}$	1.6	$0.40^{+0.32}_{-0.27}$	0.0	$7.2^{+0.7}_{-1.6}$	0.0
228809391.01	$19.574436^{+0.002652}_{-0.002288}$	0.7	$0.0280^{+0.0024}_{-0.0013}$	0.4	$0.44^{+0.34}_{-0.30}$	0.1	$52.8^{+6.0}_{-15.6}$	0.0
228809550.01	$4.001536^{+0.000023}_{-0.000023}$	1.1	$0.1090^{+0.0035}_{-0.0035}$	0.7	$0.42^{+0.18}_{-0.26}$	0.2	$13.3^{+1.1}_{-1.4}$	0.3
228834632.01	$11.729360^{+0.001681}_{-0.001829}$	0.9	$0.0352^{+0.0019}_{-0.0017}$	2.2	$0.38^{+0.31}_{-0.27}$	0.5	$34.2^{+3.1}_{-7.0}$	0.4
228836835.01	$0.728083^{+0.000038}_{-0.000052}$	0.3	$0.0272^{+0.0053}_{-0.0016}$	0.0	$0.38^{+0.35}_{-0.26}$	0.2	$6.2^{+1.5}_{-1.4}$	0.7
228846243.01	$25.541849^{+0.011979}_{-0.013420}$	1.7	$0.0372^{+0.0025}_{-0.0021}$	0.7	$0.40^{+0.31}_{-0.27}$	0.2	$22.0^{+2.2}_{-4.9}$	0.0
228849382.01	$4.097290^{+0.000494}_{-0.000470}$	1.0	$0.0191^{+0.0010}_{-0.0010}$	0.9	$0.27^{+0.28}_{-0.19}$	1.2	$15.8^{+1.6}_{-2.1}$	0.0
228849382.02	$12.118887^{+0.001355}_{-0.001403}$	0.1	$0.0326^{+0.0013}_{-0.0013}$	0.8	$0.60^{+0.12}_{-0.14}$	0.5	$32.5^{+3.3}_{-4.4}$	0.2
228888935.01	$5.690115^{+0.000157}_{-0.000152}$	1.1	$0.0864^{+0.0021}_{-0.0021}$	0.2	$0.82^{+0.03}_{-0.04}$	0.8	$7.4^{+0.5}_{-0.4}$	0.7
228894622.01	$1.963920^{+0.000014}_{-0.000014}$	5.9	$0.0380^{+0.0054}_{-0.0015}$	0.1	$0.40^{+0.39}_{-0.28}$	0.1	$8.8^{+0.7}_{-2.7}$	0.1
228934525.01	$3.676107^{+0.000210}_{-0.000207}$	0.6	$0.0320^{+0.0013}_{-0.0011}$	1.3	$0.28^{+0.28}_{-0.19}$	0.3	$14.1^{+1.0}_{-1.9}$	0.1
228934525.02	$7.955047^{+0.000647}_{-0.000658}$	0.2	$0.0314^{+0.0014}_{-0.0013}$	0.4	$0.56^{+0.14}_{-0.11}$	0.4	$23.6^{+1.7}_{-3.1}$	0.2
228964773.01	$37.289381^{+0.017004}_{-0.032089}$	2.5	$0.0307^{+0.0194}_{-0.0119}$	1.2	$0.90^{+0.09}_{-0.24}$	1.2	$57.1^{+31.0}_{-21.4}$	0.1
228968232.01	$5.525028^{+0.002150}_{-0.003208}$	1.2	$0.0191^{+0.0045}_{-0.0025}$	3.5	$0.41^{+0.34}_{-0.28}$	0.0	$10.3^{+6.0}_{-3.7}$	0.7
228974324.01	$1.605873^{+0.000090}_{-0.000088}$	0.1	$0.0150^{+0.0010}_{-0.0008}$	0.3	$0.42^{+0.33}_{-0.30}$	0.1	$8.3^{+1.0}_{-2.2}$	0.0
228974907.01	$20.763514^{+0.009371}_{-0.007177}$	2.6	$0.0136^{+0.0010}_{-0.0007}$	2.7	$0.41^{+0.37}_{-0.29}$	0.0	$30.8^{+3.5}_{-9.5}$	0.2
229004835.01	$16.140711^{+0.001057}_{-0.001032}$	2.1	$0.0189^{+0.0011}_{-0.0008}$	0.4	$0.40^{+0.35}_{-0.28}$	0.0	$54.1^{+5.3}_{-14.6}$	0.0
229017395.01	$19.090353^{+0.003305}_{-0.003665}$	0.2	$0.0219^{+0.0011}_{-0.0010}$	0.5	$0.42^{+0.32}_{-0.30}$	0.1	$21.5^{+2.3}_{-5.4}$	0.0
229103251.01	$11.663465^{+0.001861}_{-0.001357}$	2.0	$0.0330^{+0.0027}_{-0.0018}$	1.3	$0.43^{+0.33}_{-0.30}$	0.0	$27.9^{+3.4}_{-7.4}$	0.0
229131722.01	$15.484081^{+0.003104}_{-0.002549}$	0.9	$0.0171^{+0.0014}_{-0.0010}$	0.9	$0.41^{+0.33}_{-0.29}$	0.0	$30.0^{+4.5}_{-7.4}$	0.0
229133720.01	$4.036851^{+0.000081}_{-0.000080}$	0.4	$0.0284^{+0.0019}_{-0.0008}$	0.0	$0.37^{+0.31}_{-0.26}$	0.0	$13.2^{+0.9}_{-2.8}$	0.1

6.10 π Mensae c: A world transiting a naked-eye star

In the final stage of preparing this thesis, the first list of planet candidates (the so called alerts) from the *TESS* space mission was released on September 5, 2018. The candidate list includes the naked-eye star π Mensae (V=5.65 mag).

Two weeks later Gandolfi et al. (2018) reported on the confirmation and mass determination of π Men c, the first transiting planet discovered by NASA's *TESS* space mission. π Men is a quiet G0 V star that was previously known to host a sub-stellar companion (π Men b) on a long-period ($P_{\rm orb} = 2091$ days), eccentric ($e = 0.64$) orbit. Using *TESS* time-series photometry, combined with *Gaia* data, published UCLES@AAT Doppler measurements, and archival HARPS@ESO-3.6m radial velocities, we find that π Men c is an close-in planet with an orbital period of $P_{\rm orb} = 6.25$ days, a mass of 4.50 ± 0.81 $M_\oplus$, and a radius of 2.08 ± 0.04 $R_\oplus$. Based on the planet's orbital period and size, π Men c is a super-Earth located at, or close to, the radius gap, while its mass and bulk density suggest it may have held on to a significant atmosphere. Because of the brightness of the host star, this system is highly suitable for a wide range of further studies to characterise the planetary atmosphere and dynamical properties. We note that an independent investigation of this system was publicly announced by Huang et al. (2018).

We performed the RV and light curve analysis as part of this thesis. We note that all the tools and methods learned with *K2* data are also applicable to *TESS* data.

6.10.1   Light curve and RV data

We downloaded the *TESS* Sector 1 light curves from the MIT website. For the *TESS* object of interest TOI-144 (aka, π Men, HD 39091, TIC 261136679), the light curve is provided by the NASA Ames SPOC center. The time-series includes 18 036 short-cadence ($T_{\rm exp} = 2$ min) photometric measurements. *TESS* observations started on 25 July 2018 and ended on 22 August 2018. We removed any measurements that have a non-zero "Quality" flag, i.e., those suffering from cosmic rays or instrumental issues. We detected the signal of π Men c with a signal-to-noise ratio (S/N) of 9.1 and our ephemeris is consistent with that reported by the *TESS* team. We did not find any additional transit signal with (S/N) > 6. We also performed a periodogram and auto-cross-correlation analysis in the attempt to extract the rotation period of the star from the out-of-transit *TESS* light curve, but we found no significant rotation signal in the light curve. Figure 6.38 shows the *TESS* light curve for π Men.

For the final set of photometric data, we extracted 10 hours of *TESS* data points centred around each of the 5 transits observed by *TESS*. The 5 segments were de-trended using the code `exotrending` (Barragán & Gandolfi, 2017, see Appendix A.1), fitting a second-order polynomial to the out-of-transit data.

Jones et al. (2002) reported on the detection of a long-period ($P_{\rm orb} \approx 2100$ days), eccentric ($e \approx 0.6$), sub-stellar companion to π Men with a minimum mass of $M_{\rm b} = 10.3\,M_{\rm Jup}$. Their discovery is based on 28 RV measurements obtained between November 1998 and April 2002 using the UCLES spectrograph mounted at the 3.92-m Anglo-Australian Telescope at Siding Spring Observatory. Fourteen additional UCLES RVs were published by Butler et al. (2006).

We also retrieved from the ESO public archive 145 high-resolution ($R \approx 115\,000$) spectra of π Men, taken with the HARPS spectrograph (Mayor et al., 2003) mounted at the ESO-3.6m telescope of La Silla observatory (Chile). The observations were carried out between 28 December 2012 and 17 March 2017 UTC, as part of the observing programs 072.C-0488, 183.C-0972, and 192.C-0852. On June 2015, the HARPS fibre bundle was
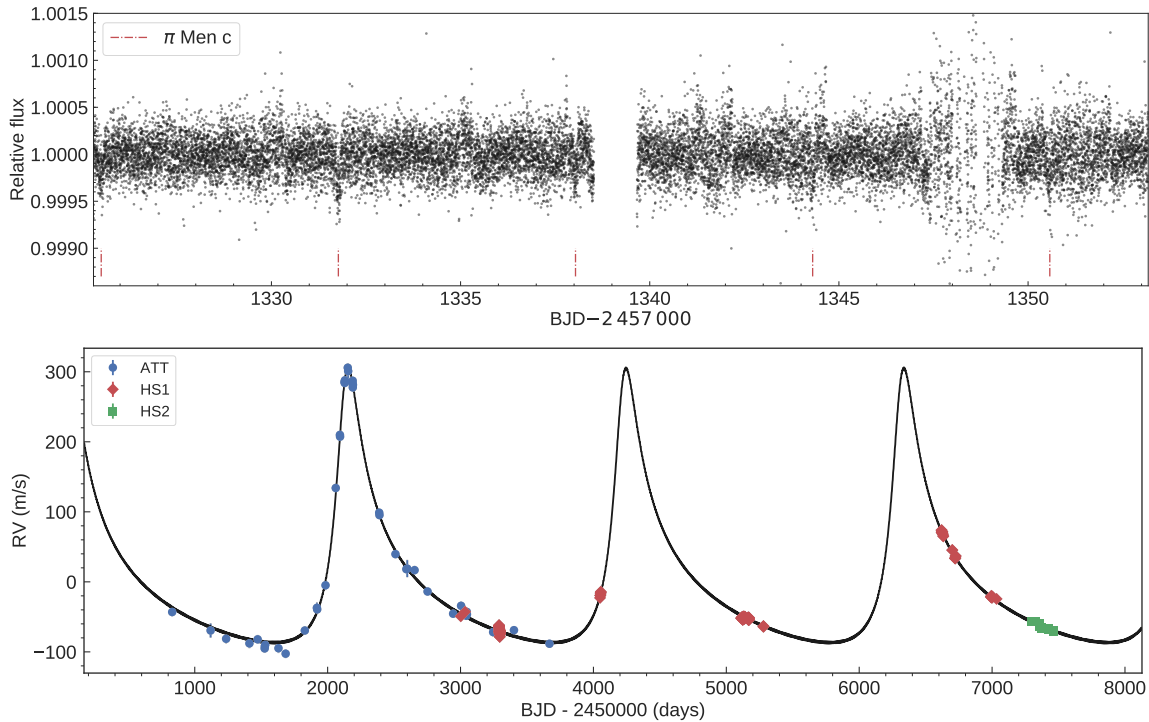
Figure 6.38: *Upper panel: TESS* Light curve for π Men. The positions of the transit signals are marked with vertical red dot-dashed lines. *Lower panel:* AAT (blue circles), HARPS HS1 and HS2 (red diamonds and green squares, respectively) RV measurements versus time, following the subtraction of the systemic velocities for each instrument. The solid line represents the inferred RV model.

upgraded (Lo Curto et al., 2015). To account for the RV offset caused by the instrument refurbishment, we treated the HARPS RVs taken before/after June 2015 as two different data-sets, HS1 and HS2.

Following Eastman et al. (2010), we converted the heliocentric Julian dates (HJD $_{\rm UTC}$) of the UCLES time stamps and the barycentric Julian (BJD $_{\rm UTC}$) of the HARPS time stamps into barycentric Julian dates in barycentric dynamical time (BJD $_{\rm TDB}$). We used all 187 Doppler measurements available and accounted for the RV offsets between the different instruments and the two HARPS set-ups. All the RV measurements are presented in Gandolfi et al. (2018). Figure 6.38 shows the RV time-series following the subtraction of the instrumental offsets.

6.10.2   Joint analysis of the transit and RV data

We performed a joint analysis of the photometric and RV time-series using the software suite `pyaneti` (Barragán et al., 2019, see also Sect. 5.3). The RV model consists of two Keplerians to account for the Doppler signal induced by planets *b* and *c*. We fitted for a RV jitter term for each instrument/setup to account for instrumental noise not included in the nominal uncertainties, and/or to account for any stellar activity-induced RV variation. We modelled the *TESS* transit light curves using the limb-darkened quadratic model of Mandel & Agol (2002). For the limb darkening coefficients, we set Gaussian priors using the values derived by Claret (2017) for the *TESS* pass-band. We imposed conservative error bars of 0.1 on both the linear and the quadratic limb-darkening term. A preliminary analysis showed that the transit light curve poorly constrains the scaled semi-major axis ($a/R_\star$). We therefore set a Gaussian prior on $a/R_\star$ using Kepler's third's law, the orbital period, and the derived stellar parameters (see Sect. 5 of Gandolfi et al., 2018). Because
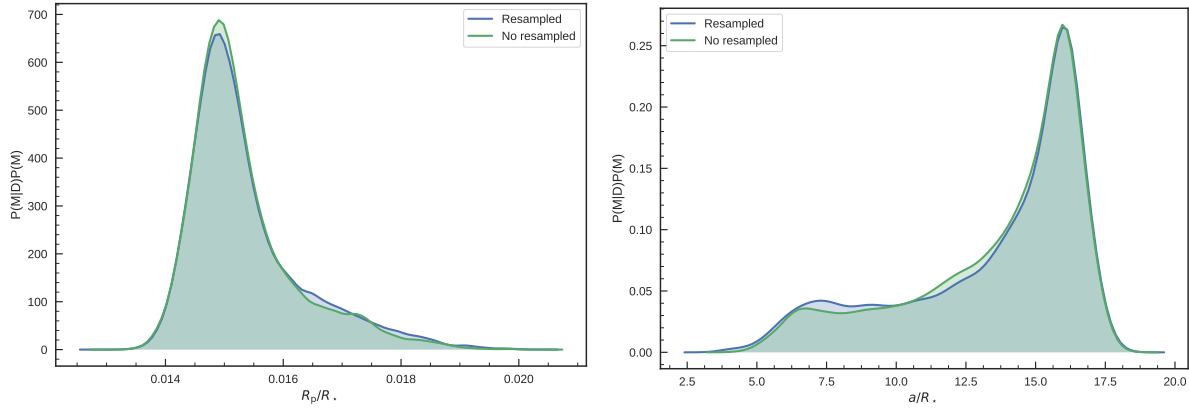
Figure 6.39: Posterior distributions for $R_\mathrm{p}/R_\star$ (left) and $a/R_\star$ (right) obtained with `pyaneti`. The distributions obtained from a resampled and non-resampled model are shown with blue and green colours.

the eccentricity of planet c is poorly constrained by the observations, we fixed it to zero for our analysis. We imposed uniform priors for the remaining fitted parameters. Details about the fitted parameters and prior ranges are given in Table 6.13.

Before performing the final analysis, we ran a numerical experiment to check if the *TESS* 2 min integration time needs to be taken into account following Kipping (2010). Figure 6.39 shows the posterior distributions for $R_\mathrm{p}/R_\star$ and $a/R_\star$ for models with and without re-sampling. We found no differences in the posterior distributions for fits with and without re-sampling. We thus proceeded with our analysis without re-sampling.

We used 500 independent Markov chains initialised randomly inside the prior ranges. Once all chains converged, we used the last 5 000 iterations and saved the chains states every 10 iterations. This approach generates a posterior distribution of 250 000 points for each fitted parameter.

Table 6.13 lists the inferred planetary parameters. They are defined as the median and 68% region of the credible interval of the posterior distributions for each fitted parameter. The transit and RV curves are shown in Fig. 6.40.

The solid line represents the inferred RV model.

6.10.3   Dynamical properties

π Men joins the growing number of stars known to host both long-period Jupiter analogues and close-in small planets ($R_\mathrm{p} < 4\,R_\oplus$). Bryan et al. (2018) recently found that the occurrence rate of companions between 0.5–20 M_Jup at 1–20 AU in systems known to host inner small planets is $39 \pm 7\%$, suggesting that the presence of outer gas giant planets does not prevent the formation of inner Earth- and Neptune-size planets.

We performed a dynamical stability analysis of π Men using the software `mercury6` (Chambers, 1999). Assuming co-planar orbits, we let the system evolve for 1 000 000 yr. For π Men b we found negligible changes of the semi-major axis and eccentricity of $< 2.6 \times 10^{-3}$ AU and 3×10^{-4}, respectively. For π Men c we found no variation larger than 1×10^{-5} of its semi-major axis, with changes of its eccentricity $\lesssim 0.05$. Figure 6.41 shows the evolution of the semi-major axis and eccentricities for both planets.

The actual orientation of the outer planet's orbit is unknown. While we know the inner planet's inclination, because it transits, its eccentricity is poorly constrained by the data. Compact multi-planet systems have been observed to have near-zero eccentricities (e.g. Hadden & Lithwick, 2014; Van Eylen & Albrecht, 2015; Xie et al., 2016). However,
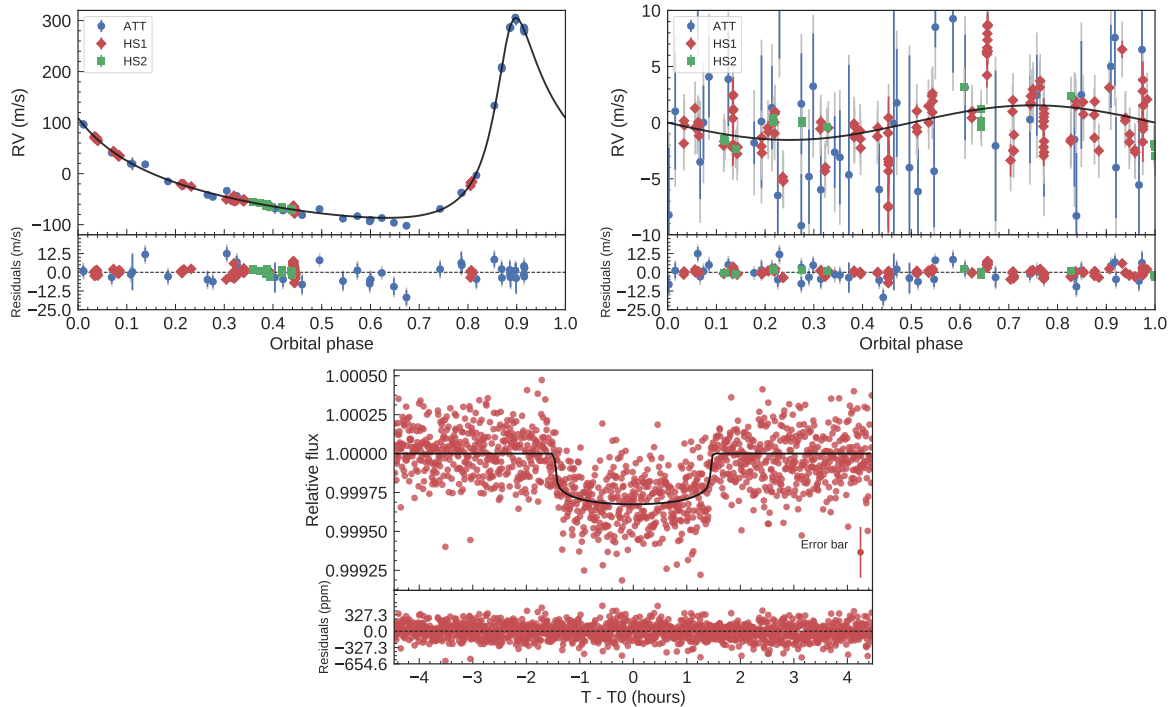
Figure 6.40: Phase-folded RV curves of π Men b (upper left) and c (upper right), and transit light curve of π Men c (lower panel). The ATT data and the two sets of HARPS RVs (HS1 and HS2) are shown with circles, diamonds, and squares, respectively. The 1-σ uncertainties are marked using the same colour used for each data-set. The vertical grey lines mark the error bars including jitter. The *TESS* data points are shown with red circles (lower panel). The best fitting transit and Keplerian models are overplotted with thick black lines.

planets with only a single transiting planet appear to often be "dynamically hotter", and many have a non-zero eccentricity, which can, e.g., be described by the positive half of a zero-mean Gaussian distribution, with a dispersion $\sigma_e = 0.32 \pm 0.06$ (Van Eylen et al., 2018c). The outer planet, π Men c, has an orbital eccentricity of ∼0.64. A far-out giant planet, such as planet c, may in fact increase the orbital eccentricity of a close-in super-Earth, such as planet b (see, e.g., Mustill et al., 2017; Hansen, 2017; Huang et al., 2017). Following Van Eylen et al. (2018c), we found an orbital eccentricity based on the transit data alone of [0, 0.45] at 68% confidence. Because the current RV observations cannot constrain the eccentricity either, we fixed it to zero in the above analysis (see Section 6.10.2). The brightness of the host star makes this planetary system an exciting target for further RV follow-up to measure the inner planet's eccentricity.

6.10.4 Mass, radius, and composition of π Men c

The transiting planet π Men c has a mass of $M_c = 4.50 \pm 0.81\ M_\oplus$ and a radius of $R_c = 2.08 \pm 0.04\ R_\oplus$, yielding a mean density of $\rho_c = 2.73^{+0.52}_{-0.51}$ g cm^{-3}. Figure 6.42 shows the mass-radius diagram for small planets whose masses have been determined with a precision better than 25%. Theoretical models from Zeng et al. (2016) are overplotted using different lines and colors. The position of π Men c suggests a composition of Mg-silicates and water. Alternatively, the planet might have a solid core surrounded by a gas envelope. At short orbital periods, super-Earths and sub-Neptunes are separated by a radius gap at ≈1.6 $R_\oplus$ (Fulton et al., 2017; Van Eylen et al., 2018a). The exact location of the radius gap is observed to be a function of the orbital period (Van Eylen et al., 2018a), as pre-
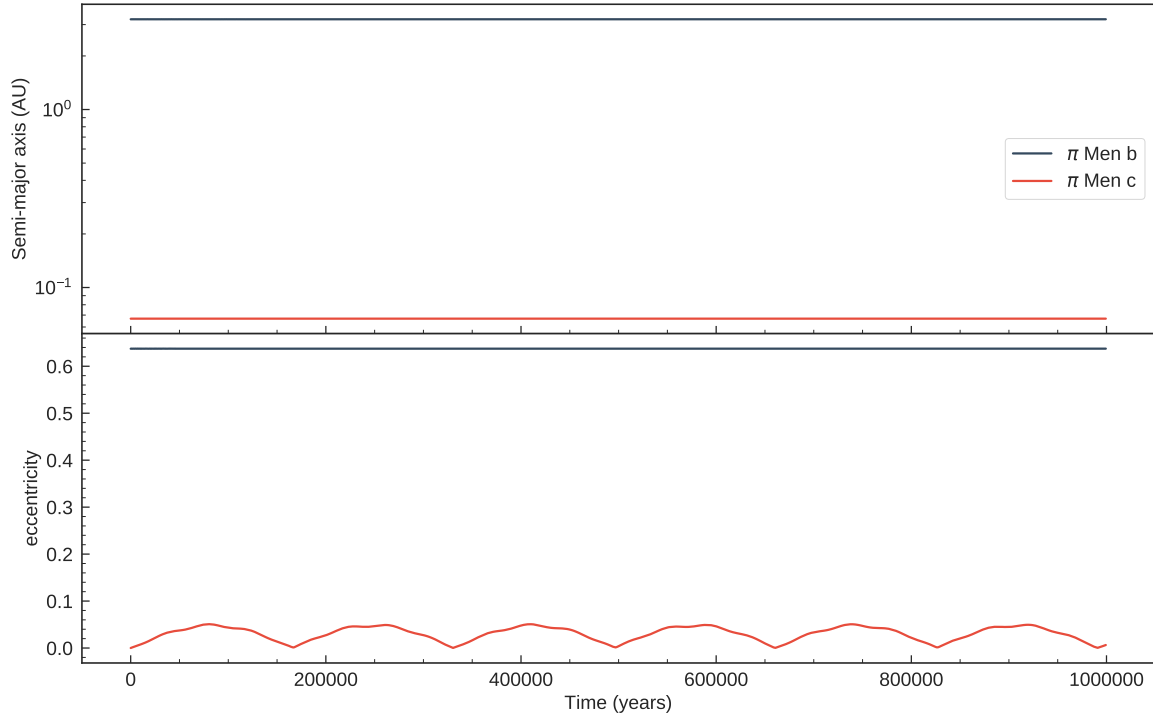
Figure 6.41: Evolution of the semi-major axes (upper panel) and eccentricities (lower panel) *vs* time for π Men b (blue line) and π Men c (orange line) as computed with the code `mercury`.

dicted by models of photo-evaporation (e.g. Owen & Wu, 2013; Lopez & Fortney, 2013). Van Eylen et al. (2018a) find that the radius gap is located at $\log R = m \times \log P + a$, where $m = -0.09^{+0.02}_{-0.04}$ and $a = 0.37^{+0.04}_{-0.02}$. At the orbital period of π Men c, i.e. $P_{\mathrm{orb}} = 6.27$ days, the radius gap is then located at $R_{\mathrm{p}} = 1.99 \pm 0.20\ R_{\oplus}$. This suggests that π Men c, with a radius of $R_{\mathrm{p}} = 2.08 \pm 0.04\ R_{\oplus}$, is located just around the radius gap, or slightly below, although the measured density suggests that the planet may have held on to (part of) its atmosphere.

6.10.5   Further characterization

The naked-eye brightness of π Men immediately argues that any transiting planet will be attractive for atmospheric characterisation. Observations of a planetary atmosphere through transmission spectroscopy during transit provide opportunities to measure the extent, kinematics, abundances, and structure of the atmosphere (Seager & Deming, 2010). Such measurements can be utilised to address fundamental questions such as planetary atmospheric escape and interactions with the host star (Cauley et al., 2017), formation and structure of planetary interiors (Owen et al., 1999), planetary and atmospheric evolution (Öberg et al., 2011), and biological processes (Meadows & Seager, 2010).
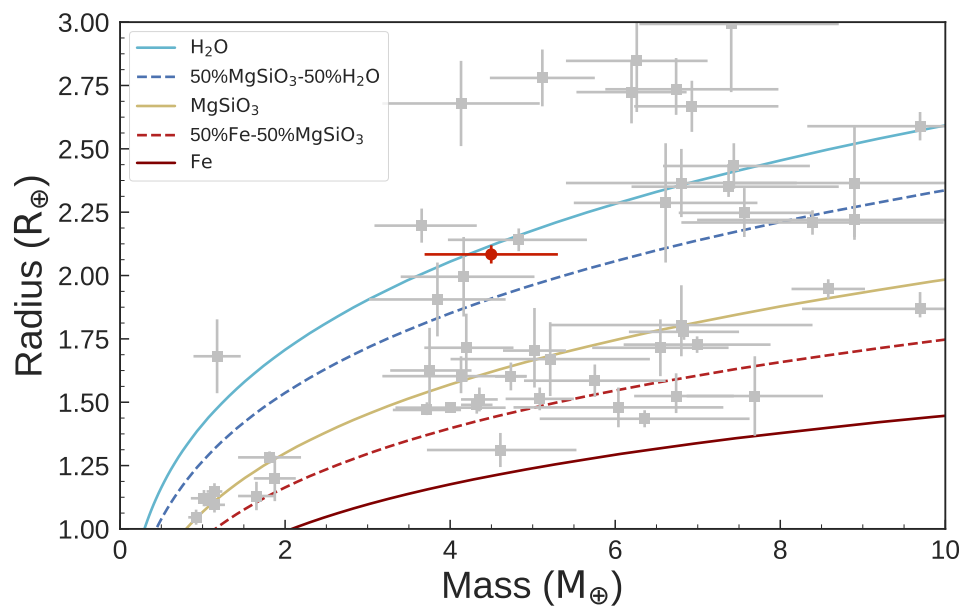
Figure 6.42: Mass-radius for low mass ($M_\mathrm{p} < 10\ M_\oplus$) small ($R_\mathrm{p} < 3\ M_\oplus$) planets with mass-radius measurements better than 25% (from http://www.astro.keele.ac.uk/jkt/tepcat/; Southworth et al., 2007). Composition models from Zeng et al. (2016) are displayed with different lines and colors. The solid red circle marks the position of π Men c.

Table 6.13: π Men system parameters.

Parameter	Prior[a]	Final value
Stellar parameters		
Star mass $M_\star$ $(M_\odot)$	$\cdots$	1.02 ± 0.03
Star radius $R_\star$ $(R_\odot)$	$\cdots$	1.10 ± 0.01
Effective Temperature T_{eff} (K)	$\cdots$	5870 ± 50
Surface gravity[b] $\log g_\star$ (cgs)	$\cdots$	4.36 ± 0.02
Surface gravity[c] $\log g_\star$ (cgs)	$\cdots$	4.33 ± 0.09
Iron abundance [Fe/H] (dex)	$\cdots$	0.05 ± 0.09
Projected rotational velocity $v \sin i_\star$ $(\mathrm{km\,s^{-1}})$	$\cdots$	3.3 ± 0.5
Age (Gyr)	$\cdots$	5.2 ± 1.1
Model parameters of π Men b		
Orbital period P_{orb} (days)	$\mathcal{U}[2079.5, 2109.5]$	2091.2 ± 2.0
Time of minimum conjunction T_0 $(\mathrm{BJD_{TDB}} - 2\,450\,000)$	$\mathcal{U}[6531.9928, 6571.9928]$	6548.2 ± 2.7
$\sqrt{e}\sin\omega$	$\mathcal{U}[-1, 1]$	-0.3922 ± 0.0075
$\sqrt{e}\cos\omega$	$\mathcal{U}[-1, 1]$	0.6968 ± 0.0053
Radial velocity semi-amplitude variation K $(\mathrm{m\,s^{-1}})$	$\mathcal{U}[0, 500]$	195.8 ± 1.5
Model parameters of π Men c		
Orbital period P_{orb} (days)	$\mathcal{U}[6.2416, 6.2916]$	6.26830 ± 0.00027
Transit epoch T_0 $(\mathrm{BJD_{TDB}} - 2\,450\,000)$	$\mathcal{U}[8325.4787, 8325.5287]$	8325.50339 ± 0.00081
Scaled semi-major axis $a/R_\star$	$\mathcal{N}[13.11, 0.17]$	13.10 ± 0.17
Planet-to-star radius ratio $R_{\mathrm{p}}/R_\star$	$\mathcal{U}[0, 0.1]$	0.01737 ± 0.00026
Impact parameter, b	$\mathcal{U}[0, 1]$	$0.611^{+0.018}_{-0.020}$
$\sqrt{e}\sin\omega$	$\mathcal{F}[0]$	0
$\sqrt{e}\cos\omega$	$\mathcal{F}[0]$	0
Radial velocity semi-amplitude variation K $(\mathrm{m\,s^{-1}})$	$\mathcal{U}[0, 10]$	1.54 ± 0.27
Additional model parameters		
Parameterized limb-darkening coefficient q_1	$\mathcal{N}[0.36, 0.1]$	0.33 ± 0.10
Parameterized limb-darkening coefficient q_2	$\mathcal{N}[0.25, 0.1]$	0.22 ± 0.10
Systemic velocity γ_{AAT} $(\mathrm{km\,s^{-1}})$	$\mathcal{U}[-0.3036, 0.2951]$	0.0021 ± 0.0011
Systemic velocity γ_{HS1} $(\mathrm{km\,s^{-1}})$	$\mathcal{U}[10.5307, 10.8832]$	10.70915 ± 0.00039
Systemic velocity γ_{HS2} $(\mathrm{km\,s^{-1}})$	$\mathcal{U}[10.5611, 10.7750]$	10.73157 ± 0.00073
RV jitter term σ_{AAT} $(\mathrm{m\,s^{-1}})$	$\mathcal{U}[0, 100]$	$4.26^{+1.08}_{-0.97}$
RV jitter term σ_{HS1} $(\mathrm{m\,s^{-1}})$	$\mathcal{U}[0, 100]$	$2.36^{+0.19}_{-0.17}$
RV jitter term σ_{HS2} $(\mathrm{m\,s^{-1}})$	$\mathcal{U}[0, 100]$	$1.69^{+0.40}_{-0.30}$
Derived parameters of π Men b		
Planet minimum mass $M_{\mathrm{p}}\sin i$ (M_{J})	$\cdots$	9.66 ± 20
Semi-major axis of the planetary orbit a (AU)	$\cdots$	3.22 ± 0.05
Orbit eccentricity e	$\cdots$	0.6394 ± 0.0025
Argument of periastron of stellar orbit $\omega_\star$ (degrees)	$\cdots$	330.63 ± 0.65
Derived parameters of π Men c		
Planet mass M_{p} $(M_\oplus)$	$\cdots$	4.50 ± 0.81
Planet radius R_{p} $(R_\oplus)$	$\cdots$	2.08 ± 0.04
Planet mean density ρ_{p} $(\mathrm{g\,cm^{-3}})$	$\cdots$	$2.73^{+0.52}_{-0.51}$
Semi-major axis of the planetary orbit a (AU)	$\cdots$	0.0670 ± 0.0011
Orbit eccentricity e	$\cdots$	0 (fixed)
Orbit inclination i_{p} (degrees)	$\cdots$	87.33 ± 0.11
Transit duration τ_{14} (hours)	$\cdots$	$2.98^{+0.04}_{-0.03}$
Equilibrium temperature[d] T_{eq} (K)	$\cdots$	1145 ± 12

Note – [a] $\mathcal{U}[a, b]$ refers to uniform priors between a and b, and $\mathcal{F}[a]$ to a fixed a value. [b] From spectroscopy and isochrones. [c] From spectroscopy. [d] Assuming albedo $= 0$.

CHAPTER 7

CONCLUSIONS

We carried out an intensive RV follow-up of transiting exoplanet candidates from the NASA's *K2* mission. Our observations validated and confirmed new exoplanetary systems. Most of the confirmed planets were well characterised in terms of mass, radius, and bulk density (see below). This allowed us to infer the planet's main properties, such as internal composition and structure, existence of an atmosphere, formation scenario, and so on.

A large fraction of the Doppler observations presented in this work were carried out by myself as part of the doctoral project presented in this thesis. Specifically, I observed for a total 33 nights with the HARPS spectrograph at the ESO-3.6 m telescope, at La Silla Observatory (Chile), and 5 nights with the FIES spectrograph at the 2.58 m Nordic Optical Telescope at Roque del los Muchachos observatory (La Palma, Spain).

We developed and tested the code `pyaneti`, a robust software suite able to simultaneously fit RV measurements and transit light curves of multi-planet systems. `pyaneti` combines the computational power of `FORTRAN` with the versatility of `PYTHON` and it offers the option to run in parallel with `OpenMP`. The package was developed under "the open source ideology", i.e., both the code and the platforms used to write the package are totally free. This code can perform a fast and robust analysis even using a personal laptop. This makes `pyaneti` a powerful tool to perform data analysis of hundreds of systems from future space- and ground-based facilities, such as `TESS`, `PLATO`, `CHEOPS`, and `ESPRESSO`.

In the present thesis work we derived masses, radii, and densities of the following planets:

- **K2-98 b** is a warm Neptune-like planet in a 10-day orbit transiting a V=12.2 mag F-type star with a mass of $M_\star = 1.074 \pm 0.042 \, M_\odot$, a radius of $R_\star = 1.311^{+0.083}_{-0.048} \, R_\odot$, and an age of $5.2^{+1.2}_{-1.0}$ Gyr. We derived a planetary mass and radius of $M_\mathrm{p} = 33 \pm 12 \, M_\oplus$ and $R_\mathrm{p} = 4.36^{+0.31}_{-0.30} \, R_\oplus$. K2-98 b joins the relatively small group of Neptune-size planets whose both mass and radius have been derived with a precision better than 30% (see Barragán et al., 2016).

- **K2-139 b** is a warm Jupiter with a mass of $M_\mathrm{p} = 0.387^{+0.083}_{-0.075} \, M_\mathrm{J}$ and radius of $R_\mathrm{p} = 0.808^{+0.034}_{-0.033} \, R_\mathrm{J}$. It transits a K0 V star every 29 days. K2-139 b is one of the transiting warm Jupiters with the lowest mass known to date. The planetary

mean density of $\rho_p = 0.91^{+0.24}_{-0.20}$ g cm^{-3} can be explained with a core of $\sim 50\,M_\oplus$. The magnitude of the host star (V=11.7 mag), the relatively short transit duration (~ 5 h), and the expected amplitude of the the Rossiter-McLaughlin effect (~ 25 km s^{-1}) make K2-139 an ideal target to measure the spin-orbit angle of a warm Jupiter. This would shed insights into the formation of warm Jupiters (see Barragán et al., 2018a).

- **K2-141 b** is an ultra-short period super-Earth with a mass of $M_{\rm p} = 5.31 \pm 0.46\,M_\oplus$ and radius of $R_{\rm p} = 1.54^{+0.10}_{-0.09}\,R_\oplus$, yielding a mean density of $\rho_{\rm p} = 8.00^{+1.83}_{-1.45}$ g cm^{-3} and suggesting a rocky-iron composition. With an orbital period of only 6.7 hours, K2-141 b is the shortest-period planet known to date with a precisely determined mass (see Barragán et al., 2018b).

- **K2-111 b** is a super-Earth transiting a very old star (~ 11 Gyr), metal-poor ($[Fe/H] = -0.53 \pm 0.05$ dex) G3 V star with a radius of $R_\star = 1.30 \pm 0.10\,R_\odot$ and a mass of $M_\star = 0.88 \pm 0.02\,M_\odot$. K2-111 b has a mass of $M_{\rm p} = 8.6 \pm 3.9 M_\oplus$ and a radius of $R_{\rm p} = 1.9 \pm 0.2\,R_\oplus$. With an age of ~ 11 Gyr this system is one of the oldest where a planet is hitherto detected. Further studies of this planetary system are important since it contains information about the planetary formation process during a very early epoch of the history of our Galaxy (see Fridlund et al., 2017).

- **K2-19** is a compact multi-planet system hosting three planets, of which the two larger ones, K2-19 b and K2-19 c, are close to the 3:2 mean motion resonance. An analysis considering only the radial velocity measurements detects K2-19 b, the larger and more massive planet in the system, with a mass of $54.8 \pm 7.5\,M_\oplus$ and provides a marginal detection of K2-19 c, with a mass of $5.9^{+7.6}_{-4.3}\,M_\oplus$ (see Nespral et al., 2017).

- **K2-106** is a transiting multi-planet system hosting an ultra-short period (P = 0.57 d) super-Earth and a mini-Neptune on a 13.3-day orbit. For K2-106 b we derived $M_{\rm b} = 8.36^{+0.96}_{-0.94}\,M_\oplus$, $R_{\rm b} = 1.52 \pm 0.16\,R_\oplus$, and a high density of $13.1^{+5.4}_{-3.6}$ g cm^{-3}. For K2-106 c, we found $M_{\rm c} = 5.8^{+3.3}_{-3.0}\,M_\oplus$, $R_{\rm c} = 2.50^{+0.27}_{-0.26}\,R_\oplus$ and a relatively low density of $2.0^{+1.6}_{-1.1}$ g cm^{-3}. It is likely that the outer planet has a hydrogen-dominated atmosphere. The mass and radius of the inner planet are in agreement with theoretical models predicting an iron core containing about $80\,\%$ of its mass. K2-106 is an excellent laboratory to study atmospheric escape because the system contains two planets of almost the same mass but at different distances from the host star (see Guenther et al., 2017).

- **HD 3167** is a bright ($V = 8.9$ mag) K0 V star hosting two transiting planets, namely HD3167 b and c. With a mass of $5.69 \pm 0.44\,M_\oplus$, a radius of $1.574 \pm 0.054\,R_\oplus$, and a mean density of $8.00^{+1.10}_{-0.98}$ g cm^{-3}, HD3167 b joins the small group of ultra-short-period planets known to have rocky terrestrial compositions. HD3167 c has a mass of $8.33^{+1.79}_{-1.85}\,M_\oplus$ and a radius of $2.740^{+0.106}_{-0.100}\,R_\oplus$, yielding a mean density of $2.21^{+0.56}_{-0.53}$ g cm^{-3}, indicative of a planet with a composition comprising a solid core surrounded by a thick atmospheric envelope. Given the brightness of the host star, HD 3167 c is an ideal target for atmospheric characterisation via transmission spectroscopy across a broad range of wavelengths (see Gandolfi et al., 2017).

- **GJ 9827** has recently been found to host a tightly packed system consisting of three transiting small planets whose orbital periods of 1.2, 3.6, and 6.2 days are near the 1:3:5 ratio. We found that the inner planet, GJ 9827 b, has a mass of $M_{\rm b} = 3.69^{+0.48}_{-0.46}\,M_\oplus$ and a radius of $R_{\rm b} = 1.58^{+0.14}_{-0.13}\,R_\oplus$, yielding a mean density of $\rho_{\rm b} = 5.11^{+1.74}_{-1.27}$ g cm^{-3}. GJ 9827 c has a mass of $M_{\rm c} = 1.45^{+0.58}_{-0.57}\,M_\oplus$, radius of

Table 7.1: Main parameters of the planetary systems whose masses, radii and bulk densities have been derived as part of the project here presented.

Name	Period (days)	Mass ($M_\oplus$)	Radius ($R_\oplus$)	Semi-major axis (AU)	Spectral type
K2-98 b	10.13675 ± 0.00033	33 ± 12	$4.36^{+0.31}_{-0.30}$	$0.089^{+0.009}_{-0.013}$	F8 V
K2-141 b	0.2803226 ± 0.0000013	5.31 ± 0.46	$1.54^{+0.10}_{-0.09}$	$0.00716^{+0.00055}_{-0.00065}$	K7 V
K2-111 b	5.35117 ± 0.00055	8.6 ± 3.9	1.9 ± 0.2	$0.0621^{+0.0092}_{-0.0085}$	G3 V
K2-19 b[a]	$7.91951^{+0.00040}_{-0.00012}$	54.8 ± 7.5	$7.23^{+0.56}_{-0.51}$	$0.077^{+0.008}_{-0.013}$	K0 V
K2-19 c[a]	$11.9066^{+0.0021}_{-0.0014}$	$5.9^{+7.6}_{-4.3}$	4.21 ± 0.31	$0.1032^{+0.0074}_{-0.0080}$	K0 V
K2-106 b	0.571292 ± 0.000012	$8.36^{+0.96}_{-0.94}$	1.52 ± 0.16	$0.0110^{+0.0014}_{-0.0016}$	G5 V
K2-106 c	$13.33966^{+0.00092}_{-0.00099}$	$5.8^{+3.3}_{-3.0}$	$2.50^{+0.27}_{-0.26}$	$0.096^{+0.030}_{-0.026}$	G5 V
HD 3167 b	0.959632 ± 0.000015	5.69 ± 0.44	1.574 ± 0.054	0.01752 ± 0.00063	K0 V
HD 3167 c	$29.84622^{+0.00098}_{-0.00091}$	$8.33^{+1.79}_{-1.85}$	$2.740^{+0.106}_{-0.100}$	0.1806 ± 0.0080	K0 V
GJ 9827 b	1.208966 ± 0.000012	3.69 ± 0.47	1.58 ± 0.14	$0.0210^{+0.0024}_{-0.0026}$	K6 V
GJ 9827 c	3.64823 ± 0.00012	1.45 ± 0.57	1.24 ± 0.11	$0.0439^{+0.0050}_{-0.0055}$	K6 V
GJ 9827 d	6.20142 ± 0.00013	2.35 ± 0.69	2.04 ± 0.18	$0.0625^{+0.0071}_{-0.0075}$	K6 V
π Men c	6.26830 ± 0.00027	4.50 ± 0.81	2.08 ± 0.04	0.0670 ± 0.0011	G0 V
Name	Period (days)	Mass (M_J)	Radius (R_J)	Semi-major axis (AU)	Spectral type
K2-139 b	28.38236 ± 0.00026	$0.387^{+0.083}_{-0.075}$	$0.808^{+0.034}_{-0.033}$	$0.179^{+0.021}_{-0.027}$	K0 V

Note – [a] Planet radii and semi-major axes are taken from Armstrong et al. (2015).

$R_c = 1.24^{+0.11}_{-0.11}\,R_\oplus$, and a mean density of $\rho_c = 4.13^{+2.31}_{-1.77}\,\mathrm{g\,cm^{-3}}$. For GJ 9827 d we derived $M_d = 2.35^{+0.70}_{-0.68}\,M_\oplus$, $R_d = 2.04^{+0.18}_{-0.18}\,R_\oplus$, and $\rho_d = 1.51^{+0.71}_{-0.53}\,\mathrm{g\,cm^{-3}}$. GJ 9827 is one of the few known transiting planetary systems for which the masses of all planets have been determined with a precision better than 30%. We found that the planetary bulk compositions are compatible with a scenario where all three planets formed with similar core/atmosphere compositions, and we speculated that while GJ 9827 b and GJ 9827 c lost their atmospheric envelopes, GJ 9827 d maintained its atmosphere, owing to the much lower stellar irradiation (see Niraula et al., 2017; Prieto-Arranz et al., 2018).

- π **Mensae** is a naked-eye (V=5.65 mag), quiet G0 V star that was previously known to host a sub-stellar companion (π Men b) on a long-period (P_{orb} = 2091 days), eccentric ($e = 0.64$) orbit. We reported on the confirmation and mass determination of an additional planet, π Men c, which is the first transiting planet discovered by NASA's TESS space mission. We found that π Men c is a close-in planet with an orbital period of $P_{orb} = 6.27$ days, a mass of $4.50 \pm 0.81\,M_\oplus$, and a radius of $2.08 \pm 0.04\,R_\oplus$. Based on the planet's orbital period and size, π Men c is a super-Earth located at, or close to, the radius gap, while its mass and bulk density suggest it may have held on to a significant atmosphere. Because of the brightness of the host star, this system is highly suitable for a wide range of further studies to characterise the planetary atmosphere and dynamical properties (see Gandolfi et al., 2018).

We summarise the main parameters of these planetary systems in Table 7.1.

Figure 7.1 shows a mass-radius diagram similar to the one presented in Sect. 1.5.1. The red dots highlight the planets listed in Table 7.1. We note that "our planets" fall in different radius regimes covering super-Earths, icy giants, and gas giants exoplanets.

Stellar irradiance on close-in planets can play a major role in explaining some of the observed diversity in small planet densities. Photo-evaporation can strip the atmosphere
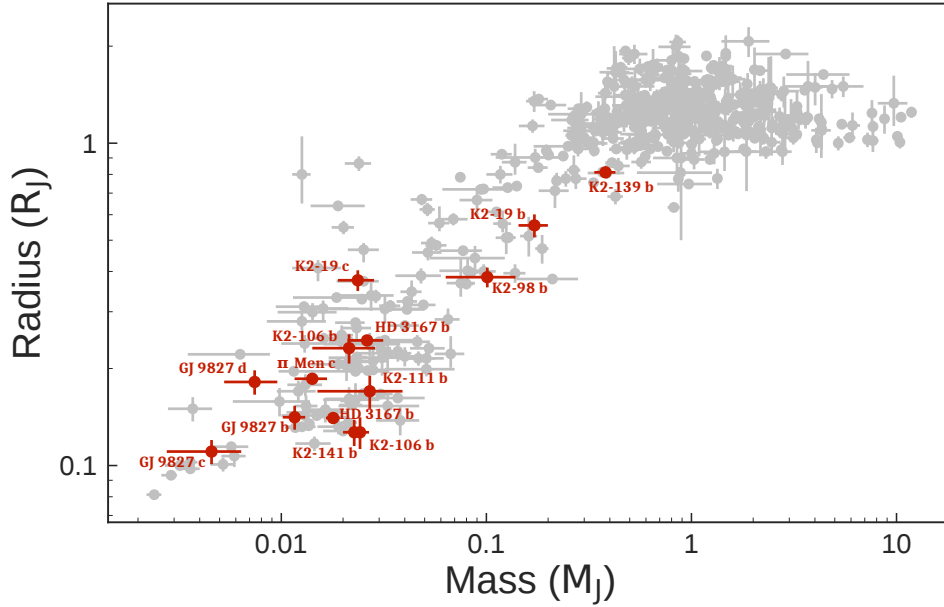
Figure 7.1: Mass-radius diagram. Gray points represent exoplanets whose masses and radii are known with a precision better than 50%. The red points mark the exoplanets that have been characterised in the course of this thesis work (see also Chapter 6 and Table 7.1). This plot has been created using the planet parameters listed in www.astro.keele.ac.uk/jkt/tepcat/ as of Sept. 07, 2018.
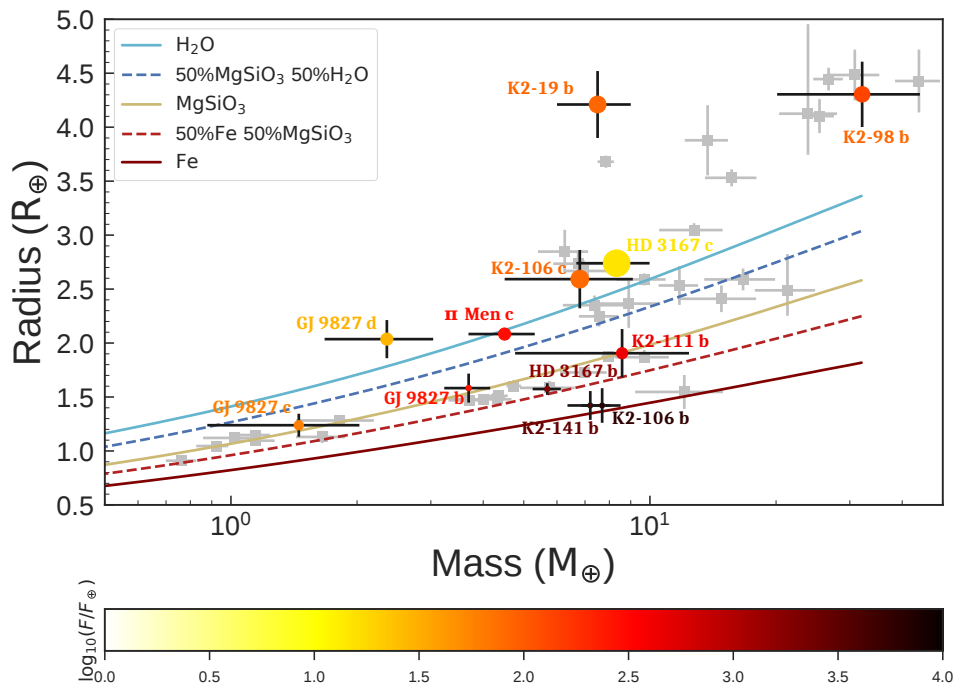
Figure 7.2: Mass-radius diagram for exoplanets with radii $< 5\,R_\oplus$. The gray squares represent exoplanets in literature whose masses and radii are known with a precision better than 30%. The coloured circles mark the exoplanets that have been characterised in the course of this thesis work (see also Chapter 6 and Table 7.1). The colour code represents the insolation received by the planet ($\log_{10}(F/F_\oplus)$, where $F_\oplus$ is the Earth's insolation). The sizes of the circle are proportional to the orbital periods (the larger is the circle, the longer is the period). This plot has been created using the planet parameters listed in www.astro.keele.ac.uk/jkt/tepcat/ as of Sept. 07, 2018.

of a Neptune-like planet leaving behind a dense rocky core. Ultra-short period planets (USPs) may be important objects in understanding the role of photo-evaporation. USPs have $R_p < 1.7 R_\oplus$ and $P < 1$ day (Sanchis-Ojeda et al., 2014). Given the proximity to their host stars, USPs are expected to be stripped cores of planets that have lost their atmospheres due to photo-evaporation. As part of this thesis, we have also vastly increased our knowledge of USPs. Sanchis-Ojeda et al. (2014) found that all USPs are in multi-planet systems, yet there are only 5 USP systems where the mass has been determined for more than one planet and we have provided characterisation for 2 of these systems (K2-106 and HD 3167). Thanks to our detections we see a trend that USP planets have densities $5 - 10$ times higher than the outer planets in the system indicating that photo-evaporation may indeed play a role in the observed diversity of densities in multi-planet systems. USPs could provide important clues in understanding the diverse planet compositions and the effects of photo-evaporation.

Our results confirm that small planets with similar masses can have different radii. Those with $R_p \lesssim 1.5\,R_\oplus$ have internal compositions consistent with different mixtures of rocks and iron. Objects with radii $R_p \gtrsim 2.0\,R_\oplus$, have densities indicative of planets with compositions comprising a solid core surrounded by a thick atmospheric envelope. Figure 7.2 shows the mass-radius diagram for planets with masses $<50\ M_\oplus$. We highlight the planets characterised in this thesis using both a colour code that depends on the planet insolation, and a marker whose size depends on the orbital period. The planets with the shortest orbital periods are those that receive a higher level of stellar irradiation. These planets have the higher density in our sample and are likely bare cores whose atmospheres have been stripped away. On the other hand, planets with longer period and lower irradiation levels, have larger radii. These can be explained by the presence of volatile envelopes, which account for a small fraction of the mass.

The characterisation of the super-Earth and sub-Neptune-size planets presented in this thesis represent a leap forward in understanding small planets. GJ 9827 d, HD 3167 c, K2-106 c, and π Men c are excellent laboratories to perform atmospheric studies.

Perspectives

We are now living in a fascinating era in which we know that *other Suns are the centres of concentric systems of many worlds.* Planets are ubiquitous in the Galaxy and – we can safely assume – in the Universe. Missions such as *Kepler* and *K2*, and instruments such as HARPS and HARPS-N have helped us to understand the nature of other worlds. The most exiting thing is that exoplanet science is still at the beginning of its era. The future for exoplanet science is promising. The on-going and planned exoplanet hunters (e.g., `TESS`, `PLATO`, `CHEOPS`, `ESPRESSO`) will reveal new mysteries about new worlds. Future exoplanet discoveries will remember us that there are faraway worlds waiting to be unveiled. One by one, these discoveries will contribute to the legacy of curiosity, the main distinctive quality of humankind.

Appendices

APPENDIX A

Issues with stellar light curve data

A.1 Intrinsic stellar flux variations

The light curve of a star can display flux variability induced by, e.g., flares, pulsations, Sun-like spots, plages, etc. Figure 6.6 shows the *K2* light curve of K2-139, a magnetically active star hosting a transiting warm Jupiter on a 29-day orbit (Sect. 6.2). Three transits are visible at $BJD - 2454833 \approx 2493$, 2521, and 2550 days super-imposed on a quasi-periodic flux variation induced by the presence of active regions carried around by stellar rotation. Stellar photometric variability can allow us to measure, e.g., the rotation period of the star (e.g., Barragán et al., 2018a,b), perform asteroseismic studies (e.g., Van Eylen et al., 2018b), and estimate the impact of stellar activity on RV measurements (e.g., Dumusque et al., 2014).

When modelling a transit light curve, it is convenient to remove any trend caused by stellar variability and analyse "flattened" light curves. One of the most common method to flatten a transit light curve is by removing the local trend around each transit. This can be achieved by fitting a N-order polynomial to the out-of-transit data around each transit, and divide each light curve segment – including the in-transit data – by the best-fitting polynomial. Figure A.1 shows the local detrending performed around each of the three transit light curves of K2-139 (Sect. 6.2).

In order to flatten transit light curves, we developed a code called `exotrending` (Barragán & Gandolfi, 2017), which is freely available at `https://github.com/oscaribv/exotrending`. The inputs to the code are a light curve, and the duration and ephemeris of the transit, namely, the epoch of first transit and the orbital period. The code extracts chunks of the light curve centred around each transit, fits a second order polynomial to the out-of-transit data, normalise each segment, and finally fits a Mandel & Agol (2002) model in order to remove 10-σ outliers. `Exotrending` generates a set of normalised transit light curves that can be modelled using, e.g., `pyaneti` (Barragán et al., 2019, see also Sect. 5.3). The code has been tested with *Kepler* and *K2* light curves and has been used for the analysis of some of the planetary systems presented in Chapter 6.
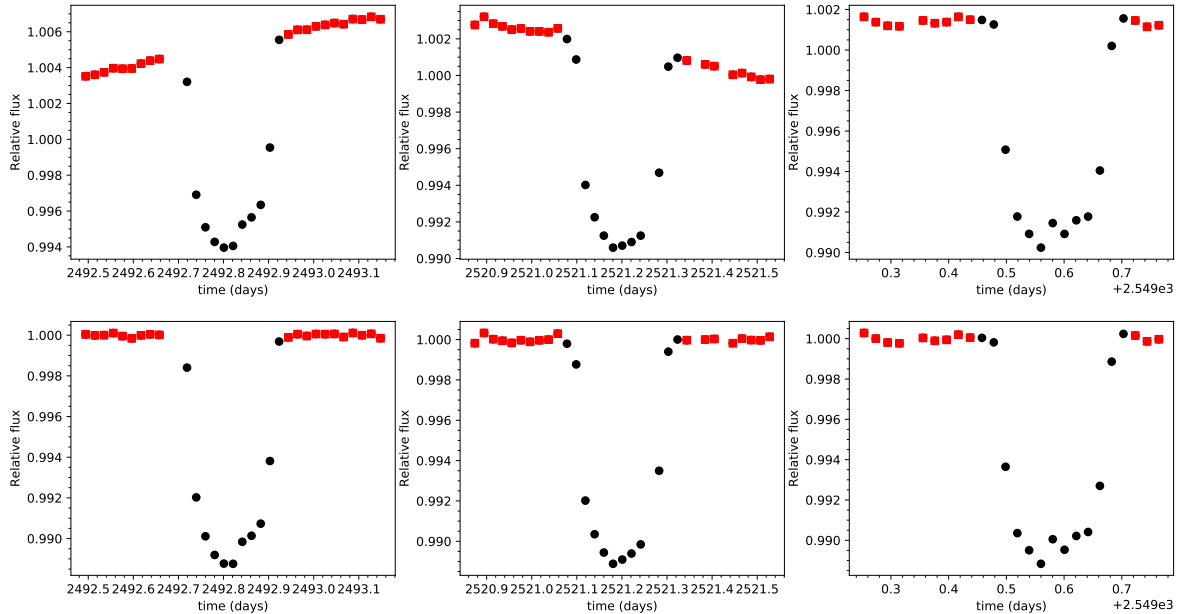
Figure A.1: *K2* transits light curve of EPIC 218916923 (K2-139). The out-of-transit and in-transit data are shown with red squares and black circles, respectively. The upper panels show the non-flattened transit light curves, as extracted from the K2 data. The trends clearly visible in the first and second transit are induced by Sun-like spots crossing the visible hemisphere as the star rotates around its axis. The lower panels display the transit light curves flattened using the code `Exotrending`.

A.2   Finite integration time

In Sect. 2.3 we described the equations used to model a transit light curve. However, these equations give the instantaneous flux, whereas CCD photometers integrate the stellar light for a finite amount of time. The finite integration stretches out the ingress and egress transit duration and suppresses the limb darkening effects (Kipping, 2010). If not taken into account, the finite integration time may lead to severe systematic errors on the parameter estimates. The so-called light curve "smearing" becomes clearly visible when the exposure time is comparable to the transit duration. Figure A.2 shows the effects of the *K2* 30-min integration time on the light curve of K2-141 (Barragán et al., 2018b, see Sect. 6.3).

Kipping (2010) demonstrated that the best approach to account for the finite integration time is by resampling the transit model. The resampling method works as follows: for a flux measurement F_i at the time t_i with an integration time $\mathcal{I}$, the resampling of the time t_i into N sub-time stamps with labels $j = 1, \ldots, N-1, N$, can be written as

$$t_{i,j} = t_i + \left(j - \frac{N+1}{2}\right)\frac{\mathcal{I}}{N}. \tag{A.1}$$

Let us define $F_{i,j}$ as the theoretical flux at each time $t_{i,j}$. The model flux $\hat{F}_i$ can be derived by rebinning the N fluxes $F_{i,j}$ as

$$\hat{F}_i = \frac{1}{N}\sum_{j=1}^{N} F_{i,j}. \tag{A.2}$$

The quantity $\hat{F}_i$ is the integrated flux model corresponding to the time stamp t_i. The synthetic flux $\hat{F}_i$ can then be compared with the measurement F_i when modelling the
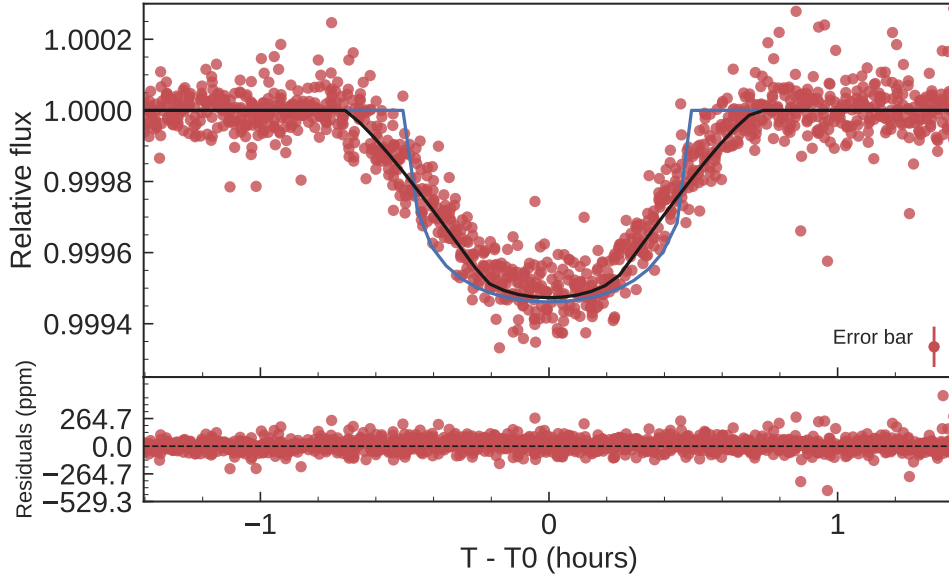
Figure A.2: Light curve of K2-141 folded to the orbital period of K2-141 b and residuals. The red points mark the *K2* data. The thick black line the re-binned transit model. The blue line shows how the transit would look like if the exposure time were 1 second.

transit light curve (see Chapter 5).

Kipping (2010) showed that the error on the resampling method varies as $\propto N^{-2}$. This implies that a resampling computed with a large number of subsamples produces better results. However, a large number of subsamples has a computational cost. For instance, an optimal N value has to be chosen in order to resample the model without compromise the computational resources. We note that it is possible to speed-up the computations using selective resampling, i.e., the resampling is done only for in-transit points (Kipping, 2010).

In this thesis we analysed long cadence time-series photometry from the *K2* mission. We performed a numerical test to choose the optimal value of N. This has to be large enough to properly account for the long exposure time, but not too large to preserve the numerical efficiency of the modelling. We utilised `pyaneti` (see Sect. 5.3) to model the *K2* long-cadence data using $N = 1$, 10, and 30. We modeled light curves with different transit durations and depths. The tests with $N = 1$ provided parameter estimates that did not agree with those abstained with $N = 10$ and 30. Moreover, for $N = 1$ the derived stellar densities did no agree with the spectroscopic densities. We found that $N = 10$ and 30 provided consistent results well withing the 1-σ uncertainty. We therefore adopted $N = 10$ – which is ~ 3 faster than $N = 30$ – to resample the transit models when fitting the *K2* long cadence data.

APPENDIX B

Techniques to mitigate stellar activity

The mass determination of low-mass extra-solar planets through Doppler spectroscopy is currently hindered by the intrinsic magnetic activity of the host stars (Hatzes, 2016). The RV signal induced by stellar activity can mimic or conceal planetary signals. For solar-like stars, one of main source of stellar RV signal – also known as stellar noise or jitter – is the presence of cool spots, hot faculae, and plagues combined with stellar rotation. Typical values of the RV jitter range from a few $m\,s^{-1}$ to tens of $m\,s^{-1}$ (see, e.g., Dumusque et al., 2014). The stellar RV signal is thus of the same order of magnitude or even larger than the expected RV amplitude induced by a close-in low-mass planet.

In this Appendix we describe three techniques that were used in this thesis to disentangle planetary signals from stellar activity signal.

B.1 Floating Chunk Offset (FCO) method

The floating chunk offset (FCO Hatzes et al., 2011) method is useful to disentangle the RV signal induced but a planet whose orbital period is shorter than the period of other signals, such as stellar activity or additional planets in long-period orbits.

This technique divides a given RV time series into segments of duration Δt, long enough to encompass a significant fraction of the orbital signal of a planet. Each segment has to include at least two measurements. If additional RV signals with periods $\gg \Delta t$ are present in the data, we can assume that they remain constant within the time interval Δt. We can also assume that the RV variation observed within each segment mainly reflects the orbital motion of the short period planet rather than other, longer period signals, such as those induced by stellar rotation, magnetic activity, and/or additional planets in long period orbits. For each sub-segment, we can fit an offset that account for any long period signal, assuming that it remains nearly constant within the time interval Δt.

This method is ideal for planets whose orbital period is shorter than one day – the so-called ultra-short period (USP) planets. By acquiring multiple RV measurements per night, we can cover a significant fraction of the orbital signal of an USP planet. We can divide the data in nightly chunks and fit for an offset for each night. Examples of the use of the FCO method are given in this thesis for the USP planets K2-141 b (Sect. 6.3),

K2-106 b (Sect. 6.6), and HD 3167 b (Sect. 6.7). A good example of the use of the FCO method for a planet whose orbital period is longer than one day is given in Persson et al. (2018).

B.2   Stellar activity as a coherent signal

Radial velocity variations due to active regions coupled to stellar rotational modulation can be complex with not only the stellar rotational period $P_{\rm rot}$ present, but also its harmonics, e.g., $P_{\rm rot}/2$, $P_{\rm rot}/3$. Assuming that the surface structures responsible for this modulation (e.g., cool spots) are not evolving rapidly, then the simplest representation of the rotational modulation is through the Fourier components defined by the rotation period and its harmonics.

   If the RV follow-up spans a time interval that is shorter than the evolution time-scale of active regions, we can assume that any activity-induced RV signal is coherent within this observing window. This approach has been used previously for planetary systems orbiting active stars (e.g., Pepe et al., 2013). This approach has been largely used in this thesis, as described in Sect. 6.2, 6.3, 6.7, and 6.8.

B.3   Gaussian processes

The stellar activity-induced RV signal can also be treated as a stochastic process. If we assume that the "stellar noise" follows a normal distribution, it can be modelled using Gaussian processes (GPs). Usually, GPs require a computationally expensive inversion of an $n \times n$ covariance matrix, where n is the number of data points. However, some techniques have been developed to evaluate correlated time-series with numerical efficient methods. They allow GPs to be used many problems encountered in exoplanet research (see, e.g., Díaz, 2018; Parviainen, 2017).

Bibliography

Adams, E. R., Jackson, B., Endl, M., et al. 2017, AJ, 153, 82

Aigrain, S., Parviainen, H., & Pope, B. J. S. 2016, MNRAS, 459, 2408

Albrecht, S., Winn, J. N., Johnson, J. A., et al. 2012, ApJ, 757, 18

Allard, F., Homeier, D., & Freytag, B. 2011, in Astronomical Society of the Pacific Conference Series, Vol. 448, 16th Cambridge Workshop on Cool Stars, Stellar Systems, and the Sun, ed. C. Johns-Krull, M. K. Browning, & A. A. West, 91

Alonso, R., Brown, T. M., Torres, G., et al. 2004, ApJ, 613, L153

Anderson, D. R., Collier Cameron, A., Hellier, C., et al. 2011, ApJL, 726, L19

Angus, R., Aigrain, S., Foreman-Mackey, D., & McQuillan, A. 2015, MNRAS, 450, 1787

Armstrong, D. J., Santerne, A., Veras, D., et al. 2015, A&A, 582, A33

Auvergne, M., Bodin, P., Boisnard, L., et al. 2009, A&A, 506, 411

Bakos, G., Noyes, R. W., Kovács, G., et al. 2004, PASP, 116, 266

Bakos, G. Á., Torres, G., Pál, A., et al. 2010, ApJ, 710, 1724

Bakos, G. Á., Csubry, Z., Penev, K., et al. 2013, PASP, 125, 154

Baranne, A., Queloz, D., Mayor, M., et al. 1996, A&AS, 119, 373

Barnes, S. A. 2010, ApJ, 722, 222

Barnes, S. A., & Kim, Y.-C. 2010, ApJ, 721, 675

Barragán, O., & Gandolfi, D. 2017, Exotrending, ASCL, ascl:1706.001

Barragán, O., Gandolfi, D., & Antoniciello, G. 2019, MNRAS, 482, 1017

Barragán, O., Grziwa, S., Gandolfi, D., et al. 2016, AJ, 152, 193

Barragán, O., Gandolfi, D., Smith, A. M. S., et al. 2018a, MNRAS, 475, 1765

Barragán, O., Gandolfi, D., Dai, F., et al. 2018b, A&A, 612, A95

Barros, S. C. C., Demangeon, O., & Deleuil, M. 2016, A&A, 594, A100

Barros, S. C. C., Almenara, J. M., Demangeon, O., et al. 2015, MNRAS, 454, 4267

Baruteau, C., Crida, A., Paardekooper, S.-J., et al. 2014, Protostars and Planets VI, 667

Batalha, N. M., Borucki, W. J., Bryson, S. T., et al. 2011, ApJ, 729, 27

Batalha, N. M., Rowe, J. F., Bryson, S. T., et al. 2013, APJS, 204, 24

Batygin, K., Bodenheimer, P. H., & Laughlin, G. P. 2016, ApJ, 829, 114

Bayes, M., & Price, M. 1763, Philosophical Transactions (1683-1775), 53, 370

Benedict, G. F., McArthur, B. E., Forveille, T., et al. 2002, ApJL, 581, L115

Boccaletti, A. 2011, in Astronomical Society of the Pacific Conference Series, Vol. 450, Molecules in the Atmospheres of Extrasolar Planets, ed. J. P. Beaulieu, S. Dieters, & G. Tinetti, 163

Boley, A. C., Granados Contreras, A. P., & Gladman, B. 2016, ApJL, 817, L17

Bond, I. A., Udalski, A., Jaroszyński, M., et al. 2004, ApJL, 606, L155

Borucki, W., Koch, D., Basri, G., et al. 2008, in IAU Symposium, Vol. 249, Exoplanets: Detection, Formation and Dynamics, ed. Y.-S. Sun, S. Ferraz-Mello, & J.-L. Zhou, 17

Bouchy, F., Díaz, R. F., Hébrard, G., et al. 2013, A&A, 549, A49

Boyajian, T. S., von Braun, K., van Belle, G., et al. 2013, ApJ, 771, 40

Bressan, A., Marigo, P., Girardi, L., et al. 2012, MNRAS, 427, 127

Broeg, C., Fortier, A., Ehrenreich, D., et al. 2013, in European Physical Journal Web of Conferences, Vol. 47, European Physical Journal Web of Conferences, 03005

Bruno, G., & Williams, L. 1887, The Heroic Enthusiasts (London)

Bryan, M. L., Knutson, H. A., Fulton, B., et al. 2018, ArXiv e-prints, arXiv:1806.08799

Buchhave, L. A., Bakos, G. Á., Hartman, J. D., et al. 2010, ApJ, 720, 1118

Buchhave, L. A., Latham, D. W., Johansen, A., et al. 2012, Natur, 486, 375

Burnham, K., & Anderson, D. 2002, Model Selection and Multimodel Inference: A Practical Information-Theoretic Approach (New York: Springer-Verlag)

Butler, R. P., Wright, J. T., Marcy, G. W., et al. 2006, ApJ, 646, 505

Cabrera, J., Csizmadia, S., Erikson, A., Rauer, H., & Kirste, S. 2012, A&A, 548, A44

Cagigal, M. P., Valle, P. J., Colodro-Conde, C., Villó-Pérez, I., & Pérez-Garrido, A. 2016, MNRAS, 455, 2765

Cameron, A. C. 2016, Extrasolar Planetary Transits, ed. V. Bozza, L. Mancini, & A. Sozzetti (Cham: Springer International Publishing), 89

Campbell, B., Walker, G. A. H., & Yang, S. 1988, ApJ, 331, 902

Cardelli, J. A., Clayton, G. C., & Mathis, J. S. 1989, ApJ, 345, 245

Cauley, P. W., Redfield, S., & Jensen, A. G. 2017, AJ, 153, 185

Chabrier, G. 2001, ApJ, 554, 1274

Chakraborty, A., Roy, A., Sharma, R., et al. 2018, AJ, 156, 3

Chambers, J. E. 1999, MNRAS, 304, 793

Charbonneau, D., Brown, T. M., Latham, D. W., & Mayor, M. 2000, ApJL, 529, L45

Charbonneau, D., Berta, Z. K., Irwin, J., et al. 2009, Natur, 462, 891

Charpinet, S., Fontaine, G., Brassard, P., et al. 2011, Natur, 480, 496

Chen, G., Guenther, E. W., Pallé, E., et al. 2017, A&A, 600, A138

Chen, J., & Kipping, D. 2017, ApJ, 834, 17

Christen, J. 2007, Technical Report I-07-16, CIMAT, Guanajuato

Christiansen, J. L., Vanderburg, A., Burt, J., et al. 2017, AJ, 154, 122

Claret, A. 2017, A&A, 600, A30

Claret, A., & Bloemen, S. 2011, A&A, 529, A75

Claret, A., & Hauschildt, P. H. 2003, A&A, 412, 241

Cohen, I. B., Whitman, A., Budenz, J., & Cohen, I. B. 1999, The Principia: Mathematical Principles of Natural Philosophy, 1st edn. (University of California Press)

CoRot Team. 2016, The CoRoT Legacy Book: The adventure of the ultra high precision photometry from space, by the CoRot Team

Cosentino, R., Lovis, C., Pepe, F., et al. 2012, in Ground-based and Airborne Instrumentation for Astronomy IV, Vol. 8446, 84461V

Crane, J. D., Shectman, S. A., Butler, R. P., et al. 2010, in Ground-based and Airborne Instrumentation for Astronomy III, Vol. 7735, 773553

Crane, J. D., Shectman, S. A., Butler, R. P., Thompson, I. B., & Burley, G. S. 2008, in Ground-based and Airborne Instrumentation for Astronomy II, Vol. 7014, 701479

Csizmadia, S., Pasternacki, T., Dreyer, C., et al. 2013, A&A, 549, A9

Csizmadia, S., Moutou, C., Deleuil, M., et al. 2011, A&A, 531, A41

Dai, F., Winn, J. N., Gandolfi, D., et al. 2017, AJ, 154, 226

Damiani, C., & Lanza, A. F. 2015, A&A, 574, A39

Demory, B.-O. 2014, ApJL, 789, L20

Díaz, R. F. 2018, Asteroseismology and Exoplanets: Listening to the Stars and Searching for New Worlds, 49, 199

Donati, J.-F., Kouach, D., Lacombe, M., et al. 2017, SPIRou: A nIR Spectropolarimeter/High-precision Velocimeter for the CFHT, 107

Dressing, C. D., Charbonneau, D., Dumusque, X., et al. 2015, ApJ, 800, 135

Dumusque, X., Bonomo, A. S., Haywood, R. D., et al. 2014, ApJ, 789, 154

Eastman, J., Gaudi, B. S., & Agol, E. 2013, PASP, 125, 83

Eastman, J., Siverd, R., & Gaudi, B. S. 2010, PASP, 122, 935

Ehrenreich, D., Bourrier, V., Wheatley, P. J., et al. 2015, Natur, 522, 459

Espinoza, N., & Jordán, A. 2015, MNRAS, 450, 1879

Fabricius, C., Bastian, U., Portell, J., et al. 2016, A&A, 595, A3

Fisher, R. 1925, Statistical methods for research workers (Edinburgh Oliver & Boyd)

Foreman-Mackey, D., Hogg, D. W., Lang, D., & Goodman, J. 2013, PASP, 125, 306

Fortney, J. J., Marley, M. S., & Barnes, J. W. 2007, ApJ, 659, 1661

Fossati et al. 2017, A&A, submitted, arXiv:0901.2573 [astro-ph.IM]

Frandsen, S., & Lindberg, B. 1999, in Astrophysics with the NOT, ed. H. Karttunen & V. Piirola, 71

Fridlund, M., Gaidos, E., Barragán, O., et al. 2017, A&A, 604, A16

Fulton, B. J., Petigura, E. A., Howard, A. W., et al. 2017, AJ, 154, 109

Gaia Collaboration, Brown, A. G. A., Vallenari, A., et al. 2016, A&A, 595, A2

Gandolfi, D., Alcalá, J. M., Leccia, S., et al. 2008, ApJ, 687, 1303

Gandolfi, D., Collier Cameron, A., Endl, M., et al. 2012, A&A, 543, L5

Gandolfi, D., Parviainen, H., Fridlund, M., et al. 2013, A&A, 557, A74

Gandolfi, D., Parviainen, H., Deeg, H. J., et al. 2015, A&A, 576, A11

Gandolfi, D., Barragán, O., Hatzes, A. P., et al. 2017, AJ, 154, 123

Gandolfi, D., Barragán, O., Livingston, J. H., et al. 2018, A&A, 619, L10

Gelman, A., Carlin, J. B., Stern, H. S., & Rubin, D. B. 2004, Bayesian Data Analysis, 2nd edn. (Chapman and Hall/CRC)

Gelman, A., & Rubin, D. B. 1992, Statistical Science, 7, 457

Gillon, M., Jehin, E., Delrez, L., et al. 2013, in Protostars and Planets VI Posters

Gillon, M., Jehin, E., Magain, P., et al. 2011, in European Physical Journal Web of Conferences, Vol. 11, 06002

Gillon, M., Triaud, A. H. M. J., Demory, B.-O., et al. 2017, Natur, 542, 456

Goodman, J., & Weare, J. 2010, Commun Appl Math Comput Sci, 5, 65

Gray, D. F. 2005, The Observation and Analysis of Stellar Photospheres, 3rd edn. (Cambridge University Press)

Grziwa, S., Pätzold, M., & Carone, L. 2012, MNRAS, 420, 1045

Guenther, E. W., Barragán, O., Dai, F., et al. 2017, A&A, 608, A93

Hadden, S., & Lithwick, Y. 2014, ApJ, 787, 80

Han, E., Wang, S. X., Wright, J. T., et al. 2014, PASP, 126, 827

Hansen, B. M. S. 2017, MNRAS, 467, 1531

Hastings, W. K. 1970, Biometrika, 57, 97

Hatzes, A. P. 2002, Astronomische Nachrichten, 323, 392

Hatzes, A. P. 2016, The Radial Velocity Method for the Detection of Exoplanets, ed. V. Bozza, L. Mancini, & A. Sozzetti (Cham: Springer International Publishing), 3

Hatzes, A. P., Cochran, W. D., Endl, M., et al. 2003, ApJ, 599, 1383

Hatzes, A. P., & Rauer, H. 2015, ApJL, 810, L25

Hatzes, A. P., Fridlund, M., Nachmani, G., et al. 2011, ApJ, 743, 75

Haywood, R. D., Collier Cameron, A., Queloz, D., et al. 2014, MNRAS, 443, 2517

Henry, G. W., Marcy, G., Butler, R. P., & Vogt, S. S. 1999, IAU Circ., 7307

Hogg, D. W., & Foreman-Mackey, D. 2018, APJS, 236, 11

Hou, F., Goodman, J., Hogg, D. W., Weare, J., & Schwab, C. 2012, ApJ, 745, 198

Howell, S. B., Everett, M. E., Sherry, W., Horch, E., & Ciardi, D. R. 2011, AJ, 142, 19

Howell, S. B., Sobeck, C., Haas, M., et al. 2014, PASP, 126, 398

Huang, C., Wu, Y., & Triaud, A. H. M. J. 2016, ApJ, 825, 98

Huang, C. X., Petrovich, C., & Deibert, E. 2017, AJ, 153, 210

Huang, C. X., Burt, J., Vanderburg, A., et al. 2018, ArXiv e-prints, arXiv:1809.05967 [astro-ph.EP]

Hunter, J. D. 2007, Computing in Science and Engineering, 9, 90

Irwin, J. M., Berta-Thompson, Z. K., Charbonneau, D., et al. 2015, in 18th Cambridge Workshop on Cool Stars, Stellar Systems, and the Sun, Vol. 18, 767

Jehin, E., Gillon, M., Queloz, D., et al. 2011, The Messenger, 145, 2

Jensen, O. G., & Ulrych, T. 1973, AJ, 78, 1104

Johnson, J. L., & Li, H. 2012, ApJ, 751, 81

Johnson, M. C., Dai, F., Justesen, A. B., et al. 2018, MNRAS, 481, 596

Jones, H. R. A., Paul Butler, R., Tinney, C. G., et al. 2002, MNRAS, 333, 871

Kant, I. 1755, Universal Natural History and Theory of the Heavens (translated by Johnston, I., California State University, 2008)

Kipping, D. M. 2010, MNRAS, 408, 1758

—. 2013, MNRAS, 435, 2152

Kley, W., & Nelson, R. P. 2012, ARA&A, 50, 211

Koch, D. G., Borucki, W., Dunham, E., et al. 2004, in Proc. SPIE 5487, Vol. 5487, Optical, Infrared, and Millimeter Space Telescopes, ed. J. C. Mather, 1491

Koch, D. G., Borucki, W. J., Basri, G., et al. 2010, ApJ, 713, L79

Kulow, J. R., France, K., Linsky, J., & Loyd, R. O. P. 2014, ApJ, 786, 132

Lanza, A. F., Damiani, C., & Gandolfi, D. 2011, A&A, 529, A50

Lanza, A. F., & Mathis, S. 2016, Celestial Mechanics and Dynamical Astronomy, 126, 249

Laplace, P. S. 1976, The System of the World (R. Phillips, 1809)

Latham, D. W., Mazeh, T., Stefanik, R. P., Mayor, M., & Burki, G. 1989, Natur, 339, 38

Léger, A., Rouan, D., Schneider, J., et al. 2009, A&A, 506, 287

Lenz, P., & Breger, M. 2004, in IAU Symposium, Vol. 224, The A-Star Puzzle, ed. J. Zverko, J. Ziznovsky, S. J. Adelman, & W. W. Weiss, 786

Lenz, P., & Breger, M. 2005, Communications in Asteroseismology, 146, 53

Li, Y., Stefansson, G., Robertson, P., et al. 2017, Research Notes of the American Astronomical Society, 1, 49

Livingston, J. H., Endl, M., Dai, F., et al. 2018, AJ, 156, 78

Lo Curto, G., Pepe, F., Avila, G., et al. 2015, The Messenger, 162, 9

Lopez, E. D., & Fortney, J. J. 2013, ApJ, 776, 2

—. 2014, ApJ, 792, 1

López-Morales, M., Haywood, R. D., Coughlin, J. L., et al. 2016, AJ, 152, 204

Lucy, L. B., & Sweeney, M. A. 1971, AJ, 76, 544

Luger, R., Agol, E., Kruse, E., et al. 2016, AJ, 152, 100

Lundkvist, M. S., Kjeldsen, H., Albrecht, S., et al. 2016, Nature Communications, 7, 11201

Malavolta, L., Mayo, A. W., Louden, T., et al. 2018, AJ, 155, 107

Mamajek, E. 2018, (@EricMamajek) #IAU Comm F2 #Exoplanets & Solar System: #IAU2018 bus. meeting, results from vote of comm members this summer. Updated working definition of planet (relevant for exoplanets) and nomenclature guidelines. Now includes mass ratio limit; planets can orbit brown dwarfs @IAU_org #AAS, Aug. 28, 2018, Tweet.

Mandel, K., & Agol, E. 2002, ApJL, 580, L171

Marcy, G. W., Weiss, L. M., Petigura, E. A., et al. 2014, Proceedings of the National Academy of Science, 111, 12655

Mayor, M., & Queloz, D. 1995, Natur, 378, 355

Mayor, M., Pepe, F., Queloz, D., et al. 2003, The Messenger, 114, 20

Mazeh, T., Holczer, T., & Faigler, S. 2016, A&A, 589, A75

McQuillan, A., Mazeh, T., & Aigrain, S. 2014, APJS, 211, 24

Meadows, V., & Seager, S. 2010, Terrestrial Planet Atmospheres and Biosignatures, ed. S. Seager, 441

Metropolis, N., Rosenbluth, A. W., Rosenbluth, M. N., Teller, A. H., & Teller, E. 1953, Journal of Computational Physics, 21, 1087

Morton, T. D., & Johnson, J. A. 2011, ApJ, 729, 138

Mulders, G. D., Pascucci, I., Apai, D., Frasca, A., & Molenda-Żakowicz, J. 2016, AJ, 152, 187

Murray, C. D., & Correia, A. C. M. 2010, Keplerian Orbits and Dynamics of Exoplanets, ed. S. Seager, 15

Murray, C. D., & Dermott, S. F. 2000, Solar System Dynamics

Mustill, A. J., Davies, M. B., & Johansen, A. 2017, MNRAS, 468, 3000

Narita, N., Fukui, A., Kusakabe, N., et al. 2015, Journal of Astronomical Telescopes, Instruments, and Systems, 1, 045001

Nespral, D., Gandolfi, D., Deeg, H. J., et al. 2017, A&A, 601, A128

Niraula, P., Redfield, S., Dai, F., et al. 2017, AJ, 154, 266

Noguchi, K., Aoki, W., Kawanomoto, S., et al. 2002, Publications of the Astronomical Society of Japan, 54, 855

Nutzman, P., & Charbonneau, D. 2008, PASP, 120, 317

Öberg, K. I., Murray-Clay, R., & Bergin, E. A. 2011, ApJL, 743, L16

Ogilvie, G. I., & Lin, D. N. C. 2007, ApJ, 661, 1180

Oscoz, A., Rebolo, R., López, R., et al. 2008, in Proc. SPIE 5487, Vol. 7014, Ground-based and Airborne Instrumentation for Astronomy II, 701447

Owen, J. E., & Wu, Y. 2013, ApJ, 775, 105

Owen, T., Mahaffy, P., Niemann, H. B., et al. 1999, Natur, 402, 269

Palle, E., Nowak, G., Luque, R., et al. 2018, ArXiv e-prints, arXiv:1808.00575 [astro-ph.EP]

Parviainen, H. 2017, Bayesian Methods for Exoplanet Science, 149

Pecaut, M. J., & Mamajek, E. E. 2013, APJS, 208, 9

Pepe, F., Mayor, M., Galland, F., et al. 2002, A&A, 388, 632

Pepe, F., Cameron, A. C., Latham, D. W., et al. 2013, Natur, 503, 377

Pepe, F. A., Cristiani, S., Rebolo Lopez, R., et al. 2010, in Ground-based and Airborne Instrumentation for Astronomy III, Vol. 7735, 77350F

Pepper, J., Pogge, R. W., DePoy, D. L., et al. 2007, PASP, 119, 923

Persson, C. M., Fridlund, M., Barragán, O., et al. 2018, ArXiv e-prints, arXiv:1805.04774 [astro-ph.EP]

Pollacco, D. L., Skillen, I., Collier Cameron, A., et al. 2006, PASP, 118, 1407

Pope, B. J. S., Parviainen, H., & Aigrain, S. 2016, MNRAS, 461, 3399

Prieto-Arranz, J., Palle, E., Gandolfi, D., et al. 2018, A&A, 618, A116

Prša, A., Harmanec, P., Torres, G., et al. 2016, AJ, 152, 41

Rafikov, R. R. 2006, ApJ, 648, 666

Rappaport, S., Sanchis-Ojeda, R., Rogers, L. A., Levine, A., & Winn, J. N. 2013, ApJL, 773, L15

Rauer, H., Catala, C., Aerts, C., et al. 2014, Experimental Astronomy, 38, 249

Reuyl, D., & Holmberg, E. 1943, ApJ, 97, 41

Ricker, G. R., Winn, J. N., Vanderspek, R., et al. 2015, Journal of Astronomical Telescopes, Instruments, and Systems, 1, 014003

Rodriguez, J. E., Vanderburg, A., Eastman, J. D., et al. 2018, AJ, 155, 72

Saar, S. H., & Donahue, R. A. 1997, ApJ, 485, 319

Safronov, V. S. 1972, Evolution of the protoplanetary cloud and formation of the earth and planets.

Sanchis-Ojeda, R., Rappaport, S., Winn, J. N., et al. 2014, ApJ, 787, 47

Sanchis-Ojeda, R., & Winn, J. N. 2011, ApJ, 743, 61

Sanchis-Ojeda, R., Winn, J. N., Holman, M. J., et al. 2011, ApJ, 733, 127

Sanchis-Ojeda, R., Fabrycky, D. C., Winn, J. N., et al. 2012, Natur, 487, 449

Schlegel, D. J., Finkbeiner, D. P., & Davis, M. 1998, ApJ, 500, 525

Schlichting, H. E. 2014, ApJ, 795, L15

Seager, S., & Deming, D. 2010, ARA&A, 48, 631

Seager, S., Kuchner, M., Hier-Majumder, C. A., & Militzer, B. 2007, ApJ, 669, 1279

Seager, S., & Mallén-Ornelas, G. 2003, ApJ, 585, 1038

Sharma, S. 2017, ARA&A, 55, 213

Silburt, A., Gaidos, E., & Wu, Y. 2015, ApJ, 799, 180

Sinukoff, E., Howard, A. W., Petigura, E. A., et al. 2016, ApJ, 827, 78

—. 2017, AJ, 153, 271

Smith, A. M. S., Cabrera, J., Csizmadia, S., et al. 2017, ArXiv e-prints, arXiv:1707.04549 [astro-ph.EP]

Southworth, J. 2011, MNRAS, 417, 2166

Southworth, J., Wheatley, P. J., & Sams, G. 2007, MNRAS, 379, L11

Sozzetti, A., Torres, G., Charbonneau, D., et al. 2007, ApJ, 664, 1190

Strand, K. A. 1943, PASP, 55, 29

Struve, O. 1952, The Observatory, 72, 199

Swedenborg, E. 1734, Principia: Philosophical and Mineralogical Works (translated by Clissold, A., Swedenborg Scientific Association, 1988)

Szabó, G. M., & Kiss, L. L. 2011, ApJ, 727, L44

Telting, J. H., Avila, G., Buchhave, L., et al. 2014, Astronomische Nachrichten, 335, 41

Teske, J. K., Wang, S., Wolfgang, A., et al. 2018, AJ, 155, 148

Thompson, S. E., Fraquelli, D., van Cleve, J. E., & Caldwell, D. A. 2016, Kepler Archive Manual

Torres, G., Andersen, J., & Giménez, A. 2010, A&ARv, 18, 67

Trifonov, T., Kürster, M., Reffert, S., et al. 2018, ArXiv e-prints, arXiv:1809.09638 [astro-ph.EP]

Valenti, J. A., & Fischer, D. A. 2005, APJS, 159, 141

Valsecchi, F., Rasio, F. A., & Steffen, J. H. 2014, ApJ, 793, L3

Van Der Walt, S., Colbert, S. C., & Varoquaux, G. 2011, ArXiv e-prints, arXiv:1102.1523 [cs.MS]

Van Eylen, V., Agentoft, C., Lundkvist, M. S., et al. 2018a, MNRAS, 479, 4786

Van Eylen, V., & Albrecht, S. 2015, ApJ, 808, 126

Van Eylen, V., Dai, F., Mathur, S., et al. 2018b, MNRAS, 478, 4866

Van Eylen, V., Albrecht, S., Huang, X., et al. 2018c, ArXiv e-prints, arXiv:1807.00549

Vanderburg, A., & Johnson, J. A. 2014, PASP, 126, 948

Vanderburg, A., Latham, D. W., Buchhave, L. A., et al. 2016, APJS, 222, 14

Vanderburg, A., Bieryla, A., Duev, D. A., et al. 2016, ApJ, 829, L9

Vogel, H. 1873, Astronomische Nachrichten, 82, 291

Vogt, S. S., Allen, S. L., Bigelow, B. C., et al. 1994, in Instrumentation in Astronomy VIII, ed. D. L. Crawford & E. R. Craine, Vol. 2198, 362

Weiss, L. M., & Marcy, G. W. 2014, ApJL, 783, L6

Winn, J. N. 2010, Exoplanet Transits and Occultations, ed. S. Seager (University of Arizona Press), 55

Winn, J. N., & Fabrycky, D. C. 2015, ARA&A, 53, 409

Wolfgang, A., & Lopez, E. 2015, ApJ, 806, 183

Wolszczan, A., & Frail, D. A. 1992, Natur, 355, 145

Wurm, G., Trieloff, M., & Rauer, H. 2013, ApJ, 769, 78

Xie, J.-W., Dong, S., Zhu, Z., et al. 2016, Proceedings of the National Academy of Science, 113, 11431

Zeng, L., & Sasselov, D. 2013, PASP, 125, 227

Zeng, L., Sasselov, D. D., & Jacobsen, S. B. 2016, ApJ, 819, 127